THE UNIVERSITY of EDINBURGH

This thesis has been submitted in fulfilment of the requirements for a postgraduate degree (e.g. PhD, MPhil, DClinPsychol) at the University of Edinburgh. Please note the following terms and conditions of use:

Self-Assembly of Rod-Like Colloids
at the Air-Water Interface

Li Tao

Doctor of Philosophy

The University of Edinburgh

2016

Abstract

Two-dimensional (2D) colloidal materials and their assembly are of scientific significance and industrial importance. The development of 2D colloidal structures is a key stepping stone towards three-dimensional (3D) structures in relation to controlled chemical composition, morphology, assembly and so on. Nowadays, uniform colloidal structures with complexity in both shape and interactions have become a popular topic in fundamental colloid science and applications.

Being motivated by this, in this thesis, micro-scale colloidal rods and self-assembled dipeptides have been studied experimentally at the air-water interface. Monolayers containing these colloidal materials were created in a Langmuir trough. Surface pressure measurements, microscopic observations and many other techniques were combined for the investigation. The aim of this work is to understand the phase behaviours in complex monolayers, including the phase transitions during compression, the flipping dynamics of micro-rods, the contribution of dipole-dipole interactions between magnetic rods, and the interfacial self-assembly process of dipeptide molecules.

Iron oxide micro-rods (β-FeOOH @silica) with different aspect ratios have been synthesized to create the monolayers at an air-water interface. Microscopic observations reveal a sequence of phase transitions by compressing the monolayers. It has been proved that the aspect ratio of the rods plays an important role in the phase transitions, —short rods flip into a perpendicular position relative to the interface to relieve the compressional stress, while longer rods form multilayers under compression. Magnetic rods (Fe_3O_4) were converted from the synthesized FeOOH rods. They can be aligned in an external field, which further induces the reorganization at the interface. To study these magnetic rods, differential dynamic microscopy (DDM) was carried out to measure the magnetic moment. Their interfacial properties were investigated in an external field applied perpendicular and parallel to the interface, respectively. A magnetic field-induced flipping process has been observed, which proves the theoretical prediction.

Besides rod-like particles, naphthalene dipeptides have been successfully trapped at the interface of a low pH subphase, self-assembling into a hydrogel film. The mechanism of interfacial self-assembly has been studied. Both FTIR spectra and AFM images are used to investigate the fibrous structures of the film. The film has elastic properties and buckles under compression. Moreover, dipeptide hydrogel induced by metal ions has been used to create a wet foam system, which owns the advantages of long-term stability (more than two weeks), low cost, and easy preparation.

Lay Summary

Nowadays, liquid interfaces have been found to be an important stage for many interesting physical/biological processes. For example, mosquito eggs hatch on the water surface, and the resulting aquatic larvae feed from bacteria or microorganisms present in water. Here, the water surface is crucial for the development of these eggs. Having been suggested by these ellipsoid-shaped eggs, scientists investigated the self-assembly of ellipsoid particles at the air-water interface, which can be used in foam stabilization or other applications.

Using the air-water interface as a stage, this thesis studied the behaviours of micro-scale rod-like materials when they were spread at the interface. The results presented in the thesis can be divided into two parts. The first part investigated the interfacial properties of spherocylinders (cylinders capped by hemispherical ends) in a trough under compression. It has been found that these particles can form a monolayer at the interface, and the formed monolayer behaves different when the particles get longer. Spherocylinders with magnetic moment have been studied at the air-water interface as well.

The second part of this thesis focuses on the self-assembled dipeptide molecules. This is a material that can form a hydrogel in bulk when the pH is low. We created a hydrogel film at the air-water interface. This is an elastic film which can be used to stabilize large air bubbles. Furthermore, we created a wet foam system with a long-term stability using these dipeptide molecules as stabilizers.

Declaration

I declare that this thesis was composed by myself, that the work contained herein is my own except where explicitly stated otherwise in the text, and that this work has not been submitted for any other degree or professional qualification except as specified.

Parts of this work have been published in:

[1] Li T.; Brandani, G.; Marenduzzo, D.; Clegg, P. S. Colloidal spherocylinders at an interface: flipper dynamics and bilayer formation, *in preparation*. – Chapter 3

[2] Li, T.; Kalloudis, M.; Cardoso, A. Z.; Adams, D. J.; Clegg, P. S. Drop-Casting Hydrogels at a Liquid Interface: The Case of Hydrophobic Dipeptides. *Langmuir* **2014**, *30*, 13854–13860. – Chapter 5

[3] Li, T.; Nudelman, F.; Tavacoli, J. W.; Vass, H.; Adams, D. J.; Lips, A.; Clegg, P. S. Long-Lived Foams Stabilized by a Hydrophobic Dipeptide Hydrogel. *Adv. Mater. Interfaces*, **2016**, *3*, 1500601. – Chapter 6

(*Li Tao, 2016*)

Acknowledgements

On 31st January 2012, an email from Jane Patterson started my PhD. Now, four years later, as my PhD is drawing to a close, I would like to express my gratitude for my wonderful stay in Edinburgh University.

I am very privileged to work with my supervisor Paul Clegg. His encouragement and guidance ensured the smoothness of my project. He also provided a great deal of help in my daily life. For me, Paul is a real mentor, and a respectable friend.

At the beginning of my PhD, I received some great help from Niek Hijnen, who became a close friend of my life. I am also very lucky to have Andy Schofield during my PhD study. He is the most trusted chemist in our group, and always be there for assistance. Dr. Jochen Arlt and Mr. Andrew Garrie built an observational setup for my experiments, which is vitally important for my entire project. I am grateful for their efforts.

I would like to thank Professor Dave J. Adams from the University of Liverpool for offering the dipeptides, as well as his contributions to our published papers. Thanks to Dr. Vincent Martinez for the DDM measurements, Dr. Joe Tavacoli for the rheology experiments, Steve Mitchell for his assistance with the TEM, Dr. Michail Kalloudis for the help with AFM, and Dr. Fabio Nudelman for the cryo-SEM analysis.

As a Chinese student, I was afraid that integrating into the Western lifestyle would be very difficult. However, the reverse is true. I made a lot of true friends. Among them, Giovanni Brandani is my officemate, co-worker, and bosom friend. Ionut Magdau, this clever boy has moved to the US and started a new life. I am thankful to Ben Guy, Petra, Dario, Alex, Iain, Yuan Meng, Jagath, and Susana for being friend with me. I also want to thank all my badminton, squash and frisbee teammates. The amazing moments we shared will never be forgotten. Last but not the least, to my flatmates, Ben Little and Iris Coe, I love both of you so very much. May the friendship between us last forever.

My PhD was supported by Chinese Scholarship Council (CSC)/University of Edinburgh Scholarships. Dr. Michiel Hermes, Elena Blanco, Andy Schofield, Keith Bromley, Teun Vissers and Nick Koumakis advanced some modifications for this thesis. I am really thankful to all of them for their time and energy.

Finally, I am so appreciated to thanks for my great parents and all my family members. I could not make any achievement without their support. Here, I would like to extend my best regards to all my family, and wish them sound and healthy.

Contents

Chapter 1

Introduction

This chapter first gives a general introduction to the main topics investigated in the current study, including colloids, self-assembly and Langmuir films. Subsequently, the emphasis in this thesis is briefly described. At the end of this chapter, there is an outline of the topics discussed in each chapter of the thesis.

1.1 Colloids

Since Thomas Graham first introduced the word "colloid" in 1861 [1], colloidal systems have made an indispensable contribution to physical chemistry, advanced materials and nanotechnology. Generally, a colloid can be described as a system that small particles are distributed evenly throughout another continuous phase. The small particles are usually in the size-range from 1 nanometer (nm) to 10 micrometers (μm), while the continuous phase can be a solid, liquid or gaseous medium.

When the dispersed particles and the continuous phase are both liquid, the colloid is called an emulsion, which exists in many food products (*e.g.*, milk). Foam can also be considered as colloidal systems where gas particles dispersed in a liquid. Another kind of colloid is classified as sols, which consist of solid particles distributed in liquid phases. It should be noted that nowadays, the meaning of the term "colloid" has been considerably broadened. Solutions of polymers and proteins have been recognized as colloids, whilst surfactants and peptide molecules can self-assemble into colloidal objects.

Colloids have been used in many area of industry. They exist in our food, drinks and personal products. As a result, the study of colloids is important in industry and our daily life. Of course, colloid science has been a popular field of research with a long history. However, in the past few years, novel synthesis strategies have led to a

spectacular development of synthesis procedures for colloidal particles with different shapes, compositions, patterns and functionalities [2]. Figure 1.1, taking the example of metal particles, summarizes the shapes that have been achieved so far. Anisotropic particles, including Janus particles, arrows, rods, starts and many other exotic structures, exhibit many peculiar properties because of their unusual shape and interactions. This further extends the applications of colloids in self-assembly, magnetic storage [3, 4], and even future materials [2].

Structures	Shapes	Schematic drawings	Metals
single-crystal	perfect/truncated cube[a]		Pd, Ag, Au, Pt, Cu, Rh, Bi, Fe
	perfect/truncated octahedron[a]		Pd, Ag, Au, Pt
	perfect/truncated tetrahedron[a]		Ag, Au, Pt, Rh
	rectangular bar		Pd, Ag, Pt
	octagonal rod		Pd, Au, Fe, Co, Ni
	rectangular or octagonal wire		Pb, In, Sn, Sb, Fe, Co
singly twinned	right bipyramid		Pd, Ag
	beam		Ag
multiply twin-ned	decahedron[a]		Pd, Ag, Au
	icosahedron[a]		Pd, Au
	five-fold twinned pentagonal rod		Pd, Ag, Au, Cu
	five-fold twinned pentagonal wire		Ag, Au, Cu
	triangular/hexagonal plate		Pd, Ag, Au, Cu, Pb, Bi, Co, Ni
	disc		Sn, Co

[a] Platonic solid.

Figure 1.1 *A summary of different shapes that have been synthesized for metal colloidal particles. Taken from [5].*

Anisotropic colloidal materials, *e.g.*, rod-like solid particles and self-assembled dipeptide molecules, are the main subjects of this thesis. Compared to their spherical counterparts, these materials lead to exciting possibilities. For example, anisotropic magnetic particles are easily manipulated by an external field, and the corresponding orientation can be visualized by simple optical techniques. Besides, some spatially complex structures might be formed by these anisotropic building blocks via self-assembly.

1.2 Self-Assembly

Self-assembly is a phenomenon which can be harnessed to organize the nano or micro size building blocks into required and/or functional structures, making them important in condensed matter and advanced materials (Figure 1.2a). Self-assembly processes involve different kinds of components and interactions, and are common throughout nature and technology. It is also believed that self-assembly offers great potential for future applications, such as robotics and three-dimensional (3D) microsystems [6].

Generally, there are two main kinds of self-assembly processes: dynamic self-assembly and static self-assembly [6]. Dynamic self-assembly is able to form non-equilibrium structures which are maintained far from equilibrium by dissipating useful energy [7]. Such structures can be assembled in low entropy systems, and is of fundamental interest in the context of life (*e.g.*, mitosis in cells). Static self-assembly, however, refers to the formation of stable quiescent structures without a supply or subsequent dissipation of energy. Most folded proteins are formed by static self-assembly. It should be noted that in static self-assembly, extra energy might be needed to form the ordered structures, but once formed, they are stable. Besides, recent studies also use physical templates and external field to direct the self-assembly processes. They are classified as templated and field-directed self-assembly, respectively [7].

Self-assembly occurs not only in the bulk, but also at liquid interfaces. Colloidal particles can assemble into two-dimensional (2D) colloidal crystals using liquid interfaces as platforms, where the dominating driving force could be the reduction in interfacial energy, and the lateral capillary interactions between the particles [8]. This
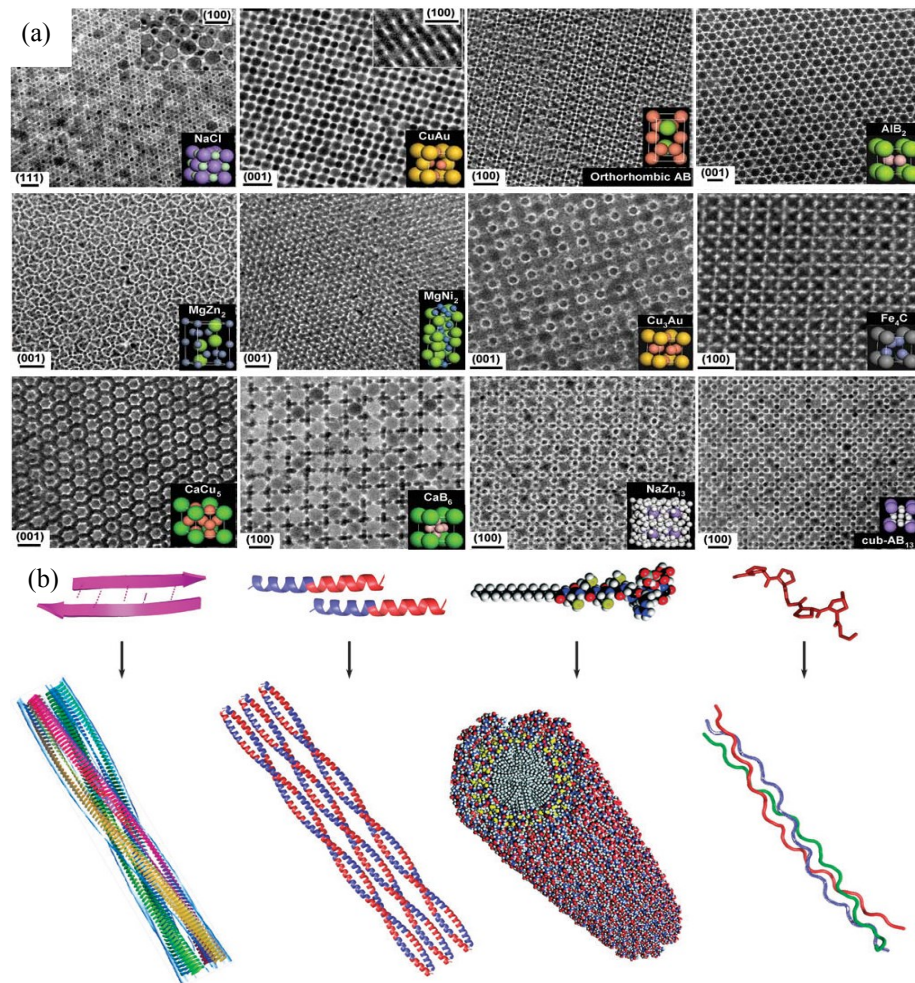
***Figure 1.2** (a) TEM images of the characteristic projections of some binary superlattices, self-assembled from different nanoparticles, and modelled unit cells of the corresponding 3D structures. Taken from [10]. (b) Different types of peptide-based self-assembling fibrous biomaterials, including Amyloid-like assemblies, α-Helical assemblies, peptide amphiphiles and collagen-like assemblies. More information can be found in [11].*

has been evidenced by the ability of these particles to stabilize emulsions and foams against decomposition [9]. For anisotropic particles, more complex 2D structures can be formed at liquid interfaces. It has been demonstrated that these complex structures can impart superior mechanical stability to liquid droplets and air bubbles. Moreover, the orientation and packing structures of anisotropic particles at liquid interfaces are much more complicated than their spherical counterparts, which can be affected by controlling the aspect ratio, surface properties, concentration and surface pressure [8]. A better understanding of the interfacial behaviours of anisotropic colloidal particles is one of the primary objectives of this thesis.

By static self-assembly, some peptide molecules can form fibre-like structures, i.e., amyloid fibrils (Figure 1.2b). It is believed that most of the peptide molecules adopt β-sheet secondary structure, thus driving assembly into cylindrical fibres as opposed to spherical shapes. Amyloid fibrils are highly ordered peptide aggregates with high mechanical and chemical stability, and find several applications in nanotechnology [12, 13]. On one hand, these fibre-like structures exhibit anisotropic properties similar to the rod-like colloidal particles because of the shape effect. On the other hand, the extensive hydrogen bonding and π-π stacking interactions between the fibres can drive the self-assembly process even further. As a result, besides forming a colloid in a solvent, these fibre-like structures can also cross-link with each other to form a hydrogel. This is also a self-assembly process, which is called gelation, and is commonly induced by temperature, pH, salt or solvent composition. The bulk behaviour of hydrogel has been investigated both in experiments [14-16] and computer simulations [17, 18]. Here, in this thesis, self-assembled dipeptide molecules are gelated at liquid interfaces. Their interfacial properties are investigated, as well as their application prospects in foam stability.

1.3 Langmuir Films

The study of colloidal materials at liquid interfaces basically involves the formation of Langmuir films. A Langmuir film is usually understood to be a monomolecular layer of surface-active organic substances at a liquid-liquid interface or gas-liquid interface. Nowadays, colloidal monolayers and molecular multilayer structures at liquid interfaces can also be called Langmuir films. When such a film is transferred onto a solid substrate, it is known as a Langmuir-Blodgett film.

Amphiphilic materials, such as lipids [19], surfactants, as well as some proteins [20], can form a Langmuir film easily at the air-water interface. The hydrophobic tail of the amphiphile can be insoluble in water while its hydrophilic head facilitates spreading and makes sure it stay at the interface. For colloidal particles, special surface modification might be needed to change their surface hydrophobicity. When colloidal particles are spread on a liquid surface, they can normally form a Langmuir film with
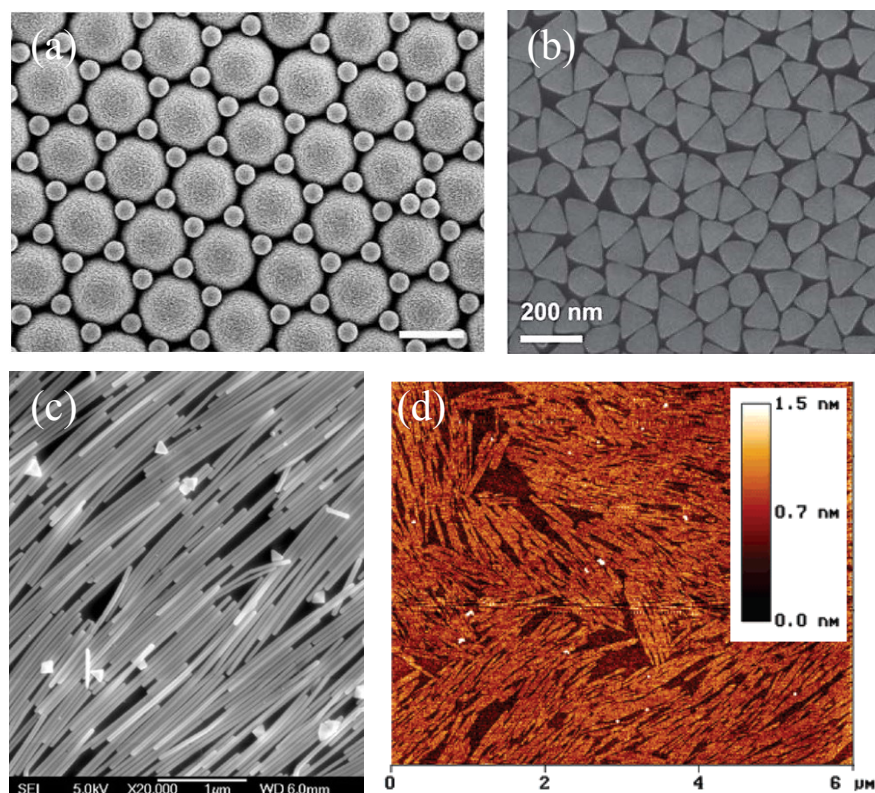
Figure 1.3 *(a) Co-crystallization of binary monolayer consisting of small and large spheres. The scale bar is 1 μm* [24]*. (b) SEM image of a nanoprism monolayer* [25]*. (c) SEM image of a silver nanowire monolayer* [26]*. (d) AFM image of an amyloid peptide (12 amino acidpeptide, LSFDNSGAITIG-NH2) monolayer* [27]*.*

one particle thickness, *i.e.*, a monolayer. Particle monolayers have received special attention due to the variety of uses such as photonic crystals [21] and chemical sensors [22]. Moreover, monolayers of ordered colloidal particles have the potential to be applied industrially, including optical devices and physical masks [23]. So far, various monolayers containing colloidal particles with many different sizes and shapes have been prepared in the laboratory (Figure 1.3a-c) [24-27].

As mentioned before, self-assembly of peptide molecules can also occur at liquid interfaces. This opens up the possibility to create a Langmuir film with hydrogel properties, *i.e.*, a hydrogel film (Figure 1.3d). Although the study of hydrogel films is a relatively new field of research, great progress has been made in recent years. It has been pointed out that the potential of hydrogel films is not yet exploited and there are virtually endless opportunities for the development of new functional devices and "smart" materials from these building blocks.

1.4 Emphasis in This Thesis

As mentioned above, 2D colloidal materials and their assembly are of scientific significance and industrial importance because of their unique size- and dimension-dependent mechanical and optical properties, and also their promising applications as a superlattice in sensors, biomedical applications, magnetic storage media and so on. It is believed that the development of 2D colloidal structures is the key stepping stone towards three-dimensional (3D) structures in relation to controlled chemical composition, morphology, dimensionality, phase purity, and assembly. Furthermore, it is also believed that the development of uniform colloidal structures with complexity in both shape and interactions will ultimately enable significant advances in fundamental colloid science and applications.

As a matter of fact, colloid shape and interactions affect the fundamental aspects of their behaviour. At liquid interfaces, monolayers containing anisotropic particles found applications in "Pickering" emulsions, foams and biological systems [28-33]. Although experiments have shown that anisotropic particles can improve the stability of liquid droplets or air bubbles, the relationship between the structural changes and the possible colloidal phenomena still need to be understood. For example, when a monolayer containing microscale ellipsoids is compressed, it undergoes a series of phase transitions due to the reduction in area available for each particle. Much attention has been paid over the years to probe respectively structure and thermodynamics of these phase transitions. Besides, the various catastrophes which occur as the rod-like particles are forced beyond the point of maximum packing remain to be documented and understood. So, colloidal materials with anisotropic shape and interactions have brought new excitement and also challenges to the field of 2D self-assembly.

This thesis, being motivated by this, specifically focuses on the self-assembly of microscale rod-like colloids at liquid interfaces. In the first part of this thesis, we experimentally explore the behaviour of spherocylinders, rather than ellipsoids or cylinders, at liquid interfaces, both under compression and in magnetic fields. The phase transition process in their monolayers is found to be different form another two rod-like particles. The role played by aspect ratio is discussed in details. Moreover,

microscopic observations combined with numerical simulations (done by others) are carried out to study the behaviour beyond maximum packing. Magnetic rods, which can be aligned by an external field, are also investigated at the air-water interface. A DDM method (differential dynamic microscopy) is used to measure the magnetization. The formed magnetic monolayers can be used to stabilize some oil-in-water droplets with magnetic properties.

In the second part, we created a hydrogel film at the air-water interface by drop casting, showing that the dipeptide molecules assemble into fibre-like strands in the spreading solution, so they attach to the water-air interface as colloidal entities. The resulting hydrogel films exhibit some elastic properties, which can be used to stabilize large air bubbles for several days, i.e. we also used this dipeptide hydrogel to create wet foams with long-term stability.

1.5 Thesis Outline

Chapter 2 reviews the theoretical background to the topics of the thesis. Based on existing literature, the interfacial properties of different colloidal materials (*i.e.*, rod-like particles, self-assembled dipeptide molecules) have been presented, which provides a basis for presenting and discussing the results.

The results are divided into two parts. In the **results part I**, micro-scale spherocylinders are synthesized and spread at the air-water interface to form a monolayer. **Chapter 3** focuses on the compressed monolayers of rods with different aspect ratios, while **Chapter 4** presents a preliminary study about the interfacial properties of magnetic rods in an external field. The **result part II** studies the self-assembly of dipeptide molecules at the air-water interface. Specifically, **Chapter 5** presents a drop-casting method to form an elastic hydrogel film, and **Chapter 6** demonstrates a long-lived wet foam stabilized by the self-assembled dipeptides.

After the results part, **Chapter 7** summarizes the conclusions and provides a general outlook.

References:

[1] Liquid Diffusion Applied to Analysis, Thomas Graham, Philosophical Transactions of the Royal Society of London, **1861**, *151*, 183–224.

[2] Glotzer, S. C.; Solomon, M. J. Anisotropy of building blocks and their assembly into complex structures. *Nat. Mater.* **2007**, *6*, 557–562.

[3] Lemaire, B. J.; Davidson, P.; Ferré, J.; Jamet, J. P.; Panine, P.; Dozov, I.; Jolivet, J. P. Outstanding Magnetic Properties of Nematic Suspensions of Goethite (α-FeOOH) Nanorods. *Phys. Rev. Lett.* **2002**, *88*, 125507.

[4] Zeng, H.; Li, J.; Liu, J. P.; Sun, S. Exchange-coupled nanocomposite magnets by nanoparticle self-assembly. *Nature* **2002**, *420*, 395–398.

[5] Xia, Y.; Xiong, Y.; Lim, B.; Skrabalak, S. E. Shape-Controlled Synthesis of Metal Nanocrystals: Simple Chemistry Meets Complex Physics? *Angew. Chem., Int. Ed.* **2009**, *48*, 60–103.

[6] Whitesides, G. M.; Grzybowski, B. A. Self-assembly at all scales. *Science*, **2002**, *295*, 2418–2421.

[7] Grzybowski, B. A.; Wilmer, C. E.; Kim, J.; Browne, K. P.; Bishop, K. J. M. Self-assembly: from crystals to cells. *Soft Matter*, **2009**, *5*, 1110–1128.

[8] Grzelczak, M.; Vermant, J.; Furst, E. M.; Liz-Marzan, L. M. Directed Self-Assembly of Nanoparticles. *ACS nano*, **2010**, *4*, 3591–3605.

[9] Morrison, I. D.; Ross, S. Colloidal Dispersions: Suspensions, Emulsions, and Foams; Wiley-Interscience: New York, **2002**.

[10] Shevchenko, E. V.; Talapin, D. V.; Kotov, N. A.; O'Brien, S.; Murray, C. B. Structural diversity in binary nanoparticle superlattices. *Nature*, **2006**, *439*, 55–59.

[11] Woolfson, D. N.; Mahmoud, Z. N. More than just bare scaffolds: towards multi-component and decorated fibrous biomaterials. *Chem. Soc. Rev.*, **2010**, *39*, 3464–3479.

[12] Maity, I.; Mukherjee, T. K.; Das, A. K. Photophysical Study of a π-stacked β-sheet Nanofibril Forming Peptide Bolaamphiphile Hydrogel. *New J. Chem.*, **2014**, *38*, 376–385.

[13] Mankar, S.; Anoop, A.; Sen, S.; Maji, S. K. Nanomaterials: Amyloids Reflect Their Brighter Side. *Nano Rev.*, **2011**, *2*, 6032.

[14] Dudukovic, N. A.; Zukoski, C. F. Mechanical Properties of Self-Assembled Fmoc-Diphenylalanine Molecular Gels. *Langmuir* **2014**, *30*, 4493−4500.

[15] Chen, L.; Morris, K.; Laybourn, A.; Elias, D.; Hicks, M. R.; Rodger, A.; Serpell, L.; Adams, D. J. Self-assembly mechanism for a naphthalene-dipeptide leading to hydrogelation. *Langmuir* **2010**, *26*, 5232–5242.

[16] Piepenbrock, M.-O. M.; Lloyd, G. O.; Clarke, N.; Steed, J. W. Metal- and Anion-Binding Supramolecular Gels. *Chem. Rev.* **2010**, *110*, 1960–2004.

[17] Lee, O. S.; Cho, V.; Schatz, G. C. Modeling the Self-Assembly of Peptide Amphiphiles into Fibers Using Coarse-Grained Molecular Dynamics. *Nano Lett.* **2012**, *12*, 4907−4913.

[18] Kubelka, J.; Keiderling, T. A. Differentiation of β-sheet-forming structures: ab initio-based simulations of IR absorption and vibrational CD for model peptide and protein β-sheets. *J. Am. Chem. Soc.* **2001**, *123*, 12048−12058.

[19] McConnell, H. M. Structures and transitions in lipid monolayers at the air-water interface. *Annu. Rev. Phys. Chem.* **1991**, *42*, 171−195.

[20] Cicuta, P. Compression and shear surface rheology in spread layers of beta-casein and beta-lactoglobulin. *J. Colloid Interface Sci.* **2007**, *308*, 93–99.

[21] Ozin, G. A.; Yang, S. M. The Race for the Photonic Chip: Colloidal Crystal Assembly in Silicon Wafers. *Adv. Funct. Mater.* **2001**, *11*, 95–104.

[22] Joseph, Y.; Besnard, I.; Rosenberger, M.; Guse, B.; Nothofer, H.-G.; Wessels, J.-M.; Ute, W.; Knop-Gericke, A.; Su, D.; Schlo¨gl, R.; Yasuda, A.; Vossmeyer, T. Self-assembled Gold Nanoparticles/Alkanedithiol Films: Preparation, Electron Microscopy, XPS-Analysis, Charge Transport, and Vapor-Sensing Properties. *J. Phys. Chem. B* **2003**, *107*, 7406–7413.

[23] Okubo, T.; Chujo, S.; Maenosono, S; Yamaguchi, Y. Microstructure of silica particle monolayer films formed by capillary immersion force. *J. Nanopart. Res.* **2003**, *5*, 111–117.

[24] Vogel, N.; de Viguerie, L.; Jonas, U.; Landfester, K.; Weiss, C. K. Wafer-Scale Fabrication of Ordered Binary Colloidal Monolayers with Adjustable Stoichiometries. *Adv. Funct. Mater.* **2011**, *21*, 3064–3073.

[25] Lee, Y. H.; Lee, C. K.; Tan, B.; Rui Tan, J. M.; Phang, I. Y.; Ling, X.Y. Using the Langmuir-Schaefer Technique to Fabricate Large-Area Dense SERS-Active Au Nanoprism Monolayer Films. *Nanoscale* **2013**, *5*, 6404–6412.

[26] Tao, A.; Kim, F.; Hess, C.; Goldberger, J.; He, R.; Sun, Y.; Xia, Y.; Yang, P. Langmuir−Blodgett Silver Nanowire Monolayers for Molecular Sensing Using Surface-Enhanced Raman Spectroscopy. *Nano Lett.*, **2003**, *3*, 1229–1233.

[27] Lepère, M.; Chevallard, C.; Hernandez, J.; Mitraki, A.; Guenoun, P. Multiscale Surface Self-Assembly of an Amyloid-like Peptide. *Langmuir* **2007**, *23*, 8150–8155.

[28] Kalashnikova, I.; Bizot, H.; Cathala, B.; Capron, I. New Pickering Emulsions Stabilized by Bacterial Cellulose Nanocrystals. *Langmuir* **2011**, *27*, 7471–7479.

[29] Capron, I.; Cathala, B. Surfactant-free high internal phase emulsions stabilized by cellulose nanocrystals. *Biomacromolecules* **2013**, *14*, 291−296.

[30] Zhou, W. Z.; Cao, J.; Liu, W. C.; Stoyanov, S. How Rigid Rods Self-Assemble at Curved Surfaces. *Angew. Chem. Int. Ed.* **2009**, *48*, 378–381.

[31] Alargova, R. G.; Warhadpande, D. S.; Paunov, V. N.; Velev, O. D. Foam superstabilization by polymer microrods. *Langmuir* **2004**, *20*, 10371−10374.

[32] Madivala, B.; Fransaer, J.; Vermant, J. Self-Assembly and Rheology of Ellipsoidal Particles at Interfaces. *Langmuir* **2009**, *25*, 2718−2728.

[33] Thiruvengadathan, R.; Korampally, V.; Ghosh, A.; Chanda, N.; Gangopadhyay, K.; Gangopadhyay, S. Nanomaterial processing using self-assembly-bottom-up chemical and biological approaches. *Rep. Prog. Phys.* **2013**, *76*, 066501.

Chapter 2

Theoretical Background

This chapter reviews the existing literatures which sets the scene for the results presented later in this thesis. Section 2.1 and 2.2 focus on particle monolayers at liquid interfaces. The interfacial behaviours of three different rod-like particles are compared. The mechanism of the flipping phenomenon is also discussed. Section 2.3 first provides the theoretical background associated with the dipeptide hydrogel, and then introduces the recent progress made on 2D hydrogel films. Section 2.4 discusses the mechanisms of foam stability, which is helpful for understanding the long-lived wet foams demonstrated later in the thesis.

2.1 Particle Monolayer and Langmuir-Blodgett (LB) Technique

As described in the introduction, monolayers of colloidal particles are of both fundamental and practical importance. A particle monolayer is often formed on a gas-liquid interface or a liquid-liquid interface, as a Langmuir film. Experiments mainly use micrometer-size particles to allow direct observation by microscope. To study the monolayers of nanoscale particles, transferring them onto a solid substrate is normally necessary. There has been a great interest in the behaviour of particle monolayers, including the phase transition process, particle interactions and the deliberate control of organization. Several techniques, including phase contrast microscopy, light scattering, Brewster angle microscopy and LB techniques have been used to probe respectively structure and thermodynamics in these monolayers.

Surface tension is an important factor in the behaviour of particle monolayers at a liquid interface. Surface tension is the work (or energy) required to increase the surface area of a liquid due to the cohesive forces between surface molecules. The cohesive

forces vary depending on the nature of the liquid. Take water for example, its surface tension is 72.8 mN/m at 20 ºC, which is higher compared to that of most other liquids. Once covered by a monolayer, the complex interface would have a reduced surface tension.

Three important aspects regarding interfacial properties of particle monolayers are: the role of particle-particle interactions in modifying the surface tension in compression experiments; the ability to change their conformation during compression; the interaction between the adsorbed particles. The measurement of surface pressure can give information about all these aspects. Surface pressure refers to the change of the measured surface tension as a function of the subphase area available to each particle at the interface. When the available area is large, the interactions between adjacent interfacial particles are weak. In this case, the particles have little effect on the surface tension of the subphase and can be regarded as a two-dimension gas. If the available surface area is reduced, the adsorbed particles start to exert a repulsive effect on each other and lead to a reduction in surface tension. Surface pressure Π, is given by the following equation:

$$\Pi = \gamma_o - \gamma \tag{2.1}$$

where γ_o is the surface tension of the subphase without a monolayer, and γ is the surface tension with the monolayer present. In other words, surface pressure is the difference in surface tension measured between a clean liquid surface and a monolayer-covered surface.

Langmuir-Blodgett (LB) technique is the most common method to deposit particle monolayers at a liquid interface and measure the surface pressure change upon compression (or expansion). This methodology allows the continuous variation of particle density, spacing, and arrangement by compressing (or expanding) the films. So, it opens up the possibility of preparing reproducible monolayers with the control of interparticle distance. This method also permits the creation of a monolayer containing colloidal particles with different size and shape, and allows interesting structures to be assembled [1]. Furthermore, it is the most commonly used method for exploring the surface pressure of a given system.
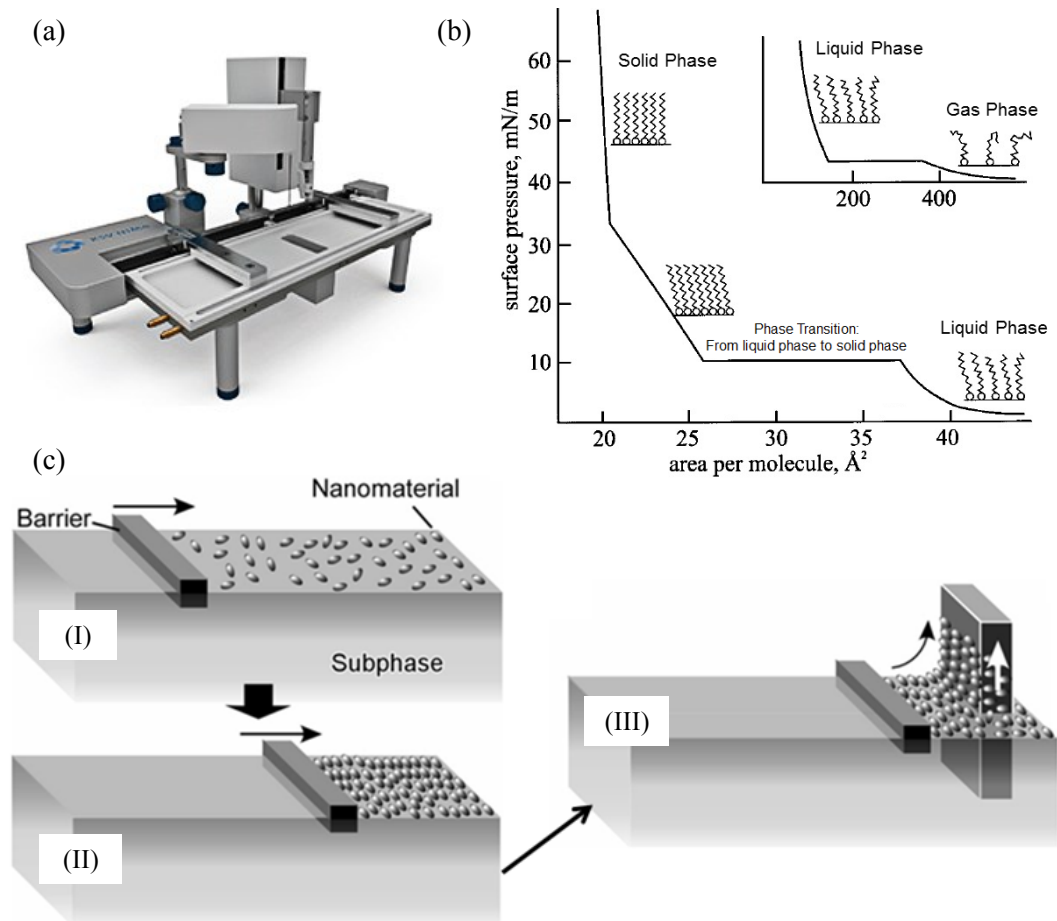
Figure 2.1 *(a) A Langmuir trough. (b) A typical Π- A isotherm of glycerophospho-lipid monolayer at air-water interface. (c) LB technique for hard nanomaterials: (I) compression of the materials by a barrier (or two barriers) at the air-water interface; (II) the formation of a solid phase of the monolayer; (III) the monolayer can be transferred onto a solid substrate. Taken from [4].*

The instrument behind LB technique is called Langmuir trough (Figure 2.1a), which contains a set of barriers and a surface pressure sensor. In this trough, a monolayer can be created by spreading the amphiphilic particles on the liquid surface. The monolayer can then be dynamically manipulated by compression or expansion with the barriers. Usually, a surface pressure-area isotherm (Π-A isotherm) is recorded at constant temperature by compressing the monolayer at a constant rate. Several distinct regions are apparent on examining the isotherm, which are called phases. As mentioned above, a monolayer could be regarded as a two-dimension gas when the available area is large, so a Π-A isotherm always starts with a gas phase. By compressing the monolayer, a typical isotherm can progress through the gas phase to a liquid phase, and then a solid

phase (Figure 2.1b). In the liquid phase, molecules become more closely packed and start to interact with each other. After that, the surface pressure increases dramatically at the solid phase, where the particles are close to their maximum packing. Depending on the size, shape and surface chemistry of the material being studied, as well as the properties of the subphase (*e.g.*, the temperature or pH), the shape of the Π-A isotherm would be different in detail [2, 3].

Figure 2.1c shows the working process of a Langmuir trough for hard nanomaterials. The organization of the monolayer components is affected strongly by the application of surface pressure since typical two-dimensional surface pressure of a Langmuir monolayer is of the order of a few dozen megapascals [4]. For micro sized or nano sized particles, ordered arrays are achieved at high surface pressure, which are also greatly affected by particle size, shape and surface chemistry. As the area of the monolayer is changed by controlling the barriers, the space between particles changes as well. This makes it possible to observe the transition from non-interacting to interacting particle arrays. The interaction of one-dimensional rod-like particles within a Langmuir monolayer is currently the focus of intense research and will be discussed in detail later in this thesis.

LB technique has been shown to be a low-cost, high-throughput and easy operating method for the controlled assembly and patterning of both organic and inorganic materials. In addition to the surface pressure measurement, LB technique can also be used to make films for the fabrication of nanoscale electronics such as graphene sheets, or to make the films into biological materials to improve cell adhesion or research the properties of biofilms [5].

2.2 Rod-Like Particles at Liquid Interfaces

For an isolated spherical particle of micro- or nanometer scale, once it has been adsorbed at a liquid interface, the free energy of the system is changed since the surface energies are rebalanced [6]. Take air-water interface (Figure 2.2a), for example, the corresponding free energy change, or the trapping energy, can be expressed as:

$$\Delta E = -\gamma(A_{a-w} - A_{p-a} \cos \theta_c) \qquad (2.2)$$

where γ is the surface tension, θ_c is the contact angle, A_{a-w} is the area reduction of air-water interface, and A_{p-a} is the area of the particle exposed to air. For spherical particles, both A_{a-w} and A_{p-a} can be given in terms of its radius and θ_c. In this case, the trapping energy can be up to $10^7 \, kT$ for a micro-sphere. This is also the reason that micron size particles with finite contact angles can be irreversibly adsorbed at the interface. This equation, however, is only valid for isolated particles, and hence can be used for low surface coverage. In a dense monolayer, the trapping energy should also include surface pressure contributions (*e.g.* the work done against the repulsive forces between the particles) [6]. Properties of monolayers containing spherical particles have been studied previously, such as the effects of particle size [4] and hydrophobicity [7]. A buckling transition has also been observed when a sphere monolayer is compressed [8].

Shape can fundamentally change structure and properties of colloidal systems [9]. From a purely geometrical viewpoint, the condition of a constant contact angle (θ_c) at a three-phase contact line (as required by Young's equation), cannot be met for most anisotropic particles if the contact line remains flat. In this case, the interface need to be distorted. It is believed that the particle shape plays an important role in determining non-planar contact lines [10, 11]. The resulting interfacial distortion are the source of capillary interactions between the particles. Besides, large aspect ratio can lead to a low maximum random jammed packing density [12], which is helpful to control and to quantify characteristics like surface viscosity and surface moduli. Both experiments and simulations have revealed important effects of particle shape on equilibrium phase behaviour [13-15], packing [16-19], rheology [10, 20, 21] and structures formed by self-assembly [22, 23].

This section reviews the interfacial properties of colloidal particles, mainly focusing on micron scale rod-like particles. Three different kinds of rod-like particles, *i.e.* cylinders, ellipsoids and spherocylinders, as well as their interfacial properties are introduced in turn. Capillary interactions between these particles are also discussed. At the end of this section, flipping phenomenon is presented. This corresponds a 90-degree rotation of a particle, which makes its major axis perpendicular to the interface.
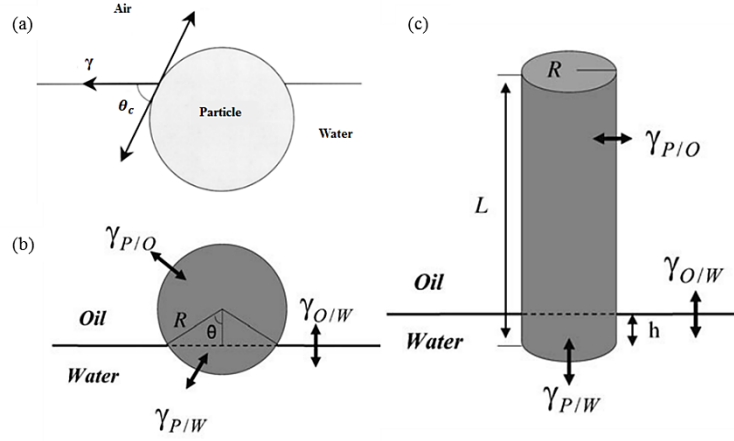
Figure 2.2 *(a) A spherical particle adsorbed onto a flat air-water interface. (b, c) An isolated cylinder oriented parallel (b) and perpendicular (c) to the oil-water interface. Taken from [29].*

2.2.1 Cylinders at liquid interfaces

For individual cylinders, the dependence of their trapping energy has been investigated previously [9, 24-26]. These studies pointed out that the equilibrium orientation with the minimum energy is the one in which the single cylinder makes the largest area reduction of the liquid interface. Experiments confirmed that cylinders with very small aspect ratio (or finite thickness disks) adsorb in an end-on state, with its major axis perpendicular to the interface; while long cylinders mostly orient side-on, with its major axis parallel to the interface. The trapping energy for an isolated cylinder at the oil-water interface has been calculated [27-29], which complicates equation 2.2 as:

$$\Delta E_{/\!/} = 2\pi RL[\pi(\gamma_{p/o} - \gamma_{p/w}) + \theta_c(\gamma_{p/w} - \gamma_{p/o}) + \gamma_{o/w}\sin\theta_c], \qquad (2.3)$$

$$\text{where} \quad \cos\theta_c = \frac{\gamma_{p/w} - \gamma_{p/o}}{\gamma_{o/w}} \qquad (\text{L} >> \text{R}),$$

$$\Delta E_{\perp} = \pi R^2(\gamma_{p/w} - \gamma_{o/w} - \gamma_{p/o}) + 2\pi Rh(\gamma_{p/w} - \gamma_{p/o}), \qquad (2.4)$$

$\Delta E_{/\!/}$ and $\Delta E_{\perp}$ are the trapping energy when the cylinder is parallel or perpendicular to the interface (Figure 2.2b and c), respectively. *R* and *L* are the radius and length of the cylinder, and γ is the interfacial tension. *p, o,* and *w* represent the particle, oil and water. θ_c is the contact angle at the interface, and *h* is the penetration depth of the cylinder

into the water phase when assembled normal to the interface. On the basis of known and previously estimated values ($\gamma_{p/w} \approx$ 40mN/m; $\gamma_{o/w} \approx$ 35.7mN/m; $\gamma_{p/o} \approx$ 15mN/m), a nano-size cylinder (~8nm in diameter and ~40nm in length, aspect ratio $\approx$ 5) oriented parallel to the interface has a trapping energy which is about 40 times more than that of cylinders oriented perpendicular to the interface [29]. Lichun Dong and Duane T. Johnson also investigated the trapping energy of a cylinder remaining at the interface in an oblique configuration. They pointed out that line tension plays an important role in determining the adsorption of an anisotropic particle. For a cylinder, when the line tension is high, the side-on state will not be the most energy-favourable configuration. Instead, the cylinder will "prefer" to stay at the interface with a small tilt angle [29].

K. J. Stebe and coworkers have simulated the interface distortion and the wetting configuration for a cylinder trapped at a liquid-liquid interface, and have computed the corresponding energy landscapes [9]. Figure 2.3a shows the trapped cylinder (aspect ratio = 3, contact angle = 80º), where the inset demonstrates the corresponding contact line profile. It is very clear that a capillary rise occurs at the ends of the cylinder, while a depression occurs along the sides. The height difference, which is $z_{max} - z_{min} =$ 0.2574R (see the text for Figure 2.3), indicates that it is a relatively sharp turn at the edges of the cylinder, however, the tangent to the contact line appears continuous. As described above, the undulated contact line is induced by the inability of a flat interface to satisfy the uniform contact angle boundary condition. It is widely believed that this anisotropic particle-induced distortion is the main reason for capillarity at liquid interfaces.

Capillary interactions arise when interface distortions by neighbouring cylinders overlap. Botto *et al.* reported that the minimum energy configuration for cylinders at liquid interfaces is end-to-end resulting from a large interface distortion at the ends, and the sharp edge of the planar face. The latter creates a steric barrier to rearrangement [9]. As shown in Figure 2.3b, the total capillary energy has a minimum value for the end-to-end configuration. Note here ϕ is the bond angle between two cylinders, and ϕ =0º corresponds to these two cylinders being aligned. A substantial energy is thus needed to switch between end-to-end and side-to-side configurations. It is of the order
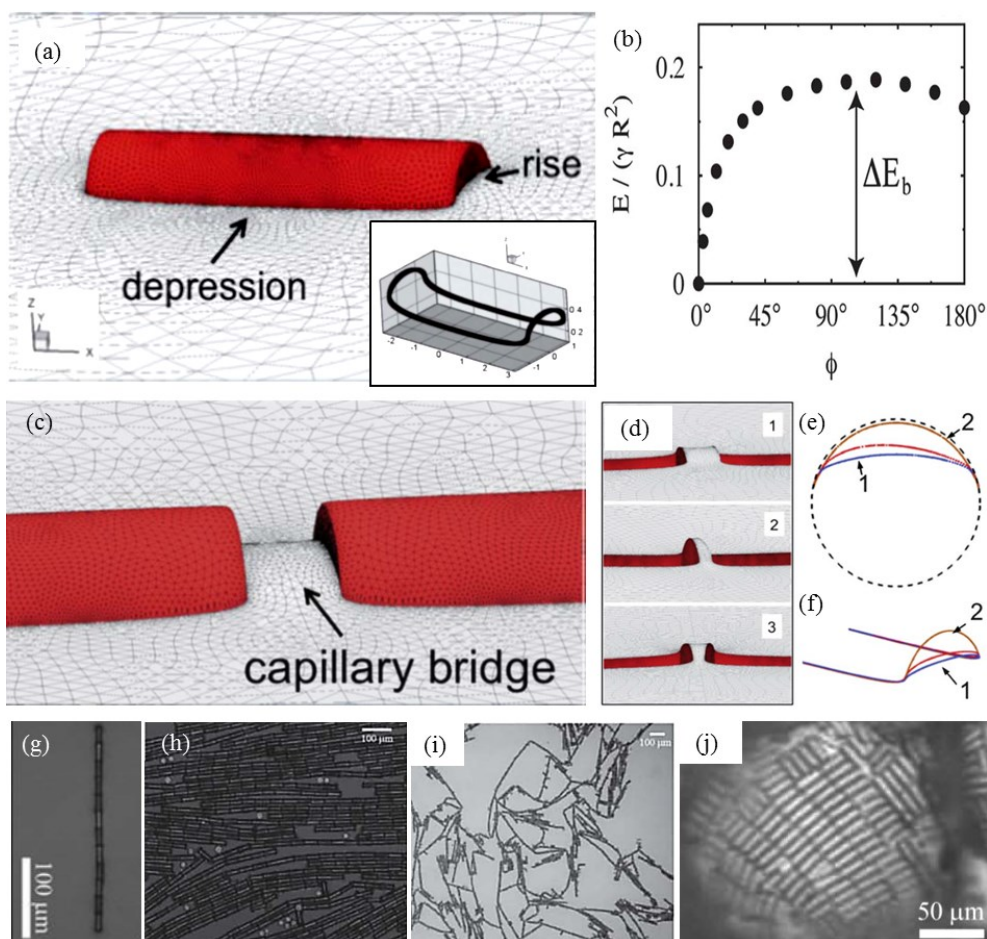
Figure 2.3 *(a) Perspective top view of an isolated cylinder (red, radius is R, aspect ratio= 3, contact angle= 80º) at a liquid interface (grey). (Inset) Contact line profile of the cylinder in (a), with the height values given in R. The maximum and minimum contact line height are $z_{max}= 0.4563R$ and $z_{min}= 0.1989R$, respectively. Here z=0 stands for the cylinder centre of mass, which located 0.2878R below the interface far from the cylinder. (b) Capillary energy vs. band angle for pairs of cylinders in contact. (c) Interfacial distortion between two aligned cylinders for d= 0.9R. (d) Interfacial shape for three different configurations: configuration "1", for d= 0.9R and $\phi= 0º$; configuration "2", for d= 0.3R and $\phi= 0º$; configuration "3", for d= 0.3R and $\phi= 20º$. (e) Contact line profiles of the end face for each cylinder. (f) Perspective views of the contact line in (e). (g) SEM image of chains of cylinders formed at air-water interface by capillary interactions. (h) A monolayer of cylinders formed by compression after chains formation. (i) Irregular networks of SU-8 cylinders at oil-water interface. (j) The surface of a water drop in hexadecane, which was stabilized by a dense rectangular lattice of cylinders. (a) - (d) are taken from [9]; (g) - (j) are taken from [26].*

of 10^6 kT for cylinders with 1 μm radius and 80° contact angle. Figure 2.3c shows the capillary bridge at the tips of two cylinders when the distance between them decreases. Besides, the shape of the contact line for each cylinder depends significantly on the separation and bond angle with the neighbouring one. Figure 2.3d illustrates three different configurations: for configuration "1", d= 0.9R and ϕ= 0°; for configuration "2", d= 0.3R and ϕ= 0°; for configuration "3", d= 0.3R and ϕ= 20°. Here d is the distance between these two cylinders and ϕ is the bond angle. Figure 2.3e and f give the corresponding contact line profiles along the end-face and perspective views, respectively. As two aligned cylinders approach each other, the area of their ends covered by the liquid increases. However, the contact lines along the sides moves very marginally. Configuration "3" also demonstrates that the capillary bridge between two cylinders can be distorted as the bond angle increases, resulting in a significant variation in the wetted area of their end faces (Figure 2.3e).

The capillary interactions between these cylinders not only enforce a stable end-to-end configuration for cylinder pairs, but also impart rigidity to chains of cylinders (Figure 2.3g) [9]. These chains can form "bamboo" structures under compression at an air-water interface, as shown in Figure 2.3h. On the other hand, the cylinders tend to form irregular networks at oil-water interfaces, where rigid chains are dominant microstructural features (Figure 2.3i) [6]. On crowded surfaces, cylinders form lattices upon assembly. Figure 2.3j shows a dense structure at the interface of a water droplet in hexadecane after gentle agitation. This droplet was stabilized by adsorbed cylinders, which formed a regular rectangular lattice of cylinders aligned both end-to-end and side-to-side.

2.2.2 Ellipsoids at liquid interfaces

Figure 2.4a shows a perspective view of an isolated ellipsoid (aspect ratio= 3, θ_c= 80°) at an air-water interface. Figure 2.4a (inset) is the corresponding contact line. The water interface is depressed at the tip, and rises along the sides of the ellipsoid. Here the maximum and minimum contact line heights are z_{max}= 0.1546R and z_{min}= 0.0872R, respectively. And again, R is the radius of the cylinder, and z= 0 means the height of the ellipsoid centre of mass, which is located 0.1238R below the interface far from the particle. It should be noted that if the contact angle θ_c is larger than 90°, an opposite
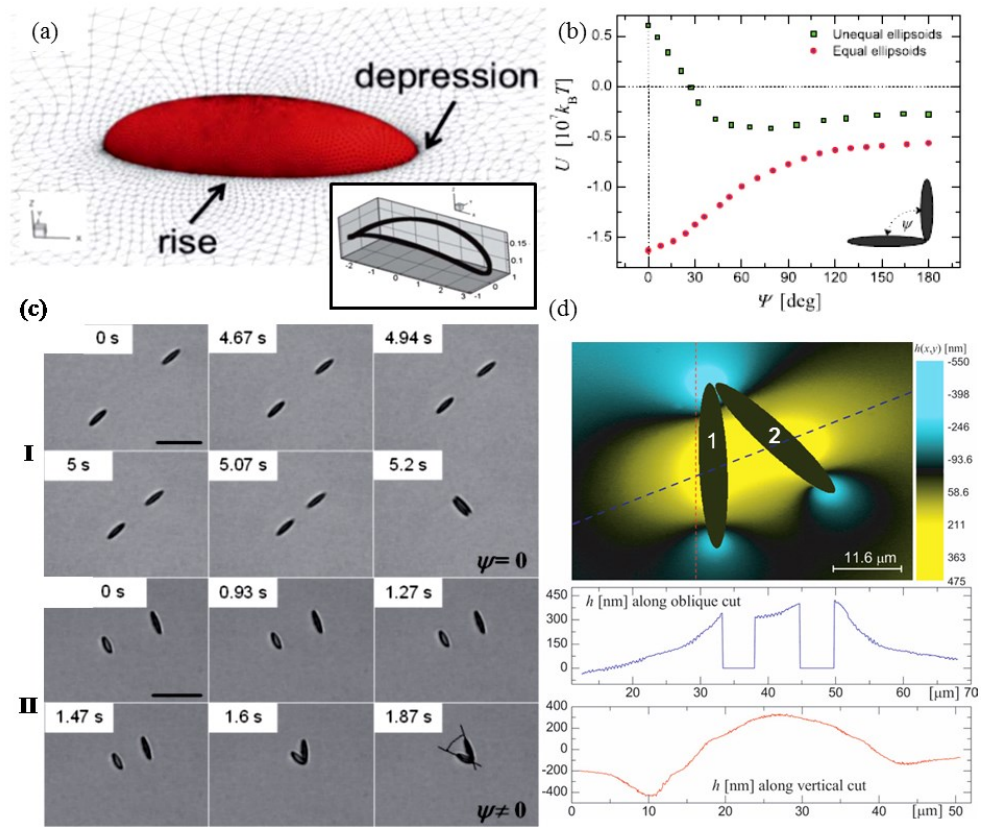
Figure 2.4 *(a) Perspective top view of an isolated ellipsoid (red) at liquid interface. (Inset) Contact line profile of the ellipsoid in (a). (b) Capillary energy vs. bond angle for two identical and different ellipsoids in contact. (c) Time series of optical microscopy images of two approaching ellipsoids at the air-water interface. (I), Two identical ellipsoids; (II), A size-mismatched ellipsoid pair. (d) The interfacial profile around the aggregated ellipsoids. Bottom images are the interface height along the oblique and vertical dashed lines in the top image. Note here the height origin is arbitrary. (a) is taken from [9]; (b) - (d) are taken from [11].*

distortion would occur, *i.e.* the rise occur at the tip and the ellipsoid would be predominantly immersed in the upper phase (air). Similar to the isolated cylinders, Lichun Dong and Duane T. Johnson have shown that the side-on state is also the most energy-favourable position for isolated ellipsoids at a liquid-liquid interface [27].

The dependence of the capillary interaction energy on the bond angle for pairs of ellipsoids in contact is shown in Figure 2.4b (red dotted curve). Different from the contacting cylinder pairs, side-to-side configuration is the minimum energy state for ellipsoids, which have been reported previously [11, 30]. J. C. Loudet and B. Pouligny investigated the case of two contacting ellipsoids through both experiments and

numerical calculations [11, 31]. They concluded that the most stable configuration actually depends on the degree of polydispersity of the ellipsoid pairs, in terms of their size or aspect ratio. Figure 2.4c presents the behaviour of two approaching ellipsoids at the air-water interface. Two identical ellipsoids (situation I) form a side-to-side configuration, which corresponds to an energy minimum as mentioned above.

However, a pair of ellipsoids with a slight length or aspect ratio difference (situation II) does not end up side-to-side but with a finite angle ψ (note here $\psi = 180° - \phi$) between their long axes. This vector configuration is named "capillary arrow" and remains stable over time, indicating that it should also coincide with an energy minimum. This has been confirmed by the dependence of capillary interaction energy on the bond angle for two unequal particles (upper curve in Figure 2.4b). The energy minimum occurs at a certain angle. The interfacial profile of a capillary arrow is displayed in Figure 2.4d. The interface is depressed at the tips of the ellipsoids while it rises near the centre of symmetry. Bottom graphs in Figure 2.4d represent the interface height along the oblique and vertical dashed line drawn in the top image, where the height origin is arbitrary. The oblique line is perpendicular to the arrow bisector, to reveal asymmetries in the interface profile inside the arrow. The first plot (blue curve) shows that the interface raises towards the shorter ellipsoid (number 2) with a ~70nm height difference. The second plot (red curve) reveals that the joint tip of the ellipsoid causes a lower interface than the free tip. For an isolated ellipsoid, the interface profile has the same height at both ends (see Figure 2.4a). Therefore, the interface height around the ellipsoids is actually free to adjust to accommodate various situations.

It is reasonable to expect many metastable states in experiments since the synthesized ellipsoids can never be perfectly identical. The side-to-side configuration coexist with linear chains [32], triangles and flower like structures [10, 33]. J. Vermant and coworkers investigated the behaviour of monolayers of ellipsoids in a Langmuir trough. Surface pressure measurements and detailed microscopy observations were combined to gain mechanistic insight into the sequential changes during compression and expansion. Figure 2.5a and b compares the surface pressure isotherms of a monolayer containing spherical particles and ellipsoidal particles. In Figure 2.5a, the corresponding particle

structure in region A is a gas phase. As the monolayer is compressed, the spheres start to touch each other and form a percolating network, which leads to an abrupt increase in surface pressure. In region B, the resistance to further compression increases with the formation of a densely packed monolayer. At the end of region B, the monolayer is close to its maximum packing. Further compression causes the interface buckling, and particle rearrangements are no longer possible (region C). Figure 2.5b shows the
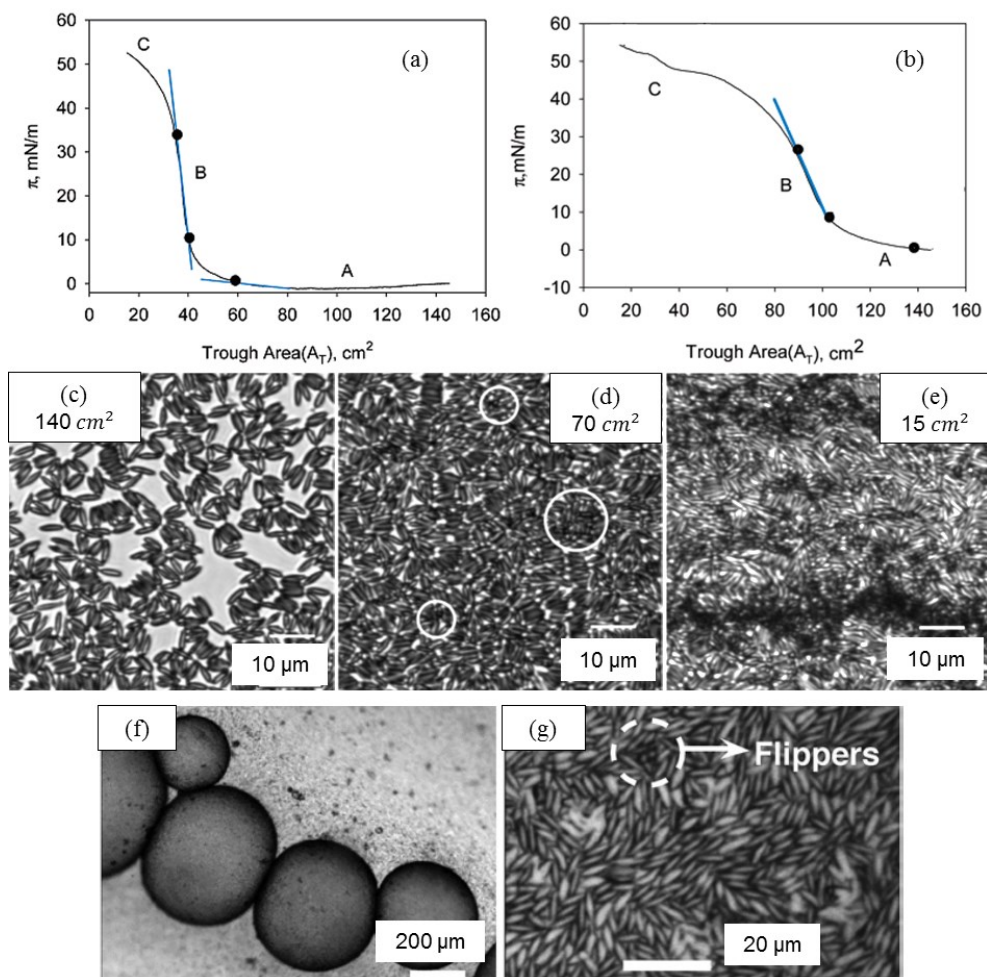
Figure 2.5 *Π-A isotherms for a monolayer containing (a) 2.8 μm diameter spherical particles and (b) ellipsoids of aspect ratio 5.5. (c-e) Optical microscopy observations for an ellipsoidal monolayer during compression. The trough area are 140 cm² (c), 70 cm² (d) and 15 cm² (e), respectively. Flippers are marked in white in (d). (e) Optical microscopy images of water-in-oil emulsions stabilized by polystyrene ellipsoids. (f) Particle packing in the interfacial layer of the emulsion droplets. Taken from [33] and [12].*

Π-A isotherm for ellipsoids with aspect ratio 5.5. There is a more gradual transition for the surface pressure from region A to B and an even more gentle transition from B to C, which indicates that the rearrangement in monolayers containing ellipsoids are more complex than the case of spheres. Microscopy was used to observe the behaviour of the monolayer during compression. Both end-to-end and side-to-side contacts were observed after spreading the ellipsoids in the Langmuir trough (Figure 2.5c), which is consistent with the discussion above. As the monolayer is compressed, the number density of some ordered regions increases. Figure 2.5d shows the close-packed monolayer where the trough area is about 70 cm^2. It should be noted that some ellipsoids appear as small spheres in the plane of view (marked white). This corresponds an upright position of the ellipsoids with their major axis perpendicular to the interface. It is called the "flipping" process, which is helpful for the monolayer to relieve some compression stress. Upon further compression, the flipping becomes more collective. Some arrays of flippers can be organized and span the entire width of the image (Figure 2.5e). Buckling also becomes evident since not all of the monolayer remains in focus. The flipping phenomena will be discussed in details in section 2.2.4.

In another work Vermant used ellipsoids to stabilize oil-in-water and water-in-oil emulsions (Figure 2.5f) [12]. Optical microscopy and cryo-SEM observations demonstrate a dense packed layer around the droplets with some local ordering and a number of out-of-plane oriented particles (flippers, as shown in Figure 2.5g). Surface rheological measurements show that the ellipsoid layers are highly elastic. The control over the emulsion stability is linked to the surface rheology and can be affected by the particles' aspect ratio and surface coverage.

2.2.3 Spherocylinders at liquid interfaces

For cylinder-shaped colloidal particles, the edges are often designed with different degrees of flatness [13, 34]. This can affect the resulting interfacial distortion and capillary interactions when these particles are trapped at liquid interfaces [9]. The capillary energy is reduced when the particle surface is rounded in the neighbourhood of the point of contact, *i.e.*, when the edge sharpness decreases. Correspondingly, the interfacial distortion induced by the particle is also mitigated, which can be noticed from the interfacial height difference of isolated cylinders ($z_{max}-z_{min}= 0.2574R$) and
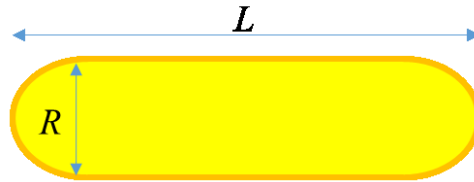
Schematic 2.1 *A spherocylinder with L in length and R in diameter. Its aspect ratio is A= L/R.*

ellipsoids ($z_{max}-z_{min}$= 0.0674R). The limiting case should be spherocylinders, which would not induce any interface deformation and thus zero capillary interactions.

Spherocylinders, which are called "rods" in this thesis, are cylinders capped by hemispherical ends (Schematic 2.1). In experiments, their ends can never be synthesized perfectly round, and surface defects are also unavoidable. Therefore, capillary interactions between interfacial spherocylinders should not be a surprise. Peidong Yang and coworkers explored the organization of nanorods at the air-water interface [35]. TEM was used to observe the pressure-induced phase transitions. At sufficiently low densities, the rods align side-to-side to form raft-like aggregates due to the capillary interactions and van der Walls attraction. During the compression, the monolayer first undergoes a nematic assembly process, and then a more ordered smectic arrangement. The latter is characterized by a layer-by-layer stacking of ribbon-like superstructures. With further compression, a transition from monolayer to multilayer was observed, which destroys the 2D smectic ordering. The whole system eventually resumes a disordered 3D nematic configuration. Additionally, Acharya and Efrima showed that end-to-end configurations of nanorods (~5 nm in length) can also be obtained, resulting in 150 nm long nanowires retaining the same 1.2 nm width of one nanorod [36]. The authors believe that the ability to arrange these nanomaterials in one direction is important in the design of nano-size electronic devices.

For micrometer scale spherocylinders, so far most studies have been carried out in 3D systems [37, 38], and not many of them focus on their interfacial properties. In this thesis, micro-size akaganéite rods are synthesized and form a monolayer at the air-water interface. Their interfacial properties are investigated in detail. The related results are present in chapter 4.

2.2.4 Mechanism of flipping

As described above, for isolated rod-like particles, the planer configuration is always the most energy-favourable position. However, when the particles form a monolayer, capillary interactions are induced. As the monolayer is compressed beyond its percolation threshold, some individual particles can flip around their long axis to be perpendicular to the interface (Figure 2.6a). This is helpful to reduce the surface area occupied by the particles and relieve some of the compression stress. From J. Vermant's observation, flippers do not occur completely at random, but typically appear in rather dense regions of the monolayer, although some void regions can be still present [33]. Further compression leads to the formation of flipper arrays running perpendicular to the compression direction (see Figure 2.5e). By comparing two images before and after a localized collapse of the monolayer, it can be noticed that the more open regions do not become denser while the reorganizations occur in regions that are already dense. The authors believe this is caused by the inhomogeneous compression stress, because compressing a void region should require much less energy compared to the flipping of a particle. The transmission of the compression stress in dense regions might be similar to the way stresses are transmitted in a granular material [39].

Figure 2.6b shows the monolayer during expansion, where some regions are cracked and flippers remain in an upright position. This indicates the brittle nature of the compressed monolayer, as well as the irreversibility of flippers. If the particle is neutrally wetting (contact angle θ_c equal to 90º), and the interfacial distortion is ignored, the energy difference between a flat and flipped ellipsoid at air-water interface can be calculated easily. Similar to the discussion of equation 2.2, the energy required to remove an ellipsoid lying flat on the interface is given by: $E_{\parallel} = -\pi\gamma ab$, where a is the length of the semimajor axis and b is the length of semiminor axis. Likewise the energy required to remove a flipped ellipsoid is given by: $E_{\perp} = -\pi\gamma b^2$. Hence the energy difference is

$$E_{\parallel} - E_{\perp} = -\pi\gamma ab(1 - b/a) \tag{2.5}$$

To flip a micro-size ellipsoid, a change in the energy of $10^9\ kT$ is needed. Note that in the actual process, this value will be larger since some additional energy barriers also need to be overcome at the interface. The elastic energy stored in a compressed monolayer is given by $E = \int \epsilon h\ \mathrm{d}h$, where ϵ is the modulus and h the interface deformation. The measured modulus is on the order of 200 mN/m, and the elastic energy could be on the order $10^{11}\ kT$, which is sufficient to support the flipping process. This explains why the Π-A isotherms are always continuous during the compression, and also suggests that the flipping phenomenon is an activated process. The dynamics of the flippers, however, have not been investigated in detail.
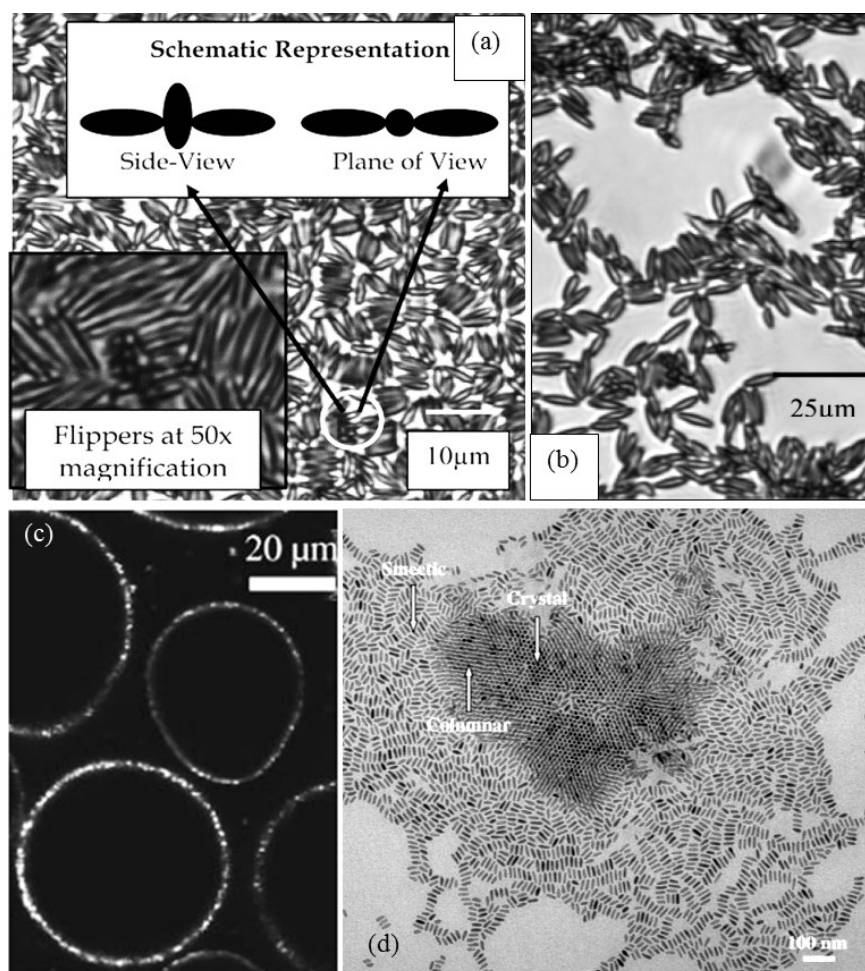
Figure 2.6 (a) Optical microscopy observations for an ellipsoidal monolayer during compression. The trough area are 100 cm². (b) The cracking of the monolayer and the persistence of flippers upon expansion. (c) Fluorescence confocal microscopy image of water droplets stabilized by CdSe nanorods in toluene. (d) TEM image of a water droplet in (c) after drying on a carbon-coated copper grid. (a), (b) are taken from [33]; (c), (d) are from [29].

Similar flipping process has been observed in some dried nanorod-stabilized water droplets. Jinbo He *et al.* have found that the thickness of the droplet surface is consistent with the diameter of the nanorods (Figure 2.6c), suggesting that the nanorods form a monolayer around the droplets with their long axis parallel to the interface [29]. After these droplets dried, the surface area of the droplet decreased, and the nanorods exhibited a range of two-dimensional structures. Figure 2.6d shows the transmission electron microscopy (TEM) image of one dried droplet. As the concentration of the nanorods increases from the periphery of the droplet to the centre area, the structures formed span the range from a smectic packing to a columnar ordering to a crystalline-like phase. This supports the idea that the surface energy and mobility of the particles at the interface are important in the packing of the particles. During the solvent evaporation, the change of the surface energy or surface tension could be considered as an in-plane compression, which force these nanorods to orient normal to the interface.

2.3 Two-Dimensional Dipeptide Hydrogel

As with colloidal particles, some other rod-like colloidal materials are also worth investigating in two dimensions, for example, the self-assembled dipeptide molecules. This opens up the possibility of hydrogel thin films. Compared with the monolayers containing colloidal particles, hydrogel thin films exhibit good biocompatibility, feasibility and inherent ability to self-assemble in microscopic dimensions, which make them attractive candidates for applications in personal care industries [40], drug delivery [41, 42], and the fabrication of miniaturized devices [42].

This section first introduces dipeptide hydrogels in the bulk as well as the related gelation mechanisms. After that, the recent progress in the field of hydrogel thin films is reviewed.

2.3.1 Dipeptide hydrogels

Hydrogel: "cross-linked macromolecular networks swollen in water or in biological fluids" [43], is an important class of soft material and has attracted great attention over
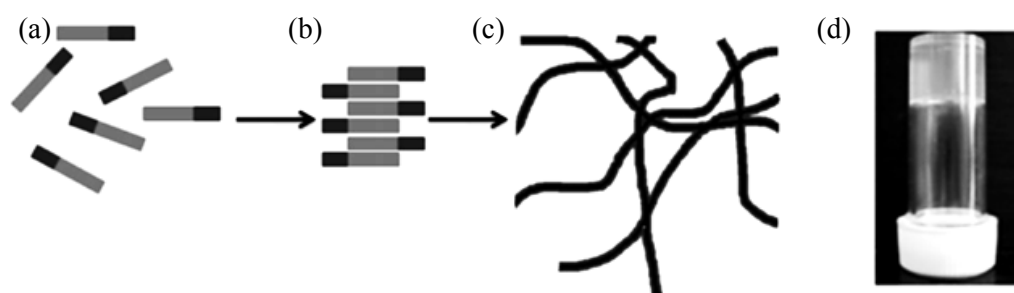
Figure 2.7 The gelation process of LMWGs. Firstly, these gelators (a, they are normally amphiphiles) self-assemble into some fibrous structures (b) via non-covalent forces. Subsequently, these fibrous structures cross-link with each other to form a three-dimensional network (c). This results in the formation of a self-supporting hydrogel, demonstrated by stability to vial inversion (d). Taken from [46].

the past decades. Most hydrogelators are polymers, with the gels being formed by cross-linking or entanglement of polymer chains [44, 45]. In recent years, low molecular weight hydrogelators (LMWGs) have attracted significant attention since the simplicity and relatively low cost of the molecules, and their potential applications in various biological processes (*e.g.* cell culturing, energy transfer) [46]. LMWGs can self-assemble in solution to form long, fibre-like structures, which can further associate into a three-dimensional network (Figure 2.7). This self-assembly process typically arises from non-covalent interactions such as van der Waals interactions, hydrogen-bonding, electrostatic interactions, etc.

One class of LMWGs are the dipeptides, including dipeptide molecules and their conjugates (dipeptides joined onto a large aromatic group such as fluorenylmethoxycarbonyl (Fmoc) [47, 48], naphthalene (Nap) [47, 49], or spiropyran [50]). Compared with other LMWGs, dipeptide hydrogelators exhibit interesting potential opportunities, such as the fluorescent properties [51] and the dramatic improvement of mechanical properties [52]. Two kinds of dipeptide conjugates, Fmoc-dipeptides and Naphthalene-dipeptides, are the most intensively investigated hydrogelators in the published studies [47-49, 53)]. The first Fmoc-dipeptide hydrogelator was reported in 1995, where a hydrogel was formed by the N-terminal protected anionic Fmoc-Leu-Asp dipeptide at a concentration of 2 mg/mL [48]. Gazit and coworkers demonstrated that Fmoc-Phe-Phe dipeptides (Figure 2.8a) can self-assemble into fibers with average

diameters ranging from 10-100nm, which formed an optically transparent hydrogel with a storage modulus of 10^4 Pa [54, 55]. Ulijn *et al.* investigated the properties of Fmoc-Phe-Phe hydrogel using fluorescence, circular dichroism (CD) and FTIR spectroscopy. Fluorescence spectra were consistent with antiparallel stacking of the Fmoc groups, which was further supported by the observation of an Amide *I* shoulder at 1685 cm^{-1} in the FTIR spectra. This is consistent with the formation of antiparallel β-sheets structures [56]. TEM images and X-ray powder diffraction were carried out to obtain the packing model of Fmoc-Phe-Phe dipeptides in self-assembled hydrogels (Figure 2.8b). It was observed that when the pH of the dipeptide solution was lowered to 9, fiber-like structures consisting of antiparallel β–sheets start to be formed. Lowering of the pH further to 4.6 resulted in the formation of cross-linked networks [57]. There is a strong correlation between solution pH and assembly kinetics on the ultimate rheological properties of the hydrogel. Adams and coworkers have investigated the influence of molecular structure on the gelation behaviour of a range of Fmoc-dipeptides; this work demonstrates that the ability to form a stable gel is determined by the overall hydrophobicity of the dipeptide molecules [58].

In addition to Fmoc functionalization, naphthalene functional groups also promote the self-assembly of dipeptides into fibrils that form a bulk hydrogel. Xu and coworkers studied a series of Nap-dipeptides with varying configuration of N-terminal naphthalene groups, and observed a relationship between self-assembly and the length of the linker joining the Naphthalene group to the dipeptide backbone. This relationship reveals that the conformational flexibility at the N-terminus dramatically affects the establishment of effective π-π interactions that lead to gelation process [49]. Adam *et al.* screened a library of sequences with N-terminal naphthalene groups bearing hydrogen, bromine, or cyano substituents at 6-position (Figure 2.8c) in order to probe the influence of varying dipeptide hydrophobicity on the C-terminal p*Ka*. These dipeptides have apparent carboxyl p*Ka* values of ~5-6. By adjusting the pH of the system with Glucono-δ-lactone (GdL), it is observed that self-assembly did not occur until the pH was brought below the apparent p*Ka* (Figure 2.8d). The formation of β-sheet structures was also observed by IR spectra and X-ray fiber diffraction [59].

In another work, Adam and coworkers further demonstrated that energy transfer is

(a)

(b)

(c)

dipeptide	R₁	R₂	R₃
1	H	CH₃	H
2	H	CH₃	CH₃
3	H	CH₃	CH(CH₃)₂
4	H	CH₂Ph	H
5	H	CH₂Ph	CH(CH₃)₂
6	H	CH₂Ph	CH₂Ph
7	Br	CH₃	H
8	Br	CH₃	CH₃
9	Br	CH₃	CH(CH₃)₂
10	Br	CH₂Ph	H

(d)
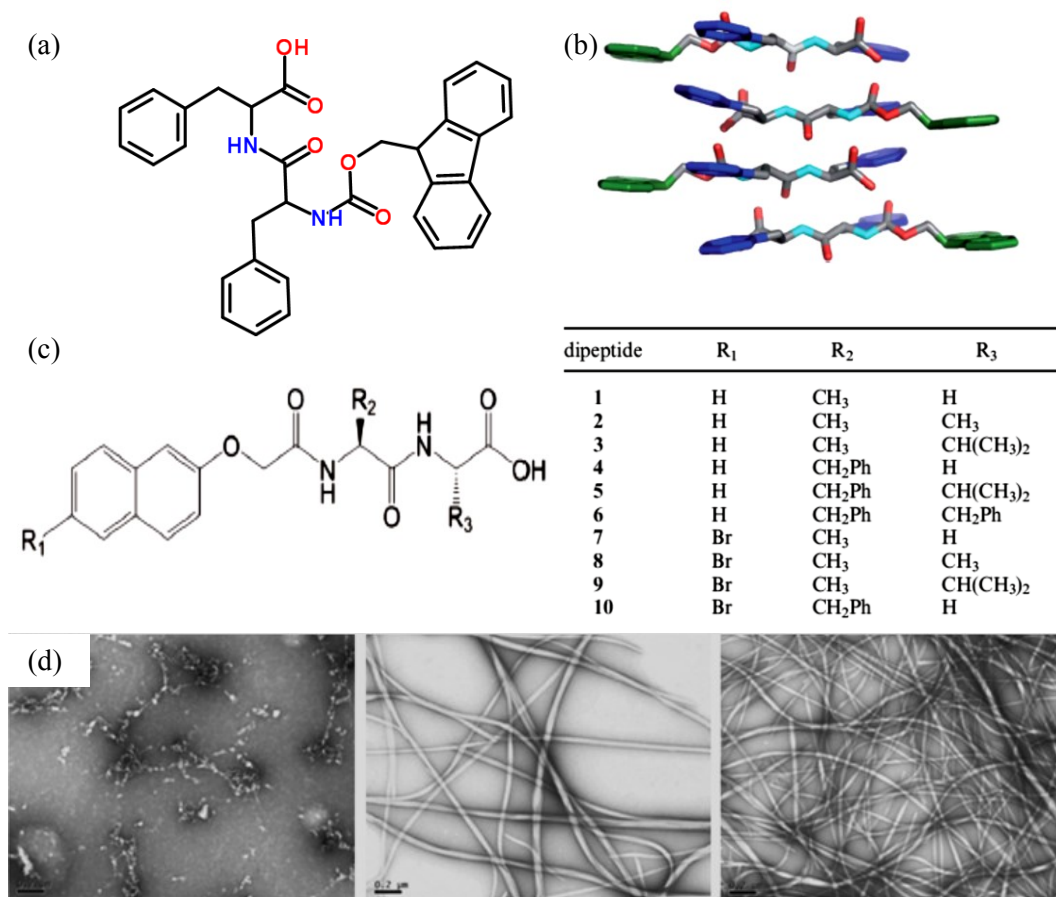
Figure 2.8 (a) Fmoc-Phe-Phe dipeptide molecules. Taken form www.chemspider.com. (b) The packing model of Fmoc-Phe-Phe dipeptides in bulk hydrogels. (c) Left: General structure of naphthalene-dipeptides. Right: Table for R1, R2 and R3 for each naphthalene-dipeptide. (d) TEM of evolution of structures with pH for dipeptide in the presence of GdL. From left to right: immediately after GdL addition, 200min, and 280min after GdL addition. In all cases, the scale bar represents 200 nm. (b) is taken from [47]; (d) is taken from [59].

possible from a Nap-dipeptide to dansyl or anthracene chromophores as a hydrogel is induced by pH varying. The emission spectra for the naphthalene rings can be tuned by substituents [51].

2.3.2 Controlling the gelation process

The temporal and spatial control of the assembly process is one of the important challenges in the field of hydrogel formation. It is believed that the mode of preparation can significantly affect the physical properties of the hydrogel systems.

For dipeptide hydrogel, two important methods for the control of the gelation process,-pH modulation and metal ions addition, are described below:

pH modulation: A controlled pH decrease has been developed to induce gelation, with the aim of forming homogeneous and reproducible hydrogel systems. Glucono-δ-lactone (GdL) had been used to finely adjust the pH of the dipeptide solution. On lowering the pH, the carboxylate becomes protonated and self-assembly occurs. The slow GdL hydrolysis allows a uniform pH change, resulting into a homogenous gel with reproducible mechanical properties. Besides, using GdL, the gelation process can be monitored in time and the final pH of the system can be determined easily. The timescale for hydrolysis is suitably slow that it is possible to observe the assembly process (Figure 2.8d) [60, 61]. GdL has been used for the gelation of a range of Fmoc- and Nap-dipeptide hydrogelators [59, 62]. Aqueous HCl can also be used for the pH modulation. Adams and coworkers observed that HCl resulted in rapid local assembly, which might also cause structural defects in the fibril networks. For some Fmoc-dipeptides, it is found that the hydrogel prepared *via* GdL acidification is nearly 30 times more rigid than HCl-induced system [63]. Other routes to controlling the pH to induce gelation process include the use of photoacid generators (PAG) where protons can be released on exposure to UV light [64], and the use of glucose in the presence of glucose oxidase [65].

Metal ions addition: Recently, a novel method to initiate dipeptide self-assembly and gelation was reported based on the addition of metal ions [66, 67]. Metal ions have a strong affinity to molecules bearing multiple carboxylic acid groups or phosphoric acid group at neutral or high pH values. Therefore, they can be used to cross-link self-assembled fibers of dipeptide which incorporate such chemical groups [68]. Adams and coworkers have demonstrated that the addition of divalent cations to a Nap-dipeptide solution at high pH could lead to hydrogel formation. The worm-like micelles present in the solution cross-link with Ca^{2+} and then form a bulk gel [67].Previous studies report that metal ions have a dramatic effect on the molecular self-assembly of the dipeptides in aqueous media [69]. For example, the rheological properties of a hydrogel system based on metal ion binding is also metal-dependent. Divalent cations lead to gels with much higher storage moduli (*G'*) than monovalent cations. Particularly, Ca^{2+} leads to

a NapFF (a Nap-dipeptide) gel with the highest G' (~10^4 Pa), followed by Mg^{2+} (~10^3 Pa), Na^+ and K^+ (~10^2 Pa) [69].

Other methods, like enzymatic control, temperature, external stimulus (*e.g.*, UV light) and the hydrolysis of carboxylic ester bond, have been used to induce the gelation process for other hydrogelators [68, 70]. These methods could also be used for the applications of designed self-assembly dipeptide systems in biotechnology (3D cell culture, biosensing) and nanotechnology.

2.3.3 Dipeptide hydrogel properties and characterization

Over the years, much work has been devoted to study designed hydrogels for different applications. The structures and mechanisms of the formation of the gel networks involved, and their mechanical properties required investigation. As mentioned above, under some specific conditions, dipeptide molecules can form fiber-like structures which further cross-link with each other to form a three-dimensional network. This is important for its use as a biomaterial, like in drug delivery systems. The related properties of dipepide hydrogel have been reported in previous studies.

Structural properties: Self-assembled dipeptides can form a well-defined three-dimensional hydrogel which exhibits three levels of structure: primary, secondary and tertiary. The primary structure is the genetically determined sequence of amino acids. It is often modelled as beads on a string, where each bead represents one amino acid unit. The tertiary structure might be modelled as a tightly-packed snowball, where each atom in the protein has a well-defined location. An intermediate level is called secondary structure, which includes α-helices and β-sheets, allowing the amides to hydrogen bond very efficiently with one another. In an α-helix the polypeptide backbone is coiled in a right-handed helix where the hydrogen bonding occurs between successive turns of the helix. In β-sheets, the strands of polypeptide are stretched out and lie either parallel or antiparallel to one another [71]. In experiments, TEM, AFM, SEM and confocal microscopy were mainly used to observe the primary structure. X-ray crystallography and NMR spectroscopy provide information about the tertiary structure, while FTIR spectroscopy provides information about the secondary structure.

In previous studies, the parallel and antiparallel structures of β-sheets structures, which are well known for their ability to assemble into long fibres, were identified in most of the dipeptide hydrogels [59, 68, 72]. *β*-sheets consist of multiple peptide chains that have an extended backbone arrangement that permits hydrogen bonding between the backbone amides and carbonyls. Each chain is referred to as a strand, the hydrogen bonded strands are referred to as a sheet. β-sheets can be orientated so that all their C-termini are at one end of a structure, described as a parallel structure, or so that the N and C termini alternate, described as an antiparallel structure. This has an important impact on the orientation of hydrogen bonds between sheets and side chain orientations and interactions [70].

In microscopic observations, Thioflavin T (ThT) is introduced as a probe to enhance the fluorescent signal from amyloid fibrils. This dye is widely used to probe the formation of β-sheet structures, especially in amyloid-forming materials. This is because ThT undergoes a change in fluorescence upon its interaction with the ordered assemblies. Figure 2.9a shows the normalized change in ThT fluorescence at 485nm on addition of solutions of dipeptide derivative to GdL (blue curve), where no increase of fluorescence is observed until a pH of 5.4 is reached (*i.e.* a hydrogel is formed) [59]. Figure 2.9b demonstrates a FTIR spectra of a hydrogel assembled by Fmoc-AA molecules. A peak at 1686 cm^{-1} and a shoulder at 1634 cm^{-1} stand for the *β*-sheet formation. Another strong absorbance at 1644 cm^{-1} correlates to random coil- or polyproline-like shift in amide C=O stretch frequency [72].

Rheological (elastic) properties: Rheology studies the flow of matter, primarily in a liquid state, but also as "soft solid" (*i.e.*, sludge). Generally, substances with a complex microstructure also have complex flow characteristics, which can be affected by temperature, mechanical agitation or other factors. The rheological property of complex fluids plays an important role in materials science and many other applications, such as physiology, human biology and pharmaceutics. As an important component of soft matter, hydrogel also demonstrates some interesting rheological properties.

The shear modulus (storage modulus *G'* and loss modulus *G''*) of a dipeptide hydrogels can be measured by dynamic rheological experiments. *G'* and *G''* depend
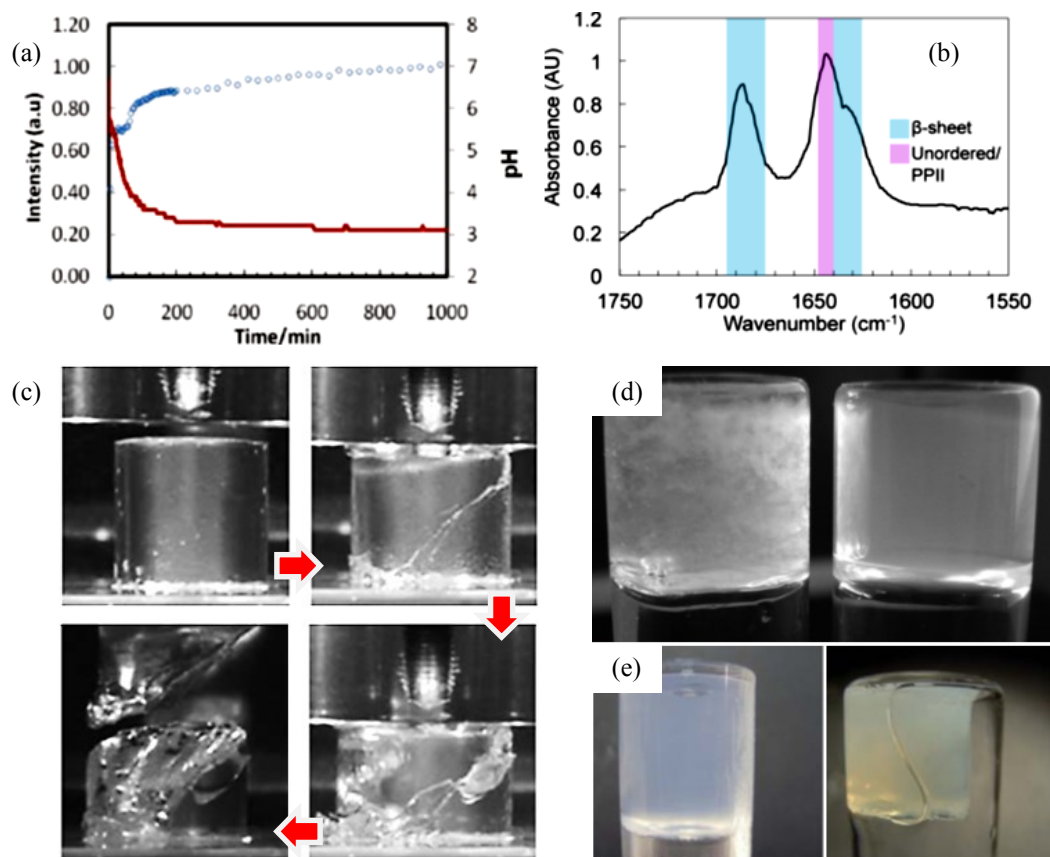
Figure 2.9 *(a) Normalized change in ThT fluorescence at 485 nm (λex =455nm) on addition of solutions of dipeptide derivative to GdL (blue data).Overlaid is the change in pH with time (red data). (b) FTIR amide I absorbance data for Fmoc-AA molecules within fibril assembly give a peak at 1686 cm⁻¹ and a shoulder at 1634 cm⁻¹, similar to that seen in predominantly β-sheet proteins. Another strong absorbance at 1644 cm⁻¹ correlates to random coil- or polyproline-like shift in amide C=O stretch frequency. (c) Photographs of FmocLG under compression at 5mm s⁻¹. (d) Photographs of hydrogels prepared from Fmoc-leucine–glycine. Left: pH changed with HCl. Turbid inhomogeneities can be seen in this gel. Right: pH changed using GdL. A transparent, uniform gel is formed. The final pH in both cases is 3.9. (e) Photographs of example hydrogels. Left: FmocLG forms a stable, transparent hydrogel after 24 hours. Right: FmocAA shows significant syneresis after 24 hours. (a) is taken from [59]; (b) is from [72]; (c) and (e) are taken from [58]; (d) is taken from [63].*

on the hydrogelators, concentration, as well as the mode of preparation (by pH change with GdL or HCl, or by metal ions). One previous study about small peptides (slightly longer than dipeptides) reported that calcium ions induce the formation of a hydrogel

with larger density and higher storage moduli than HCl [73]. Figure 2.9c demonstrates the response of a Fmoc-dipeptide hydrogel at high compression speeds (5 mm/s), which comprised an initial elastic deformation with a Young's modulus consistent with G' measured in the rheometer, followed by a brittle failure. This response is highly dependent on the compression speed [58]. Poor rheological properties often limit the hydrogels' widespread applications. As a result, various strategies have been used to improve their mechanical strength.

Other properties: It is reported that a homogeneous, uniform hydrogel can be induced by mixing GdL with Fmoc-dipeptide solutions. While under the same conditions, HCl leads into some inhomogeneities within the gel (Figure 2.9d). The latter can be explained by the high speed of the gelation process [63]. Besides, Adams and coworkers have demonstrated that for some Fmoc-dipeptide hydrogels, shrinking and expelling water occurs during the observation period (Figure 2.9e) [58]. The shrinking results in a decreased effective volume fraction and, in turn, decreased viscosity and elastic properties. Similar phenomenon has also been reported for other hydrogelators [74].

2.3.4 Hydrogel thin films

Hydrogel thin films have attracted interest as an approach to responsive surfaces and interfaces. They can be transferred from the surface of one material to another or used as free-standing films. Previous studies mainly focus on thin films of polymer hydrogel [42, 75], which can be prepared by chemical crosslinking of reactive polymers, and used as storage mass-transport, chemical sensors and actuators. In recent years, the self-assembly of peptide molecules at interfaces has become an important issue in view of their numerous applications [76]. Joel P. Schneider and coworkers prepared a peptide hydrogel film by pre-forming the hydrogel in a spray apparatus for 30 min [77]. The gel was shear-thin sprayed into the wells of a 48 well plate resulting in films with a thickness of 50-250 μm. In a Langmuir trough, Mathilde Lepère *et al.* spread a solution of peptide (a 12 amino acid peptide, named LSFD) at the free surface of an ultrapure water subphase [78, 79]. The peptide molecules self-assemble at the interface and form a hydrogel film. It is supposed that the hydrophobicity of the peptides plays an important role in the self-assembly process. The interfacial properties of the films (i.e.
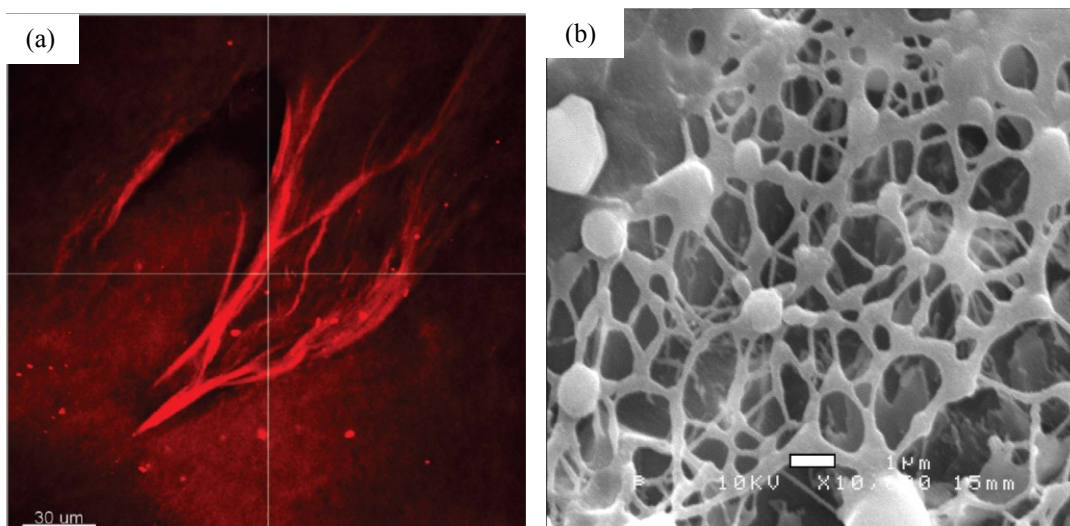
Figure 2.10 *A confocal microscope image (a) and Cryo-SEM (b) of the fibrous structure of the electrochemically grown gel films. The scale bar in (a) is 1 μm. Taken from [80].*

surface pressure) can be carried out directly by two-barrier Langmuir trough. Other properties can also be measured after transferring the film onto a solid substrate.

For dipeptide molecules, self-assembly can also be harnessed at a two-dimensional surface. In 2010, Petra J. Cameron and coworkers reported that ultra-thin films and membranes of Fmoc-dipeptide hydrogel could be grown by inducing the localised pH at the surface of an electrode (Figure 2.10a) [80]. The thickness can be closely controlled from tens of nanometers to millimetres. Figure 2.10b shows a cryo-SEM image of the top of a gel membrane, where fiber-like structures can be observed clearly. In another paper, Cameron *et al.* grow a Fmoc-dipeptide gel layer on top of a nanometer thick seeding layer. It is a nucleated growth which occurs due to some protons trapped within the seeding layer lowering the local pH. This work demonstrates the ability to grow films of hydrogel in a controllable manner, and open a range of new applications for dipeptide hydrogels.

2.4 Long-Lived Wet Foams

There already exist several applications using colloidal particle monolayers or hydrogel thin films to stabilize the interfaces in gas-liquid or liquid-liquid systems.

Examples include bijels [81], Pickering emulsions and aqueous foams. This section provides the background of wet foams stabilized by colloids, proteins and peptides. On this foundation, a long-lived wet foam system is created using the dipeptide hydrogel. The related results are presented in later chapters of this thesis.

A foam system can be created by dispersing a gas into a liquid. However, such foams are metastable and require the use of stabilising agents. Surfactants can adsorb at the gas-liquid interfaces, lower the gas-liquid surface tension and thus increase the lifetime of gas bubbles. The liquid volume fraction, which is defined as $\varepsilon = V_{liquid}/V_{foam}$, is used to characterize the degree of packing in a foam system. For dry foams ($\varepsilon \leq 0.05$), the bubbles are polyhedral, with curved faces and well defined edges. When $\varepsilon = 0.36$ (random close packing of solid spheres), the bubbles are no longer deformed in the foam (but approximately spherical in shape), which is called wet foam. Systems with much larger ε are called bubbly liquid. Figure 2.11a demonstrates a system with both dry and wet foam layer.
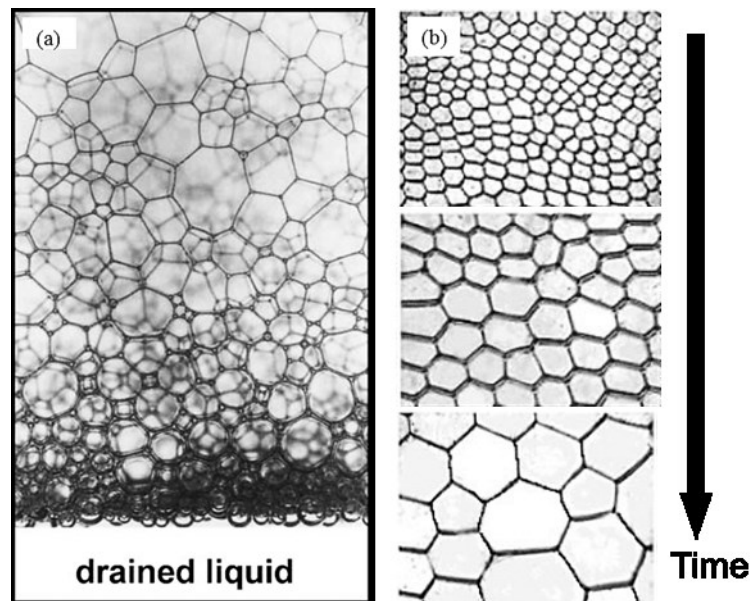
Figure 2.11 *(a) A foam at equilibrium. At the top, the foam is very dry ($\varepsilon < 0.01$), and the bubbles are polyhedral, while the bubbles at bottom are spherical, with $\varepsilon = 0.36$. (b) Coarsening process at different times in a 2D dry foam. The arrow indicates the increase in time. Taken from [88].*

This thesis mainly focus on the wet foams, which can be used in numerous different applications ranging from food industry to oil recovery and drug delivery [82, 83]. Over the last twenty years, progress has been made to obtain stable wet foams with long-term stability. Earlier reports investigated the role of surfactants in improving the foam stability [84, 85]. More recently, colloidal particles have been used to adsorb on the surface of gas bubbles to increase the lifetime of wet foam [86]. Besides, some biocompatible materials, like proteins and peptides, are also considered to be attractive stabilizers for wet foams [76]. At the outset of this section, different mechanisms involved in the destabilisation of foams are provided. Subsequently, wet foam systems stabilized by colloidal particles and protein/peptide molecules are described respectively.

2.4.1 Fundamental mechanisms of foam stability

Evaporation: Although surfactants can affect evaporation rates, foams can be destroyed easily by the liquid evaporation when it is left to open air. Paul Stevenson and coworkers investigated this issue thoroughly, which involves the effect of environmental humidity on foam stability [87]. In most reported studies, of course, measures have been taken to prevent evaporation.

Coarsening: Because of the difference in Laplace pressure, gas in the foams can diffuse from the smaller to the larger bubbles. This is called "coarsening" and tends to increase the volume of certain bubbles at the expense of others, which thus leads to the growth of the average bubble radius. Many issues on coarsening are still unsolved, including the dynamics of the growth of a single bubble, the universality obtained in the distribution of the bubble size with time, or the effects of the chemical components [88].

The study of coarsening has been initially investigated in 2D dry foams. Figure 2.11b shows experimental results of a 2D foam at different times. Bubbles with higher pressure shrink with time, which eventually vanish during the observation [88]. For 3D foams, experimentally, the coarsening process is predicated to be scale invariant, with an average bubble radius R varying with time t. Optical methods of multiple light scattering have been carried out to obtain the scaling behaviours which exist in foams

[89]. Rheological measurements can also provide confirmation by monitoring the time evolution of the foam elastic modulus, which is inversely proportional to the bubble diameter [90].

If the gas bubbles are covered by a thin film (such as a polymer layer, colloidal particle monolayer, or hydrogel film), the diffusion of gas molecules would be affected. It is reported that the characteristic coarsening time can be estimated as:

$$t = \frac{R^2}{D_{eff} f_{(\emptyset)} h}$$

Where D_{eff} is an effective diffusion coefficient, $f_{(\emptyset)}$ the fraction of total area of the bubble covered by thin films, and h the film thickness.

The mechanical properties of the thin films around the bubbles can also influence the coarsening process. For emulsions, both numerical simulations and experiments have shown that coarsening can be slowed down by increasing the compression elastic modulus E of the films [91, 92]. Using surfactants with high surface modulus, a slowing down of coarsening in foams was also observed [93]. The arrest of coarsening, however, requests both a high surface elastic modulus and a resistance to film collapse. Therefore, protein-stabilized bubbles also shrink and disappear in the long-time limit [94]. So far, only particle layers are found to irreversibly adsorb at the gas-liquid interfaces; they resist collapse and buckle, which is possibly the reason why particle-stabilized foams do not coarsen [95].

Coalescence: Coalescence occurs when the films between bubbles become thin and then rupture. So far, the main mechanisms of coalescence remain very unclear. There was a widely accepted argument that large bubbles are more fragile than the smaller ones, and the probability of rupture of the film is simply proportional to its surface area [96-98]. Some authors pointed out that coalescence in foams occurs once the bubbles have reached a critical size [99]. However, Carrier V. and Colin A. studied the fundamental role of the liquid fraction in the foam as well as the second order role played by the size of the bubbles. They concluded that the coalescence process can be dramatically enhanced below a critical liquid fraction, which depends on the surfactant concentration and the nature of the surfactant, but does not depend on the bubbles sizes

[100]. It is also believed that the film rupture mechanisms are different in different foam systems.

Drainage: Due to gravity, the liquid and gas in the foam tend to separate with time. The liquid leaks out of the foam and the bubbles become dryer. This is the phenomenon of drainage, which was extensively studied before [88, 101, 102]. The liquid flows through the continuous phase between bubbles. As mentioned above, when the liquid volume fraction ε is below than 0.36, the bubbles are no longer spherical but distort into polyhedra. If drainage continues, the films separating the bubbles thin and then break. Foam drainage does not only depend on the physical and chemical properties of the foam, but also the effects of the experimental conditions, like the height of the foam container, or the initial vertical liquid distribution.

Together, coarsening, drainage, coalescence and evaporation lead to foam instability. It should be noted that all the destabilisation processes can occur on the same timescale and can thus be coupled. In principle, adsorbed surfactants (macromolecules, particles) can provide additional stability to foams.

2.4.2 Foams stabilized by colloidal particles

Although the ability of colloidal particles to stabilize bubbles and emulsion droplets has long been recognized, the potential of particles alone or with appropriate surfactant for stabilising wet foams was demonstrated during the last two decades [103-105]. By using spherical fumed silica nanoparticles (~ 30nm diameter), Binks and Horozov obtained a very stable wet foam [106]. The foam can be prepared either by hand shaking or an Ultra Turrax homogeniser. In the latter, the foams had larger initial volumes. A slow decrease in the foam volume was detected during the first 24 hours as a result of water drainage and bubble compaction, but the foam was still wet (contained about 60% water) and even after several days. Microscopic observations revealed that there were micro-sized non-spherical bubbles (~50 μm) surrounded by branched particle aggregates. The surface of the bubbles were rough as a result of ripples, which is similar to the buckling of the particle monolayer in a Langmuir trough after compression, as mentioned in section 1.2. Alargova et al. demonstrated that rod-like particles can also act as an effective foam stabiliser [107]. By using polymer microrods

(23.5 μm in length and 0.6 μm in diameter), a wet foam can be obtained upon hand shaking the suspensions (0.2- 2.2 wt.% in pure water). The foam can survive for more than 3 weeks even under extremely harsh conditions (drying, expansion in a vacuum). Different from the bubbles stabilized by spherical particles, the foam stabilized by rodlike particles were made of approximately spherical air bubbles (10-100 μm). These bubbles were covered with dense shells of particles and did not change their shape during the observation. The strong particle attachment to the bubbles and sustaining of thick films between the bubbles were identified as the main factors for the foam stability.

It is believed that the ability of colloidal particles to stabilize a wet foam can be remarkably affected by their hydrophobicity. Partially hydrophobic particles with contact angle θ close to 90˚ can act as a foam stabiliser, whereas more hydrophilic particles ($\theta > 90$˚) cannot stabilize a foam. In Alargova's experiment, when some surfactants were added into the foam system, they can adsorb onto the surface of the rodlike particles and make them more hydrophilic. The particles are then transferred from the foam into the liquid, which destroyed the foam [107]. Too hydrophobic particles, however, can stabilise water in air, making a free-flowing powder material containing up to 95 % water ("dry water"). This work has been published by Binks and Murakami in 2006 [108]. The air-water-particles inversion can be achieved either by the hydrophobicity of silica particles at a constant air/water ratio, or by changing the air/water ratio at a fixed particle wettability. Figure 2.12a shows the transitional inversion via changes to the curvature of air-water surfaces due to changes in the particle hydrophobicity.

The particle concentration in the initial dispersion is also important for the foam stability. The particle-stabilized foams are ultra-stable only if the particle concentration is large enough. It is reported that only when the particle concentration reaches 0.7 wt.% or above, the foam stability becomes remarkable [109]. Fujii reported foams from different size (0.2−1.6 μm) and concentration (1−10 wt.%) latex suspensions. The most stable foams were obtained from the largest particle concentration with biggest size. Besides hydrophobicity and concentration, particle shape and size are also identified as the main factors for the foam stability.
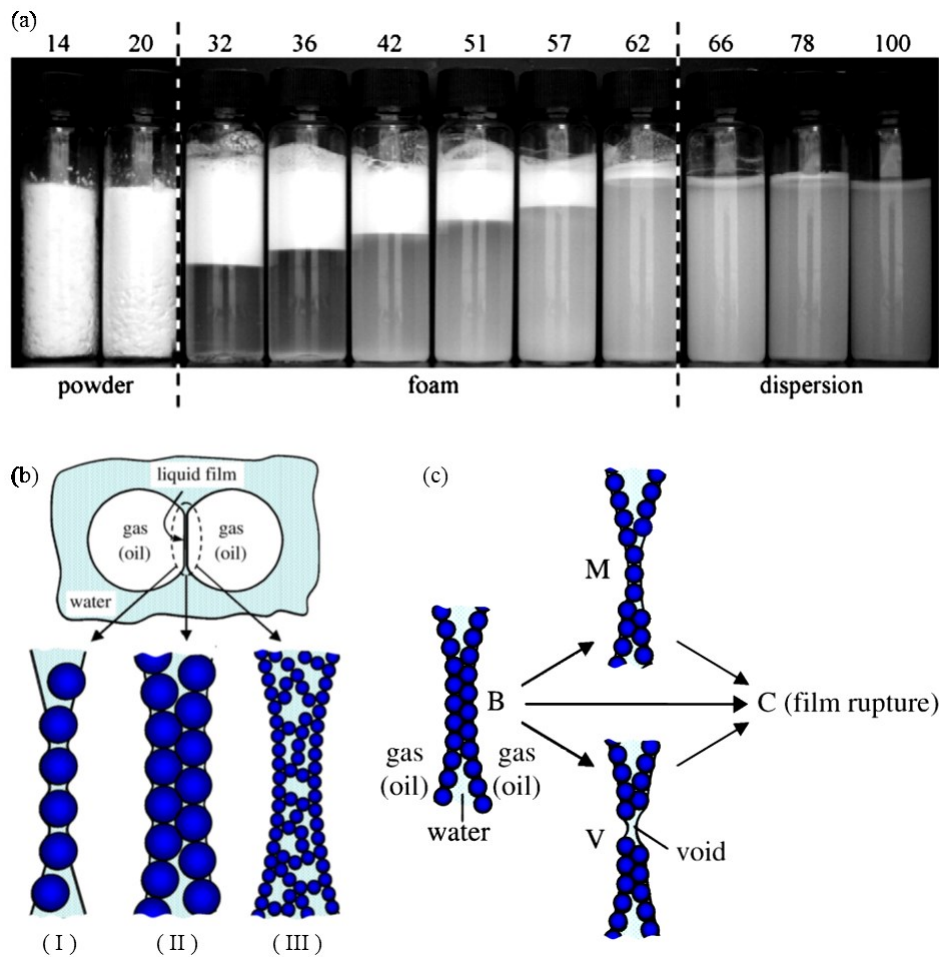
Figure 2.12 *(a) Photograph of vessels containing 2 wt.% fumed silica particle two weeks after mixing and aeration, for particles of different wettabilities. These silica particles are quasi-spherical with 20-30 nm in diameter. The (%) SiOH content on particle surfaces (written above) increases from right to left as particles become more hydrophobic. Aqueous, air-in-water foams and water-in-air powders inverted by the particle wettabilities, which are divided by the dashed line. (b) Three possible mechanisms of particle film between bubbles. (I) a particle monolayer; (II) a bilayer of close-parked particles; (III) a 3D network of particle aggregation in the continuous phase. (c) Possible rupture mechanism of a particle film between bubbles: direct rupture (process B-C); bilayer-to-monolayer transition (process B-M-C) and void formation (process B-V-C). (a) is taken from [108]; (b) and (c) are both from [104].*

Although colloidal particles are very good foam stabilisers, coarsening and coalescence can both occur in their foam systems. X-ray tomography of foams made by shaking revealed that some bubbles shrink while others become bigger. Visual

43

observations after several months also demonstrated the bubbles sometimes break [95]. Three mechanisms of foam stabilized by colloidal particles were discussed. The first two mechanisms assumed either a bridging monolayer or a bilayer of close-packed particles has been formed between the air bubbles (I and II in Figure 2.12b). Some experiments with emulsions suggest that the particle film can rupture without rearrangement, or via bilayer-to-monolayer transition. The latter occurs in two steps: particles rearrange into a monolayer followed by its rupture; alternatively, the film forms a void and then ruptures (Figure 2.12c) [103, 106, 109-112]. The third mechanism considered a network of particle aggregates (or hydrogel) inside the continuous phase (III in Figure 2.12b). It occurs when the excess particles in the bulk liquid phase are flocculated and form a three-dimensional network (gel). Foams stabilized by this mechanism are effectively stable because the particle network separates the bubbles and prevents the coalescence and coarsening.

2.4.3 Foams stabilized by protein and peptide molecules

Although the particle-stabilized foams are ultrastable, for food-related and other environmentally friendly applications, foams are mostly stabilized by protein molecules. Similar with the other foam systems, individual protein molecules transfer from the bulk aqueous phase to the air/water interface and form an interface film, stabilising the air bubbles. E. Allen Foegeding and coworkers studied the foaming properties of whey and egg white proteins [113]. A. Saint-Jalmes et al. compared the protein foams and surfactant foams and concluded that the microscopic origins of foam stability is quite different. For the surfactant foams, the mechanism of stability is related to the repulsive interaction between the adsorbed thin films around the bubbles, while for the protein foams the confinement of aggregates within the thin films plays an important role. At constant liquid fraction, the coarsening rate is slower for protein foams, which is due to the larger film thickness [114].

Compared with the unhydrolyzed proteins, peptides can markedly improve the foam-ability and foam stability, which is partially caused by the reduced size of peptides promoting a more rapid adsorption at the interface [115, 116]. Peptide molecules can adsorb rapidly at a freshly formed interface to achieve a rapid reduction in surface tension and thus can form a stable foam system [117]. The foaming properties of

peptides were shown to be influenced by the ionic strength, pH and temperature of the foaming solution [118], as well as the relative hydrophobicity of the peptides [119]. The development of functional peptides to switch the foam stability has been carried out by Middelberg group, where a "tail" has been added to the peptide molecule to make them into a relatively conventional surfactant [117]. It was reported that without metal ions or at acidic pH in bulk solution, the peptides form an interfacial film with low elasticity. In this case, the interfacial film of adsorbed peptides is in a fluid-like state. In the presence of metal ions, the interfacial elastic modulus remarkably increases, and the peptides can form a mechanically strong resistant solid-like layer to protect the bubbles [114]. By using a neutron reflectivity technique, it has been shown that the structure of the interfacial film formed by the peptides is a monolayer [120]. It is believed that the binding between metal ions and histidine residues can strengthen the interactions between the peptide molecules at the interface.

References:

[1] Paul, S.; Pearson, C.; Molloy, A.; Cousins, M. A.; Green, M.; Kolliopoulou, S.; Dimitrakis, P.; Normand, P.; Tsoukalas, D.; Petty, M. C. Nano Lett. 2003, 3, 533−536.

[2] Brzozowska, A. M.; Duits, M. H. G.; Mugele, F. Stability of Stearic Acid Monolayers on Artificial Sea Water. Colloids Surf., A 2012, 407 (0), 38−48.

[3] Goto, T.E.; Lopez, R.F.; Iost, R.M.; Crespilho, F.N.; Caseli, L. Monolayer Collapse Regulating Process of Adsorption−Desorption of Palladium Nanoparticles at Fatty Acid Monolayers at the Air−Water Interface. Langmuir 2011. 27, 2667–2675.

[4] Acharya, S.; Hill, J. P.; Ariga, K. Soft Langmuir–Blodgett technique for hard nanomaterials. Adv. Mater. 2009, 21, 2959–2981.

[5] Ji, X.; Wang, C.; Xu, J.; Zheng, J.; Gattas-Asfura, K. M.; Leblanc, R. M. Surface chemistry studies of (CdSe) ZnS quantum dots at the air-water interface. Langmuir 2005, 21, 5377–5382.

[6] Botto, L.; Lewandowski, E. P.; Cavallaro, M.; Stebe, K. J. Capillary interactions between anisotropic particles. Soft Matter 2012, 8, 9957−9971.

[7] Aveyard, R.; Clint, J. H.; Nees, D.; Paunov, V. N. Compression and structure of monolayers of charged latex particles at air/water and octane/water interfaces. Langmuir 2000, 16, 1969−1979.

[8] Aveyard, R.; Clint, J. H.; Nees, D.; Quirke, N. Structure and collapse of particle monolayers under lateral pressure at the octane/aqueous surfactant solution interface. Langmuir 2000, 16, 8820−8828.

[9] Botto, L.; Yao, L.; Leheny, R. L.; Stebe, K. J. Capillary bond between rod-like particles and the micromechanics of particle-laden interfaces. Soft Matter, 2012, 8, 4971–4979.

[10] Madivala, B.; Fransaer, J.; Vermant, J. Self-assembly and rheology of ellipsoidal particles at interfaces. Langmuir 2009, 25, 2718–2728.

[11] Loudet, J. C.; Pouligny, B. Self-assembled capillary arrows. Europhys. Lett, 2009, 85, 28003.

[12] Madivala, B.; Vandebril, S.; Fransaer, J.; Vermant, J. Exploiting particle shape in solid stabilized emulsions. Soft Matter, 2009, 5, 1717–1727.

[13] Batten, R. D.; Stillinger, F. H.; Torquato, S. Phase behavior of colloidal superballs: Shape interpolation from spheres to cubes. R. D. Batten, F. H. Stillinger and S. Torquato, Phys. Rev. E, 2010, 81, 061105.

[14] Marechal, M.; Kortschot, R. J.; Demirors, A. F.; Imhof, A.; Dijkstra, M. Phase Behavior and Structure of a New Colloidal Model System of Bowl-Shaped Particles. Nano Lett., 2010, 10, 1907–1911.

[15] Agarwal, U.; Escobedo, F. A. Mesophase behaviour of polyhedral particles. Nat. Mater., 2011, 10, 230–235.

[16] Donev, A.; Stillinger, F. H.; Chaikin, P. M.; Torquato, S. Unusually dense crystal packings of ellipsoids. Phys. Rev. Lett., 2004, 92, 255506.

[17] Zeravcic, Z.; Xu, N.; Liu, A. J.; Nagel, S. R.; van Saarloos, W. Excitations of ellipsoid packings near jamming. Europhys. Lett., 2009, 87, 26001.

[18] Delaney, G. W.; Cleary, P. W. The packing properties of superellipsoids. Europhys. Lett., 2010, 89, 34002.

[19] Torquato, S.; Jiao, Y. Dense packings of the Platonic and Archimedean solids. Nature, 2010, 460, 876–879.

[20] Mohraz, A.; Moler, D. B.; Ziff, R. M.; Solomon, M. J. Effect of monomer geometry on the fractal structure of colloidal rod aggregates. Phys. Rev. Lett., 2004, 92, 155503.

[21] Gunes, D. Z.; Scirocco, R.; Mewis, J.; Vermant, J. Flow-induced orientation of non-spherical particles: Effect of aspect ratio and medium rheology. Non-Newtonian Fluid Mech., 2008, 155, 39–50.

[22] Glotzer, S. C.; Solomon, M. J. Anisotropy of building blocks and their assembly into complex structures. Nat. Mater., 2007, 6, 557–562.

[23] Sacanna, S.; Pine, D. J. *Curr. Opin. Colloid Interface Sci.*, **2011**, *16*, 96–105.

[24] Lewandowski, E. P.; Bernate, J. A.; Tseng, A.; Searson, P. C.; Stebe, K. J. Oriented assembly of anisotropic particles by capillary interactions. *Soft Matter* **2009**, *5*, 886–105.

[25] Lewandowski, E. P.; Bernate, J. A.; Searson, P. C.; Stebe, K. J. Rotation and alignment of anisotropic particles on nonplanar interfaces. *Langmuir* **2008**, *24*, 9302–9307.

[26] Lewandowski, E. P.; Cavallaro, M.; Botto, L.; Bernate, J. C.; Garbin, V.; Stebe, K. J. Orientation and self-assembly of cylindrical particles by anisotropic capillary interactions. *Langmuir* **2010**, *26* 15142–15154.

[27] Dong, L.; Johnson, D. T. Adsorption of acicular particles at liquid-fluid interfaces and the influence of the line tension. *Langmuir* **2005**, *21*, 3838–3849.

[28] Lewandowski, E. P.; Searson, P. C.; Stebe, K. J. Orientation of a Nanocylinder at a Fluid Interface. *J. Phys. Chem. B* **2006**, *110*, 4283–4290.

[29] He, J.; Zhang, Q.; Gupta, S.; Emrick, T.; Russell, T.; Thiyagarajan, P. Drying droplets: a window into the behavior of nanorods at interfaces. *Small* **2007**, *3*, 1214–1217.

[30] Lehle, H.; Noruzifar, E.; Oettel, M. Ellipsoidal Particles at Fluid Interfaces. Ellipsoidal particles at fluid interfaces. *Eur. Phys. J. E*, **2008**, *26*, 151–160.

[31] Loudet, J. C.; Pouligny, B. How do mosquito eggs self-assemble on the water surface? *Eur. Phys. J. E.* **2011**, *34*, 76–160.

[32] Loudet, J. C.; Alsayed, A. M.; Zhang, J.; Yodh, A. G. Capillary interactions between anisotropic colloidal particles. *Phys. Rev. Lett.*, **2005**, *94*, 018301.

[33] Basavaraj, M. G.; Fuller, G. G.; Fransaer, J.; Vermant, J. Packing, flipping, and buckling transitions in compressed monolayers of ellipsoidal latex particles. *Langmuir* **2006**, *22*, 6605–6612.

[34] Rossi, L.; Sacanna, S.; Irvine, W. T. M.; Chaikin, P. M.; J., P. D.; Philipse, A. P. Cubic crystals from cubic colloids. *Soft Matter*, **2011**, *7*, 4139–4142.

[35] Kim, F.; Kwan, S.; Akana, J.; Yang, P. Langmuir-Blodgett nanorod assembly. *J. Am. Chem. Soc.*, **2001**, *123*, 4360–4361.

[36] Acharya, S.; Efrima, S. Two-dimensional pressure-driven nanorod-to-nanowire reactions in Langmuir monolayers at room temperature. *J. Am. Chem. Soc.*, **2005**, *127*, 3486–3490.

[37] Liu, B.; Besseling, T. H.; van Bladderen, A.; Imhof, A. Confinement Induced Plastic Crystal-to-Crystal Transitions in Rodlike Particles with Long-Ranged Repulsion. *Phys. Rev. Lett.*, **2015**, *115*, 078301.

[38] Besseling, T. H.; Hermes, M.; Kuijk, A.; de Nijs, B.; Deng, T. S.; Dijkstra, M.; Imhof, A.; van Blaaderen, A. Determination of the positions and orientations of concentrated rod-like colloids from 3D microscopy data. *J. Phys.: Condens. Matter* **2015**, *27*, 194109.

[39] Ebrahimi, F.; Azizpour, T. Maleki, H. Janssen effect and the stability of quasi-two-dimensional sandpiles. *Phys. Rev. E.*, **2010**, *82*, 031302.

[40] Dasgupta, A.; Mondal, J. H.; Das, D. Peptide hydrogels. *RSC Adv.*, **2013**, *3*, 9117–9149.

[41] Luo, Y.; Kirker, K. R.; Prestwich, G. D. Cross-linked hyaluronic acid hydrogel films: new biomaterials for drug delivery. *J. Controlled Release* **2000**, *69*, 169–184.

[42] Tokarev, I.; Minko, S. Stimuli-responsive hydrogel thin films. *Soft Matter*, **2009**, *5*, 511–524.

[43] Langer, R.; Peppas, N. Chemical and Physical Structure of Polymers as Carriers for Controlled Release of Bioactive Agents: A Review. *Rev. Macromol. Chem. Phys.*, **1983**, *C23*, 61.

[44] Jagur-Grodzinski, J. Polymeric gels and hydrogels for biomedical and pharmaceutical applications. *Polym. Adv. Technol.* **2010**, *21*, 27–47.

[45] Slaughter, B. V.; Khurshid, S. S.; Fisher, O. Z.; Khademhosseini, A.; Peppas, N. A. Hydrogels in regenerative medicine. *Adv. Mater.* **2009**, *21*, 3307–3329.

[46] Adams, D. J. Dipeptide and Tripeptide Conjugates as Low-Molecular-Weight Hydrogelators. *Macromol. Biosci.* **2011**, *11*, 160–173.

[47] Ryan, D. M.; Nilsson, B. L. Self-assembled amino acids and dipeptides as noncovalent hydrogels for tissue engineering. *Polym. Chem.*, **2012**, *3*, 18–33.

[48] Vegners, R.; Shestakova, I.; Kalvinsh, I.; Ezzell, R. M.; Janmey, P. A. Use of a gel- forming dipeptide derivative as a carrier for antigen presentation. *J. Pept. Sci.* **1995**, *1*, 371–378.

[49] Yang, Z. M.; Liang, G. L.; Ma, M. L.; Gao, Y.; Xu, B. Conjugates of naphthalene and dipeptides produce molecular hydrogelators with high efficiency of hydrogelation and superhelical nanofibers. *J. Mater. Chem.* **2007**, *17*, 850–854.

[50] Qiu, Z. J.; Yu, H. T.; Li, J. B.; Wang, Y.; Zhang, Y. Spiropyran-linked dipeptide forms supramolecular hydrogel with dual responses to light and to ligand–receptor interaction. *Chem. Commun.* **2009**, *23*, 3342–3344.

[51] Chen, L.; Revel, S.; Morris, K.; Adams, D. J. Energy transfer in self-assembled dipeptide hydrogels. *Chem. Commun.* **2010**, *46*, 4267–4269.

[52] Zhang, Y.; Yang, Z. M.; Yuan, F.; Gu, H. W.; Gao, P.; Xu, B. Molecular recognition remolds the self-assembly of hydrogelators and increases the elasticity of the hydrogel by 106-fold. *J. Am. Chem. Soc.*, **2004**, *126*, 15028–15029.

[53] Fichman, G.; Gazit, E. Self-assembly of short peptides to form hydrogels: Design of building blocks, physical properties and technological applications. *Acta Biomater.* **2004**, *10*, 1671–1682.

[54] Mahler, A.; Reches, M.; Rechter, M.; Cohen, S.; Gazit, E. Rigid, Self-Assembled Hydrogel Composed of a Modified Aromatic Dipeptide. *Adv. Mater.*, **2006**, *18*, 1365–1370.

[55] Jayawarna, V.; Ali, M.; Jowitt, T. A.; Miller, A. E.; Saiani, A.; Gough, J. E.; Ulijn, R. V. Nanostructured Hydrogels for Three-Dimensional Cell Culture Through Self-Assembly of Fluorenylmethoxycarbonyl-Dipeptides. *Adv. Mater.*, **2006**, *18*, 611–614.

[56] Smith, A. M.; Williams, R. J.; Tang, C.; Coppo, P.; Collins, R. F.; Turner, M. L.; Saiani, A.; Ulijn, R. V. Fmoc-Diphenylalanine Self Assembles to a Hydrogel *via* a Novel Architecture Based on π–π Interlocked β-Sheets. *Adv. Mater.*, **2008**, *20*, 37–41.

[57] Tang, C.; Smith, A. M.; Collins, R. F.; Ulijn, R. V.; Saiani, A. Fmoc-diphenylalanine self-assembly mechanism induces apparent pKa shifts. *Langmuir*, **2009**, *25*, 9447–9453.

[58] Adams, D. J.; Mullen, L. M.; Berta, M.; Chen, L.; Frith, W. F. Relationship between molecular structure, gelation behaviour and gel properties of Fmoc-dipeptides. *Soft Matter* **2010**, *6*, 1971–1980.

[59] Chen, L.; Morris, K.; Laybourn, A.; Elias, D.; Hicks, M. R.; Rodger, A.; Serpell, L. C.; Adams, D. J. Self-assembly mechanism for a naphthalene-dipeptide leading to hydrogelation. *Langmuir* **2010** *26*, 5232–5242.

[60] Yan, C. Q.; Pochan, D. J. Rheological properties of peptide-based hydrogels for biomedical and other applications. *Chem. Soc. Rev.*, **2010**, *39*, 3528–3540.

[61] Aulisa, L.; Dong, H.; Hartgerink, J. D. Self-assembly of multidomain peptides: sequence variation allows control over cross-linking and viscoelasticity. *Biomacromolecules*, **2009**, *10*, 2694–2698.

[62] Grigoriou, S.; Johnson, E. K.; Chen, L.; Adams, D. J.; James, T. D.; Cameron, P. J. Dipeptide hydrogel formation triggered by boronic acid–sugar recognition. *Soft Matter*, **2012**, *8*, 6788–2698.

[63] Adams, D. J.; Butler, M. F.; Frith, W. F.; Kirkland, M.; Mullen, L.; Sanderson, P. A new method for maintaining homogeneity during liquid–hydrogel transitions using low molecular weight hydrogelators. *Soft Matter*, **2009**, *5*, 1856–1862.

[64] Galler, K. M.; Aulisa, L.; Regan, K. R.; D'Souza, R. N.; Hartgerink, J. D. Self-assembling multidomain peptide hydrogels: designed susceptibility to enzymatic cleavage allows enhanced cell migration and spreading. *J. Am. Chem. Soc.*, **2010**, *132*, 3217–3223.

[65] Bowerman, C. J.; Nilsson, B. L. A reductive trigger for peptide self-assembly and hydrogelation. *J. Am. Chem. Soc.*, **2010**, *132*, 9526–9527.

[66] Zhang, C.; Liu, C.; Xue, X.; Zhang, X.; Huo, S.; Jiang, Y.; Chen, W.-Q.; Zou, G.; Liang, X.-J. Salt-responsive self-assembly of luminescent hydrogel with intrinsic gelation-enhanced emission. *ACS Appl. Mater. Interfaces* **2014**, *6*, 757−762.

[67] Chen, L.; McDonald, T. O.; Adams, D. J. Salt-induced hydrogels from functionalised-dipeptides. *RSC Adv.*, **2013**, *3*, 8714–8720.

[68] Wang, H.; Yang, Z.; Adams, D. J. Controlling peptidebased hydrogelation. *Mater. Today*, **2012**, *15*, 500–507.

[69] Chen, L.; Pont, G.; Morris, K.; Lotze, G.; Squires, A.; Serpell, L. C.; Adams, D. J. Salt-induced hydrogelation of functionalised-dipeptides at high pH. *Chem. Commun.* **2011**, *47*, 12071−12073.

[70] Ulijn, R. V.; Smith, A. M. Designing peptide based nanomaterials. *Chem. Soc. Rev.* **2008**, *37*, 664−675.

[71] Gallagher, W. FTIR analysis of protein structure. http://www.chem.uwec.edu/Chem455_S05/Pages/Manuals/FTIR_of_proteins.pdf. Accessed May **2009**.

[72] Mu, X.; Eckes, K. M.; Nguyen, M. M.; Suggs, L. J.; Ren, P. Experimental and computational studies reveal an alternative supramolecular structure for Fmoc-dipeptide self-assembly. *Biomacromolecules* **2012**, *13*, 3562−3571.

[73] Shi, J.; Gao, Y.; Zhang, Y.; Pan, Y.; Xu, B. Calcium ions to cross-link supramolecular nanofibers to tune the elasticity of hydrogels over orders of magnitude. *Langmuir* **2011**, *27*, 14425–14431.

[74] Gan, T.; Guan, Y.; Zhang, Y. Thermogelable PNIPAM microgel dispersion as 3D cell scaffold: effect of syneresis. *J. Mater. Chem.*, **2010**, *20*, 5937–5944**.**

[75] Suri, J. T.; Cordes, D. B.; Capuccio, F. E.; Wessling, R. A.; Singaram, B. Continuous Glucose Sensing with a Fluorescent Thin-Film Hydrogel. *Angew. Chem., Int. Ed.* **2003**, *42*, 5857–5859.

[76] Dexter, A. F.; Malcolm, A. S.; Middelberg, A. P. J. Reversible Active Switching of the Mechanical Properties of a Peptide Film at a Fluid-Fluid Interface. *Nat. Mater.* **2006**, *5*, 502–506.

[77] Haines-Buttericka, L. A.; Salick, D. A.; Pochan, D. J.; Schneider, J. P. In vitro assessment of the pro-inflammatory potential of β-hairpin peptide hydrogels. *Biomaterials* **2008**, *29*, 4164–4169.

[78] Lepère, M.; Chevallard, C.; Hernandez, J.; Mitraki, A.; Guenoun,P. Multiscale surface self-assembly of an amyloid-like peptide. *Langmuir* **2007**, *23*, 8150–8155.

[79] Lepère, M.; Chevallard, C.; Brezesinski, G.; Goldmann, M.; Guenoun, P. Crystalline amyloid structures at interfaces. *Angew. Chem., Int. Ed* **2009**, *48*, 5005 – 5009.

[80] Johnson, E. K.; Adams, D. J.; Cameron, P. J. Directed self-assembly of dipeptides to form ultrathin hydrogel membranes. *J. Am. Chem. Soc.* **2010**, *132*, 5130–5136.

[81] Hijnen, N.; Cai, D.; Clegg, P. S. Bijels stabilized using rod-like particles. *Soft Matter*, **2015**, *11*, 4351–5136.

[82] Wilson, A. J. *Springer Series in Applied Biology*; Springer: Berlin, **1989**.

[83] Hench, L. L. Bioceramics. *J. Am. Ceram. Soc.* **1998**, *81*, 1705–1728.

[84] Morrison, I. D.; Ross, S. *Colloidal Dispersions: Suspensions, Emulsions, and Foams*; Wiley-Interscience: New York, **2002**.

[85] Subramaniam, A. B.; Mejean, C.; Abkarian, M.; Stone, H. A. Micro-Structure, Morphology and Lifetime of Armored Bubbles Exposed to Surfactants. *Langmuir* **2006**, *22*, 5986−5990.

[86] Gonzenbach, U. T.; Studart, A. R.; Tervoort, E.; Gauckler, L. J. Tailoring the Microstructure of Particle-Stabilized Wet Foams. *Langmuir* **2007**, *23*, 1025–1032.

[87] Li, X. L.; Karakashev, S. I.; Evans, G. M.; Stevenson, P. Effect of environmental humidity on static foam stability. *Langmuir* **2012**, *28*, 4060–4068.

[88] Saint-Jalmes, A. Physical chemistry in foam drainage and coarsening. *Soft Matter* **2006**, *2*, 836–849.

[89] Durian, D. J.; Weitz, D. A.; Pine, D. J. Scaling behavior in shaving cream. *Phys. Rev. A*, **1991**, *44*, R7902.

[90] Höhler, R.; Cohen-Addad, S. Rheology of liquid foam. *J. Phys.: Condens. Matter*, **2005**, *17*, R1041.

[91] Meinders, M. B. J.; van Vliet, T. The role of interfacial rheological properties on Ostwald ripening in emulsions. *Adv. Colloid Interface Sci.* **2004**, *108*, 119–126.

[92] Georgieva, D.; Schmitt, V.; Leal-Calderon, F.; Langevin, D. On the possible role of surface elasticity in emulsion stability. *Langmuir* **2009**, *25*, 5565–5573.

[93] Tcholakova, S.; Mitrinova, Z.; Golemanov, K.; Denkov, N. D.; Vethamuthu, M.; Ananthapadmanabhan, K. P. Control of Ostwald ripening by using surfactants with high surface modulus. *Langmuir* **2011**, *27*, 14807–14819.

[94] Dickinson, E.; Ettelaie, R.; Murray, B. S.; Du, Z. Kinetics of disproportionation of air bub- bles beneath a planar air–water interface stabilized by food proteins. *J. Colloid Interface Sci.* **2002**, *252*, 202–213.

[95] Martinez, A. C.; Rio, E.; Delon, G.; Saint-Jalmes, A.; Langevin, D.; Binks, B. P. On the origin of the remarkable stability of aqueous foams stabilised by nanoparticles: link with microscopic surface properties. *Soft Matter* **2008**, *4*, 1531–1535.

[96] Chae, J. J.; Tabor, M. Cyclotron resonance of conduction electrons in GaAs at very high magnetic fields. *Phys. Rev. E* **1997**, *55*, 598.

[97] Hasmy, A.; Paredes, R.; Sonneville, O.; Cabane, B.; Botet, R. Dynamical transition in a model for dry foams. *Phys. Rev. Lett.* **1999**, *82*, 3368.

[98] Pays, K.; Giermanska-Kahn, J.; Pouligny, B.; Bibette, J.; Leal-Calderon, F. Double emulsions: A tool for probing thin-film metastability. *Phys. Rev. Lett.* **2001**, *87*, 178304.

[99] Georgieva, D.; Cagna, A.; Langevin, D. Link between surface elasticity and foam stability. *Soft Matter* **2009**, *5*, 2063–2071.

[100] Carrier, V.; Colin, A. Coalescence in Draining Foams. *Langmuir* **2003**, *19*, 4535–4538.

[101] Koehler, S. A.; Hilgenfeldt, S.; Stone, H. A. A generalized view of foam drainage: experiment and theory. *Langmuir* **2000**, *16*, 6327–6341.

[102] Saint-Jalmes, A.; Zhang, Y.; Langevin, D. Quantitative description of foam drainage: transitions with surfacemobility. *Eur. Phys. J. E.* **2004**, *15*, 53–60.

[103] Binks, B. P. Particles as surfactants-similarities and differences. *Curr. Op. Colloid Interface Sci.* **2002**, *7*, 21–41.

[104] Horozov, T. S. Foams and foam films stabilised by solid particles. *Curr. Op. Colloid Interface Sci.* **2008**, *13*, 134–140.

[105] Binks, B.P.; Horozov, T. S. Colloidal particles at liquid interfaces: an introduction. Cambridge University Press: Cambridge, U.K., **2006**.

[106] Binks, B.P.; Horozov, T. S. Aqueous foams stabilized solely by silica nanoparticles. *Angew. Chem., Int. Ed.* **2005**, *44*, 3722–3725.

[107] Alargova, R.G.; Warhadpande, D. S.; Paunov, V. N.; Velev, O. D. Foam super-stabilization by polymer microrods. *Langmuir* **2004**, *20*, 10371–10374.

[108] Binks, B. P.; Murakami, R. *Nature Materials* **2006**, *5*, 865–869.

[109] Stocco, A.; Rio, E.; Binks, B. P.; Langevin, D. Aqueous foams stabilized solely by particles. *Soft Matter* **2011**, *7*, 1260–1267.

[110] Tcholakova, S.; Denkov, N. D.; Lips, A. Comparison of solid particles, globular proteins and surfactants as emulsifiers. *Phys Chem Chem Phys* **2008**, *10*, 1608–1627.

[111] Hunter, T. N.; Pugh, R. J.; Franks, G. V.; Jameson, G. J. The role of particles in stabilising foams and emulsions. *Adv. Colloid Interface Sci.* **2008**, *137*, 57–81.

[112] Safouane, M.; Langevin, D.; Binks, B. P. Effect of particle hydrophobicity on the properties of silica particle layers at the air–water interface. *Langmuir* **2007**, *23*, 11546–11553.

[113] Foegeding, E. A.; Luck, P. J.; Davis, J. P. Factors determining the physical properties of protein foams. Food Hydrocolloids 2006, 20, 284–292.

[114] Saint-Jalmes, A.; Peugeot, M. L.; Ferraz, H.; Langevin, D. Differences between protein and surfactant foams: Microscopic properties, stability and coarsening. *Colloids Surf. A*, **2005**, *263*, 219–225.

[115] van der Ven, C.; Gruppen, H.; de Bont, D. B. A.; Voragen, A. G. J. Correlations between Biochemical Characteristics and Foam-Forming and -Stabilizing Ability of Whey and Casein Hydrolyzates. *Journal of Agricultural and Food Chemistry*, **2002**, *50*, 2938–2946.

[116] Davis, J. P.; Doucet, D.; Foegeding, E. A. Foaming and Interfacial Properties of Hydrolyzed *β*-Lactoglobulin. *J. Colloid Interface Sci.* **2005**, *288*, 412–422.

[117] Malcolm, A. S.; Dexter, A. F.; Middelberg, A. P. J. Foaming properties of a peptide designed to form stimuli-responsive interfacial films. *Soft Matter* **2006**, *2*, 1057–1066.

[118] Caessens, P. W. J. R.; Gruppen, H.; Visser, S.; van Aken, G.A.; Voragen, A. G. J. Plasmin Hydrolysis of β-Casein: Foaming and Emulsifying Properties of the Fractionated Hydrolysate. J. Agric. *Food Chem.***1997**, *45*, 2935–2941.

[119] Agyare, K. K.; Addo, K.; Xiong, Y. L. Emulsifying and Foaming Properties of Transglutaminase-Treated Wheat Gluten Hydrolysate as Influenced by pH, Temperature and Salt. *Food Hydrocolloids* **2009**, *23*, 72–81.

[120] Middelberg, A. P. J.; He, L.; Dexter, A. F.; Shen, H.-H.; Holt, S. A.; Thomas, R. K. The interfacial structure and Young's modulus of peptide films having switchable mechanical properties. *J. R. Soc. Interface* **2008**, *5*, 47– 54.

Results I

Rod-Like Particles
at the Air-Water Interface

Chapter 3

Monolayers of colloidal spherocylinders under compression

Micro-scale akaganéite-silica core-shell rods with different aspect ratios are synthesized to create monolayers at the air-water interface. Microscopic observations reveal a sequence of phase transitions by compressing the monolayers in a Langmuir trough. For short rods, a flipping phenomenon occurs to relieve the compressional stress. For longer rods, instead of flipping, multilayer aggregates are formed under compression. Numerical simulations are carried out by collaborators to corroborate the flipping phenomenon and the changes with the rods' aspect ratio. Finally, the self-assembly of a binary mixture of rods and spheres is investigated at the air-water interface.

3.1 Introduction

Colloidal particles are important model systems for studying self-assembly and phase behaviour. In recent years, with the development of new synthetic techniques, rod-like particles have become more viable blocks. Rod-like particles are interesting to study at an interface because they can either lie within or perpendicular to the two-dimensional surface; furthermore such assemblies can be valuable in optical, magnetic and electronic applications. Previously, micro-scale cylinders and ellipsoids were investigated at the interface (see section 2.2) [1, 2]. This chapter focuses on the interfacial properties of another rod-like particle, spherocylinders, and the samples used in this work are akaganéite (β-FeOOH) micro-rods.

Akaganéite is an anti-ferromagnetic material, and can be found as a naturally occurring mineral in rocks and soils in the presence of high concentrations of iron and chloride. Various one-dimensional structures, like needles and tubes, have been readily

synthesized, and can also be easily converted into other iron oxides, such as hematite (α-Fe_2O_3) and magnetite (Fe_3O_4). These interesting properties make akaganéite particles attractive in many fields of application [3].

Nowadays, the most important methods for synthesizing akaganéite rods are hydro-thermal synthesis [4] and forced hydrolysis [5]. Compared with other methods, these two methods are quicker and easier to carry out, and have relatively clear reaction mechanisms. An $FeCl_3$ solution is needed for both of the methods. The process of the hydrolysis of $FeCl_3$ solution as well as the systhesis of the akaganéite rods can be summarized as:

$$FeCl_3 + 3H_2O \rightarrow Fe(OH)_3 + 3HCl \tag{3.1}$$

$$Fe(OH)_3 \rightarrow \beta\text{-}FeOOH + H_2O \tag{3.2}$$

Generally, in this process, akaganéite precipitates first due to its lower energy of nucleation, but ultimately dissolves in favour of the formation of hematite. However, increasing Fe(III) and Cl^- concentrations favours akaganéite nucleation, effectively suppressing the formation of hematite [6]. The dissolved Fe^{3+} ions initially form a complex with water molecules. The heating of the solution will cause the hydrothermal reaction, accelerating the akaganéite nucleation. As the reaction continues, the formed crystal structure becomes more defined into a lattice which has different surface energies. The β-FeOOH (100) and (110) surfaces have a minimal interaction with the anions. On the contrary, the interactive anions (*e.g.*, Cl^-) will be highly adsorbed on the (001) surface, which favours a rod-like growth selectively along the [001] direction [7]. As a result, at high Fe (III) and Cl^- concentrations, akaganéite particles with large aspect ratios can be obtained [5]. Hydro-thermal synthesis is usually chosen to synthesize nano-scale akaganéite rods [8], while forced hydrolysis method, which involves higher temperature and longer reaction, can be used to obtain rods with much larger size and aspect ratios.

To study the rods at liquid interfaces, chemical modification of the rod surfaces is essential [9]. This is normally achieved by surface coating which can change the surface chemistry of the particles and therefore change their contact angle at the interface. The coating employed should not only prevent particle aggregation, be chemically inert

and optically transparent, but also not have any influence on the solid properties of the particles. Silica coating, which has been used in a wide range of industrial products [10], meets all of these criteria. The possibility of subsequently, being able to modify the chemistry of the silica surface, makes it particularly attractive. In recent years, various methods for silica coating have been studied at the forefront of materials science. Tetraethyl orthosilicate (TEO) is widely used in all of these methods. It has been shown that by carefully controlling the thickness of the silica shell, core-shell particles can be prepared which exhibit a sensitive and tunable response to external stimuli, such as the incident light or an applied magnetic field. Moreover, in the assembly process, the distance between the core particles could also be controlled through the silica thickness.

By combined the forced hydrolysis method with silica coating techniques, Hijnen developed a simple method to prepare akaganéite-silica core-shell rods with different aspect ratios [11]. In his work, the synthesis approach was explored in detail, and the irreversible aggregation of the akaganéite particles during the synthesis was found to be fatal for the production of rods. By increasing ferric chloride and hydrochloric acid concentrations, the aggregation could be almost completely removed while maintaining a high yield. Using these akaganéite-silica core-shell rods at a liquid-liquid interface, Hijnen *et al.* created a bijel (bicontinuous interfacially jammed emulsion gel) [12], where rapid jamming seems to be the main driving force for the arrangements of the rods. Some rods were observed sticking out of the interface and some of them are even perpendicular to the interface. This is similar to the flipping phenomenon observed in the compressed monolayer of ellipsoids. Recently, a theoretical study of magnetic rods perturbed by an applied magnetic field perpendicular to the interface demonstrates that flipping becomes more energetically expensive as the aspect ratio increases [13]. Hence the aspect ratio of the rods is also an important parameter for the flipping process. So far however, the fundamental properties of the akaganéite-silica core-shell rods at liquid interfaces, the effect of the rods' aspect ratio, as well as the flipping and other organizational motifs, have not yet been studied.

Below, the particles used in the experiments are the first focus of this chapter. The synthesis method and the silica coating process are first described in detail, followed by the characterization of the resulting rods. Subsequently, the interfacial behaviour of the rods is presented in section 3.3. Langmuir trough and microscopy techniques are combined to study the rods at the air-water interface. Surface pressure-area isotherms (Π-A isotherms) are measured using the Langmuir trough. Microscopic observations reveal that the monolayers undergo a sequence of phase transitions during the compression. The aspect ratio is found to be important when in-plane rearrangements are no longer possible beyond a limiting surface pressure. Flipping occurs for short rods and bilayer aggregates are formed for longer rods. Section 3.4 presents a simulation study by collaborators, which focuses on the effect of the rods' aspect ratio, as well as the flipping dynamics under the compression. Section 3.5 is a preliminary study about the binary mixture of rods and spheres. The final section of this chapter contains discussions and a conclusion.

3.2 Particle Preparation

Using forced hydrolysis method, akaganéite templated needles were first synthesized. These needles have a large aspect ratio (~27). Silica layers can then be grown onto the surface of these needles, which make them spherocylinders. Depending on the size of the needles, spherocylinders with different aspect ratios can be obtained.

Akaganéite templated needles

Synthesis method: A solution of 0.6 M $FeCl_3$ and 0.07 M hydrochloric acid (HCl) was prepared to synthesize the akaganéite templated needles using the forced hydrolysis method. Firstly, 50g $FeCl_3$ (reagent-grade, 97%, from Sigma Aldrich) was dissolved in 250 mL distilled water in a 500-mL Pyrex bottle. After this, 3.47g HCl (fuming, 37%, from Fisher) was added, followed by topping off the solution to 500 mL with water. The solution was filtered (Whatman, qualitative) to remove impurities, and then aged in a preheated oven (Binder) at $98 \pm 1°C$ for $24 - 30$ hours (no stir is needed). The cap of the Pyrex bottle should be fitted tightly before putting it in the oven. Afterwards, the mixture was removed from the oven and cooled under a running

tap at room temperature. Then the particles were washed ~5−6 times with distilled water.

As described in reference [14], another solution of 0.1 M FeCl₃ and 4 mM HCl was prepared to make akaganéite needles with smaller aspect ratio. Specifically, 8g FeCl₃ and 0.2g HCl solution were mixed with distilled water in a 500-mL Pyrex bottle. After removing the impurities as above, the solution was placed in an oven at 98 ± 1ºC. After 24 hours, the particles were quenched to room temperature and washed several times with distilled water.
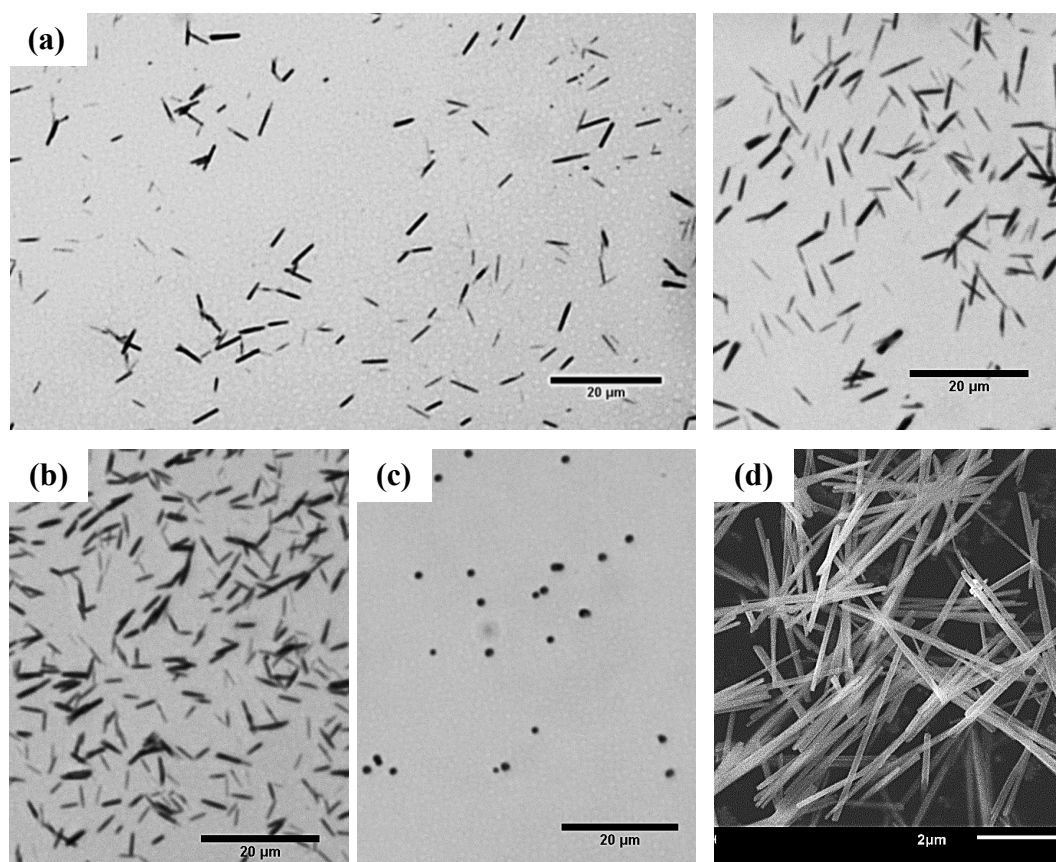
Figure 3.1 *The synthesised Akaganéite templated needles with different heating time and constituent concentrations. (a) Microscopic images before (left) and after (right) the purifying process of the akaganéite needles obtained by aging a 0.6 M [FeCl₃]/0.07 M [HCl] solution for 30 hours. (b) Purified akaganéite needles obtained by aging a 0.6 M [FeCl₃]/0.07 M [HCl] solution for 24 hours. They have a smaller aspect ratio than (a). (c) Purified akaganéite needles obtained by aging a 0.1 M [FeCl₃]/0.004 M [HCl] solution for 24 hours. The aspect ratio is even smaller. (d) SEM image of the needles in (b), the aspect ratio is ~27.*

Size selection: The synthesized particles are not particularly uniform in size, and some aggregates are also present in the solution. Therefore, purification is necessary prior to further analysis. The solution was centrifuged twice (Sorvall ST 40; Thermo Scientific, 300 rpm, 10 minutes) to remove the large particles and aggregates, and then another three times (1000 rpm, 10 minutes) to pour off the small particles in the supernatant. The resulting needles can be stored in either ethanol or distilled water.

Optical microscopy and SEM: Akaganéite needles were viewed via an Olympus BX-50 microscope equipped with a QICAM 12-bit Mono Fast 1394 camera (QImaging). Figure 3.1a demonstrates the purifying effect on the needles prepared with 30 hours heating time. Most small particles had been removed during purification. The aspect ratio of the needles can be controlled by the heating time. Figure 3.1b shows the purified needles with 24 hours heating time, which have a smaller aspect ratio. Decreasing the concentration of $FeCl_3$ and HCl can further reduce the aspect ratio. As shown in Figure 3.1c, the particles look like spheres in the image.

The needles in Figure 3.1b were also imaged using a JEOL JSM-6010PLUS/LV SEM, and present cuboidal morphologies (Figure 3.1d). By calculating the length and diameter of more than 50 particles (with ImageJ), the aspect ratio for aging a 0.6 M [$FeCl_3$]/0.07 M [HCl] solution for 24 hours is calculated to be approximately 27.

Akaganéite-silica core-shell rods

Silica coating: Akaganéite needles were dispersed (2.5 mg/mL) in a 55 mg/mL aqueous poly (vinylpyrrolidone) (PVP, average M_w = 40 kg/mol, from Sigma Aldrich) solution. The solution was then sonicated for a few hours and left to stir overnight. After this, the particles were sedimented by centrifuging at 2000 rpm for 1 hour and redispersed in 160g ethanol by sonication. This is the pre-coating solution.

An ethanol solution (~3.5 mL, from VWR) of 0.66 mM fluorescein-isothiocyanate (FITC, Isomer I, 90%, from Sigma Aldrich) and 0.17 M (3-aminopropyl) triethoxysilane (APTES, from Sigma Aldrich) was prepared and stirred overnight in darkness. This solution was then mixed with an equal volume of tetraethyl orthosilicate (TEOS, reagent-grade, 98%, from Sigma Aldrich). This mixture is the fluorescent coating solution.

Under stirring, 14.6g of ammonium hydroxide solution (35%, from Fisher) was first added into the pre-coating solution, followed by 8 additions of the fluorescent coating solution (0.75-mL each addition) with intervals of 20 – 30 minutes to ensure the growth of a smooth silica shell and to avoid secondary nucleation. Here, before the 5th addition, another 25-mL solution of PVP in ethanol (100g/L) should also be added. After all the 8 additions, the mixture was left overnight under stirring. The particles were washed multiple times with ethanol and distilled water, and then purified by centrifugation as described above.
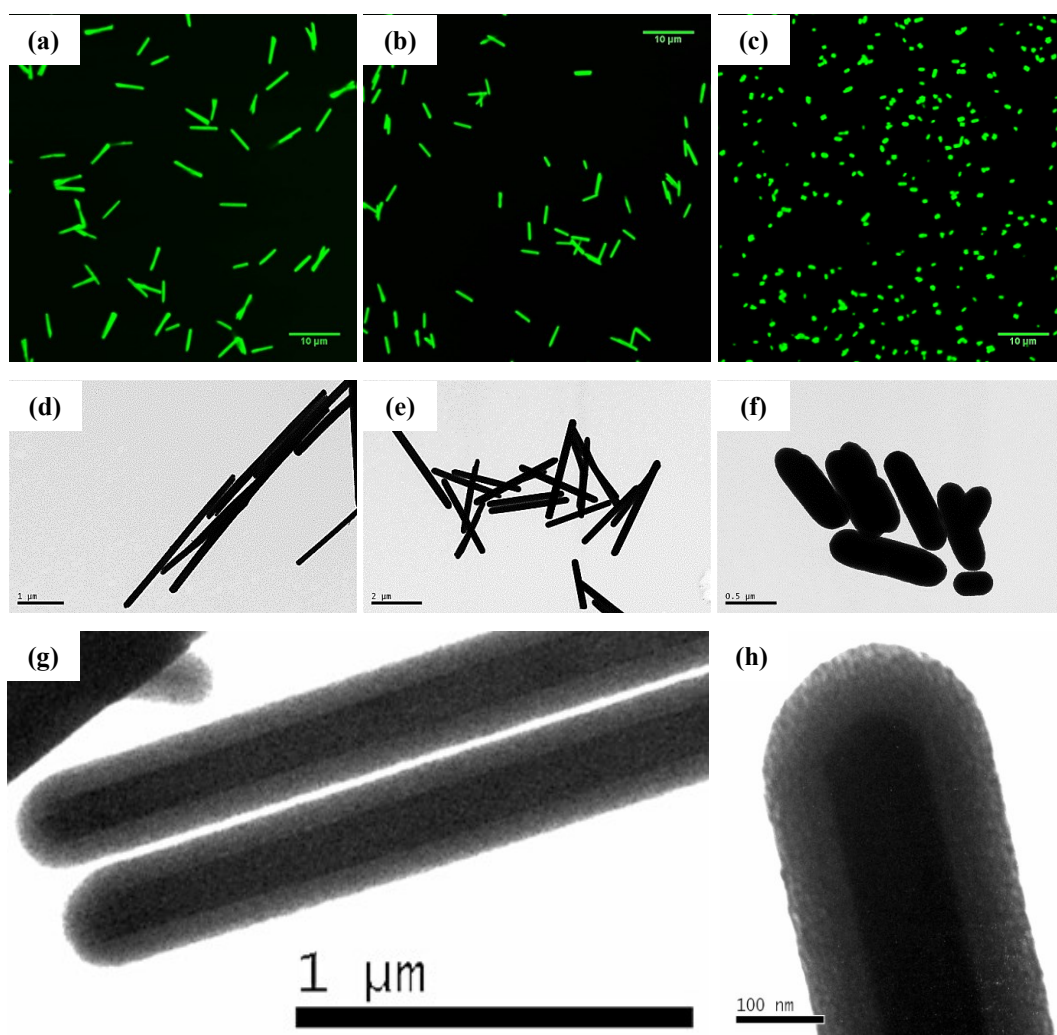
Figure 3.2 *Confocal (a-c) and TEM (d-f) images of akaganéite-silica core-shell rods with three different aspect ratios (~15 for a and d; ~9 for b and e; ~3 for c and f). (g, h) Zoomed-in TEM images reveal the rod morphology and the core-shell structure (aspect ratio ~15 and 9, respectively).*

Confocal microscopy and TEM: Confocal microscopy was performed using a Zeiss Observer.Z1inverted microscope in conjunction with a Zeiss LSM 700 scanning system 9 and a 63× 1.40 NA oil immersion objective. The FITC fluorescence was excited using the 488 nm line from an Ar ion laser. Figures 3.2a-c demonstrate the confocal images of purified Akaganéite-silica core-shell rods with three different sizes.

TEM micrographs (Philips/FEI CM120, typically operating at 80 kV) were taken to inspect particle morphology and determine size/aspect ratio distribution. The length and diameter of about 200 particles were measured by hand using ImageJ. As shown in Figure 3.2d-f, all of the particles are spherocylinders with a smooth surface and an average diameter of 0.32 ± 0.02 μm. Three different lengths, *i.e.* ~4.75 ± 0.02 μm, ~2.97 ± 0.03 μm, and ~0.93 ± 0.05 μm, were synthesized, giving average aspect ratios of ~15, ~9 and ~3, respectively. The thickness of the silica shells is fairly homogeneous around the needles. For longer rods, they are ~ 67nm thick (Figure 3.2g); for shorter rods, they are slightly thinner at around 63 nm thick (Figure 3.2h).

3.3 Compressed Monolayer of Akaganéite-Silica Rods

This section presents the interfacial behaviour of the synthesized rods using both a Langmuir trough and microscopy observations. To stay at the interface, the rods need to be hydrophobic. Isopropyl alcohol (IPA) was previously found to be an excellent solvent to improve hydrophobicity [15]. Here the rods were washed several times with IPA, in which they were stored for further use. Solutions with different concentrations (by weight) were prepared.
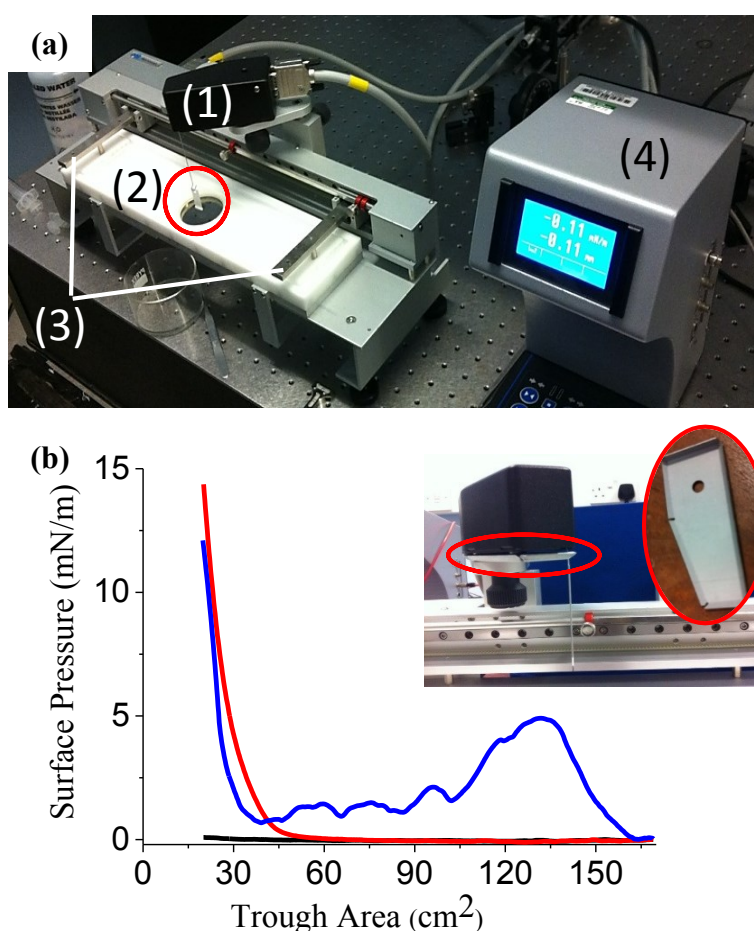
3.3.1 Surface Pressure Measurement

To study the interfacial properties of the synthesized rods, a deep understanding of the Π-A isotherm is necessary. Below is the detailed description of the surface pressure measurements carried out with a Langmuir trough system.

Trough preparation: A Langmuir trough (5.4 cm ×31.3 cm, KSV mini-trough, KSV Instruments Ltd., Finland) was used to measure the isotherms at room temperature

(Figure 3.3a). Before starting an experiment, the trough and barriers are cleaned by brushing with a soft brush covered in ethanol and then rinsing with distilled water. After this, the trough was filled with distilled water as subphase. The contaminants at the interface were removed by running the tip of an aspirator along the barriers several times, as well as over the area between the barriers. The surface pressure was measured using a paper Wilhelmy plate (10.3 mm in width, wetting angle = 0 ºC), which was aligned perpendicular to the barriers (marked red in Figure 3.3a). Before attaching the paper plate to the balance, it was soaked in the subphase liquid in a separate beaker for 30 minutes. This cleans the plate by dissolving any contaminants. The balance was calibrated by a pre-weighed object (313 mg).

Figure 3.3 (a) The Langmuir trough system used to measure the surface pressure: (1) Balance, (2) Trough, (3) Barriers, (4) LayerBuilder (Electronics). The paper plate is placed perpendicular to the barriers (circled in red). (b) Unusable Π-A isotherms of an air-water interface caused by electrostatic interactions (blue) and contaminants (red). The balck curve is acceptable. Inset: The metal cover (circled in red) which is responsible for the noisy data.

The air-water interface was considered clean if the surface pressure (subphase only) changed less than 0.1 mN/m when the barriers were moved in. In the early stages of the measurements, the pure water isotherms were very noisy and unstable (*e.g.* the blue curve in Figure 3.3b). It has been found that the metal cover (the inset of Figure 3.3b) under the surface pressure sensor is responsible, which causes some electrostatic interactions with the surface pressure sensor and leads to the noise in the recordings. After removing the metal cover, the signal-to-noise ratio of the isotherm decreases, and the surface pressure becomes stable. The red line in Figure 3.3b rises beginning from trough area of 40 cm^2, which might be caused by the hydrophilic trough surface, or some contaminants at the interface. Rinsing the trough and barriers with ethanol several times (and then distilled water) can improve the results (the black curve in Figure 3.3b). When the trough area is smaller than 15 cm^2, the barriers move within 1.5 cm of the paper plate, causing a meniscus at the interface and thus a significant interaction that unavoidably changes the surface pressure. Therefore, in this thesis, the measured surface pressure at $\leq$ 15 cm^2 will not be discussed.

Preliminary measurements: Stearic acid (SA, 284.5 g/mol) has been regarded as a standard material for Langmuir trough films due to its well-known properties [16]. In this case, repeating the standard isotherm of SA (Figure 3.4a) is needed before the measurements of the rods. After washing the trough and barriers thoroughly, an air-water interface was created in the trough. Subsequently, the interface was cleaned several times as described above. 20 μL SA solution in Chloroform (1 mg/mL) was spread carefully on the surface by first forming a small droplet on the tip of the syringe needle and then touching the subphase surface. The solvent was left to evaporate for at least 10 minutes, after which the interface was compressed (at 2 mm/min) to measure the Π-A isotherm. As shown in the inset of Figure 3.4a, the measured isotherm of SA on pure water is consistent with the standard isotherm, which can be divided into 3 distinctive regions, *i.e.*, the gas phase (molecular area > 30 Å^2), the liquid phase (molecular area between 20 and 30 Å^2) and the solid phase (molecular area below 20 Å^2). After the solid phase, the monolayer collapses. After the experiment, the water surface was cleaned with a suction pipette prior to removal of the paper plate. The barriers were removed after the subphase was poured away and then the trough and the barriers were both washed.
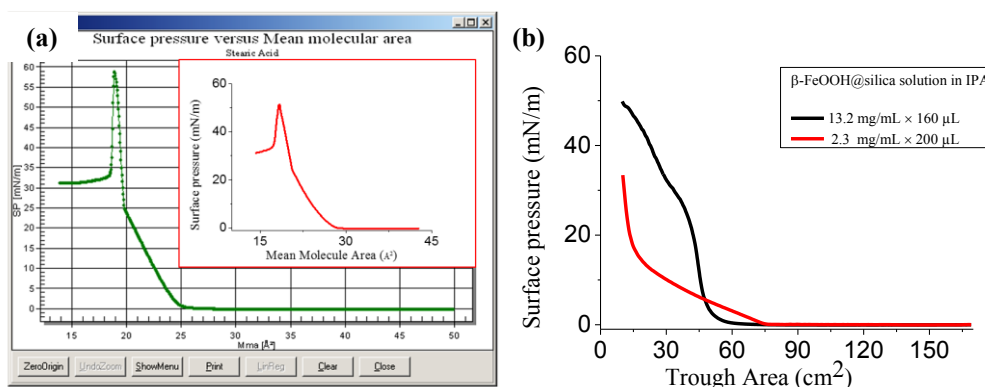
Figure 3.4 *(a) A standard Π-A isotherm of SA at pure water surface. Inset: the measured Π-A isotherm of SA in our lab. (b) Too low or too high concentration of the spreading solution cause inaccuracies in the surface pressure measurements of akaganéite-silica core-shell rods.*

During the surface pressure measurement, the exact concentration and volume of the monolayer material should be defined correctly. The amount of monolayer material in the sample solution depends first of all on the concentration of the spreading solution, but also on what size of trough is used. For the synthesized akaganéite-silica core-shell rods, different concentrations (and volume) were used to find the most suitable parameters. It was found that if the concentration is very low (< 3 mg/mL), a large volume of the spreading solution is needed, which makes the spreading process time-consuming. This can further disturb the stability of the interface and produces some inaccuracies. Besides, the quantity of rods might not be enough to form a monolayer at the end of the compression, as with the red curve shown in Figure 3.4b (2.3 mg/mL, 200 µL). On the other hand, when the concentration of the spreading solution is very high (> 10 mg/mL), the rods might form aggregates before the measurements, which can obscure the phase transitions in the isotherm (the black curve in Figure 3.4b, 13.2 mg/mL, 160 µL). After many attempts, it has been found that a concentration between 3 and 10 mg/mL is acceptable for all the aspect ratios of akaganéite-silica core-shell rods. The amount of the rods used in the measurements is typically 4.25 mg. For all the measurements, the barriers were usually moved together at a rate of 2 mm/min.

Π-A isotherms of akaganéite-silica core-shell rods: Figure 3.5a compares Π-*A* isotherms for the monolayers containing different particles. Here silica micro-spheres (~0.7 µm in diameter, Figure 3.5b) was used to investigate the effect of shape during the compression. Similar to previous reports [17], for spherical particles, the changing
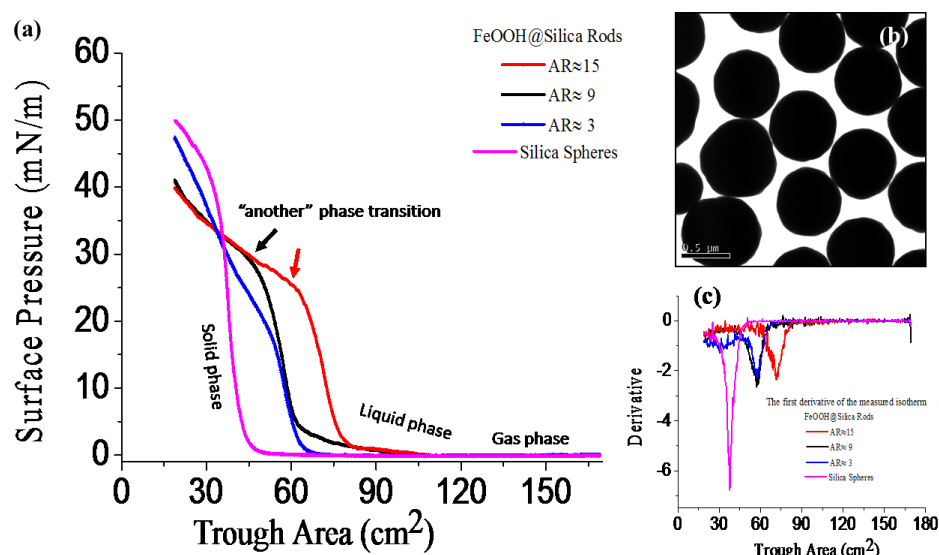
Figure 3.5 *(a) The Π-A isotherms of monolayers containing akaganéite-silica core-shell rods and silica spheres. Inset: Silica spheres used in the measurements. The scale bar is 0.5 μm. (b) The first derivative of the measured isotherms.*

of surface pressure shows three distinct regions (pink curve in Figure 3.5a). When the spheres come into contact, the isotherm starts to rise markedly, corresponding the transition from a gas phase to a solid phase. In the solid phase, surface pressure of the monolayer achieves a high value rapidly. After that, these spheres can no longer rearrange in the monolayer, interface buckling and monolayer collapse become unavoidable [18, 19].

It can be observed that the Π-*A* isotherms for spherocylinders have a more gradual evolution compared to spherical particles. Particularly, in the monolayers containing longer rods (aspect ratio ~15 and 9, red and black curves in Figure 3.5a), a liquid phase appears between gas phase and solid phase. In this liquid phase, the rods rearrange themselves under compression to form a monolayer, which gently increases the surface pressure. Further compression induces another phase transition after the solid phase, where the slope of the isotherm decreases and the surface pressure steadily rises to higher values without collapse. This phase transition appears to be the combined result of flipping and buckling, and will be discussed later in this section. Short rods (aspect ratio ~3, blue curve in Figure 3.5a) act as hard spheres in the gas-to-solid transition. No obvious liquid phase has been observed. However, after a brief solid phase, the
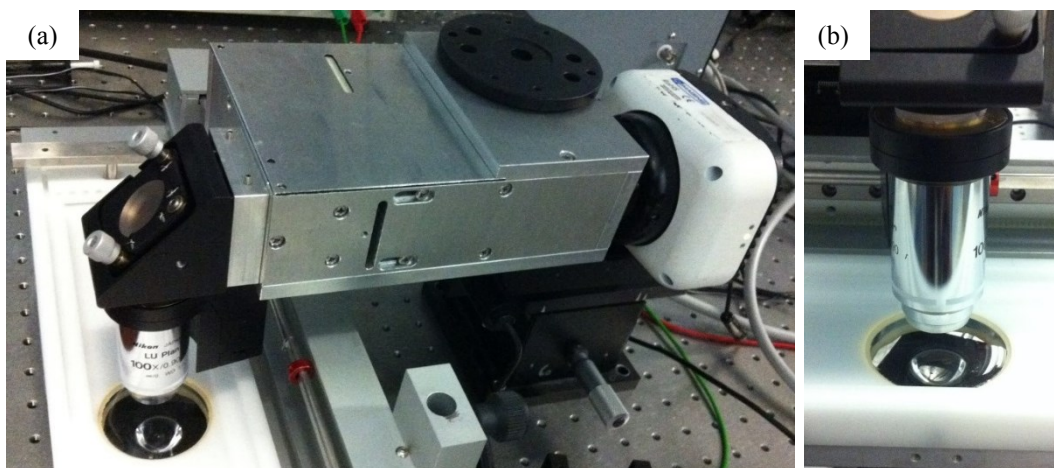
Figure 3.6 *(a) The home-built observational setup. (b) The observation area of the trough/monolayer.*

surface pressure for short rods increases much more steeply than for the long rods. Moreover, the first derivative of its Π-A isotherm (blue curve in Figure 3.5c) have two peaks which align with the peaks from spheres and long rods respectively. This indicates that the short rods as somewhat like hard spheres and somewhat like rods, which can make the rearrangements in the monolayers more complex. This aids the formation of a dense packing during compression and increases the resistance to further compression.

3.3.2 Phase Transitions in Compressed Monolayers

As mentioned above, the measured Π-A isotherms suggest that the structural rearrangements in the monolayers containing akaganéite-silica core-shell rods are more complicated than for the case of spheres. In this section, microscopic observations were used to evaluate the phase transitions in these compressed monolayers. Images were obtained with a home-built device (Figure 3.6a) consisting of a 100× objective (Nikon, LU Plan Fluor, 0.90 NA) mounted via a ~21 cm extension tube onto a 10 bit CCD camera (Qimaging, Canada). The objective can be controlled via a motorized *X-Y* stage, and a Polytec PI E-662 controller in Z direction. A miniature halogen lamp was used as the light source. Here it should be noted that only the central area of the trough/monolayer was observed during the compression (Figure 3.6b). Trough and barriers were washed before the observations. The amount of the rods and the compression speed remain the same as in surface pressure measurements.

Packing fraction of rods: Due to the spherical end caps, these rods cannot reach a packing fraction of 1. In 2D structures, the rods are best packed when their end caps are inter-leaved (similar to close-packed discs); the expected packing fraction should also depends on their aspect ratio, A. Three rods, of length L and radius r, best packed as below:
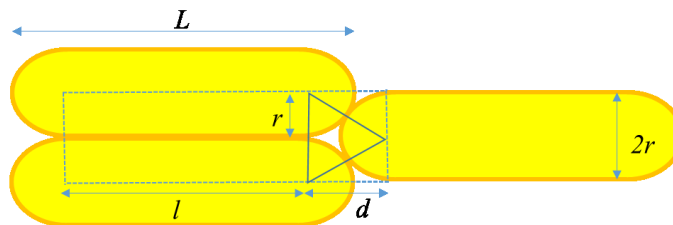
The aspect ratio $A = L/2r$; the length of the straight section of the rods is: $l = L - 2r$.

The dashed area delineates the motif which is repeated throughout the packing. The width of this unit cell is $2r$, and the length is $d + l$, where $d = \sqrt{3}r$ is the height of the blue triangle. Furthermore, it is clear that this unit cell includes two complete interstitial spaces.

Area of the repeated unit cell: $S_1 = (l + d) \times 2r = (l + \sqrt{3}r) \times 2r$

Area of occupied by rods: $S_2 = 2lr + \pi r^2$

Thus the packing fraction is: $v = S_2/S_1 = \frac{A-(1-\pi/4)}{A-(1-\sqrt{3}/2)}$, where A is the aspect ratio.

Therefore, the packing fraction is about 97.2%, 99.1% and 99.4% for the rods with aspect ratio 3, 9 and 15, respectively.

This is useful for estimating the close-packing area of the monolayers containing the rods with different aspect ratios. Using 3.64 g/cm^3 as the density of the rods, combined with the size information from the TEM images, as well as the mass of the rods spread at the interface, it can be calculated that the close-packing area of the monolayer containing rods with aspect ratio 3 is about 50.9 cm^2, and the related trough area should be 52.5 cm^2. This is consistent with the position of the final phase transition in the isotherm (Figure 3.5, blue curve). For aspect ratio 9, close packing occurs when the area of the trough is about 50 cm^2. This is also close to the final phase transition in the

measured isotherm (Figure 3.5, black curve). For rods with even larger aspect ratio (~15), the calculated close-packing area is about 49 cm^2, which does not coincide with the final transition in the measured isotherm (Figure 3.5, red curve, around 65 cm^2). To better understand these data, the phase transition process of the monolayers and the rearrangement of the rods were observed.
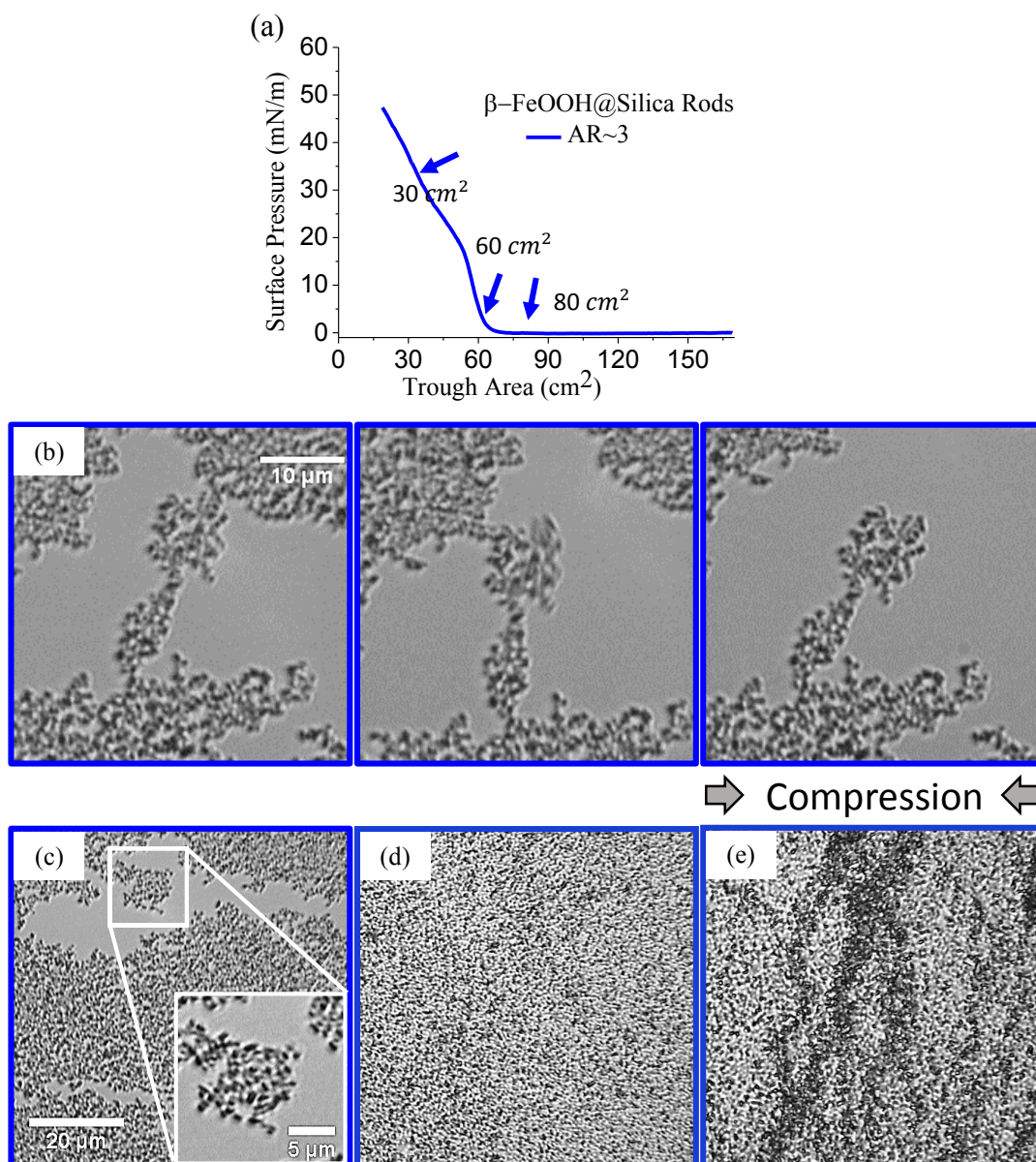
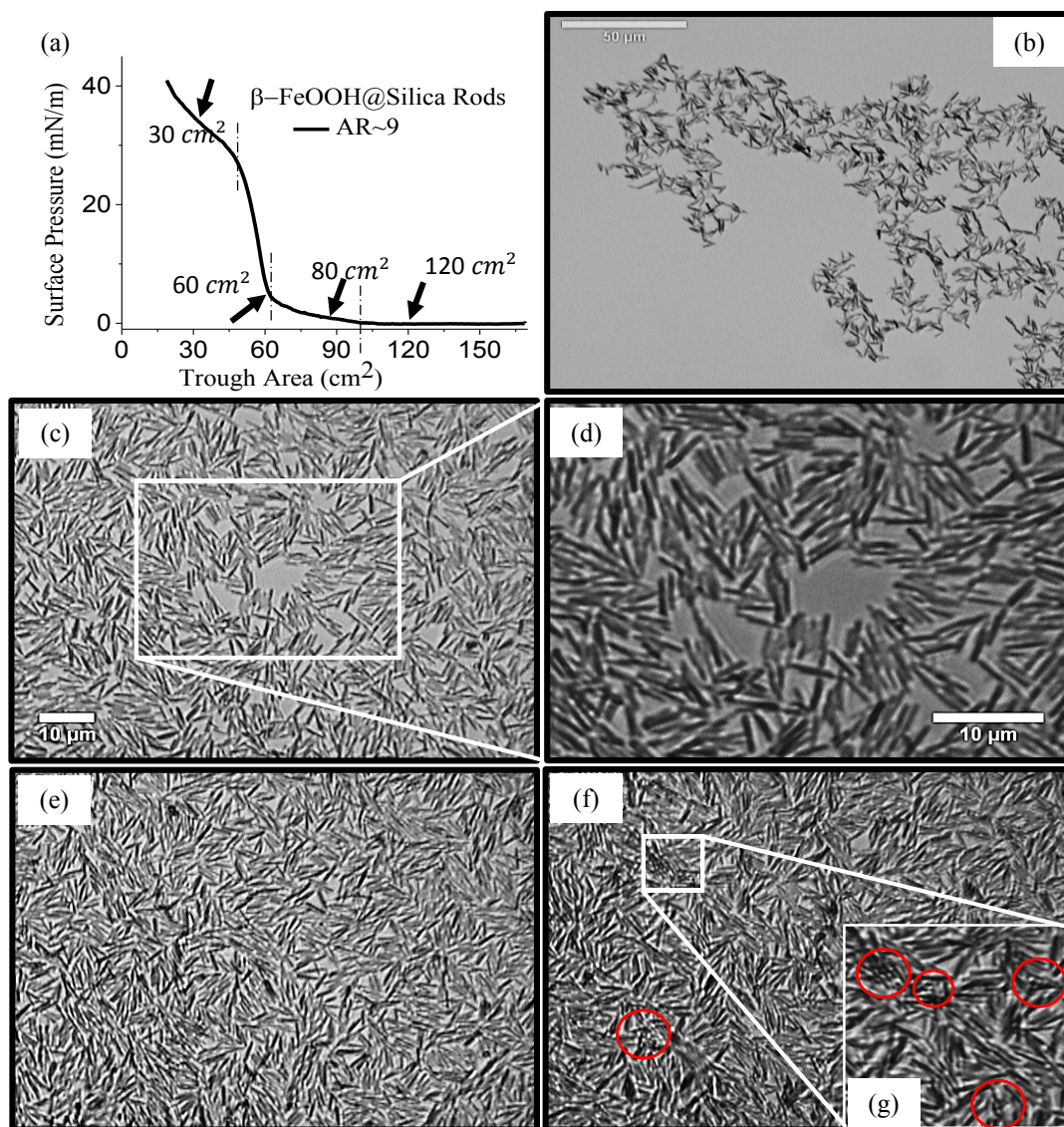**Figure 3.7** *(a) The Π-A isotherm of a monolayer containing rods with aspect ratio ~3. Three different interfacial area (80, 60 and 30 cm^2) were compressed for the purposes of observation. (b) The movements of rod aggregates at 80 cm^2. (c-e) Phase transitions in the monolayer under compression, corresponding 80, 60 and 30 cm^2 trough area, respectively.*

Phase transitions in monolayers of rods (aspect ratio ~3): A monolayer of akaganéite-silica core-shell rods with aspect ratio ~3 was created at the air-water interface. Three different interfacial area were compressed for the microscopic observations (Figure 3.7a). Strong capillary interactions cause the rod to aggregate before the monolayer formed (Figure 3.7b and c). These aggregates appear in various shapes and reach a large average domain size (up to ~1000 μm^2). Figure 3.7b shows the aggregates movement at 80 cm^2 trough area. It can be observed that individual rods mainly move together with their contacts because of the capillary interactions. The compression process can connect all the aggregates and creates a homogeneous and continuous monolayer (Figure 2d, trough area = 60 cm^2). After this, jamming occurs since the rod concentration nears close-packing (~97 %, at trough area = 52.5 cm^2), and in-plane rearrangements cannot be achieved under further compression. Previous reports about ellipsoids show that some ellipsoids can flip into an upright position to relieve the compressional stress [17]. Here because of the small aspect ratio of the rods, flipping and buckling can happen at the same time. The slope change of the Π-*A* isotherm might be a combined result of these two processes. Figure 3.7e (trough area = 30 cm^2) demonstrates the buckling during the compression, characterized by the folding of the monolayer spanning the entire field of view. These folds are perpendicular to the compression direction and are even visible to the naked eye. The rearrangements for these short rods under compression, which are difficult to observe in the microscope, can be further investigated in numerical simulations.

Phase transitions in monolayers of rods (aspect ratio ~9): Unlike spheres and short rods, the phase transitions in the monolayer of rods with aspect ratio ~9 can be divided into four phases (Figure 3.8a, indicated by dashed lines). Both end-to-end and side-to-side configurations of rods have been observed at low surface coverage (Figure 3.8b, trough area = 120 cm^2). This can be caused by the lateral capillary interactions between the particles. At this stage, the surface pressure is zero (gas phase of Figure 3.8a); a monolayer has not yet been formed at the interface. The rods are randomly oriented and can move freely. Again, individual rods mainly move together with their neighbours. As the rods are compressed, a monolayer starts to be formed, which causes rearrangements of the configurations associated with the increase in surface pressure, corresponding to the liquid phase in the Π-*A* isotherm. The formed monolayer is
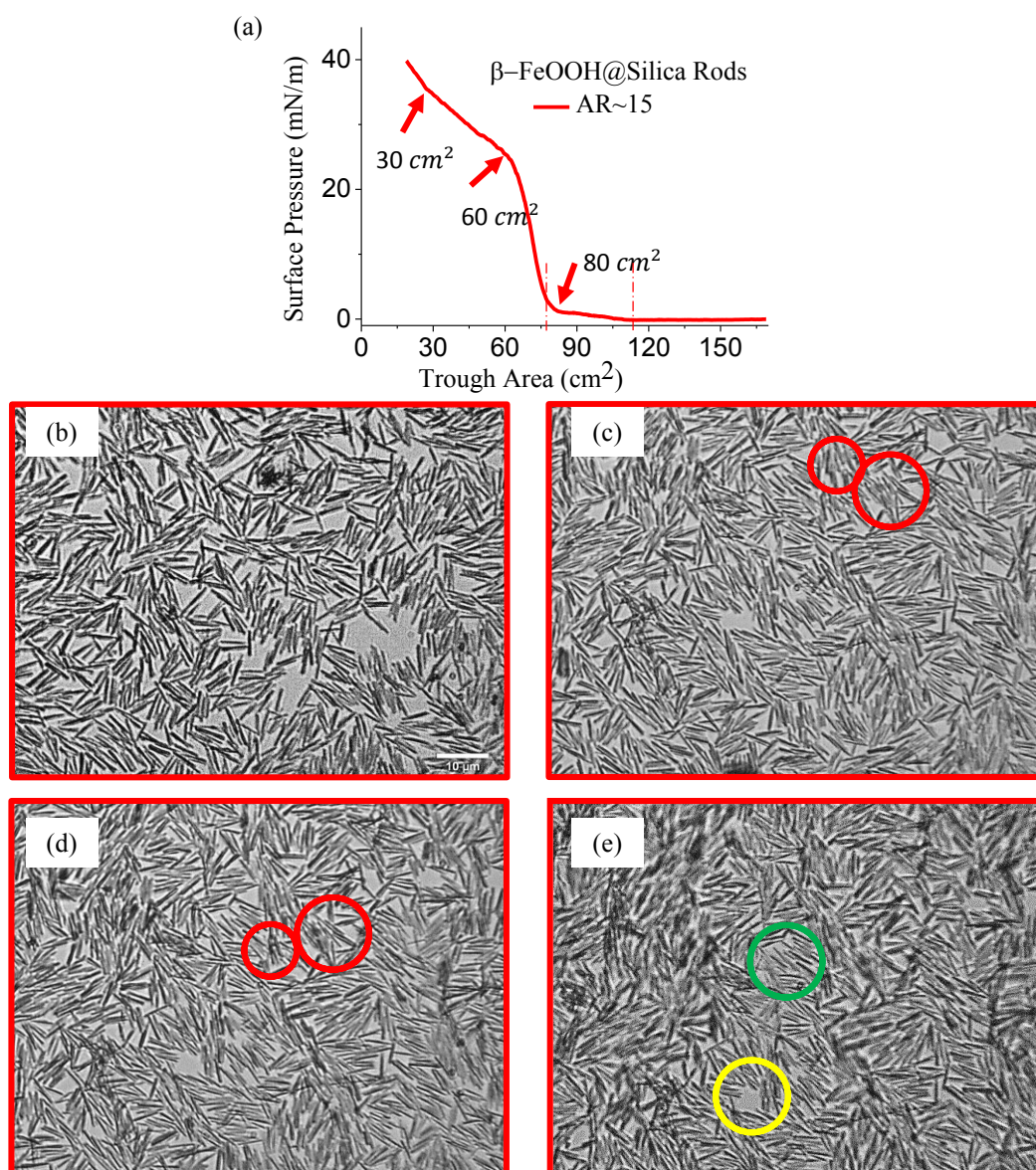
Figure 3.8 *(a) The Π-A isotherm of a monolayer containing rods with aspect ratio ~9. (b-g) Phase transitions in the monolayer under compression. The trough area is 120 cm² (b), 80 cm² (c and d), 60 cm² (e), and 30 cm² (f and g), respectively. Flippers are marked in the red circles.*

locally inhomogeneous. Microscopic observations reveal a fractal network (Figure 3.8c and d, trough area = 80 cm²), where the dense regions exhibit different degrees of translational ordering. For example, both random jammed aggregates and more ordered raft-like domains can be found in the monolayer. Meanwhile, the presence of void regions provides space for rearranging the rods under compression. Further compression, on one hand, can progressively occupy these void regions (Figure 3.8e, trough area = 60 cm²), on the other hand, leads to close-packing (~99.1%) in the monolayer and increases the surface pressure dramatically (solid phase). As shown in

Figure 3.8f and g (trough area = 30 cm^2), some localized aggregations of flippers can be observed clearly (marked in red), although other unoccupied regions are still present. Previous reports suggested that the compressive stress acting on the monolayer is inhomogeneous, which results in this peculiar coexistence. Buckling occurs at the end of the compression, where the folds can be visible to the naked eye.

Figure 3.9 *(a) The Π-A isotherm of a monolayer containing rods with aspect ratio ~15. (b-e) Phase transitions in the monolayer under compression. The trough area is 80 cm^2 (b), 60 cm^2 (c), 30 cm^2 (d) and 25 cm^2 (e), respectively. Bilayer aggregates are marked in the red circles. More ordered structures (marked in green) and void regions (marked in yellow) can survive at the end of the compression. The scale bar for b-e is 10 μm.*

Phase transitions in monolayers of rods (aspect ratio ~15): The Π-A isotherm of the rods with larger aspect ratio (~15) exhibits an obvious liquid phase (Figure 3.9a, indicated by dashed lines). From the microscopic observations, they form a more open network at the interface, as shown in Figure 3.9b (trough area = 80 cm^2). Dynamic compression causes the rearrangement of the rods and a similar phase transition as that described above (Figure 3.9c-e, trough area = 60, 30 and 25 cm^2, respectively). Compared with other monolayers, the void regions and ordered regions in Figure 3.9 are much more stable and can even survive at the end of the compression (marked in yellow and green). This might be the reason that the final phase-transition (~65 cm^2) in this monolayer occurs earlier than the calculated close-packing area (~49 cm^2). Moreover, the flipping process is not obvious for these long rods. Instead, rods in dense and disordered regions seem to form some bilayer aggregates under compression (marked in red). Bilayer formation is another approach to relieve the compressional stress, which has been reported in previous works [20, 21]. Here, apparently, the aspect ratio plays an important role in determining the interfacial behaviour of the rods.

3.3.3 Flipping Phenomenon and the Effect of Aspect Ratio

Generally, in response to the compression, a monolayer can transform into a multilayer, buckle at the interface, or collapse into some random three-dimensional structure. Monolayer to multilayer transitions mainly occurs in the compressed monolayers of charged amphiphilic molecules [22] and nanoscale particles [23, 24]. For the monolayers containing microscale colloidal particles, over-compression often causes buckling or collapse. However, experiments with ellipsoids reported the flipping phenomenon [17]. As discussed in section 2.2.4, the elastic energy stored in a compressed monolayer is sufficient to support the flipping process. In this case, some individual ellipsoids flip their long axes to be perpendicular to the interface under compression. Similar flippers have been found in water-in-oil emulsions stabilized by these ellipsoids, where limited coalescence acts as a compression process [25]. From equation 2.5, one can easily derive the energy difference between a flat and flipped configuration of a rod. These rods are small enough to neglect the effect of gravity. The energy required to remove a rod lying flat on the interface is given by: $E_{\parallel} = -\gamma(\pi r^2 + 2rd)$, where γ is the surface tension of water, r is the radius of the rod, and d is the length of the straight section

(see the sketch in the discussion of packing fraction). The energy needed to remove a flipped rod is: $E_\perp = -\pi\gamma r^2$. Hence the energy difference is given by:

$$E_{/\!/} - E_\perp = -\gamma 2rd = -\gamma 2r(L - 2r) = -\gamma 4r^2(A - 1) \qquad (3.1)$$

Again, A is the aspect ratio of the rods.

This equation indicates that when the radius is fixed, the energy required for a rod to flip is directly proportional to its aspect ratio. Much more energy would be needed to flip a rod with very large aspect ratio. In this case, if the system does not have enough energy, the flipping process cannot be achieved.

As observed in the experiments, rods with aspect ratio ~9 can be seen to flip in response to the compression. Indeed, flipping plays an important role in the phase transitions, especially in the solid phase. Figure 3.10 further compares the microscopic features of the same field of view at trough area 50 cm^2 and 32 cm^2, corresponding the π-A isotherm before and after the final "shoulder" (Figure 3.5, aspect ratio ~9), respectively. In figure 3.10a, the monolayer is in the solid phase, where some void regions (marked in yellow) coexist with flipper aggregations (marked in red). It can be observed that flippers do not occur randomly, but typically appear in some dense and disordered regions. In these regions, during the compression process, the rod position and orientation have to be rearranged to find the equilibrium configuration. In this case, flipping happens to reduce the area occupied by the rods and hence relieve some compressional stress. Rods in more ordered structures, for instance the raft-like domains, are more stable and less likely to flip (marked in green). This stability could help these more ordered rods keep their configurations under compression, as shown in Figure 3.10b. At the same time, most void regions are slightly occupied by the rearranged rods, while more flippers can be found in particular regions. The latter are localized flipper arrays organized perpendicular to the compression direction, which can decrease the growth rate of the surface pressure. Moreover, buckling starts to appear primarily at edges of the monolayer (Figure 3.10c), indicating that the compressional stress is stronger close to the approaching barriers. This is similar to the Janssen effect at the bottom of granular columns [26], and can also reduce the slope of the surface pressure isotherm. Therefore, the phase transition corresponding to the
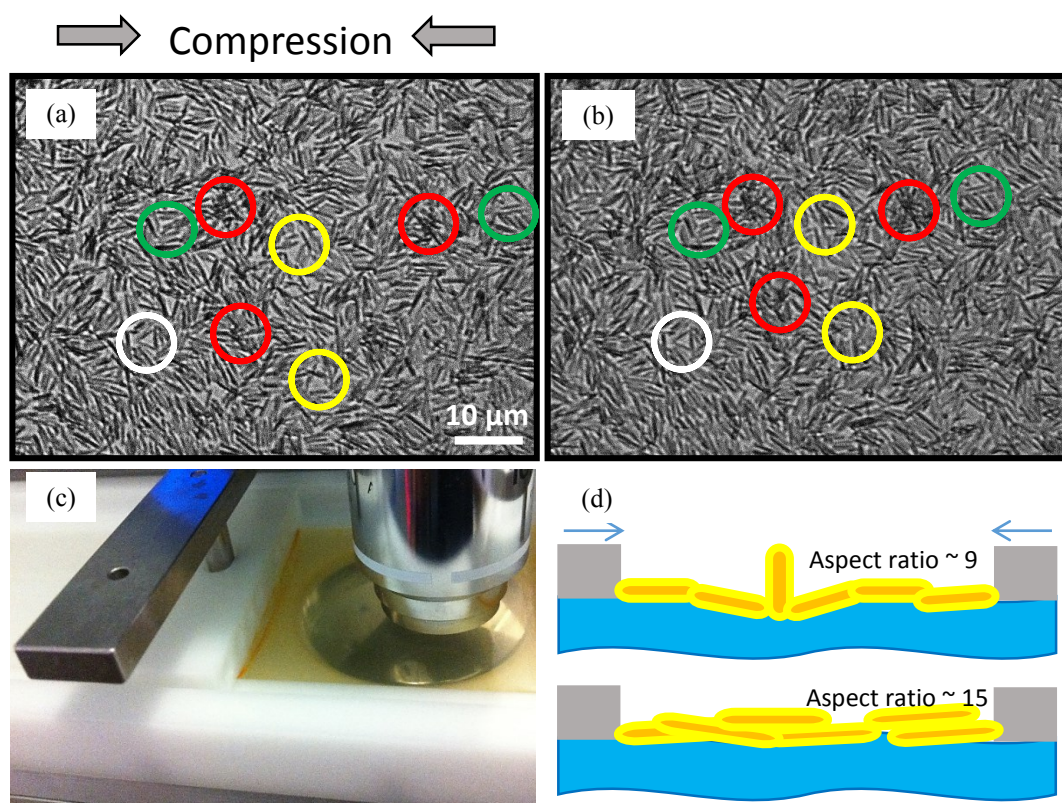
Figure 3.10 *(a) Microscopic features of the monolayer containing rods with aspect ratio ~9 at 50 cm^2 trough area. The flippers are marked in red circles. More ordered structures and void regions are marked green and yellow, respectively. One triangle structure can be found in the white circle. (b) The monolayer compressed to 32 cm^2, where the void regions are occupied by the rods (marked yellow). More flippers appear in a collective manner (in red circles). Raft-like domains and triangle structures survive from the compression process. (c) Buckling preferentially happens close to the barriers. (d) Compression effect in monolayers of rods with aspect ratio ~9 (top) and ~15 (bottom).*

final shoulder of the isotherm could be the combined effect of buckling and collective flipping. Additionally, some triangle structures are stable enough to resist the dynamic compression (marked white), suggesting that the compressional stress around these triangles could be locally homogeneous.

Figure 3.10d demonstrates the compression effect in monolayers of rods with aspect ratio~9 and ~15. For longer rods (aspect ratio ~15), bilayer aggregates are formed to relieve the compressional stress instead of flipping up. One possible reason is that the stored energy in the monolayer is not enough to support the flipping process. Meanwhile, the formation of a bilayer leads to gradual changes in the interface covered

by the rods, which requires less energy. This effect is more obvious for long rods. When the aspect ratio goes to infinity, the energy cost for bilayer formation can be close to zero. Besides, the formation of bilayers in a Langmuir trough can also related to the compression speed and other parameters.
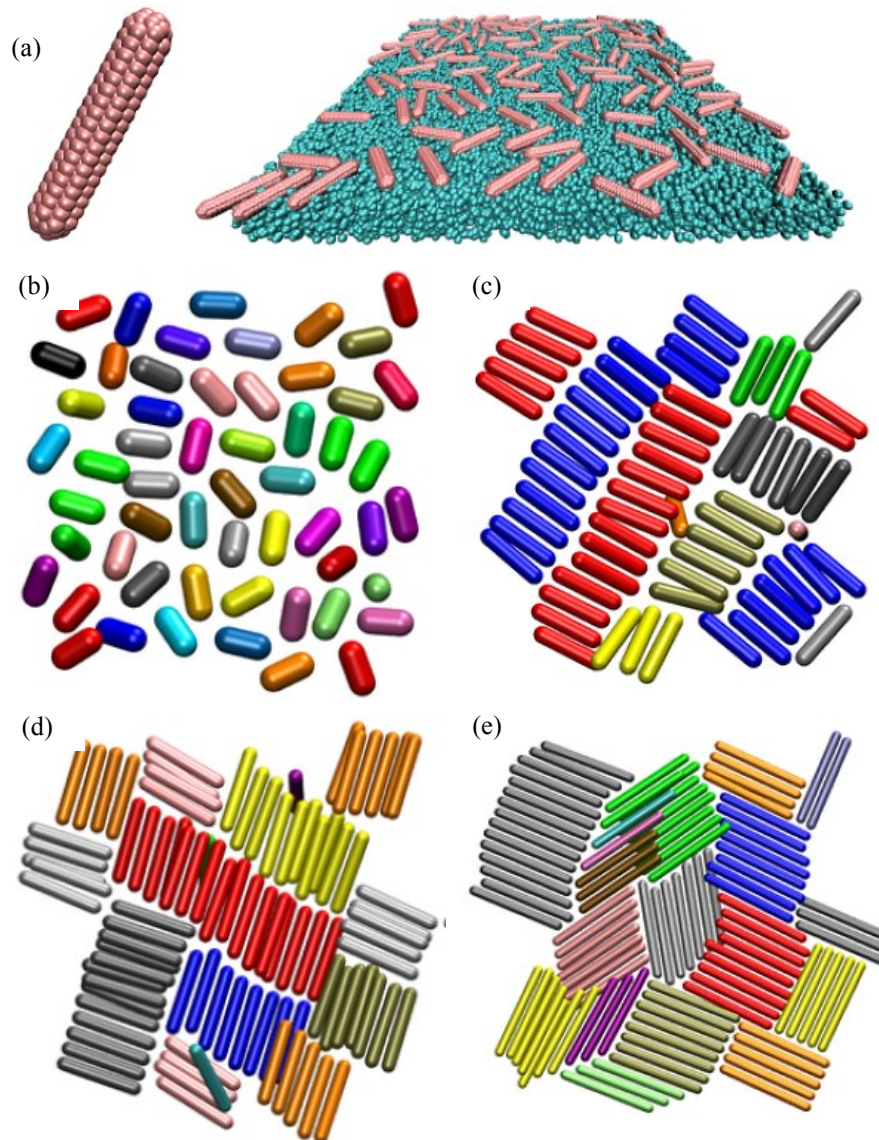
Figure 3.11 (a) (Left) Geometry of an individual colloidal rod with aspect ratio AR=6, formed by coarse-grain beads arranged in a fcc lattice. (Right) Initial configuration of the system for AR=6; with the colloids in pink and the water fluid phase in cyan. The oil phase is omitted for the sake of clarity. (b-e) Snapshots of the rods at the interface for rods of aspect ratio AR=3, 6, 9 and 15. Rods that belong to the same cluster are represented using the same colour. Simulations due to Giovanni Brandani.

3.4 Simulations of the Compressed Monolayers

To better understand the dynamics of the rods in the compressed monolayer, molecular dynamics simulations (Figure 3.11a) have been performed by Giovanni Brandani, PhD student at the University of Edinburgh.

In Brandani's simulations, rods with aspect ratio 3, 6, 9 and 15 are used to form monolayers at a liquid interface. For the shortest rods (aspect ratio ~3), continuous compression leads to rod desorption from the interface. Increasing the aspect ratio makes this rod desorption occur via a tilting of the rod perpendicular to the interface, and that this 'flipping' happens at the boundary between other ordered domains, or equivalently in a locally disordered region (Figure 3.11 b-d). Moreover, the simulations also demonstrate the relationship between rod desorption and the ordered domains of the monolayer. Even longer rods (aspect ratio ~15) do not desorb from the interface, instead, they form bilayers during the compression process (Figure 3.11e). These results are consistent with the experimental observations. For more simulation details, please refer to Brandani's PhD thesis [27], the University of Edinburgh.

3.5 Mixtures of Rods and Spheres

As discussed above, rods with aspect ratio ~3 exhibit the properties of both hard spheres and longer rods, which makes the rearrangements in the compressed monolayers more complex. Indeed, it is believed that colloidal mixtures of different sized and shaped particles promise a great diversity of superlattices and phase behaviours beyond those of single-component systems [28]. A mixture of spherical and rod-like colloidal particles is a well-studied model system for condensed matter exhibiting rich and complex phase behaviours [29, 30]. For a binary mixture containing nano-scale particles, entropically driven phase separation occurs when these two building blocks have significant differences in size and/or shape [31-33]. Overcoming the entropically and energetically unfavourable interactions is thus critical for the binary assembly of nanospheres and nanorods. Y. Charles Cao and co-workers reported a 2D binary assembly of CdSe/CdS nanorods with spherical metal particles [30], where the spheres intercalated into nanorod arrays with parallel alignment. So far, the self-assembly of binary mixtures of micro-scale distinct shapes have not been
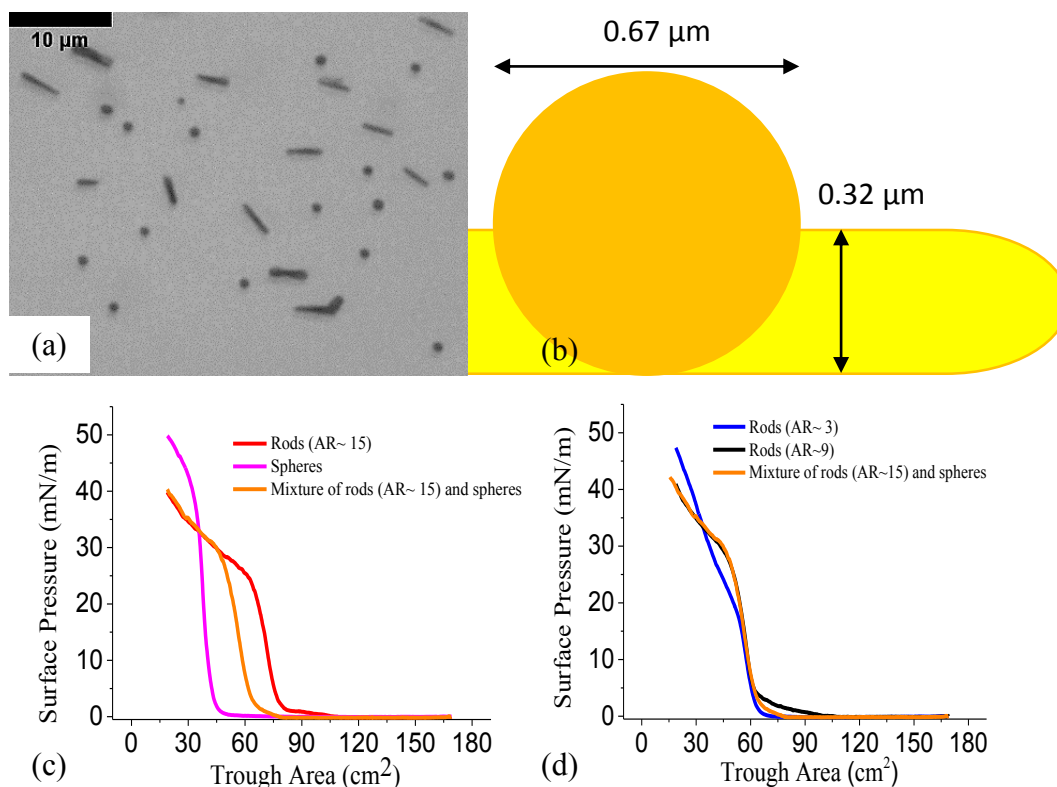
Figure 3.12 (a) The prepared binary mixture. (b) The size difference between the rods and spheres in the mixture. (c, d) Comparison of the measured Π-A isotherms of the binary mixture (the orange curve) and the single-component systems.

reported quantitatively and remained largely unexplored. In this section, to better understand the interfacial properties of short rods, monolayers containing long rods and silica spheres are formed at the air-water interface. Surface pressure measurements and microscopic observations are both carried out to study their phase behaviours.

Silica spheres (diameter of ~0.67 μm) and the synthesized β-FeOOH@silica rods with aspect ratio ~15 (Figure 3.2d) were dispersed in isopropyl alcohol (IPA). The sphere-to-rod number ratio of the binary mixture is 3:2 (Figure 3.12a) and 4:1. It is worth mentioning that the average diameter of the rods was measured to be 0.32 ± 0.02 μm, *i.e.*, half of the sphere diameter. Figure 3.12b demonstrates the size difference between these two components. Binary monolayers were obtained by drop-casting ~4.2 mg of the binary particles (note not 4.2 mg solution) at the air-water interface. Surface pressure measurements and microscopic observations were carried out with the same methods presented previously.

Figure 3.12c (orange curve) shows the measured Π-A isotherm of the binary mixture (the sphere-to-rod number ratio here is 3:2), which lies between the isotherms of those single-component systems. It can be seen that the binary monolayers also undergo phase transitions under compression. A small liquid phase can be noticed prior to the sharp rise in surface pressure (*i.e.*, the solid phase). Figure 3.12d compares the isotherm of the mixture with another two rods. It is clear that the binary mixture demonstrates similar behaviours as the rods with aspect ratio ~9 in the solid phase. There is a strong overlapping when the trough area was compressed below 60 cm^2. In the gas and liquid phase, however, the mixture behaves more similar to the short rods. These data indicate that a binary mixture of micro-scale rods and spheres can form a monolayer at the air-water interface. The binary monolayer first presents properties of spherical particles at the beginning of compression, and then exhibits rod-like character under further compression. The mechanism of this behaviour can be better understood with the help of numerical simulations. This can be a subject of future work.

Microscopic observations demonstrate the rearrangements of the binary monolayers under compression. When the trough area is 80cm^2, the monolayer starts to be formed at the interface, corresponding to the liquid phase of the isotherm. As shown in Figure 3.13b, the rods attracts spheres maximally if the spheres attach to the side of the rod. This suggests that the capillary force is much stronger along the long axis of the rods than at the rod ends. Besides, some raft-like structures formed only by the rods can be observed, although no obvious phase separation was noticed. Further compression gathers these raft-like structures together, where the spheres are randomly distributed as shown in Figure 3.13c (trough area = 60 cm^2). Bilayer aggregates and buckling are evidenced at the end of the compression (Figure 3.13d, trough area = 30 cm^2). When adding more spherical particles into the binary mixture, the measured Π-A isotherm exhibits more spherical characters. As shown in Figure 3.13a (the green curve and the inset, the sphere-to-rod number ratio is 4:1), the liquid phase becomes even smaller and an obvious collapse occurs after the solid phase. Microscopic features of the monolayer (Figure 3.13e-g) confirmed that most of the rods are surrounded by the spheres on their long side. In this case, raft-like structures are difficult to form. Once the monolayer is close-packed, buckling and collapse can happen immediately upon further compression.
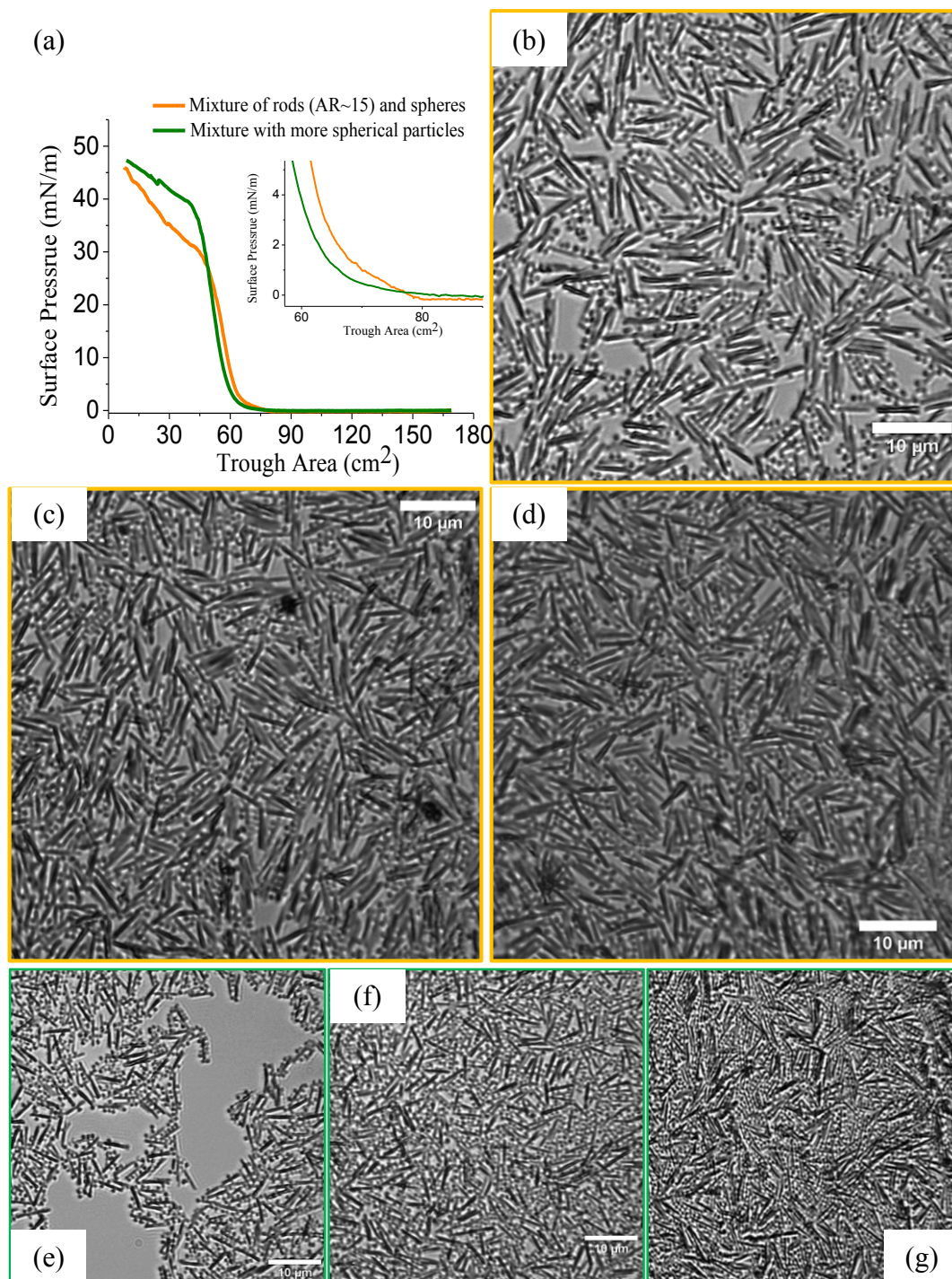
Figure 3.13 *(a) Π-A isotherms of the binary mixtures with different amounts of spherical particles (~5mg spheres for the orange curve and ~14mg for the green curve. ~15.2mg rods for both samples). (b-d) Phase transitions in the binary monolayer under the compression. (e-g) Phase transitions in the monolayer when adding more spheres in the mixture. The trough area is 80 cm² (b and e), 60 cm² (c and f), and 30 cm² (d an g).*

3.6 Conclusions

The interfacial properties of β-FeOOH@silica micro-rods were studied experimentally and then compared to simulation results which were carried out by collaborators. Compared with cylinders and ellipsoids, these spherocylinders show more complex interfacial behaviour under compression. A sequence of phase transitions can be observed not only from the measured Π-A isotherms, but also from the microscopic observations. Specifically, it has been proved that the aspect ratio of the rods plays an important role in the phase transitions. At the end of the compression process, to relieve some compressional stress, shorter rods can flip their long axes to be perpendicular to the interface, and longer rods prefer to form multilayers. Some similar results were obtained in the molecular dynamics simulations from Giovanni Brandani. This work could be helpful to better understand the 2D self-assembly of anisotropic colloidal particles, and some related applications, *e.g.*, the stability of foam/emulsion systems stabilized by these particles.

Besides, a preliminary study about the binary mixture of rods and spheres shows that spheres can attach to the side of the rods. This can further control the inter-particle separation when a monolayer is formed and compressed at an interface. The formed binary monolayer exhibits properties of both rod-like particles and spherical particles, which can be affected by the particle geometry, attractive contact interactions, and the difference between these two components. These preliminary results can be helpful in sensing or optoelectronic devices, where controlled inter-particle separation is required.

Acknowledgment

References:

[1] Lewandowski, E. P.; Cavallaro, M.; Botto, L.; Bernate, J. C.; Garbin, V.; Stebe, K. J. Orientation and self-assembly of cylindrical particles by anisotropic capillary interactions. *Langmuir* **2010**, *26* 15142–15154.

[2] Madivala, B.; Fransaer, J.; Vermant, J. Self-assembly and rheology of ellipsoidal particles at interfaces. *Langmuir* **2009**, *25*, 2718–2728.

[3] Chaudhari, N. K.; Yu, J. S. Size Control Synthesis of Uniform *β*-FeOOH to High Coercive Field Porous Magnetic r-Fe2O3 Nanorods. *J. Phys. Chem. C* **2008**, *112*, 19957–19962.

[4] Yue, J.; Jiang, X. C.; Yu, A. B. J. Experimental and theoretical study on the β-FeOOH nanorods: growth and conversion. *Nanoparticle Res.* **2011**, *13*, 3961−3974.

[5] Matijevic, E.; Scheiner, P. Ferric hydrous oxide sols: III. Preparation of uniform particles by hydrolysis of Fe(III)-chloride, -nitrate, and -perchlorate solutions. *J. Colloid Interface Sci.* **1978**, *63*, 509−524.

[6] Blesa, M. A.; Matijevic, E. Phase transformations of iron oxides, oxyhydroxides, and hydrous oxides in aqueous media. *Adv. Colloid Interface Sci.* **1989**, *29*, 173−221.

[7] Yue, J.; Jiang, X.; Yu, A. Experimental and Theoretical Study on The *β*-FeOOH Nanorods: Growth and Conversion. *J. Nanopart. Res.* **2011**, *13*, 3961−3974.

[8] Wang, X.; Chen, X. Y.; Gao, L. S.; Zheng, H. G.; Ji, M. R.; Tang, C. M.; Shen, T.; Zhang, Z. D. Synthesis of β-FeOOH and α-Fe2O3 nanorods and electrochemical properties of β-FeOOH. *J. Mater. Chem.* **2004**, *14*, 905−907.

[9] Grzelczak, M.; Vermant, J.; Furst, S. M.; Liz-Marzan, L. M. Directed Self-Assembly of Nanoparticles. *ACS Nano* **2010**, *4*, 3591−3605.

[10] Iler, R. K. *The Chemistry of Silica.* Wiley: New York, **1979**.

[11] Hijnen, N.; Clegg, P. S. Simple Synthesis of Versatile Akaganéite-Silica Core–Shell Rods. *Chem. Mater.* **2012**, *24*, 3449−3457.

[12] Hijnen, N.; Cai, D.; Clegg, P. S. Bijels stabilized using rod-like particles. *Soft Matter*, **2015**, *11*, 4351−4355.

[13] Newton, B. J.; Brakkeb, K. A.; Buzza, D. M. A. Influence of magnetic field on the orientation of anisotropic magnetic particles at liquid interfaces. *Phys. Chem. Chem. Phys.*, **2014**, *16*, 26051−26058.

[14] Matijevic, E.; Scheiner, P. J. Ferric Hydrous Oxide Sols: III. Preparation of uniform particles by hydrolysis of Fe (III)-chloride,-nitrate, and-perchlorate solutions. *Colloid Interface Sci.* **1978**, *63*, 509−524.

[15] Dai, Z-W.; Wan, L-S.; Huang, X-J.; Ling, J.; Xu, Z-K. Selective Adsorption of Isopropyl Alcohol Aqueous Solution on Polypropylene Surfaces: A Molecular Dynamics Simulation. *J. Phys. Chem. C* **2011**, *115*, 22415−22421.

[16] Iakovenko, S. A.; Trifonov, A. S.; Giersig, M.; Manedov, A.; Nagesha, D. K.; Hanin, V. V.; Soldatov, E. C.; Kotov, N. A. One- and Two-Dimensional Arrays of Magnetic Nanoparticles by the Langmuir-Blodgett Technique. *Adv. Mater.* **1999**, *11*, 388−392.

[17] Basavaraj, M. G.; Fuller, G. G.; Fransaer, J.; Vermant, J. Packing, flipping, and buckling transitions in compressed monolayers of ellipsoidal latex particles. *Langmuir* **2006**, *22*, 6605–6612.

[18] Bordács, S.; Agod, A.; Hórvölgyi, Z. Compression of Langmuir Films Composed of Fine Particles: Collapse Mechanism and Wettability. *Langmuir* **2006**, *22*, 6944–6950.

[19] Pugnaloni, L. A.; Ettelaie, R.; Dickinson, E. Computer simulation of the microstructure of a nanoparticle monolayer formed under interfacial compression. *Langmuir* **2004**, *20*, 6096–6099.

[20] Das, K.; Kundu, S. Variation in surface plasmonic response due to the reorganization of Au nanoparticles in Langmuir-Blodgett film. *J. Appl. Phys.* **2014**, *116*, 024316.

[21] Maganti, L.; Jash, M.; Radhakrishuan, T. P. Nanoparticle assembly following Langmuir–Hinshelwood kinetics on a Langmuir film and chain networks captured in LB films. *Phys. Chem. Chem. Phys.* **2015**, *17*, 7386–7394.

[22] Matharu, Z.; Bandodkar, A. J.; Gupta, V.; Malhotra, B. D. Fundamentals and application of ordered molecular assemblies to affinity biosensing. *Chem. Soc. Rev.* **2012**, *41*, 1363−1402.

[23] Sau, T. K.; Murphy, C. J. Self-Assembly Patterns Formed upon Solvent Evaporation of Aqueous Cetyltrimethylammonium Bromide-Coated Gold Nanoparticles of Various Shapes. *Langmuir*, **2005**, *21*, 2923−2929.

[24] Kim, F.; Kwan, S.; Akana, J.; Yang, P. Langmuir-Blodgett nanorod assembly. *J. Am. Chem. Soc.*, **2001**, *123*, 4360–4361.

[25] Madivala, B.; Vandebril, S.; Fransaer, J.; Vermant, J. Exploiting particle shape in solid stabilized emulsions. *Soft Matter*, **2009**, *5*, 1717–1727.

[26] Ebrahimi, F.; Azizpour, T. Maleki, H. Janssen effect and the stability of quasi-two-dimensional sandpiles. *Phys. Rev. E.*, **2010**, *82*, 031302.

[27] Brandani, G. Molecular Dynamics Simulations of Protein Adsorption at Interfaces -chapter 5. The University of Edinburgh. **2016.**

[28] Ye, X.; Millan, J. A.; Engel, M.; Chen, J.; Diroll, B. T.; Glotzer, S. C.; Murray, C. B. Shape Alloys of Nanorods and Nano-spheres from Self-Assembly. *Nano Lett.* **2013**, *13*, 4980–4988.

[29] Sánchez-Iglesias, A.; Grzelczak, M.; Pérez-Juste, J.; Liz-Marzán, L. M. Binary Self‑Assembly of Gold Nanowires with Nanospheres and Nanorods. *Angew. Chem., Int. Ed.* **2010**, *49*, 9985−9989.

[30] Nagaoka, Y.; Wang, T.; Lynch, J.; LaMontagne, D.; Cao, Y. C. Binary assembly of colloidal semiconductor nanorods with spherical metal nanoparticles. *Small* **2012**, *8*, 843−846.

[31] Yasarawan, N.; van Duijneveldt, J. S. Arrested Phase Separation of Colloidal Rod−Sphere Mixtures. *Soft Matter* **2010**, *6*, 353−362.

[32] Koenderink, G. H.; Vliegenthart, G. A.; Kluijtmans, S.; van Blaaderen, A.; Philipse, A. P.; Lekkerkerker, H. N. W. Depletion-induced crystallization in colloidal rod-sphere mixtures. *Langmuir* **1999**, *15*, 4693−4696.

[33] Bolhuis, P.; Frenkel, D. Numerical study of the phase diagram of a mixture of spherical and rodlike colloids. *J. Chem. Phys.* **1994**, *101*, 9869−9875.

Chapter 4

Magnetic Rods at the Air-Water Interface

Using hydrazine-treatment, β–FeOOH @silica rods are converted into magnetic rods. The obtained rods are analysed by X-ray powder diffraction and the differential dynamic microscopy (DDM) technique. After spreading the rods at the air-water interface, their moments can be aligned in the same direction as an applied magnetic field. When the field is perpendicular to the interface, a field-induced flipping process has been observed. When the field is applied in the plane of the interface, a magnetic monolayer can be formed under compression and show slightly different isotherms to the non-magnetic case. Finally, these magnetic rods can be used to stabilize an oil-in-water emulsion, which has a strong response to an external field.

4.1 Introduction

In recent years, magnetic colloidal particles have been exploited extensively as the materials of choice for labelling and sorting of cells, separation of biochemical products, various biomedical applications [1], and alone as ferrofluids. The magnetic particles are normally dispersed in water or an oily solvent to form a magnetic fluid, which is usually described as a gas of particles interacting through an anisotropic potential, taking into account the van der Waals attractions, the dipolar magnetic interactions, and the short-range repulsions. A gas-liquid-like phase transition can occur according to ionic strength, temperature, and magnetic field [2].

Magnetic particles are also exploited in the form of thin films in a range of protective or sensitive coatings [3, 4]. In 1994, Fendler *et al.* first prepared monolayers of Fe_3O_4 nanoparticles on a water subphase [5]. This pioneering work proved that it is possible to obtain uniform monolayers of magnetic particles. Gallet and coworkers found that

the shape of the Π-*A* isotherms and the electron-micrograph pictures of these magnetic monolayers are strongly dependent on the particle size [6]. Particularly, smaller particles can be organized in more compact aggregates, while larger ones form chained and rather compressible aggregates. This is consistent with the size-dependent balance between van der Waals and magnetic dipolar-dipolar interactions. Pichon *et al.* studied the magnetic properties of iron oxide nanocrystals as a function of size at the air-water
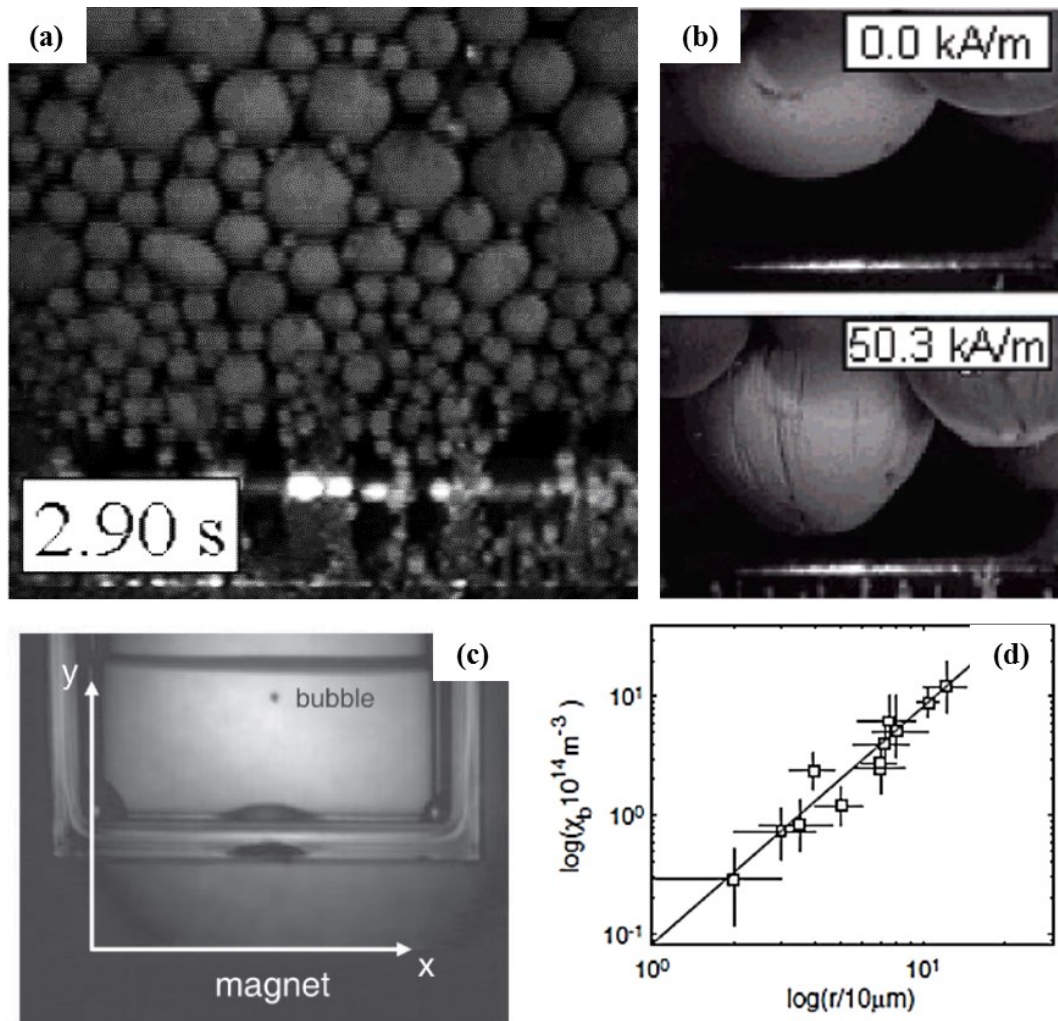
Figure 4.1 *(a) A magnetic field is applied to a magnetic Pickering emulsion. The drops move through the continuous phase toward the bottom of the vial after turning ON the field. (b) Shape deformation of decane drops: on top, emulsion drop when no magnetic field is applied; on bottom, drop elongation in the direction of the field when applying a magnetic field. (c) Experimental setup for measuring the magnetic bubble trajectory. (d) The dependence of the modelled trajectory on the magnetic susceptibility of the bubble (χ_b, in units of volume) through the fitting procedure. (a) and (b) are taken from [9]; (c) and (d) are taken from [8].*

interface [7]. The authors found that the dipolar interactions are stronger for particles assembled in thin films compared to powdered samples, which can be caused by the shape anisotropy induced by the thin film structuring.

Indeed, armoured bubbles and Pickering emulsions stabilized by magnetic particles were both achieved previously [8, 9]. In the magnetic emulsion systems, the drop size can be controlled by varying magnetic particle concentration. As shown in Figure 4.1a and b, an external field can be able to destabilize the emulsion, leading to a macroscopic phase-separated system [9]. Claus-Dieter Ohl and co-workers modelled the motion of the magnetic bubbles in a magnetic field with a force balance (Figure 4.1c, d) [8]. These systems exhibit unique encapsulation behaviours and show strong magnetic response properties, which can find potential applications in magnetic controlled biomedical systems and drug delivery.

At liquid interfaces, magnetic particles subjected to a uniform constant magnetic field experience a torque, forcing their magnetic moments to be aligned with the applied field. Snezhko and coworkers studied the dynamic self-assembled structures of nickel microspheres at a liquid interface. In a vertical alternating (ac) magnetic field, the spheres can form some ordered dynamic snakelike structures (Figure 4.2a) in a limited range of field magnitudes and frequencies. These multi-segment structures exhibit long range antiferromagnetic ordering between segments, while each segment consists of aligned chains of ferromagnetically ordered microspheres. This phenomenon can be caused by the effective exchange interaction between the snake's segments mediated by the surface wave [10, 11]. With the ac magnetic field at the interface between two immiscible liquid, these microspheres dynamically self-assemble into localized asters and arrays of asters (Figure 4.2b), which exhibit locomotion and shape change [12]. The asters can capture, transport and position target spheres by controlling a small external field applied parallel to the interface. The authors believe this interesting work gives new insights into the engineering of 'smart' synthetic materials and new design concepts for 'soft robotics'.

Anisotropic magnetic particles have become a recent trend in colloid science as structural motifs for an interesting array of synthetic materials. Various physical and chemical methods have been reported in the literature for the preparation of anisotropic
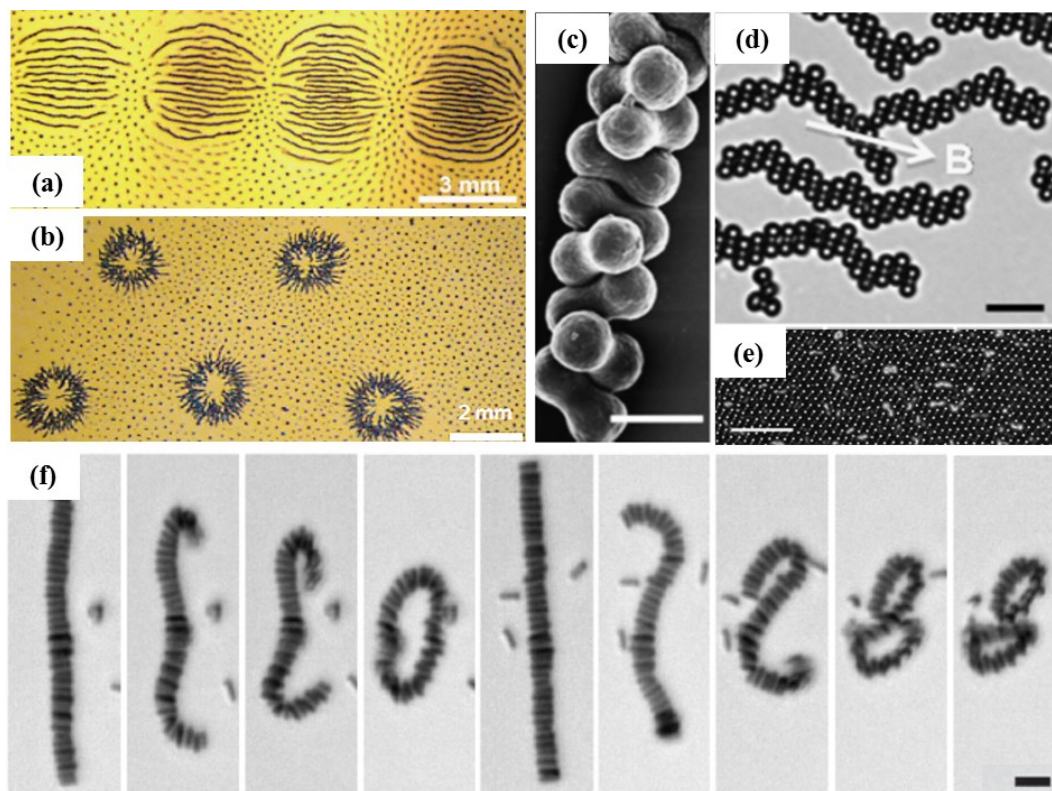
Figure 4.2 *(a, b) Snakelike structures at air-water interface and asters formed at liquid-liquid interface generated by a vertical alternating magnetic field [10, 12]. (c-e) Magnetic peanut-shaped colloids can be driven into complex 1D and 2D structures. Scale bar: 2 μm, 5 μm, and 10 μm, respectively [13]. (f) Self-assembled ribbons of magnetic Janus rods and the formation of one and two rings from a ribbon by reversing the applied field, scale bar is 4 μm [14].*

magnetic colloids [15, 16]. These colloids are characterized by an induced or spontaneous magnetization dependent on a particular direction. Magnetic anisotropic can mainly result from the magnetocrystalline structure of the material and the particle shape. Anisotropic and directional interactions between the particles can give rise to highly complex structures and dynamics, bringing novel physical questions and challenges [17]. So far, most studies of anisotropic magnetic colloids focus on their behaviours in bulk. For example, Liddell *et al.* found that magnetic peanut-shaped colloids can be driven into complex 1D and 2D structures by the balance of dipolar, electrostatic, and entropic forces (Figure 4.2c, d). These particles can form an orientationally ordered monolayer on a glass substrate (Figure 4.2e) [13]. Under a static field, anisotropic magnetic Janus particles can assemble into complex structures with magnetic poles facing each other to minimize the magnetic energy of the aggregate. Yan and

coworkers reported the ribbons formed by ferromagnetic rods which oriented perpendicular to the field direction. Figure 4.2f shows that the formed ribbons can further evolve into a low energy ring state upon reversing the direction of the external field [14]. In the past few years, iron oxides (such as α-Fe_2O_3, and Fe_3O_4) the most popular magnetic material, have been developed as particles of various shapes giving rise to anisotropic properties [18-20]. Yin *et al.* produced a magnetically actuated liquid crystal systems based on Fe_3O_4 rods (~1.5 μm in length and 200 nm in diameter) and demonstrated its instantaneous and reversible orientational tuning using very weak magnetic fields [21]. Motivated by these works, it is important to study the interfacial properties of anisotropic magnetic particles at liquid interfaces, especially when an external field has been applied.

In this chapter, the synthesized β–FeOOH @silica rods were converted into magnetic rods. In section 4.2, the converted rods were first analysed by X-ray powder diffraction (XRD) to verify the oxides. After this, a differential dynamic microscopy technique (DDM) was carried out to measure the rods' magnetic moment. After spreading the rods at the air-water interface, an external field was applied to control their interfacial behaviours. When the applied field is perpendicular to the interface (section 4.3), the orientation of the rods with respect to the interface can be influenced by the field strength. When the field is parallel to the interface (section 4.4), the rods are aligned and form a magnetic monolayer. Using these magnetic rods, an oil-in-water emulsion can be stabilized for months. The droplets in the emulsion can be controlled by a magnet.

4.2 Magnetic Rods

This section presents the magnetic rods used in the experiments, including the particle conversion reaction, the XRD analyses and the magnetic moment measurements.

4.2.1 Particle conversion

As mentioned before, akaganéite micro-scale particles can be easily converted into other iron oxides, such as hematite (α-Fe_2O_3) and magnetite (Fe_3O_4). The conversion can be achieved by two methods. The first one uses diethylene glycol as decomposition

agent. High temperature (220 ℃) and long reaction (24 hours) are involved [21]. This method has a high conversion efficiency, but a low yield of magnetic particles. The second method, which has been widely used before, uses hydrazine as a reducing agent [22]. By using hydrazine, Fe (III) ions can be reduced to Fe (II). The change in coordination number of the Fe atom therefore converts Fe-OH to Fe-O following dehydration:

$$12\text{FeOOH} + \text{N}_2\text{H}_4 \rightarrow 4\text{Fe}_3\text{O}_4 + 8\text{H}_2\text{O} + \text{N}_2 \quad\quad\quad (4.1)$$
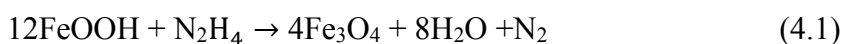
The proposed approach could be used for a controlled conversion of akaganéite to magnetite structures without high-temperature treatment. However, the conversion efficiency of this method is relatively low. In other words, the akaganéite particles cannot be completely converted into magnetite structures.

In this present work, magnetic rods were obtained by the second method, *i.e.*, the hydrazine treatment. Specifically, 5 mL β–FeOOH @silica aqueous solution (3mg/mL) with 500 µL hydrazine were aged in an oven (~5 hours, Binder VD23, 120 ℃). During the treatment, regular shaking (every half an hour) is required for homogenization. As shown in Figure 4.3a, the hydrazine treatment changes the colour of the particles from yellow to brown.

Hydrazine is a strong base, which raises the pH in the solution. For these β–FeOOH @silica rods, the high pH promotes the dissolution of the silica shells. This process can be accelerated at high temperatures. In this case, the initially smooth and homogeneous silica shells can be partially dissolved after the treatment. Therefore, "fixing" the shells is necessary. To do this, the hydrazine-treated particles were first stored in a 0.1g/g PVP (molecular weight = 40,000 g/mol) in ethanol solution for about 5 hours. After this, the particles (0.01g) were re-dispersed in 10 mL ethanol, followed by the addition of 0.8g ammonium hydroxide solution (35%), and 3 additions (20 – 30 minutes intervals) of 0.05 mL fluorescent coating solution (TEOS and FITC & APTES, see the experimental section in chapter 3). Between these additions, the solution was shaken using a mechanical shaker, after all additions it was left overnight. Note that magnetic stirring cannot be used in this experiment. The "fixed" particles were washed several times with ethanol, and stored in ethanol or IPA.
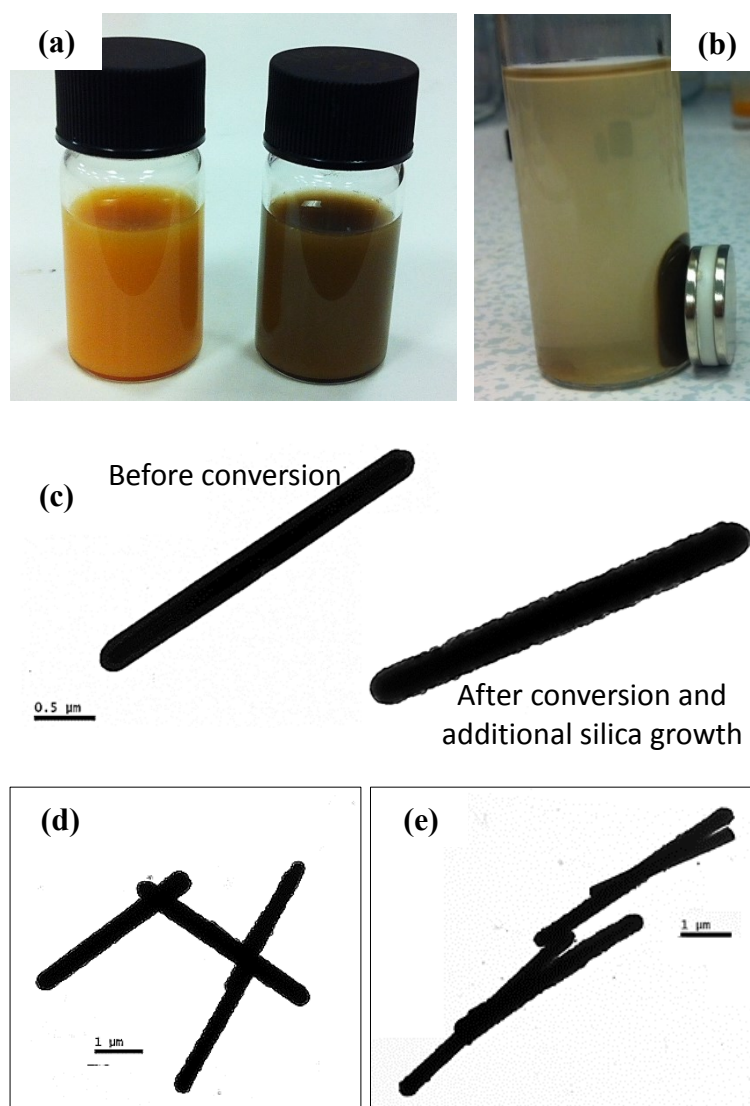
Figure 4.3 (a) The original β–FeOOH @silica rod solution (left) and the magnetic rods after the conversion (right). (b) The magnetic rods can be attracted to one side of the vial (diameter = 20 mm) under an external magnetic field. (c) TEM images of a β–FeOOH @silica rod (left) and a magnetic rod (right). (d) Magnetic rods with aspect ratio ~9. (e) Magnetic rods with aspect ratio ~15.

The rods obtained from the conversion have a strong magnetic response. As soon as a magnet was brought up to one side of the vial, the rods rapidly moved along the direction of the field, as shown in Figure 4.3b. After releasing the magnet, gentle shaking can lead to a rapid redispersion. Figure 4.3c compares two TEM images between an original β–FeOOH @silica rod and a magnetic rod. It appears that both the shape and size of the original rod can be maintained after the conversion process, but

the magnetic rod has a bumpier surface. The latter can be caused by the heterogeneities in silica density introduced by the dissolution process. The additional silica growth on individual rods can also be hindered by the tendency of rods to aggregate due to their magnetic dipole moments (this is measured in section 4.2.3). Also because of the additional silica growth, the diameter of the magnetic rods is measured to be 0.34 ± 0.03 µm, which is slightly larger than the original rods (0.32 ± 0.02 µm). Two rod lengths were obtained from the conversion, which are 3.2 ± 0.4 µm and 5.1 ± 0.2 µm, corresponding to aspect ratio ~9.4 and ~15, respectively (as shown in Figure 4.3d and e).

4.2.2 XRD Analyses

Reaction (4.1) suggests that these magnetic particles are magnetite (Fe_3O_4). However, as mentioned above, the conversion efficiency of hydrazine-treated method is relatively low. In this case, the converted rods might be a mixture of Fe^{2+} oxides and Fe^{3+} oxides. Although the Fe^{2+}: Fe^{3+} molar ratio can be measured after individual determination of Fe^{2+} and Fe^{3+} [23], the whole process is too complicated and not necessary for our experiments. Here, in order to verify the oxides, X-ray powder diffraction (XRD) was carried out.

XRD is a laboratory-based rapid analytical technique commonly used for phase identification of crystalline materials and analysis of unit cell dimensions. Currently, this technique is widely used for the identification of some unknown crystalline materials. For the magnetite Fe_3O_4 particles, the diffraction peaks can be indexed to the JCPDS File Card 19-0629 and 87-0245 (as shown in Figure 4.4a) [24, 25]. Figure 4.4b shows a previous work which compared the XRD patterns for FeOOH and Fe_3O_4 samples. Fe_3O_4 sample has two obvious peaks at 30.1º and 56.9º, corresponding to the crystal planes of (220) and (511), respectively [24]. However, no peaks appear at the same position in the XRD pattern for FeOOH sample.

For the magnetic rods obtained in our experiments, the XRD measurements were recorded using a Bruker D8 advance powder diffractometer (Cu Kα radiation, λ=1.5406 Å, 2θ range 5-90º, 0.1º/min). The rods were transferred into a glass capillary after drying at 50 ºC. Figure 4.4c shows the measured XRD pattern. Peaks appear at both 30º and 57º, indicating that the converted rods contain magnetite Fe_3O_4. However,
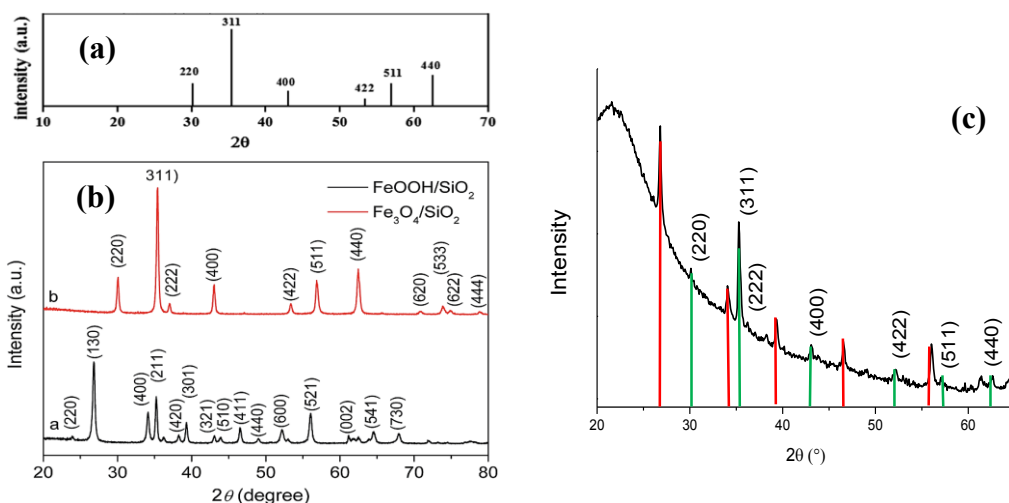
Figure 4.4 *(a) XRD pattern of pure Fe₃O₄ (JCPDS card No. 19-0629). (b) XRD patterns of FeOOH@SiO₂ (black) and Fe₃O₄@SiO₂ (red) samples. Taken from [24]. (c) XRD pattern of the magnetic rods obtained from the hydrazine treatment. The main diffraction peaks were labelled as the Fe₃O₄ phase (marked green). Diffraction peaks belong to FeOOH were shown in red.*

there are some peaks only belong to FeOOH diffraction (peaks marked red in Figure 4.4c), which suggests that these hydrazine-treated rods are mixtures of β–FeOOH and Fe₃O₄. Note here that the "mixture" does not mean some of the rods are Fe₃O₄, while the others are still β–FeOOH. Because of their strong magnetic response property, it is believed that all the β–FeOOH rods have been converted. However, this conversion process is usually incomplete. As a result, every single rod would become a mixture which contains both β–FeOOH and Fe₃O₄. The broad background peak is likely to be due to scattering from the silica shell.

4.2.3 DDM measurements

Theoretical background

Magnetic properties of the rods were measured using differential dynamic microscopy (DDM). This technique, introduced by Cerbino and Trappe [26], has been developed as a simple, reliable, and low-cost method for characterizing the anisotropic dynamics of a colloidal sample [27]. In DDM, a time series of digital video images is acquired in bright-field with a fast camera fitted to a conventional research microscope. These time-lapsed images are then Fourier analysed as a function of the time delay between
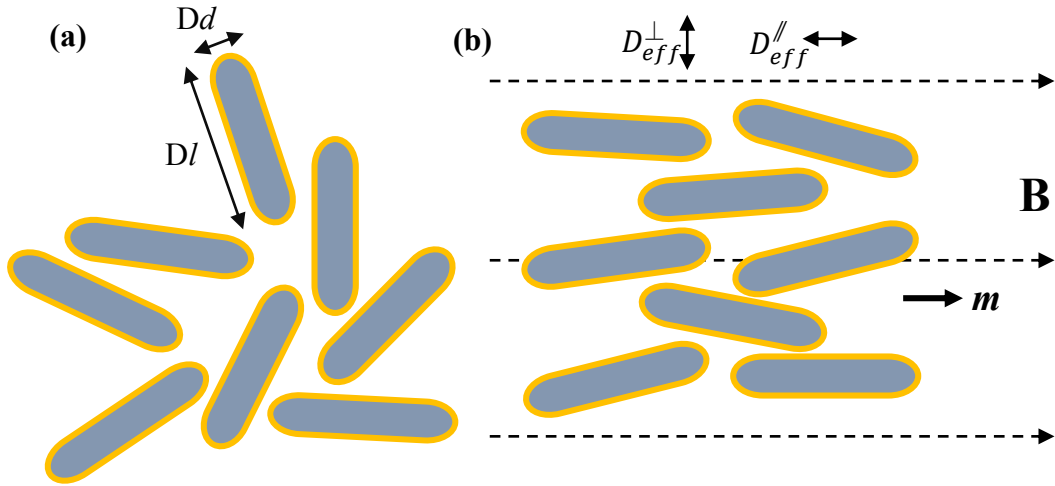
Figure 4.5 *(a) Randomly oriented rods with corresponding translation diffusion coefficients.*
(b) Ensemble of partially aligned rods with definition of effective diffusion coefficients parallel
*and perpendicular to the external magnetic field **B**.*

them. After this, the averaged power spectrum of the Fourier-transformed difference images is used to calculate the intermediate scattering function (ISF), which describes the dynamics of the system. The theoretical derivation of DDM does not average over spatial directions in the image plane, and so can access the dynamics along any direction in real space. This opens the possibility for analysing asymmetric and anisotropic dynamics [27].

At zero field, the rods are randomly oriented, and the measured dynamics are therefore isotropic (Figure 4.5a). When an external magnetic field is applied, an aligned ensemble of Fe_3O_4 rods leads to anisotropic dynamics, as illustrated in Figure 4.5b. The hydrodynamic behaviour of these rods can be approximated by a spherocylinder with major length l and diameter d. The isotropic translational diffusion coefficient is defined as the average over the diffusion coefficient along the three different axes

$$D_{iso} = \frac{1}{3}(D_l + 2D_d) \tag{4.2}$$

Where D_l and D_d are the translational diffusion coefficients parallel to the rod's major axes and diameter, respectively. Note that for all finite aspect ratios, $D_l/D_d < 2$; for infinite long and thin cylindrically symmetric rods, $D_l/D_d = 2$.

Hence, with increasing magnetic field, the dynamics measured parallel to **B** should change from D_{iso} at zero field to D_l; while the dynamics perpendicular to **B** changes from D_{iso} to D_d. The field-dependent effective diffusion coefficients are given by

$$D_{eff}^{/\!/} = D_{iso} + \frac{2}{3}(D_l - D_d)S_2(B) \rightarrow D_l \text{ (when } B \rightarrow \infty)$$

$$D_{eff}^{\perp} = D_{iso} - \frac{1}{3}(D_l - D_d)S_2(B) \rightarrow D_d \text{ (when } B \rightarrow \infty) \tag{4.3}$$

where the $S_2(B)$ is the second-order orientational order parameter. For a randomly oriented rod, $S_2 = 0$, and a fully aligned rod with its long axes parallel to **B**, $S_2 = 1$.

In equation (4.3), since $S_2(B)$ is field-dependent, the measured anisotropic dynamics are therefore sensitive to the magnetic-field strength. By measuring $D_{eff}^{\perp}$ and $D_{eff}^{/\!/}$ at different magnetic-field strength, combined with their saturation values, D_l and D_d can be calculated easily, and $S_2(B)$ can also be extracted. By increasing the magnetic-field strength, the measured anisotropic dynamics would become more obvious at a certain strength, which corresponds to the critical field strength, *i.e.*, the B_{crit}. For an unknown magnetic material, its magnetic moment *m* can be calculated using the following expression:

$$B_{crit} = k_B T/m \tag{4.4}$$

with k_B the Boltzmann constant and *T* the temperature.

Experimental section

The magnetic rods (aspect ratio ~15) were dispersed in ethanol at a concentration of 0.25 mg/g. The solution (~190 µL) was then carefully filled in a customized observation chamber (~400 µm in thickness, Figure 4.6a) glued with UV-cured adhesive and sealed with vacuum grease. Air bubbles are always avoided. The sample was mounted in an air gap between two Helmholtz coils. The diameter of the coils is 15 cm, which is much larger than the sample and thus ensures a homogeneous magnetic field in the plan of view.

Figure 4.6b demonstrates the experimental setup. A horizontal field was created at the stage of an inverted research microscope (Nikon TE300 Eclipse). The images (movies)
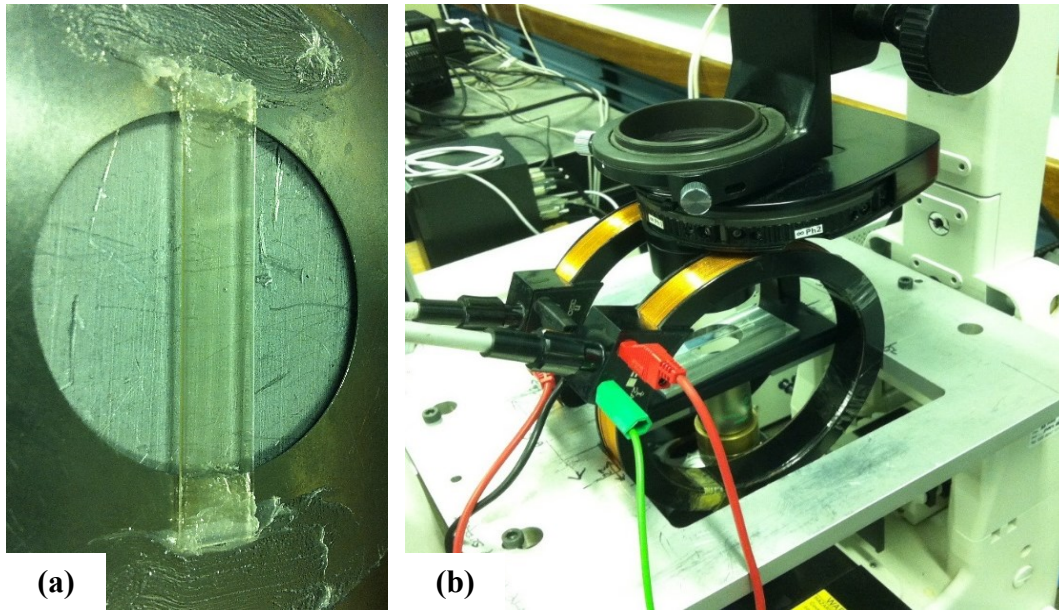
Figure 4.6 *A prepared sample (a, sealed with vacuum grease) and the magnetic field setup (b) for DDM measurements. The diameter of the coil is ~15 cm. All the measurements were carried out at room temperature.*

were collected with a Nikon Plan Fluor 20× objective (NA = 0.45) and a CMOS camera (Mikrotron MC 1362, frame grabber card Mikrotron Inspecta 5). During the measurements, wall effects were always avoided by collecting the images from the bulk of the sample chamber. The camera was rotated by 45º to reduce the impact of the artefacts stemming from the Fourier transform, which are mainly along the horizontal and vertical directions. In each measurement, a movie with 4129 images (520×500 pixels at frame rate 1000 fps) was collected and then analysed.

Results and discussion

Figure 4.7a shows the microscopic observations of the rods with time. It seems that the rods can move randomly at zero field. After turning the horizontal field on, the rods start to align in the field direction. This alignment becomes stronger at a high field strength.

Ideally, when no horizontal field is applied, the randomly oriented rods lead to isotropic dynamics. However, in our measurements, the earth's field (~5×10^{-5} T) [28] can orient the rods in a vertical direction. In this case, the measured dynamics at zero horizontal field is anisotropic, *i.e.*, the measured $D_{eff}^{/\!/}$ and $D_{eff}^{\perp}$ are slightly different,

as shown in Figure 4.7b. To remove this effect, the translational diffusion coefficient obtained at zero external field is normalised, which equalizes the measured $D_{eff}^{\parallel}$ and $D_{eff}^{\perp}$ (Figure 4.7c). From equation (4.4), the calculated magnetic moment of the rods used in the measurements is 1.6×10^{-15} A·m². This value is relatively high but still lower than the previous measurements ($\sim 10^{-12}$ A·m²), where the higher conversion efficiency method has been used [21].
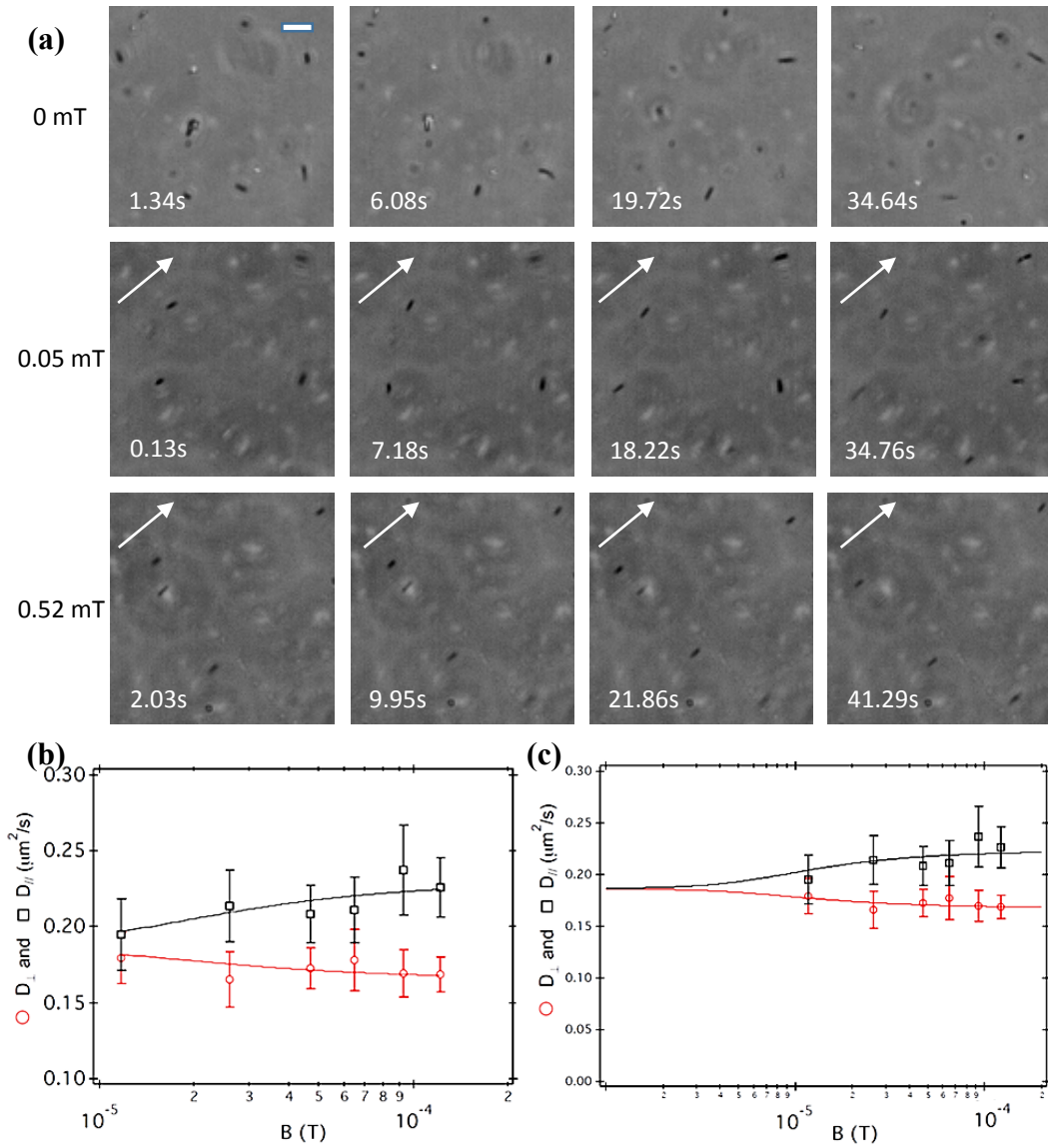
Figure 4.7 (a) The behaviours of the rods with time at different field strength (The scale bar is 5 μm). Arrows indicate the field direction. (b) Measured effective diffusion along the field direction (black squares) $D_{eff}^{\parallel}$ and perpendicular to the field (red circles) $D_{eff}^{\perp}$. (c) Measured $D_{eff}^{\parallel}$ and $D_{eff}^{\perp}$ after normalizing the diffusion coefficient at zero external field.

4.3 Influence of a Vertical Magnetic Field on Rods Orientation at Liquid Interface

In this section, the magnetic rods are spread at the air-water interface, where a vertical magnetic field is applied. Previous theoretical studies of magnetic ellipsoids reported that the tilt angle of an ellipsoid with respect to the interface increases with the applied field strength, until it undergoes a discontinuous phase transition to a vertical (flipped) orientation at a critical field strength [29, 30]. So far, this magnetic field-induced flipping process has been studied theoretically only and there are no experimental data available. The present experiment is an attempt to investigate this flipping process. By applying an external field perpendicular to the interface, the tilt angle of the rods changes sensitively with the field strength. Flippers are observed when the field strength is high. We hope this work is helpful to engineer and control the configuration of anisotropic magnetic rods at liquid interfaces.

4.3.1 Sample preparation and experimental setup

CTAB effect

The TEM images (Figure 4.3) of the magnetic rods demonstrate a bumpy surface generated by additional silica growth. Compared to β–FeOOH @silica rods with smooth surfaces, these magnetic rods are easier to aggregate (Figure 4.8a) since their bumpy surfaces cause much stronger capillary interactions at liquid interfaces. In this case, cetyltrimethylammonium bromide (CTAB) is used to modify the silica surface. CTAB dissociates to positive charged cetyl trimethyl ammonium cation (CTA$^+$), which can adsorbs on the negative charged SiO$_2$ surface to form a CTA$^+$ adsorption layer. The formed CTA$^+$ layer induce a strong repulsive interaction between the rods at short separation distances.

It has been reported that the hydrophobicity of the CTAB-silica surface can be affected by the thickness of CTAB adsorption layer. When CTAB was absorbed as a monolayer (~2.6 nm in thickness), its hydrophobic group (*i.e.*, hydrocarbon chain) towards the
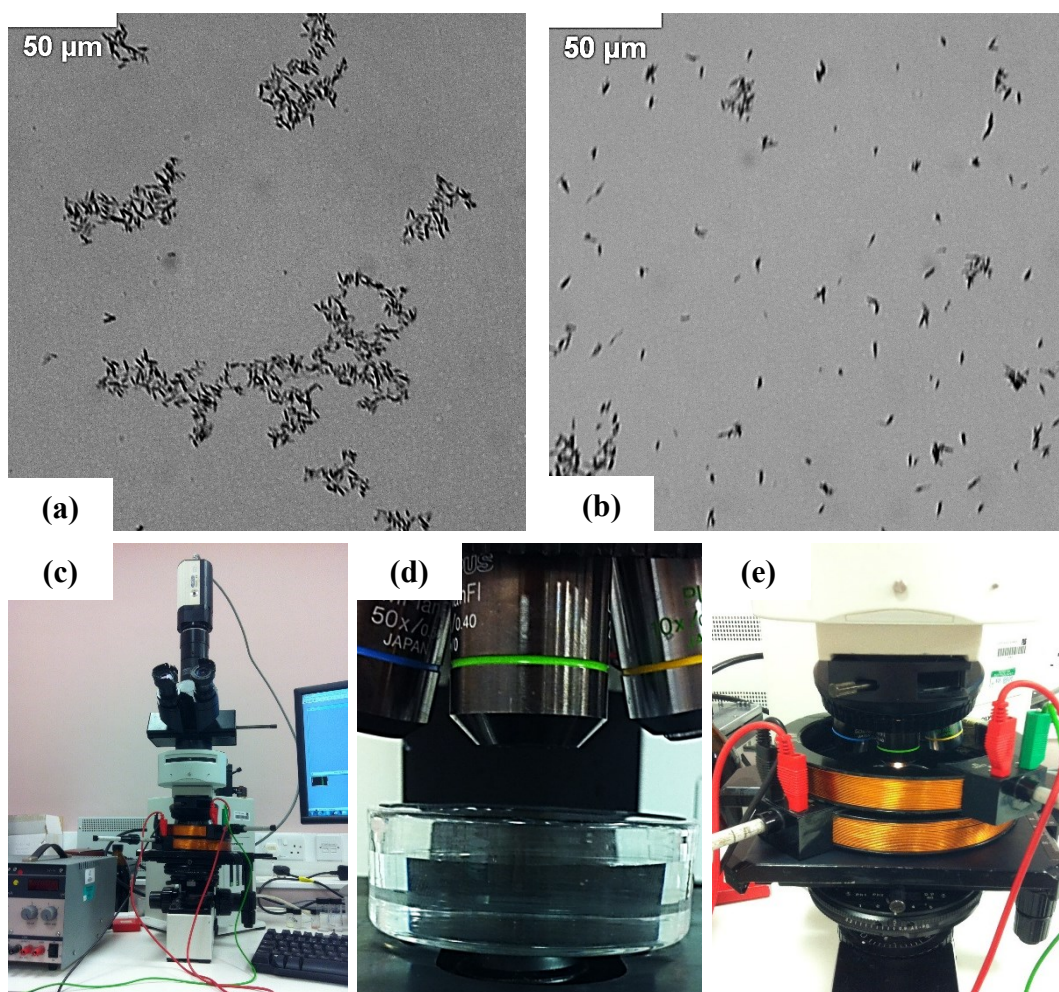
Figure 4.8 *(a, b) Magnetic rods before (a) and after (b) modification by CTAB at the air-water interface. (c) Experimental setup for the microscopic observations. (d) The Petri dish used in the experiments. The height of the water phase is about 13 mm. (e) The magnetic field setup on the stage of the microscope.*

water phase, making the surface less hydrophilic (contact angle ~84°). If the absorption layer turns to a double layer, they hydrophobic group of the second layer is opposite to that in the first layer, with the polar group towards water. In this case, the CTAB-silica surface exhibits weak hydrophilic properties (contact angle < 50°) [31].

In our experiments, IPA was used as the solvent for modifying the silica surface with CTAB. Magnetic rods (aspect ratio ~15) were dispersed into a 0.5 wt% CTAB-IPA solution. After shaking the solution overnight, the rods were washed and stored in pure IPA prior to the experiments. These CTAB-modified rods aggregate less strongly at the air-water interface, where more individual rods can be observed (Figure 4.8b).

Optical microscopy and magnetic field setup

The experimental setup is illustrated in Figure 4.8c. Specifically, an air-water interface was first prepared with distilled water in a Petri dish (50 mm in diameter, Figure 4.8d). The interface is sufficiently large compared to the interacting rods that it is flat in the far field and considered an unbounded interface. The Petri dish was then transferred onto the stage of an optical microscope (Olympus BX-50). ~10 µL solution of CTAB-modified magnetic rods (2.7 mg/g in IPA) was spread at the air-water interface.

A roughly homogeneous vertical magnetic field was created by means of two coils (diameter = 12.4 mm, Figure 4.8e). The field intensity can be controlled by changing the current passing through the coils, and the maximum field strength is about 13.5 mT (measured with a "Smart Magnetic Sensor" model SMS102 by ASONIK).

Rods orientations were examined using the Olympus BX-50 microscope (20× objective, NA = 0.4) equipped with a QICAM 12-bit Mono Fast 1394 camera (Qimaging). All the recorded images were analysed within the ImageJ analysis software.

4.3.2 Influence of magnetic field on rods orientation

As shown in Figure 4.9a, the tilt angle θ of a rod is defined as the angle between its long axes and the air-water interface. From the microscopy observations, the projection area of the rod can be calculated as:

$$S = l \times D \times cos\,\theta + \pi \times (D/2)^2 \tag{4.5}$$

where L and D are the length and diameter of the rod, respectively. $l = L - D$.

When the long axes of a rod is perpendicular to the interface, its projection at the interface becomes a round area with a diameter of D, corresponding to a 90º tile angle and $S_{(\perp)} = \pi \times (D/2)^2$ in equation (4.5).

For a rod lying at the interface, $\theta = 0º$, and its projection area is:

$$S_{(//)} = l \times D + \pi \times (D/2)^2 \tag{4.6}$$

From these two equations, it is easy to obtain the relationship between the projection area of the rods, the tile angle θ and the aspect ratio A of the rods:

$$\frac{S}{S_{(/\!/)}} = \frac{\cos\theta + \frac{\pi}{4(A-1)}}{1 + \frac{\pi}{4(A-1)}} \tag{4.7}$$

where A = L/D, is the aspect ratio of the rods.

Therefore, by measuring the projection area of the rods at different field strength, combined with the size information obtained from the TEM images, the tilt angle θ can be roughly calculated.

Figure 4.9b shows the relationship between the calculated θ and the applied field strength. Note that each calculated θ was averaged from ~ 40 observed individual rods, and no aggregates and contact particles were analysed in the calculation. It can be seen that the tilt angle is very sensitive to the applied field strength. A weak field (~1.36 mT) can incline the rods with ~16º at the interface. Enhancing the field strength increases the averaged θ up to ~40º. One possible explanation to this phenomena could be the balance between the magnetic force working on the rod and the restoring interfacial force. The latter can be enhanced by the tilting process, which induces a larger interface deformation. When the strongest field (~13.5 mT) was applied, some of the rods (~ 5%) flipped at the interface, as shown in Figure 4.9c. This observation is reasonably consistent with the theoretical prediction, *i.e.*, the tilt angle of an ellipsoid with respect to the interface increases with the applied field strength, until it undergoes a discontinuous phase transition to a vertical (flipped) orientation at a critical field strength [29, 30]. Moreover, the field-induced flipping process occurs very quickly, consistent with the discontinuous orientational transition predicted in the theoretical studies [29, 30]. It should be noted that since most of the rods do not flip, the averaged tilt angle at the maximum field strength is calculated as ~48º.

4.3.3 Discussion of error and improvement

It should be pointed out that observations from an optical microscope cannot reflect the real size (or aspect ratio) of the rods. As a result, the measured projection area are not accurate enough to calculate the tilt angle with equation (4.7). However, the
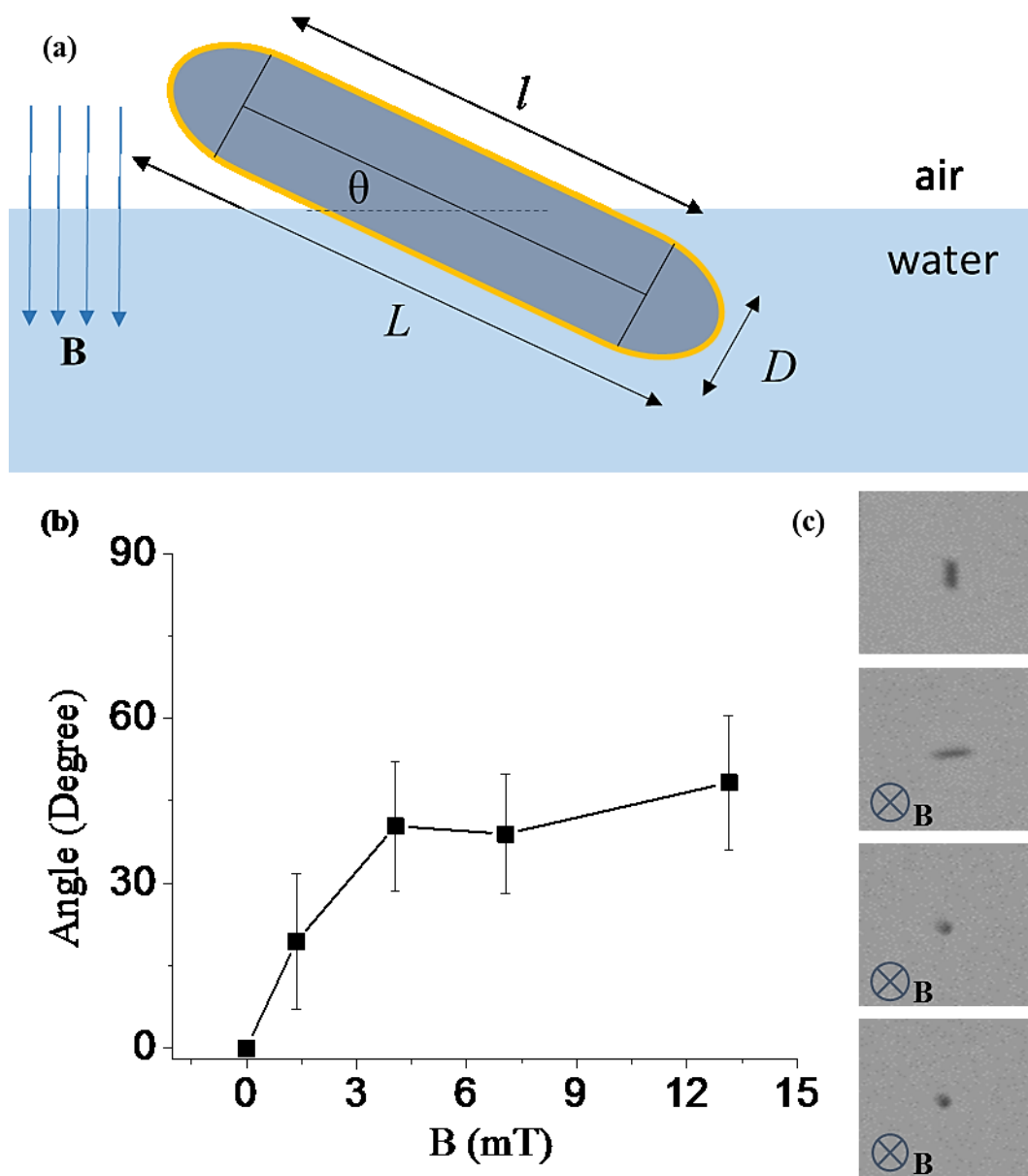
Figure 4.9 *(a) The definition of the tilt angle θ of a magnetic rod at the air-water interface where a vertical field is applied. (b) The calculated tilt angle changes with the applied field strength. (c) A magnetic field-induced flipping process.*

obtained data indicates that magnetic field can be used to control the orientation of the magnetic rods at liquid interfaces. When the applied field is strong enough, the rods can flip their long axes perpendicular to the interface, which is similar to the observed flippers in a compressed monolayer of non-magnetic rods (discussed in chapter 3).

In our experiments, it is observed that most rods can be inclined at ~40º in the applied field, and only a limited number of them can flip at the interface (θ ~90º). A major reason for this is that the applied field strength is not high enough. Also, as mentioned in section 4.2.2, the rods used in this experiment are not pure magnetite, and the magnetic moment is quite different between the rods. In this case, the response to an external field from different rods can be very different. This causes a relatively big error bar in the calculations, *e.g.*, in Figure 4.9b, the error bar is ~12º. Besides, the fluctuation of the interface and the movements of the rods also make the measurements challenging.

To improve the accuracy of the measurements, a high-speed, high-resolution CCD camera can be helpful. Creating a stable air-water interface is also important as is having a greater range of applied field strengths available. With freeze-fracture shadow-casting cryo-scanning electron microscopy (cryo-SEM), the wetting properties of a single nanoparticle can be measured [32]. This could be an accurate method for the tilt angle measurements. Furthermore, the relationship between the magnetic field and the size of the rods, the magnetic moment of the rods, as well as the surface tension of the subphase still need to be better understood.

4.4 Magnetic monolayers

At an interface the rods can reorient to align their magnetic moment with a magnetic field. When the applied field is perpendicular to the interface, as observed in section 4.3, the equilibrium tilt angle of the rods can reach 90º at a critical field strength. Similarly, when the field is parallel to the interface, the rods can align parallel to each other. Under compression, these aligned rods can form a monolayer which is expected to exhibit different behaviour compared to the rods with random orientations [6]. This section is a preliminary study which focuses on the monolayers consisting of aligned rods in a horizontal magnetic field. Surface pressure measurements were carried out to study these magnetic monolayers. Using the magnetic rods as stabilizers, a magnetic emulsion system has also been created.

4.4.1 Magnetic alignment

The magnetic response of the rods in a horizontal field was observed under the microscope. DDM setup was used for the observations (Figure 4.10a). ~10 µL solution of CTAB-modified magnetic rods (2.7 mg/g in IPA) was spread at the air-water interface created in a Petri dish (50 mm in diameter). When no external field is applied, the rods can move randomly at the interface, as shown in Figure 4.10b. The magnetic alignment can be observed immediately after turning the field on (~0.2 mT, Figure 4.10c). During the alignment, a single rod undergoes a rotational motion to make its
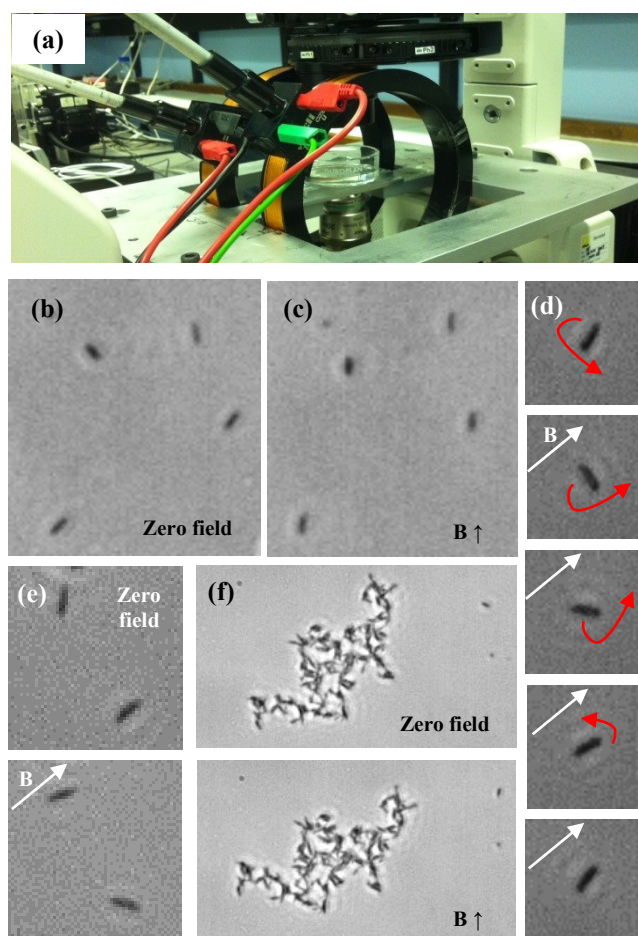

Figure 4.10 *(a) The experimental setup for the microscopic observations. (b, c) Rod orientations before and after turning the applied field on (~0.2 mT). (d) A single rod rotates its long axis to be parallel to the field direction. Red arrows indicate the motions of the rod. (e) A weak field (0.02mT) cannot align the rods at the air-water interface. (f) Rods in an aggregate structure cannot be aligned by an external field (~5 mT). Note that all the rods in these images are ~5.1 µm in length and ~0.32 µm in diameter.*

long axis, *i.e.*, its magnetic moment direction, parallel to the field direction (Figure 4.10d). This leads to the side-by-side orientations of the rods.

Not surprisingly, if the field strength is too small (< 0.1 mT), the rods are barely influenced by the external field. In this case, as shown in Figure 4.10e, the alignment cannot be achieved. In an aggregate structure, the rods bond with each other with strong capillary interactions. As a result, the applied field is unable to align the rods in an aggregate, even with a somewhat higher field strength (~5 mT), see Figure 4.10f.

4.4.2 Magnetic monolayers

Langmuir trough and a horizontal magnetic field were combined as shown in Figure 4.11a. The diameter of the coils is ~16 cm. To create a homogenous field, the Helmholtz pair has to be separated by a distance equal to the radius of the coil (~8 cm).
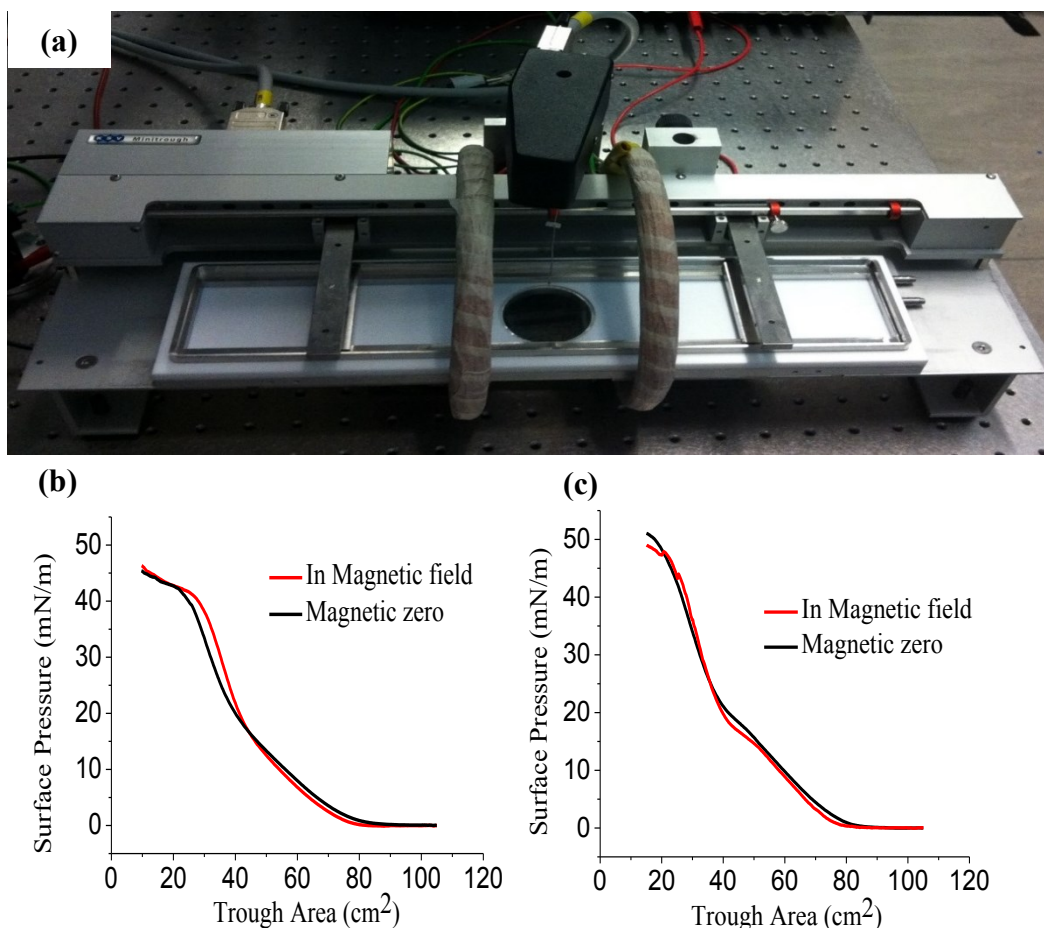
Figure 4.11 *(a) Langmuir trough with two Helmholtz coils. (b, c) Π-A isotherms for monolayers containing magnetic rods with aspect ratio ~9 and ~15, respectively.*

However, the obtained field is relatively small compared to the trough. In this case, we reduced the trough area from ~170 cm^2 to 105 cm^2. After the pre-measurement surface cleaning, ~2.3 mg CTAB-modified magnetic rods (in IPA) were carefully spread at the interface. The external field (~5 mT) is turned on before the spreading step, and is turned off after the surface pressure measurements. The measured Π-A isotherms (averaged over several measurements) are illustrated in Figure 4.11b and c for rods with aspect ratio ~ 9 and ~15, respectively.

As shown in Figure 4.11b, for the monolayer formed and compressed in an external field (red curve), a slight hysteresis was observed for the gas-liquid phase transition. This can be caused by the alignment of the rods in the gas phase, which induces more space for the rods to rearrange under compression. It can be supposed that in an applied field, a dense and more ordered monolayer can be formed in the liquid phase. This would lead to a steeper solid phase compared to the case when no field is applied. Since the magnetic force aligning the rods decreases with their size, the applied field has a weaker effect on the longer rods (Figure 4.11c, red curve). Although they are reversible, the hysteresis and steeper solid phase observed here are admittedly very weak. The field strength applied for each measurements is not exactly the same, i.e. setting the same current does not always result in the same field strength, which is why error bars have not been plotted in these these isotherms. Therefore, more detailed work is required to better understand the influence of the field. Increasing the field strength can be helpful to obtain a more substantial effect on the isotherms.

4.4.3 Magnetic emulsions

Inspired by the results described above, an attempt was made to use the magnetic rods to stabilize emulsion droplets. Here, at room temperature, 1.7g aqueous solution (~5 mg/mL) of rods (aspect ratio ~9) was mixed with 0.65g mineral oil by shaking with a Fisons Whirlimixer for ~30 seconds. Figure 4.12a shows the obtained emulsion after the mechanical agitation. The droplets coalesce in the next few hours and then become very stable over time. An extra-water volume remains underneath the emulsion, and some extra rods can also be observed at the bottom of the vial.

Figure 4.12b is a confocal microscopy image of the obtained emulsion. It can be seen that the emulsion consists of oil-in-water droplets of different sizes. Most of the droplets appear to be spherical in shape. The droplet size was found to be in the range of 50−800 μm with an average diameter of 300 μm. The magnetic rods are observed to adsorb onto the surface of the droplets. Figure 4.12c shows the surface of a mineral oil droplet covered with a dense monolayer of rods. It is a complex packing. Buckling and flippers can both be observed.

Previously, *Pickering* magnetic emulsions have exhibited the ability to travel through a continuous phase with the help of a magnetic field gradient [9]. In our systems, the droplets can also be manipulated with a permanent magnet, as shown in Figure 4.12d. Compared to the bigger droplets, the smaller ones are easier to move. This manipulation has potential in applications of novel materials and drug-delivery mechanisms.
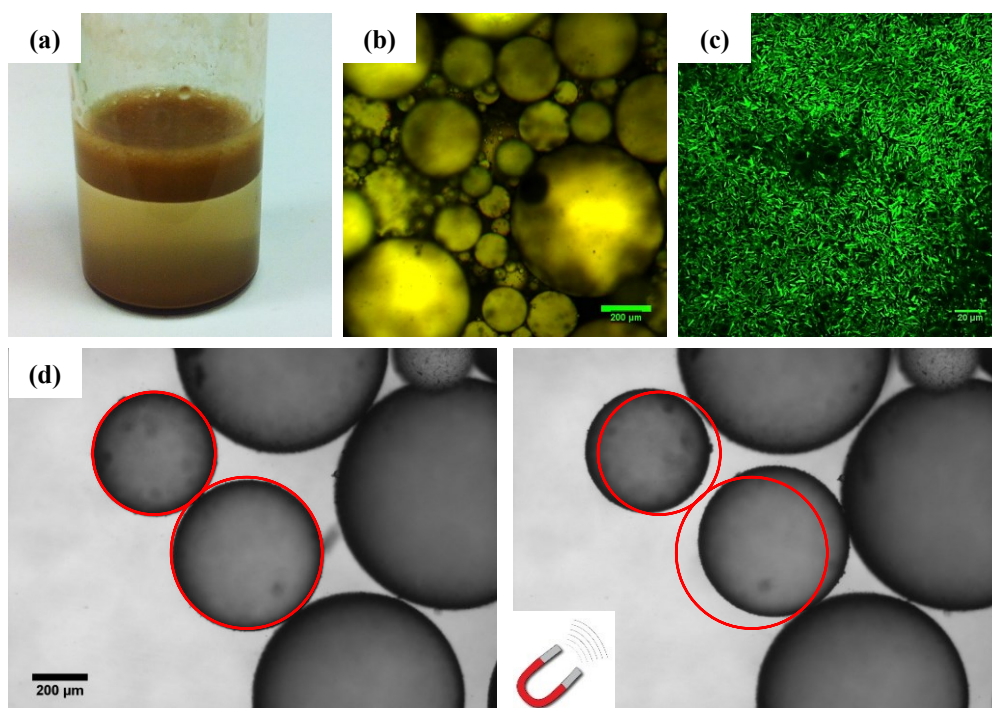
Figure 4.12 *(a) A mineral oil-in-water emulsion stabilized by the magnetic rods. (b) A confocal image of the emulsion. (c) A complex packing monolayer of rods on the surface of the droplets. The scale bar is 20 μm. (d) The smaller droplets are easier to be controlled to move by a permanent magnet (marked in red).*

4.5 Conclusions and Outlook

This chapter is a preliminary study of the interfacial properties of magnetic rods in an external field. Magnetic rods were converted with hydrazine-treatment. XRD results demonstrate that the rods are mixtures of β–FeOOH and Fe_3O_4. The DDM technique was used to measure the rods' magnetic moment, which has not been reported before. When the rods are spread at the air-water interface, their orientation can be affected by an external field. A field-induced flipping process has been observed when a strong field is applied perpendicular to the interface. On the other hand, a horizontal field was found to be helpful to the formation of magnetic monolayers in a Langmuir trough. The formed monolayers exhibit slightly different phase transitions compared with the monolayers of non-magnetic rods. By forming a monolayer, these magnetic rods can also be used to stabilize an oil-in-water emulsion. The droplets are easy to manipulate with a permanent magnet

DDM technique is a new method for measuring the magnetic moment. In the present experiments, the earth's field induced magnetic noise since the rods in bulk are very sensitive to an external field. In future work, the earth's field needs to be cancelled before the DDM measurements. The field-induced flipping phenomena observed here is very interesting, which has only been predicted in previous theoretical studies. As discussed in section 4.3.2, the relationship between the applied field and the tilt angle of the rods need to be better measured. For the magnetic monolayers, it is believed that if the applied field can be even stronger, their phase transitions would exhibit more interesting properties.

It has been reported that the average droplet size in an emulsion increases with the particle dimension [33]. Here, the relationship between the droplet size and the rods' aspect ratio can be studied in more detail. The response of the magnetic droplets to an external field needs to be better understood. Controlling the droplets precisely is of the main challenges.

Acknowledgment

References:

[1] Lee, D. K.; Kim, Y. H.; Kim, C. W.; Cha, H. G.; Kang, Y. S. Vast Magnetic Monolayer Film with Surfactant-Stabilized Fe3O4 Nanoparticles Using Langmuir-Blodgett Technique. *J. Phys. Chem. B* **2007**, *111*, 9288–9293.

[2] Bacri, J.-C.; Perzynski, R.; Salin, D.; Cabuil, V.; Massart, R. Phase Diagram of an Ionic Magnetic Colloid: Experimental Study of the Effect of Ionic Strength. *J. Colloid Interface Sci.* **1989**, *132*, 43–53.

[3] Malchenko, S. N.; Goroshko, N. N.; Baikov, M. V.; Chudakov, V. A.; Ermolenko, V. I. Formation of iron oxide films from stabilized magnetite sols-magnetic liquids. *Thin Solid Films*, **1993**, *227*, 128–132.

[4] Krebs, J. J.; Lind, D. M.; Berry, S. D. Ferromagnetic resonance and spin anisotropy in iron oxide thin films and iron oxide/nickel oxide superlattices. *J. Appl. Phys.* **1993**, *73*, 6457–6459.

[5] Meldrum, F. C.; Kotov, N. A.; Fendler, J. H. Preparation of Particulate Mono- and Multilayers from Surfactant-Stabilized, Nanosized Magnetite Crystallites. *J. Phys. Chem.* **1994**, *98*, 4506–4510.

[6] Lefebure, S.; Menager, C.; Cabuil, V.; Assenheimer, M.; Gallet, F.; Flament, C. Langmuir monolayers of monodispersed magnetic nanoparticles coated with a surfactant. *J. Phys. Chem. B* **1998**, *102*, 2733–2738.

[7] Pauly, M.; Pichon, B. P.; Panissod, P.; Fleutot, S.; Rodriguez, P.; Drillon, M.; Begin-Colin, S. Size Dependent Dipolar Interactions in Iron Oxide Nanoparticle Monolayer and Multilayer Langmuir-Blodgett Films. *J. Mater. Chem.* **2012**, *22*, 6343−6350.

[8] Zhao, X.; Quinto-Su, P. A.; Ohl, C. D. Dynamics of magnetic bubbles in acoustic and magnetic fields. *Phy. Rev. Lett.* **2009**, *102*, 024501.

[9] Melle, S.; Lask, M.; Fuller, G. G. Pickering emulsions with controllable stability. *Langmuir* **2005**, *21*, 2158−2162.

[10] Snezhko, A.; Aranson, I.; Kwok, W.-K. Dynamic Self-Assembly of Magnetic Particles on the Fluid Interface: Surface-Wave-Mediated Effective Magnetic Exchange. *Phys. Rev. E* **2006**, *73*, 041306.

[11] Snezhko, A. Non-equilibrium Magnetic Colloidal Dispersions at Liquid-Air Interfaces: Dynamic Patterns, Magnetic Order and Self-Assembled Swimmers. *J. Phys: Condens. Matter* **2011**, *23*, 153101.

[12] Snezhko, A.; Aranson, I. S. Magnetic manipulation of self-assembled colloidal asters. *Nat. Mater.* **2011**, *10*, 698−703.

[13] Lee, S. H.; Liddell, C. M. Anisotropic Magnetic Colloids: A Strategy to Form Complex Structures Using Nonspherical Building Blocks. *Small* **2009**, *5*, 1957–1962.

[14] Yan, J.; Chaudhary, K.; Bae, S. C.; Lewis, J. A.; Granick, S. Colloidal ribbons and rings from Janus magnetic rods. *Nat. Commun.* **2013**, *4*, 1516.

[15] Roh, K.; Martin, D.; Lahann, J. Biphasic Janus particles with nanoscale anisotropy. *Nat. Mater.* **2005**, *4*, 759.

[16] Okubo, M.; Fujibayashi, T.; Terada, A. Synthesis of micron-sized, monodisperse polymer particles of disc-like and polyhedral shapes by seeded dispersion polymerization. *Colloid Polym. Sci.* **2005**, *283*, 793–798.

[17] Tierno, P. Recent Advances in Anisotropic Magnetic Colloids: Realization, Assembly and Applications. *Phys. Chem. Chem. Phys.* **2014**, *16*, 23515−23528.

[18] Chueh, Y.; Lai, M.; Liang, J.; Chou, L.; Wang, Z. Systematic Study of the Growth of Aligned Arrays of α-Fe_2O_3 and Fe_3O_4 Nanowires by a Vapor-Solid Process. *Adv. Funct. Mater.* **2006**, *16*, 2243–2251.

[19] Li, L.; Yang, Y.; Ding, J.; Xue, J. M. Synthesis of magnetite nanooctahedra and their magnetic field-induced two-/three-dimensional superstructure. *Chem. Mater.* **2010**, *22*, 3183–3191.

[20] Gupta, R. K.; Ghosh, K.; Dong, L.; Kahol, P. K. Structural and magnetic properties of phase controlled iron oxide rods. *Mater. Lett.* **2011**, *65*, 225–228.

[21] Wang, M.; He, L.; Zorba, S.; Yin, Y. Magnetically Actuated Liquid Crystals. *Nano Lett.* **2014**, *14*, 3966–3971.

[22] Milosevic, I.; Jouni, H.; David, C.; Warmont, F.; Bonnin, D.; Motte, L. Facile microwave process in water for the fabrication of magnetic nanorods. *J. Phys. Chem. C* **2011**, *115*, 18999−19004.

[23] Ficai, D.; Ficai, A.; Vasile, B. S.; Ficai, M.; Oprea, O.; Guran, C.; Andronescu, E. Synthesis of rod-like magnetite by using low magnetic field. *Digest J. Nanomater. Biostruct.* **2011**, *6*, 943–951.

[24] Liu, X.; Chen, Y.; Cui, X.; Zeng, M.; Yu, R.; Wang, G. S. Flexible Nanocomposites with Enhanced Microwave Absorption Properties Based on Fe_3O_4/SiO_2 Nanorods and Polyvinylidene Fluoride. *J. Mater. Chem. A* **2015**, *3*, 12197−12204.

[25] Sharma, R. K.; Kumar, H.; Kumar, A. A highly efficient and magnetically retrievable functionalized nano-adsorbent for ultrasonication assisted rapid and selective extraction of Pd^{2+} ions from water samples. *RSC Adv.*, **2015**, *5*, 43371.

[26] Cerbino, R.; Trappe, V. Differential dynamic microscopy: Probing wave vector dependent dynamics with a microscope. *Phys. Rev. Lett.* **2008**, *100*, 188102.

[27] Reufer, M.; Martinez, V. A.; Schurtenberger, P.; Poon, W. C. K. Differential Dynamic Microscopy for Anisotropic Colloidal Dynamics. *Langmuir* **2012**, *28*, 4618−4624.

[28] http://www.fas.harvard.edu/~scidemos/Geophysics/EarthsMagneticField/EarthsMagneticField.html (date accessed: 20/05/2016)

[29] Newton, B. J.; Brakkeb, K. A.; Buzza, D. M. A. Influence of magnetic field on the orientation of anisotropic magnetic particles at liquid interfaces. *Phys. Chem. Chem. Phys.*, **2014**, *16*, 26051−26058.

[30] Davies, G. B.; Kruger, T.; Coveney, P. V.; Harting, J.; Bresme, F. Interface deformations affect the orientation transition of magnetic ellipsoidal particles adsorbed at fluid-fluid interfaces. *Soft Matter* **2014**, *10*, 6742−6748.

[31] Bi, Z. C.; Liao, W. S.; Qi, L. Y. Wettability alteration by CTAB adsorption at surfaces of SiO_2 film or silica gel powder and mimic oil recovery. *Applied Surface Science* **2004**, *221*, 25–31.

[32] Isa, L.; Lucas, F.; Wepf, R.; Reimhult, E. Measuring Single-Nanoparticle Wetting Properties by Freeze-Fracture Shadow-Casting Cryo-Scanning Electron Microscopy. *Nat. Commun.* **2011**, *2*, 438.

[33] Madivala, B.; Vandebril, S.; Fransaer, J.; Vermant, J. Exploiting particle shape in solid stabilized emulsions. *Soft Matter*, **2009**, *5*, 1717–1727.

Results II

Two-Dimensional
Self-Assembled Dipeptides

Chapter 5

Self-Assembly of Dipeptides at the Air—Water Interface

Thin interfacial films of hydrophobic dipeptides (NapFF and BrNapFF) can be created *via* drop-casting the solution onto an aqueous interface in air. In this process, both the dipeptide concentration and subphase pH play important roles. Atomic force microscopy (AFM) reveals that the films consist of fibre-like strands ~40 nm in width and many microns in length. Fourier transform infrared spectroscopy (FTIR) is used to study the secondary structure of these films, which shows the protonation effect and β-sheet configuration of the self-assembled dipeptides. Furthermore, the interfacial film shows elastic properties when compressed in a Langmuir trough. They are able to stabilize large air bubbles (millimetre-size) for several days.

5.1 Introduction

Many dipeptide molecules can form hydrogels in bulk solution as the solvent conditions are changed.[1-3] One means for inducing gelation is in response to a pH change from high to low due to the carboxylic acid becoming protonated and hence the molecule becoming increasingly hydrophobic. This behaviour is fascinating because it is the organized supramolecular strands which are woven together to create the hydrogel. In the light of the bulk behaviour, it is important to determine what would happen if a dipeptide in a high pH solvent was drop-cast on a liquid subphase with low pH.

Previous studies of peptides at interfaces have mainly focused on amphiphilic short sequences created by tethering an alkyl tail to a hydrophilic sequence of peptides via a several glycine linker section. These are found to self-assemble into stable rods in solution with β-sheet formation observed closest to the alkyl chain [4]. In recent years, drop-casting technique has become a widespread simple and low cost method to

fabricate peptide films, which can be formed within a short time. The advantages of drop-casting are highlighted at liquid interfaces, since the other methods, such as screen printing [5], direct growth [6] and electrophoresis [7], are either difficult to be operated or require a long time. Using drop-casting technique, films of a 12 amino acid peptide (LSFDNSGAITIG-NH$_2$, *i.e.* LSFD) were built at the air-water interface. [8, 9]. Pressure-area isotherms of the resulting films exhibited hysteresis unless the surface pressure was kept below 10mN/m. This indicates that an irreversible phenomenon (e.g. formation of 3D structures) occurs at around this surface pressure. AFM studies demonstrated that the interface was (heterogeneously) coated in rod-shaped assemblies which are 0.5–1nm in thickness, 50–100 nm in width and ~1μm in length. The thickness makes these structures inconsistent with fibrils. FTIR revealed the almost exclusive presence of antiparallel *β*-sheets [8]. For much shorter peptide sequences tethered to an organic group, Fmoc-Phe-Phe has been deposited at an air-water interface as one component of a liquid marble [10]. Additionally, the formation of films has been demonstrated via electrochemistry using the molecule Fmoc-Leu-Gly-OH which is known to form a hydrogel in bulk when the solvent pH is lowered below pH 4. Film growth was successfully induced by creating a localized pH drop at an electrode surface by the oxidation of hydroquinone [7].

Our experiments mainly focus on NapFF molecules, which is a small naphthalene dipeptide (Figure 5.1a) and can be easily prepared on gram scale. Previous studies show that it is an excellent material for enabling self-assembly and gelation due to its strong supramolecular interactions arising from aromatic-aromatic interactions and hydrogen bonds among the molecules [11]. NapFF exhibits a critical micelle concentration (cmc) of as low as 0.5 wt %, and has a measured apparent pKa of 6 [12]. It forms a transparent hydrogel in water when the pH of water is lower than the pKa. Before the gelation occurs, some long, worm-like micelles have been observed in the solution (Figure 5.1b). It is believed that the gel formation is caused by the formation of some "bridges" between carboxylates on these worm-like micelles, forming cross-links and hence a three-dimensional network (Figure 5.1c) [13]. Other works also studied the ability of NapFF to convert bioactive molecules into molecular hydrogelators and the properties as well as the applications of these NapFF-derived

hydrogelators [14]. However, the interfacial properties of NapFF hydrogel have not been reported so far.

Other two naphthalene dipeptides, ─BrNapFF and BrNapAV (Figure 5.1a), were also studied in the experiments. BrNapFF has properties similar to NapFF. BrNapAV, however, is more hydrophilic with the apparent air-water partition coefficient (K_{aw}) of 13.2 ± 0.8 (1/au), which is much lower than BrNapFF (602 ± 140) and NapFF (237 ± 20) [12]. Also, NapFF and BrNapFF are known to form worm-like micelles at high pH, whilst BrNapAV forms spherical structures [13].

This chapter reports the self-assembly of these naphthalene dipeptides at the air-water interface *via* drop-casting. The results demonstrate that it becomes a thin interfacial film when brought into contact with a low-pH subphase. AFM and FTIR spectra are used to study the structure of the films. The mechanism for interfacial trapping is also discussed. The interfacial film has the character of an elastic sheet which can be compressed in a Langmuir trough. Large air bubbles can be stabilized by these interfacial films for several days.
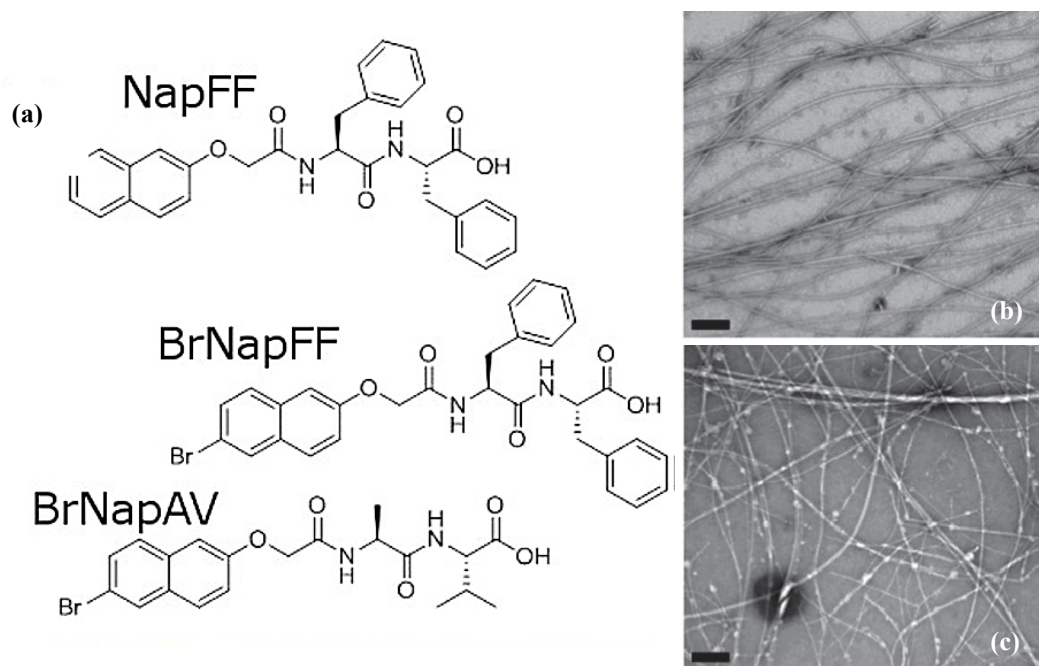

Figure 5.1 *(a) Naphthalene dipeptides molecules used in this study. (b) Transmission electron microscopy (TEM) of the worm-like micelles in NapFF solution at high pH. (c) TEM of the cross-linked network in NapFF hydrogel.*

5.2 Experimental Section

Naphthalene-Dipeptide Interfacial Films

The NapFF, BrNapFF and BrNapAV molecules used in this study were prepared using the procedures described in ref. [2]. These dipeptides were suspended in deionized water with a concentration between 0.05 and 8 mg/mL. NaOH (0.1M, aq) was added into the mixture and the liquid was stirred until a clear solution was formed. The dipeptide/NaOH mol ratio is 1:1.5. To prepare the gel film, 2μL of 5mg/mL NapFF solution was deposited drop-wise at the free surface (~12 cm^2) of an aqueous HCl subphase (pH = 3.0) at room temperature. The formed interfacial film was transferred onto a solid substrate with a syringe pump (model NE-1010, New Era Pump Systems Inc., Farmingdale, NY, USA) at constant rates between 0.25 mm/min and 0.4 mm/min (Figure 5.2a). After isolation, the films were studied using AFM and confocal microscopy.
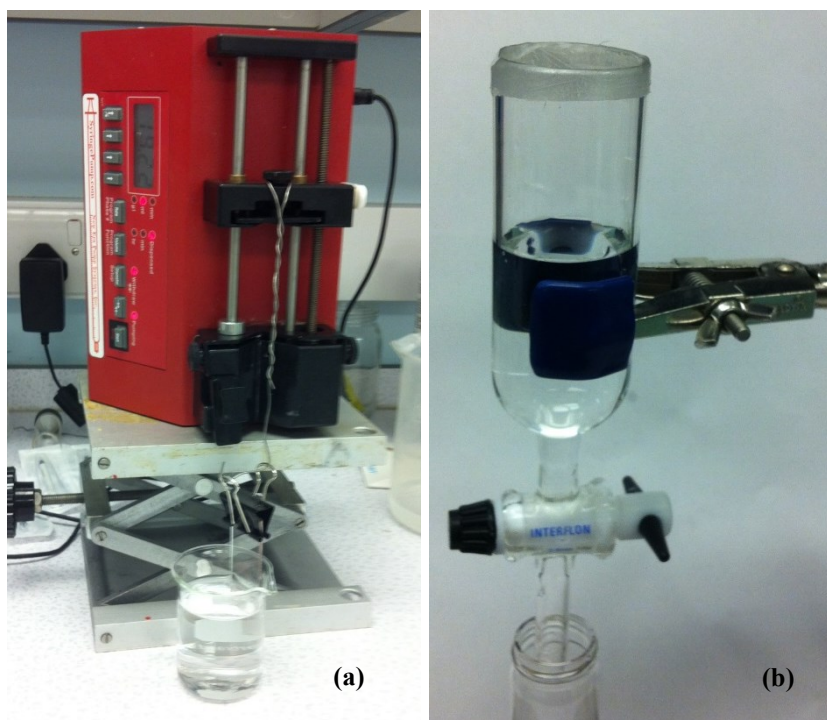
Figure 5.2 (a) Using a syringe pump, the formed interfacial film can be transferred onto a solid substrate by vertical deposition. (b) Lower subphase can be isolated to measure the naphthalene fluorescence and detect the interfacial trapping.

To check the role of pH in the experiments, subphases with different pH values were prepared. The pH of the subphase was measured with an electronic pH meter (Mettler-Toledo AG, 8603 Schwerzenbach, Switzerland), which had been calibrated using standard buffer solutions at pH 4.0 and 7.0. To make the interfacial trapping process more visible, sodium fluorescein (1 wt %) was added in the dipeptide solution before drop-casting. Thioflavin-T fluorescent dye (ThT) was used for confocal microscopy imaging. The ThT concentration was at or below 2 μM to avoid dye self-assembly [15].

Naphthalene Fluorescence

To demonstrate that the dipeptides were indeed interfacially trapped, fluorescence from the naphthalene end group was measured to establish the location of the dipeptide molecules as the subphase pH is modified. To this end, UV-visible absorption spectra of NapFF solution were first recorded with a Cary 1E spectrophotometer. Aqueous HCl (36 mL) solutions with different pH values (2.0–7.0) were added to a separation funnel as subphases. NapFF solutions (2μL, 5mg/mL, without fluorescent dye) were deposited drop-wise at the surface of these subphases. After a relaxation time of 5 min, 10mL of lower subphase was isolated from the bottom of the funnel (Figure 5.2b). The fluorescence spectra from the isolated subphases were recorded on a Varian Cary Eclipse spectrophotometer. In all cases, excitation was measured at a wavelength of 220nm, and a 3mL quartz cell with an optical path length of 10mm was utilized.

Characterization

Bright-Field Microscopy: To demonstrate the role of dipeptide concentration in the formation of interfacial films, bright-field microscopy images from NapFF dispersions with different concentrations were imaged using an Olympus BX-50 microscope equipped with a QICAM 12-bit Mono Fast 1394 camera (QImaging). The dispersions were observed inside a sealed observation chamber with 1 mm height.

Confocal Microscopy: Confocal microscopy was performed using a Zeiss Observer.Z1 inverted microscope in conjunction with a Zeiss LSM 700 scanning system 9 and a 63×1.40 NA oil immersion objective. The ThT fluorescence was excited using the 488nm line from an Ar ion laser.

Atomic Force Microscopy: AFM and Confocal microscopy studies were often carried out on different regions of the same film. A Bruker AFM Multimode/Nanoscope IIIa (Bruker, Santa Barbara, CA, USA) was used to study the morphology of the dipeptide thin films in the tapping-mode. RTESP Bruker cantilevers with a nominal spring constant and resonance frequency of 40 N/m and 300 kHz, respectively, were used to image the samples. In order to minimize the interaction force between the tip and the substrate (but without losing contact), "light tapping" was used by keeping the set-point amplitude ratio $r_{sp} = A_{sp}/A_0$ close to 1 (where A_{sp} and A_0 are the free oscillation amplitude and the reduced scanning set-point amplitude of the cantilever, respectively). Images were processed using the software WSxM (Nanotec Electronica S.L., Madrid, Spain).

FTIR Measurements: The dipeptide film formed at the interface was transferred on a low-emissivity (low-e) glass slide and then freeze-dried (Alpha 2-4 LD Plus, Martin Christ, Germany). Infrared spectra were measured using a Smiths Illuminat IR module coupled to a Renishaw InVia Raman microscope. Each spectrum was scanned between 4000 and 650 cm^{-1} at a resolution of 2 cm^{-1}. The spectrum of the blank low-e slide was used as the background reference. In FTIR measurements, no fluorescent dye was used to form the interfacial films.

Surface Pressure Measurements

The formed hydrogel films were compressed in a Langmuir trough (KSV mini-trough, KSV Instruments Ltd., Finland) with symmetric barriers and a useable area 313×54 mm^2. Surface pressure isotherms (Π-A isotherms) were measured using a Wilhelmy plate (using pre-wetted filter paper to give a wetting angle of 0°) which was aligned perpendicular to the barriers. The air-water interface was considered clean if the surface pressure of the interface changes less than 0.1mN/m when the barriers are moved in.

Dipeptide solution (~6 μL) of the desired composition was then spread drop-wise at the free surface of an aqueous HCl subphase (pH = 3.0) at room temperature and was left for 20 min prior to the start of measurements. The barriers were typically moved together at a rate of 2 mm/min.

Stabilization of Large Air Bubbles

To expand the applicability of the interfacial films, the dipeptide assemblies were used to stabilise large air bubbles. Air was bubbled from a tube (0.5 mm inner diameter) connected to a syringe (glass with metal tip, 100 mL) in an aqueous solvent (generally, pH is 3.0). A NE-1000 syringe pump (New Era Pump Systems Inc. NY) was used to control the formation rate of the bubbles. The blowing speed was ~3 mm/min. As bubbles formed, NapFF in a high pH spreading solvent was dripped onto the interface. Bubbles were stabilized by the films at the interface. A stainless steel needle was used to move the film slightly to check the stability of the bubbles. Afterwards, the bubbles were observed without further treatment.

5.3 Results and Discussion

This section first presents the experimental results of the self-assembled dipeptides at the air-water interface. The determinant factors controlling interfacial trapping process are also discussed. Subsequently, elastic properties of these molecular assemblies are investigated.

5.3.1 The Formation of a Hydrogel Film

As mentioned above, bulk hydrogels forming from the naphthalene dipeptides can be induced by a pH change from high to low due to the carboxylic acid becoming protonated. The aim of the present experiments, however, is to keep the gelation process at a liquid interface and hence form a two dimensional hydrogel film. To this end, low pH aqueous HCl was used as the subphase (pH changes from 2.0 to 5.0). NapFF solution containing sodium fluorescein (1 wt %) was deposited drop-wise at the interface of pH-adjusted subphases. The results are shown in Figure 5.3. Clearly at pH 5.2 and 3.8 substantial quantities of the yellow dispersion are seen to penetrate into the sub-phase; by contrast, for pH 3.2 and 2.0 the dyed dispersion remained at the interface, forming a film of millimetre diameter. Since sodium fluorescein itself cannot be trapped by the interface even at a low pH (Figure 5.3b), it indicates that these dipeptides molecules can stay at the surface when the subphase pH is low.
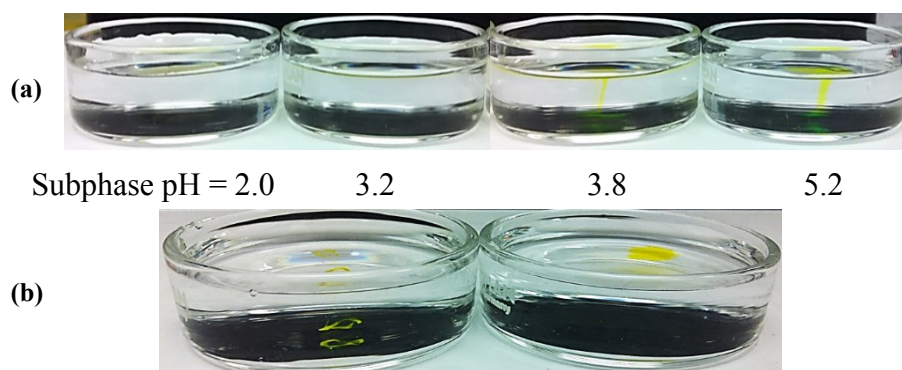
Figure 5.3 *(a) A dispersion of NapFF dipeptide is deposited on the interface of pH adjusted water. The dipeptide is dyed with sodium fluorescein (1 wt %) making it yellow. At low subphase pH the dipeptide and dye are trapped at the interface; as the subphase pH is raised the yellow deposit can be seen to sink through the interface. (b) Demonstrating the co-localization of sodium fluorescein and NapFF. The subphase has pH 2.0; a 1.0 wt% solution of sodium fluorescein was drop cast into the left hand dish, a combined dispersion of NapFF and sodium fluorescein (also 1.0 wt%) were drop cast onto the interface of the right hand dish.*

To further demonstrate that the molecules are indeed trapped by the interface, the fluorescent signal from the naphthalene end group was measured to establish the location of the dipeptides as the subphase pH was modified (see Experimental Section and Figure 5.2b). Figure 5.4a shows the measurements carried out without any fluorescent dye, instead relying on fluorescence from any NapFF molecules in the subphase. Similar to other naphthalene-dipeptide systems, NapFF shows an absorption band at 220nm. Excitation at 220nm results in an emission peak centred at 350nm (see inset to Figure 5.4a). For a subphase pH < 3.5 there is very little fluorescence from naphthalene groups in the subphase, which means almost all of the molecules remained at the interface. Above this pH the fluorescence signal grew substantially; eventually it saturates (at pH 4.2) and then decreases a little. The latter signal decrease might be caused by the lower quantum yield of dipeptide molecules compared with their self-assembly structures. Between pH 3.8 and 4.2, the molecules can first self-assemble at the interface and then fall into the subphase, which cannot occur at higher pH. Evidently it is the pH of the subphase which controls the trapping of dipeptide molecules at the interface.

However, we found that the pH of the subphase might not be the only factor; a 2mg/mL NapFF solution cannot be drop-cast at the interface, even when the pH of the subphase
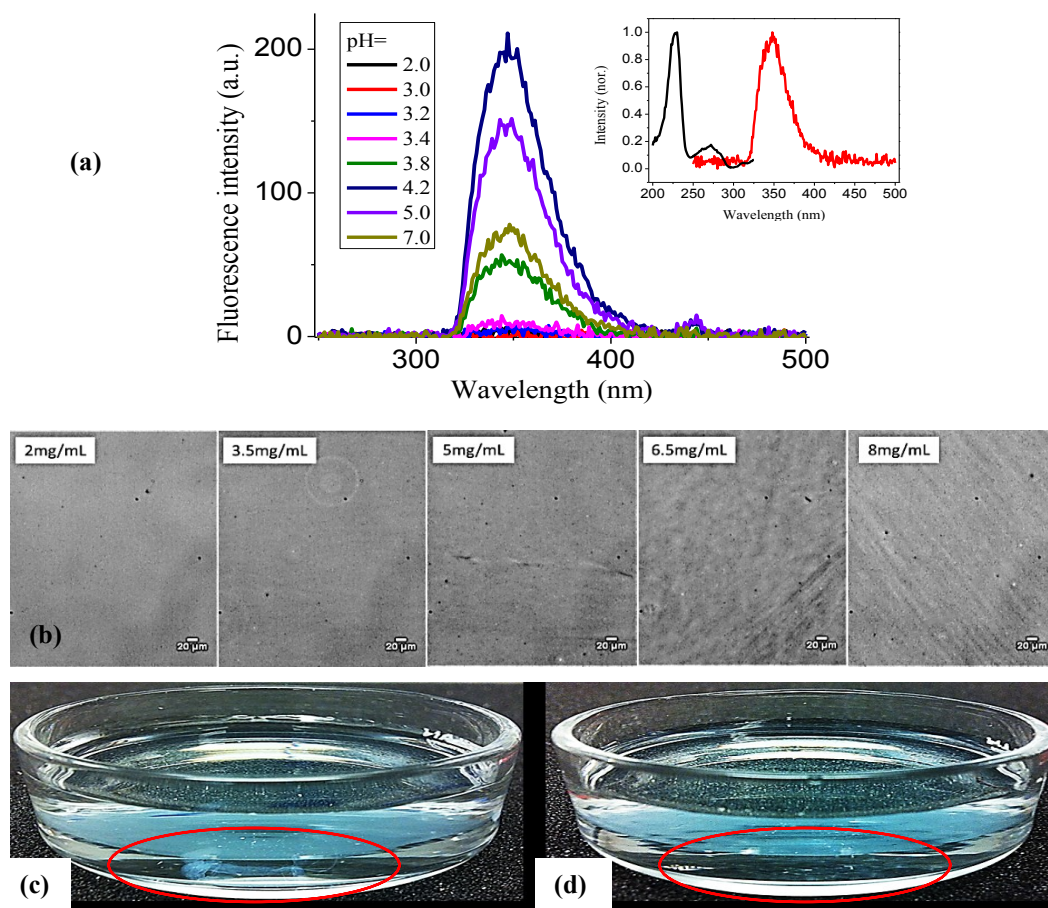
Figure 5.4 *(a) Napthalene fluorescence signal from dipeptide in the subphase. Following excitation at 220 nm, the intensity of the observed emission signal was a strong function of the subphase pH. Inset: excitation (black) and emission (red, excited at 220nm) spectra of NapFF dipeptide. (b) Bright-field microscopy images of NapFF dispersions (pH=10) as a function of concentration. Above 3.5 mg/mL shear-aligned fibres are observed. (c, d) BrNapAV solution (5mg/ml) was prepared as described in the text. At room temperature, 2μL solution was dropped onto the surface of an aqueous HCl subphase. The pH of the subphase used here was 2.5. (c) The dipeptide has fallen through the interface and remains visible as a cloudy region (marked red) for a short time after the falling. (d) Five minutes later, the dipeptide is dispersed in the subphase and is no longer visible.*

is 2.0; i.e. the mechanism for interfacial trapping involves exceeding a threshold concentration of dipeptide. From the bright-field microscopy images (Figure 5.4b), at the pH of the spreading solvent, large, fibre-like, assemblies of dipeptide molecules can be seen when the dipeptide concentration is larger than 3.5 mg/mL. By contrast,

at lower NapFF concentration there is some indication of the existence of small spherical assemblies. These two regimes meet at the concentration threshold at which the interfacial film begins to be observed. [1]NMR measurements also suggest a transition of the dipeptide molecular structures from small micelles to large fibre-like structures at the same concentration [16]. Therefore, these fibre-like structures that exist in the spreading solution should be important for the trapping process. Investigations with BrNapFF and BrNapAV dipeptides support this issue. BrNapFF was found to form interfacial films following a similar protocol to that employed with NapFF. By contrast, BrNapAV cannot be trapped by the interface for the range of concentrations and subphase pH values explored in the experiments. Instead of being trapped by the interface, BrNapAV fell into the subphase as a cloudy component (Figure 5.4c). After about five minutes, the BrNapAV dispersion ceases to be visible (Figure 5.4d). This difference in behaviour can be linked to the micellar structures formed at high pH and concentration. Both NapFF and BrNapFF are known to form fibre-like micelles as shown in Figure 5.4b, whilst BrNapAV forms spherical structures.

5.3.2 Structure Characterization

To study the structure of the film at the interface, an interfacial film was created by drop-casting 2 μL 5 mg/mL NapFF dispersions onto a subphase at pH 2.0, and then transferred onto a solid substrate with a syringe pump as shown in Figure 5.2a. The substrate used here is a cover glass slide (22mm × 50mm) with a mica disk (10mm diameter) attached (Figure 5.5a). The cover slide was used for confocal microscopy, while the mica disk was for AFM investigation.

Figure 5.5b is a confocal image of the dipeptides on the cover slide. A film with hundreds of microns in length can be observed. The film consisted of some fibre-like structures, which exhibit strong directionality. To better visualize these fibre-like structures, ThT dye was used in the dipeptide dispersions for drop-casting. Different from sodium fluorescein, ThT can selectively bind to fibres and enhance their fluorescence emission. Figure 5.5c shows the resulting film of dipeptides after labelling with ThT. A fibre-like network can be observed by the enhanced fluorescence, demonstrating that the dye molecule has been immobilized. This is commonly associated with the dyed species forming β-sheets. A similar enhancement of the ThT
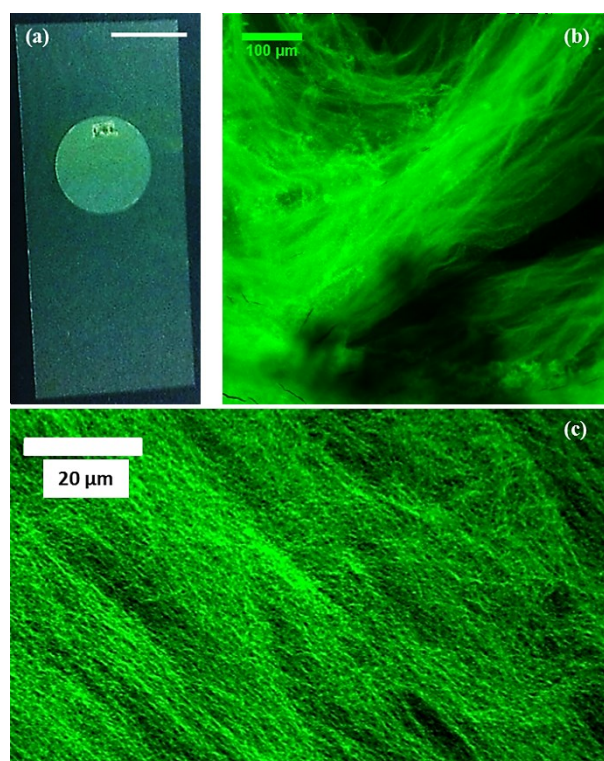
Figure 5.5 *(a) The interfacial trapped dipeptides can be transferred onto a solid substrate for both confocal microscopy and AFM investigations. The scale bar is 1 mm. (b) Confocal microscopy of NapFF dipeptide with sodium fluorescein showing the film on the scale of hundreds microns. (c) A micrograph of a film prepared from ThT labelled NapFF dipeptides.*

fluorescence has previously been observed for naphthalene-dipeptides in bulk hydrogels [2], which suggests that the interfacial film could be a hydrogel film of self-assembled dipeptides.

Previous studies demonstrate that a low-molecular-weight gelators (LMWG) like dipeptides can exhibit strong and directional intermolecular interactions that promote assembly into one dimensional strands [17]. The directional interactions can be hydrogen bonding, π stacking, and so forth. Here, AFM was used to study these fibre-like networks in more detail. As it is shown in Figure 5.6, the network consists of nanoscale-width strands of material which can be many micrometers in length. Partial monolayer films (Fig. 5.6a) were used to measure the dimensions of the strands. Averaged over more than 60 strands it was found that the in-plane width of a single fibre is 35–40 nm. The height of it, however, is less than 30 nm, which indicates that the cross-section of a single fibre is an oval. These one dimensional strands support

the issue that the dipeptide molecules self-assemble at the interface. Some irregularly shaped aggregations (~30nm) can also be observed from Figure 5.6a. They could be the early stage of the self-assembly. After further assembling and cross-linking with each other, the fibres can form an ordered fibrous network (Figure 5.6b). The thickness of the network increases with the concentration of the dipeptides (Figure 5.6c).
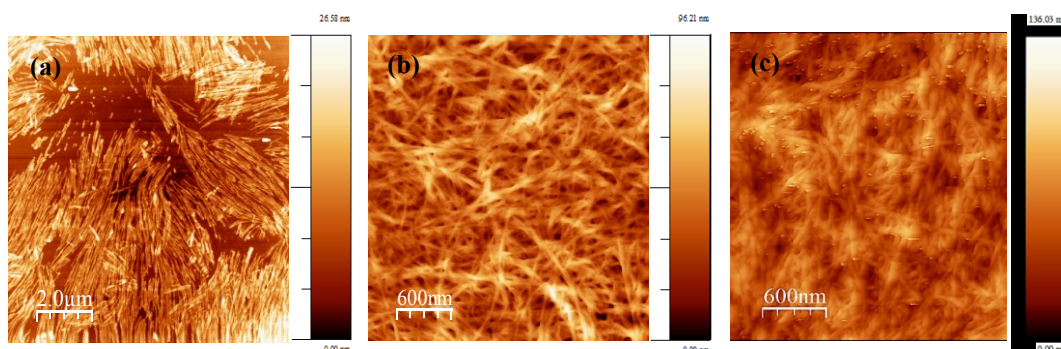
Figure 5.6 *(a) Submonolayer region, prepared from a concentration 5 mg/mL NapFF dispersion, shows that the strand width is ~40 nm and height is ~20 nm. (b) Concentration 5 mg/mL gives a film thickness of ~90 nm. (c) Concentration 8 mg/mL gives a film thickness of ~140 nm.*
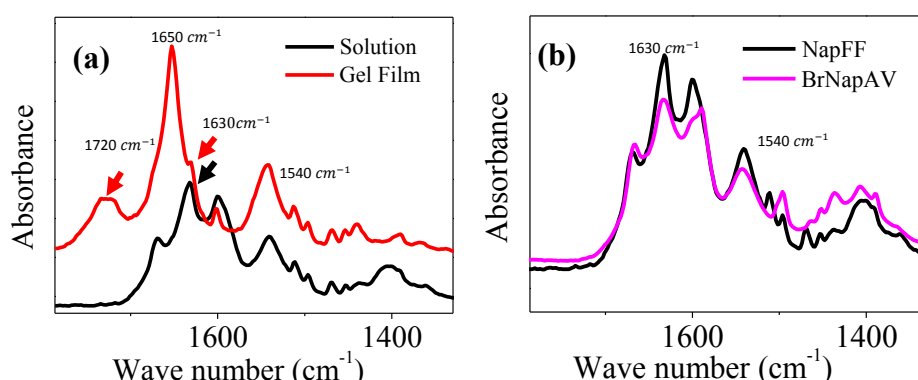
Figure 5.7 *(a) Arrangement of molecules from FTIR measurements. Black line is NapFF in solution showing the existence of β-sheet organization. The lack of peak above 1700cm^{-1} indicates that the carboxylic acid is not protonated at high pH. Red line is the same sample when formed as a film. The β-sheet organization remains together with a large new peak at 1650cm^{-1} which is likely to be due to a random coil structure. On contact with the low pH subphase the carboxylate has gained a proton. (b) Black line is NapFF in solution and magenta line is BrNapAV in solution. Here peaks are observed corresponding to β-sheet organization, however, BrNapAV does not form a film when deposited on a low pH subphase.*

Although ThT enhanced fluorescence indicates the β-sheet formation in these strands, their secondary structure still needs to be investigated. FTIR spectroscopy can provide information about the secondary structure content of self-assembled dipeptides. It works by shining infrared radiation on a sample and seeing which wavelengths of radiation in the infrared region of the spectrum are absorbed by the sample. Each compound has a characteristic set of absorption bands in its infrared spectrum. Fig. 5.7a shows the signal from NapFF before (black) and after (red) it has formed an interfacial film. The samples were freeze-dried prior to characterization. Both the original solution (at high pH) and the interfacial film exhibit an absorption peak at around 1540 cm^{-1}, which is indicative of β-sheet formation. The original solution has another peak at 1630 cm^{-1} corresponding to β-sheet formation but no peak at 1720 cm^{-1}, indicating that the carboxylic acid group is deprotonated in solution. Peaks appear at both 1720 cm^{-1} and at 1650 cm^{-1} once a film has formed. The former relates to the carboxylic acid group becoming protonated (and hence to the dipeptide becoming more hydrophobic) while the latter may well be related to the formation of a random coil structure [2]. This spectroscopic investigation suggests that β-sheet formation has already occurred in the high pH spreading solvent. From the microscopy observations of the solvent (as shown in Figure 5.4b), these β-sheet structures should be related to the large, fibre-like assemblies when the dipeptide concentration is high (> 3.5 mg/mL). Organized strands gel on impact with the interface, rather than isolated molecules. Figure 5.7b shows a comparison between the FTIR spectra for the solution of NapFF and that for a solution of BrNapAV, which does not form an interfacial film under any of the conditions probed here. Again, β-sheet organization is observed in the dispersion: hence this molecular order alone is not a predictor of interfacial assembly. This observed organization is, perhaps, unsurprising given that spherical structures are known to be formed at high pH by BrNapAV [13].

5.3.3 Elastic Properties of the Hydrogel Film

It has been shown that hydrophobic dipeptide molecules can form thin films at the interface of a low pH subphase. To expand the realm of applicability of this observation, an experiment for stabilizing large air bubbles with these molecular assemblies was carried out in the lab. Air was bubbled through a low pH solvent when

NapFF in a high pH spreading solvent was dripped onto the interface (see Experimental Section). The air bubbles can be stabilized at the interface; they did not coalesce with the hydrogel film or with other bubbles. By stirring the films with a stainless steel needle, the bubbles can be covered by the films, and can even move with the stainless steel needle (Figure 5.8). During a period of one week's observation, all the bubbles are very stable and no shrink has been observed.

From the AFM and confocal microscopy results (Figure 5.5 and 5.6), it is suggested that the hydrogel film cannot provide a complete coverage of the air interface. The long term stability of these air bubbles should be a consequence of the elastic properties of the interfacial film. Previous studies report that most hydrogels are elastic in nature because of the presence of a memorized reference configuration to which they return even after being deformed for a long time. This is important for the applications of hydrogels in biology because the fate of the cells is sensitive to the tissue-level elasticity [18]. For bulk hydrogels, rheology methods are widely used to study their elastic properties. For example, Fmoc-peptide hydrogel shows an initial elastic region at sufficiently high compression rates [1]; its storage modulus (G') was measured to be approximately an order of magnitude larger than the loss modulus (G'') [19]. The elastic properties of naphthalene-dipeptide hydrogels were also studied in previous work [2].
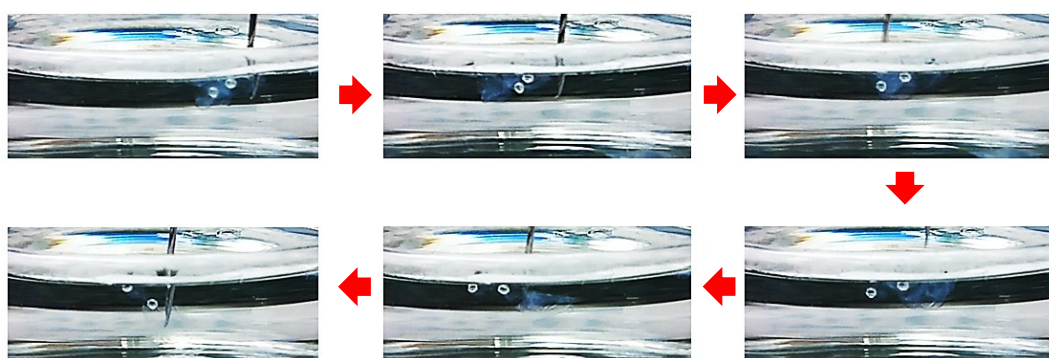
Figure 5.8 *Dipeptide coated interfaces on a macroscopic scale. Millimetre-size air bubbles were formed in a low pH solvent; dipeptide was deposited on the newly formed bubble. The coated bubbles were stable for several days.*
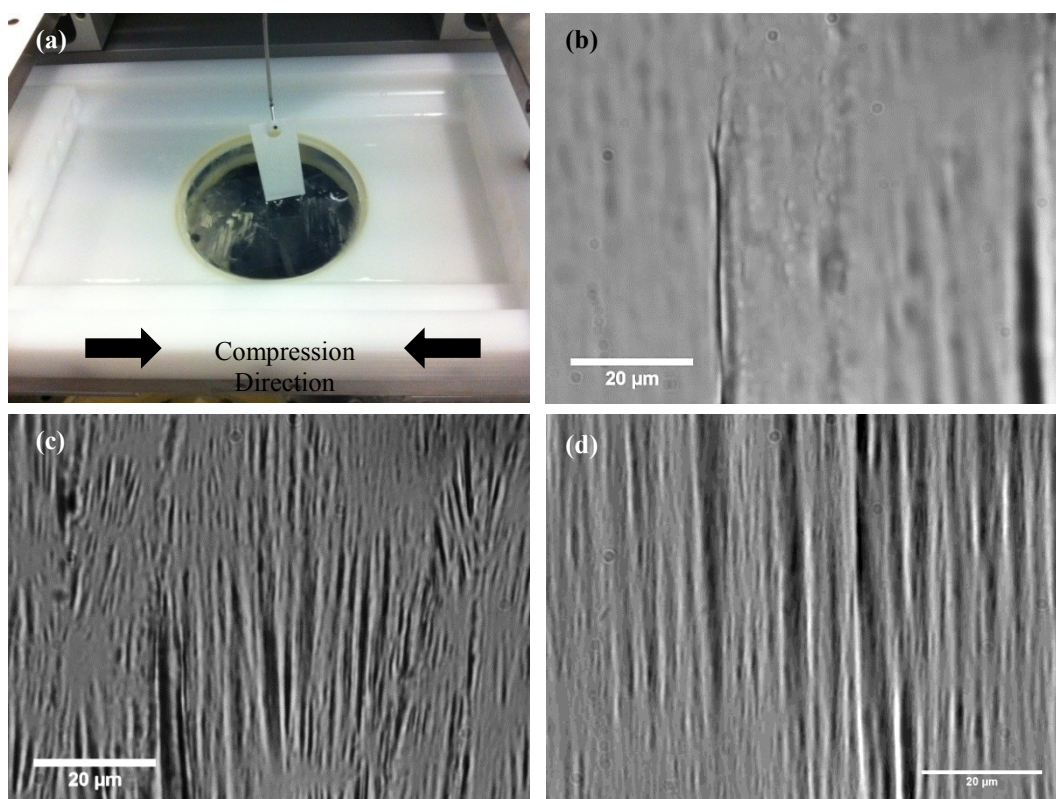
Figure 5.9 *(a) The Langmuir trough and symmetric barriers used in the compression experiment. Arrows indicate the direction of compression. (b) The border junction between two films. (c, d) Wrinkles formed in the coated interface.*

To confirm that the interfacial film has the character of an elastic sheet, compression experiments have been carried out in a Langmuir trough (Figure 5.9a). Several interfacial films were created at the same interface by drop-casting. These films were then compressed by two symmetric barriers at a rate of 2 mm/min. The observation shown in Figure 5.9b could be the border junction between two films. Under the compression, instead of the molecules detaching from the surface or forming a multilayer, the interface responds by developing a ripple with a period of hundreds of microns (Figure 5.9c and d). Ripples are parallel to the trough barriers, i.e. perpendicular to the compression direction. This behaviour is a typical response for an elastic sheet and is also observed for some surfactants [20], hydrophobin proteins [21] and colloidal particles [22] at air-water interfaces.

Cycles of compression and expansion of the hydrogel films can be used to demonstrate the underlying "stickyness" of the pre-existing strands. Surface pressure (SP) of the film was first measured in a Langmuir trough (Figure 5.10a). The isotherm shows that
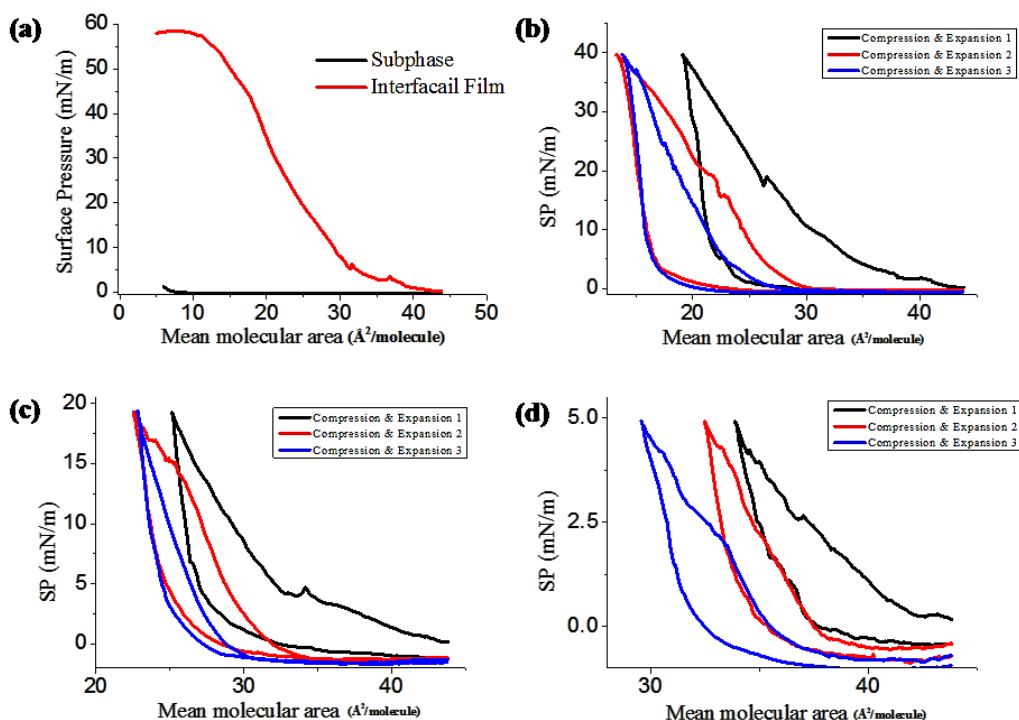
Figure 5.10 *(a) Surface pressure isotherm of the interfacial film (red) and a clean subphase (black). (b, c, d) Graphs showing the surface pressure under compression. The maximum surface pressure are 40 mN/m, 20 mN/m and 5mN/m, respectively. Hysteresis is observed between compression and expansion and the cycles (carried out at 10mm/min) are not fully reversible. If the maximum surface pressure is kept low (at 5mN/m) then the differences between cycles decrease.*

the collapse pressure of the film is about 56 mN/m, which is higher than monolayers of colloidal particles or proteins [23]. Compression followed by expansion results in hysteresis in the measured values of the surface pressure. Moreover, there is a lack of repeatability between successive cycles when the setting maximum surface pressure is high (Figure 5.10b and c). Both phenomena can be caused by the irreversible bonds between films under compression (as shown in Figure 5.9b), and can be minimized by reducing the maximum surface pressure used in the study (Figure 5.10d). The hysteresis and the lack of repeatability are due to increased hydrophobic association between the strands induced by contacts during the compression process. Such behaviour can also be noticed in a bulk gel, which cannot recover its original form if deformed beyond the elastic limit.

5.4 Conclusions

This chapter reports that hydrophobic dipeptide molecules (NapFF and BrNapFF) can become trapped at an air-water interface. The interfacial layer is created via dispersing the molecules in a high pH spreading solvent and then depositing it drop-wise on to a low pH subphase; it has the appearance of woven strands which exhibits beta-sheet order. The interfacial film only forms if the dipeptide concentration is high enough for the fibre-like strands to have assembled already in the spreading solvent. Likewise, the subphase pH must be well below the pKa of the molecule to give rapid protonation. When these two conditions are met the drop-casting procedure succeeds for naphthalene-dipeptides with high air-water partition coefficients.

The interfacial hydrogel film exhibits a periodic wrinkle under compression and is able to stabilize large air bubbles for days at least. These features strongly suggest that it is an elastic sheet. Using these molecules, it has been able to coat a bulk liquid with a supramolecular woven elastic sheet via drop-casting.

Hydrogel films are extremely versatile materials in terms of possible designs and drug delivery systems. They offer virtually endless opportunities for the development of new, exciting active materials and functional devices on their base. The experimental results in this chapter suggest that the hydrogel film offers an excellent approach to control the stability of interfaces in foams and emulsions more generally. This application will be discussed in next chapter.

Acknowledgment

References:

[1] Adams, D. J.; Mullen, L. M.; Berta, M.; Chen, L.; Frith, W. F. Relationship between molecular structure, gelation behaviour and gel properties of Fmoc-dipeptides. *Soft Matter* **2010**, *6*, 1971–1980.

[2] Chen, L.; Morris, K.; Laybourn, A.; Elias, D.; Hicks, M. R.; Rodger, A.; Serpell, L. C.; Adams, D. J. Self-Assembly Mechanism for a Naphthalene-Dipeptide Leading to Hydrogelation. *Langmuir* **2010**, *26*, 5232–5242.

[3] Ryan, D. M.; Nilsson, B. L. Self-assembled amino acids and dipeptides as noncovalent hydrogels for tissue engineering. *Polym. Chem.* **2012**, *3*, 18−33.

[4] Ulijn, R. V.; Smith, A. M. Designing peptide based nanomaterials. *Chem. Soc. ReV.* **2008**, *37*, 664–675.

[5] Zuo, S.; Teng, Y.; Yuan, H.; Lan, M. Direct electrochemistry of glucose oxidase on screen-printed electrodes through one-step enzyme immobilization process with silica sol–gel/polyvinyl alcohol hybrid film. *Sens. Actuators, B* **2008**, *133*, 555−560.

[6] Aizenberg, J.; Muller, D. A.; Grazul, J. L.; Hamann, D. R. Direct Fabrication of Large Micropatterned Single Crystals. *Science* **2003**, *299*, 1205−1208.

[7] Johnson, E. K.; Adams, D. J.; Cameron, P. J. The directed self-assembly of dipeptides to form ultrathin hydrogel membranes. *J. Am. Chem. Soc.* **2010**, *132*, 5130−5136.

[8] Lepere, M.; Chevallard, C.; Hernandez, J.-F.; Mitraki, A.; Guenoun, P. Multiscale surface self-assembly of an amyloid-like peptide. *Langmuir* **2007**, *23*, 8150–8155.

[9] Lepere, M.; Chevallard, C.; Brezesinski, G.; Goldmann, M.; Guenoun, P. Crystalline Amyloid Structures at Interfaces. *Angew. Chem., Int. Ed.* **2009**, *48*, 5005–5009.

[10] Braun, H.-G.; Cardoso, A. Z. Self-assembly of Fmoc-diphenylalanine inside liquid marbles. *Colloids Surf., B* **2012**, *97*, 43−50.

[11] Li, J. Y.; Gao, Y.; Kuang, Y.; Shi, J. F.; Du, X. W.; Zhou, J.; Wang, H. M.; Yang, Z. M.; Xu, B. Dephosphorylation of D-Peptide Derivatives to Form Biofunctional, Supramolecular Nano-fibers/Hydrogels and Their Potential Applications for Intracellular Imaging and Intratumoral Chemotherapy. *J. Am. Chem. Soc.* **2013**, *135*, 9907–9914.

[12] Chen, L.; Revel, S.; Morris, K.; Serpell, L. C.; Adams, D. J. Effect of molecular structure on the properties of naphthalene-dipeptide hydrogelators. *Langmuir* **2010**, *26*, 13466−13471.

[13] Chen, L.; Pont, G.; Morris, K.; Lotze, G.; Squires, A.; Serpell, L. C.; Adams, D. J. Salt-induced hydrogelation of functionalised-dipeptides at high pH. *Chem. Commun.* **2011**, *47*, 12071−12073.

[14] Zhang, Y.; Kuang, Y.; Gao, Y. A.; Xu, B. Versatile Small-Molecule Motifs for Self-Assembly in Water and the Formation of Biofunctional Supramolecular Hydrogels. *Langmuir* **2011**, *27*, 529−537.

[15] Khurana, R.; Coleman, C.; Ionescu-Zanetti, C.; Carter, S. A.; Krishna, V.; Grover, R. K.; Roy, R.; Singh, S. Mechanism of thioflavin T binding to amyloid fibril. *J. Struct. Biol.* **2005**, *151*, 229-238.

[16] Li, T.; Kalloudis, M.; Cardoso, A. Z.; Adams, D. J.; Clegg, P. S. Drop-Casting Hydrogels at a Liquid Interface: The Case of Hydrophobic Dipeptides. *Langmuir* **2014**, *30*, 13854–13860.

[17] Dastidar, P. Supramolecular gelling agents: can they be designed? *Chem. Soc. Rev.* **2008**, *37*, 2699–2715.

[18] Discher, D. E.; Janmey, P.; Wang, Y.-L. Tissue cells feel and respond to the stiffness of their substrate. *Science* **2005**, *310 (5751)*, 1139–1143.

[19] Smith, A. M.; Williams, R. J.; Tang, C.; Coppo, P.; Collins, R. F.; Turner, M. L.; Saiani, A.; Ulijn, R. V. Fmoc-Diphenylalanine Self Assembles to a Hydrogel via a Novel Architecture Based on π–π Interlocked β-Sheets. *Adv. Mater.* **2008**, *20*, 37–41.

[20] Milner, S. T.; Joanny, J. F.; Pincus, P. Buckling of Langmuir monolayers. *Europhys. Lett.* **1989**, *9(5)*, 495–500.

[21] Basheva, E. S.; Kralchevsky, P. A.; Christov, N. C.; Danov, K. D.; Stoyanov, S. D.; Blijdenstein, T. B. J.; Kim, H.-J.; Pelan, E. G.; Lips, A. Unique properties of bubbles and foam films stabilized by HFBII hydrophobin. *Langmuir* **2011**, *27*, 2382–2392.

[22] Aveyard, R.; Clint, J. H.; Nees, D.; Paunov, V. N. Compression and structure of monolayers of charged latex particles at air/water and octane/water interfaces. *Langmuir* **2000**, *16*, 1969−1979.

[23] Bagkar,N.; Ganguly, R.; Choudury, S.; Hassan, P. A.; Sawant, S.; Yakhmi, J. V. J. Synthesis of surfactant encapsulated nickel hexacyanoferrate nanoparticles and deposition of their Langmuir–Blodgett film. *Mater. Chem.* **2004**, *14*, 1430−1436.

Chapter 6

Long-Lived Foams Stabilized by Dipeptide Hydrogel

A wet foam system with long-term stability has been created by dipeptide hydrogel. Metal ions were used to induce the gelation process instead of a pH change. Dipeptide molecules self-assemble into fibre-like structures both at air-water interfaces and in the continuous phase. The former relates to the interfacial films stabilizing the air bubbles while the latter forms a bulk gel sustaining the entire foam system. Cryogenic scanning electron microscopy (cryo-SEM) and Raman spectra reveal that the fibres are 200nm wide and form β–sheet structures. Drainage occurs when the density of fibre-like structures in the continuous phase is reduced, which relates to the concentration of dipeptides and metal ions. Moreover, hydrogel with high storage modulus G' can stop the coarsening process between the air bubbles and thus dramatically improve the stability of the foam.

6.1 Introduction

In chapter 5, it has been found that hydrophobic dipeptide molecules (NapFF and BrNapFF) can self-assemble into an interfacial film at the air-water interface, which can be used to stabilize some large air bubbles for days at least. These features strongly suggest that the self-assembly of hydrophobic dipeptide molecules would be an excellent candidate for foams and emulsion stabilization. Ulijin and coworkers have stabilized oil-in-water and water-in-oil emulsions using dipeptide amphiphiles [1]. By had shaking of an organic/aqueous system, the dipeptides can self-assemble into nanofibrous networks to stabilize the droplets. Superior long-term stability of the emulsions has been observed [1]. However, no studies have been carried out on foams stabilized by dipeptide molecules so far.

To stabilize a foam, dipeptides either need to be gelled in the continuous phase between the air bubbles or they need to form a rigid layer on the bubble surfaces or both. Furthermore, it is required that an initially gelled, continuous phase can be melted to allow foaming and regelation to suppress drainage or coalescence [2].

Generally, gelation process can be induced by changing the solvent conditions with pH or temperature. However, for foam studies, metal ions are preferable. First of all, doubly charged metal ions efficiently promote the gelation of dipeptide fibres giving the high storage moduli (G') of the gels which have been observed using rheological measurements [3]. Second, using metal ions avoids the addition of other liquid (*e.g.*, aqueous HCl) and increases the normalized foam volume. (This is also true for gelation using a change in temperature. [4]) Moreover, a hydrogel induced by metal ions can be prepared at a broad range of pHs; in particular, this expands the range of dipeptide-based gelators that can be used at physiological pH. It is supposed that metal ions (*e.g.* Ca^{2+}) act as cross-links by bridging between adjacent gelators to form gels. This gelation mechanism is similar to the "egg box" model, which has been commonly accepted for the calcium alginate/guluronate structure [5, 6].

This chapter demonstrates a wet foam system stabilized by naphthalene dipeptides hydrogel. Here, different metal ions are used to induce the gelation process, which occurs both at air-water interfaces and in the continuous phase. The foam stability is related to the concentration of dipeptide molecules. Curiously, not only does the dipeptide gel stabilize the foam, the air bubbles also suppress the phase separation of a hydrogel phase and a water-rich phase. Raman spectra were used to study the secondary structure of these self-assembled molecules, while cryogenic scanning electron microscopy (cryo-SEM) revealed the fibre-like networks which stabilize the foam. The foam is easy to prepare and has a long-term stability (more than two weeks). The mechanism for drainage phenomena in this system is discussed. Furthermore, there is a dramatic effect of different metal ions on gelation and the resulting foam properties. The reason for this relates to the storage modulus G' of different hydrogels, *i.e.*, a hydrogel with higher G' can slow down the coarsening and coalescence of the bubbles.

6.2 Experimental Section

Wet Foam System

Dipeptide Foaming Solution: At room temperature, NapFF molecules were dispersed in 2mL deionized water at concentration of 8mg/mL. A clear foaming solution can be formed by adding 0.3mL NaOH (0.1M aq) upon continuous stirring. This caused a high pH environment for the molecules, and made them aggregate into worm-like micelles in the solution [7]. To study the effect of dipeptide concentration, foaming solutions with 2mg/mL and 5mg/mL NapFF molecules were also prepared. Vials with 20mm diameter and 7.5cm height are used for all the solutions.

Gelation and Foam Preparation: To form a three-dimensional hydrogel, 0.08g $CaCl_2 \cdot 2H_2O$ was added into the foaming solution. Gelation has been induced by the formation of Ca^{2+} bridges between carboxylates on different worm-like micelles present in the solution, which can form cross-links and hence a bulk gel. $CaCl_2 \cdot 2H_2O$ has a powder form which allows the gelation to proceed to completion before the foam preparation. Different amount of $CaCl_2 \cdot 2H_2O$, and another two salts (~0.065g MgSO4, ~0.08g KCl) were also used to induce the gelation of the foaming solution.

Foams were prepared by using a Polytron homogeniser (PT-MR 3100) with a 1cm-diameter head operating at 7000 rpm for one minute. Immediately after preparation, the height of foam is recorded and then measured as a function of time. Before further processing, all samples were stored at room temperature and sealed to prevent liquid evaporation.

Characterization

Cryo-SEM: Cryogenic scanning electron microscopy (cryo-SEM) was used to visualize the fibrous structures of the self-assembled dipeptides, *i.e.*, the networks around the air bubbles and in the continuous phase. The sample was deposited on a sample holder, frozen in slush nitrogen and transferred to a Gatan Alto 2500 cryostage. Subsequently, the frozen specimen was fractured at -170 ºC, etched for 5 minutes at -90ºC and coated with Au/Pd for 2 minutes. The sample was then transferred to a

Hitachi S-4700 scanning electron microscope and was observed using a secondary electrons detector operating at 5.0 kV, at a temperature of -170 ºC.

Confocal microscopy: Confocal microscopy was used to observe the foam samples. A small foam sample was placed on a microscopy slide. The observation was carried out before the sample starts to dry in the air. Thioflavin T (ThT) was used to label self-assembled dipeptide structures. The ThT concentration used was at or below 2μM to avoid dye self-assembly. Confocal microscopy was performed using a Zeiss Observer.Z1 inverted microscope in conjunction with a Zeiss LSM 700 scanning system 9. A 63× 1.40 NA oil-immersion objective was used to study the fibrous structures in the continuous phase. The ThT fluorescence was excited using the 488nm line from an Ar-ion laser.

Raman measurements: The Raman measurements, in right angle scattering geometry, were performed with a Coderg T800 triple-grating spectrometer using 514.5nm excitation (Argon-ion laser). Single spectrum acquisition was between 700 and 2000 cm^{-1} with spectral resolution of 3 cm^{-1} and 1 s integration time. For the measurements, a small amount of foam was deposited on a stainless steel slide and allowed to dry. Prior to beam exposure the sample was cooled to 14°C in a flow of dry nitrogen gas to compensate for laser heating. The laser power was ~150 mw partially focussed to ~1 mm diameter. To minimize the interference from the fluorescence signal, the sample was exposed to the beam for 20 minutes prior to the start of data collection which reduced the fluorescence background to a more steady value. The raw data collected for ten spectra were averaged to obtain the final representation.

Bright-field microscopy: A film of foam stability was taken by an Olympus BX-50 microscopy (5× objective, NA = 0.15) equipped with a QICAM 12-bit Mono Fast 1394 camera (QImaging). Foams were transferred by a pipette and observed inside a sealed observation chamber (4.5mm height).

Naphthalene Fluorescence: The fluorescence spectra from the liquid phase (8 mg/mL NapFF foaming solution with 0.08g $CaCl_2 \cdot 2H_2O$) were recorded on a Varian Cary Eclipse spectrophotometer. A 3mL quartz cell with an optical path length of 10mm

was utilized. Excitation was made at 220 nm. The original liquid phase was diluted by deionized water.

Rheological properties: The rheological experiments were performed on a TA Instruments AR 2000 rheometer using a plate-plate geometry (40 mm sand blasted plate, gap 200 μm). Hydrogels and foams of NapFF (8 mg/mL, ~ 4 mL) induced by different salts were prepared and left for 24 hours at room temperature before the measurement. All the samples were carefully scooped onto the rheometer plate. The shear moduli (G' and G'') were measured over a frequency range of 1–100 rad/s at a strain of 0.5%. All the measurements were carried out at 20 ºC.

6.3 Results and Discussion

A wet foam system was created by aerating the dipeptide hydrogel. Its stability relates to the dipeptides concentration and the hydrogels' storage modulus. At the outset of this section, the fibre-like structures in this foam system are studied by cryo-SEM, confocal microscopy and Raman measurements. Subsequently, the roles of concentration and other parameters on the foam stability are discussed.

6.3.1 A Long-Lived Wet Foam System

The foam-ability of NapFF solution (ungelled) was first investigated. A high concentration (8mg/mL) was used since some fibre-like micelles exist in the solution, which could improve its foam-ability. A foam was generated by aerating with a Polytron homogeniser. However, it vanished within 2 hours (Figure 6.1a, b), which means the ungelled dipeptide solution has a low foam-stability. By contrast, bulk hydrogel of NapFF with metal cations displays much higher foam-ability. Figure 6.1c illustrates a foam prepared by adding 0.08g $CaCl_2 \cdot 2H_2O$ into an 8mg/mL NapFF foaming solution (2 mL) and then aerating with a homogeniser. A small amount of liquid phase (~2.5 mm in height) can be seen at the bottom of the vial. As defined in the beginning of section 2.4, this foam (two days after preparation) has a liquid volume fraction ε ~ 0.47, which can be considered as a wet foam. Furthermore, the foam can be stabilized for more than two weeks without obvious drainage, bubble coalescence or coarsening (Figure 6.1d).
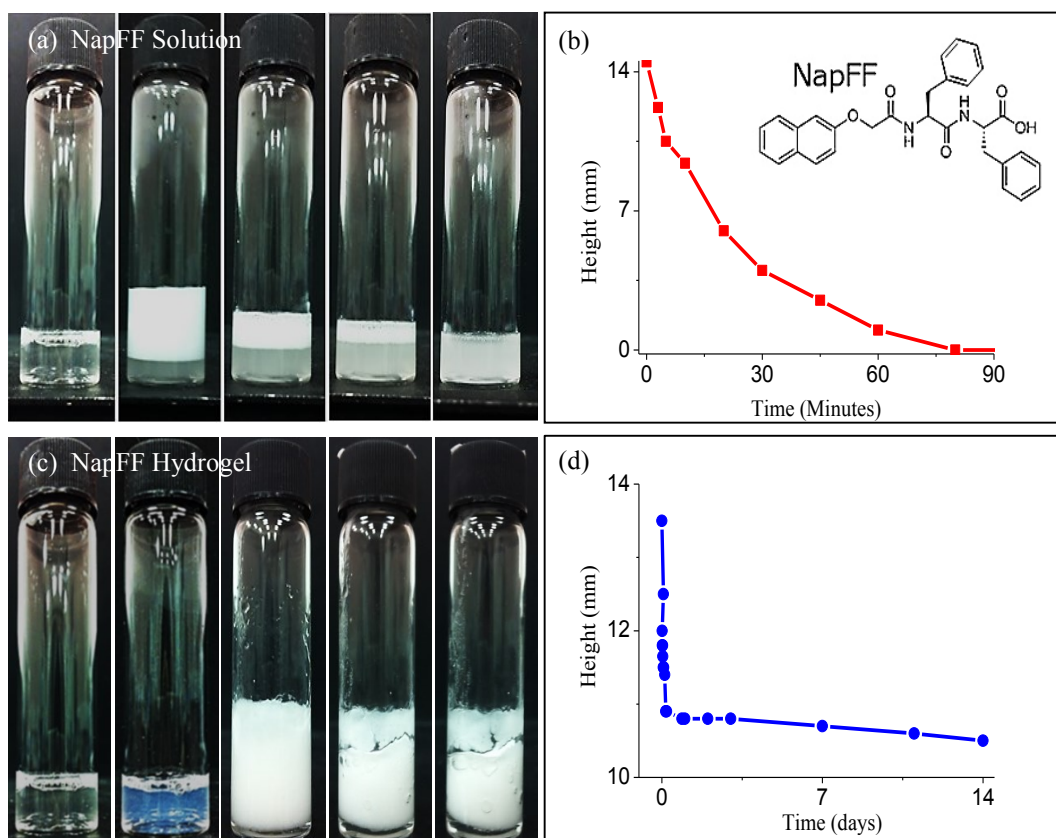
Figure 6.1 *(a) The foam-ability of NapFF solution (8mg/mL). From left to right: Solution before aerating; 3 minutes, 20 minutes, 45 minutes and 90 minutes after aerating. (b) Time dependence of the height of foam created by the dipeptide solution. The inset shows the NapFF molecules used in the experiments. (c) From left to right: NapFF solution (8mg/mL); NapFF hydrogel induced by 0.08g CaCl₂·2H₂O; a freshly prepared foam; the foam one week after preparation; the foam two weeks after preparation. (d) Time dependence of the height of foam stabilized by dipeptide hydrogel.*

Photograph of the appearance of the wet foam is given in Figure 6.2a. The foam can be extruded and shaped with a pipette, suggesting that the foam retains the gel-like character of the underlying hydrogel (*i.e.*, the foam has a yield stress). Confocal microscopy was used to study the bubbles inside a freshly prepared foam. As shown in Figure 6.2b, most bubbles are spherical shape with average diameter of 120μm. Previous studies report that one important stabilization mechanism provided by the dipeptide hydrogel is the formation of a viscoelastic physical network, *i.e.*, the gelation process, which delays drainage and protects the air bubbles against coalescence and
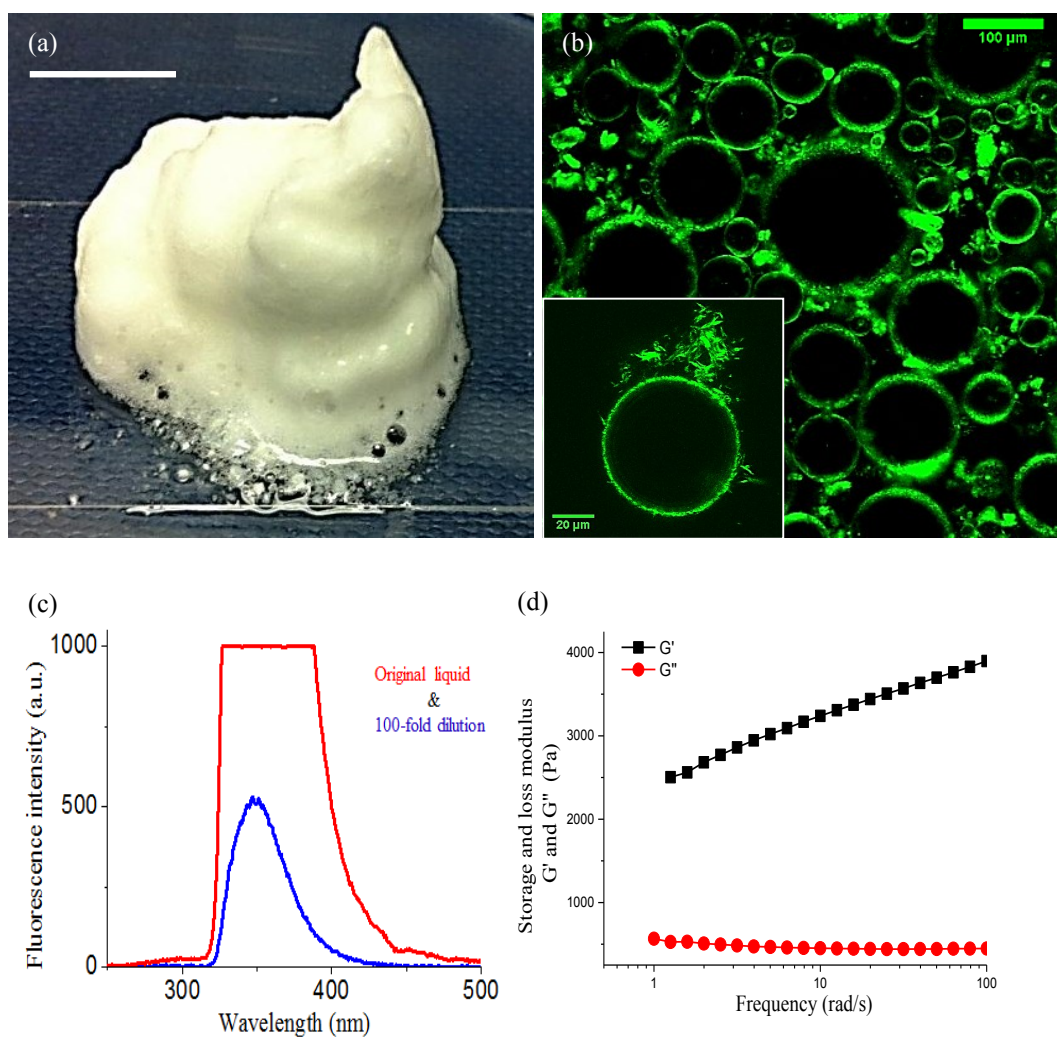
Figure 6.2 *(a) A fresh foam extruded with a pipette. The scale bar is 1 mm. (b) Confocal image of the air bubbles in the wet foam. The dipeptide is dyed using ThT. Inset: Confocal images of the self-assembled aggregations around the air bubbles. The dipeptide is dyed using ThT. (c) The Naphthalene fluorescence signal measured from the liquid phase at rest. The red curve is from the original liquid, and the blue curve is from a 100-fold dilution. (d) Response of the foam to oscillating shear plotted in the form of storage and loss moduli as a function of oscillation frequency. A foam of NapFF (8 mg mL^{-1}, 2 mL) induced by CaCl$_2$·2H$_2$O (0.08g) was prepared and left for 24 h at room temperature before the measurement.*

coarsening [8]. Here, the viscoelastic network refers not only to the gel films of self-assembled dipeptides surrounding the bubbles, but also to the aggregation of excess dipeptides within the continuous phase. When the dipeptides are labelled by ThT dye, aggregations in the continuous phase can be observed by confocal microscopy with a 63× 1.40 NA oil-immersion objective (Inset of Figure 6.2b). These aggregates are

similar to the fibre-like structures observed in the gel films at the air-water interface (see Figure 5.5). Besides the dipeptides self-assembled at the interface and in the continuous phase, excess molecules would stay in the water-rich phase at the bottom of the vial, where the fluorescence signal from Naphthalene can be measured (Figure 6.2c). The mechanical properties of the foam were further demonstrated in Figure 6.2d. Here the storage and loss moduli are presented as the frequency of the oscillating shear is varied. The storage modulus, G', is always significantly larger that the loss modulus, further proving that the foam has gel-like properties. Here as the frequency increases, the sliding of foam samples may reduce, which causes the enhancement of G' and decrease in G''. Another possibility for the increasing G' with frequency is that some air bubbles were destroyed during the measurement. This makes the samples exhibit more hydrogel properties [9].

Because of the 3D nature and the refractive index contrast of the bubbles, it is difficult to study the interfacial networks by confocal microscopy. Furthermore, nanoscale-resolution images are needed, which can be achieved by AFM, TEM or SEM. However, as mentioned earlier, the calculated liquid volume fraction of this foam is higher than 0.4. This would be a formidable specimen problem for most electron microscopies and probe microscopies. Cryo-SEM is a quick, reliable and effective way to observe some "difficult" samples with a large liquid volume fraction. It is also the most effective method of preventing sample water loss, which can be used to visualize the viscoelastic network with retention of structures.

Figure 6.3 shows the cryo-SEM images of the foam. The spectacular fibrous networks at the interface can be clearly observed (Figure 6.3a, b). The average width of a single fibre is ~200 nm (measured by hand using ImageJ), thicker than the strands in the interfacial films we created at the air-water interface (~40 nm) [10]. This is because much higher dipeptide concentration is used to self-assemble into networks in the foam. In the continuous phase, excess dipeptides were flocculated and form a three-dimensional network, which keeps the bubbles well separated (Figure 6.3c). Besides, similar to the ripples of the gel film mentioned in last chapter (shown in Figure 5.9), the surfaces of bubbles in the foam appear wrinkled as a result of buckling (Figure 6.3d). This buckling seems to be more apparent for the smaller bubbles (diameter <

100 μm), which might be caused by their larger Laplace pressure. This rippled surface has been observed in aqueous foams stabilized by nanoparticle-surfactant mixture, which was explained by the compression of a particle layer increasing the bubble's surface concentration [11].
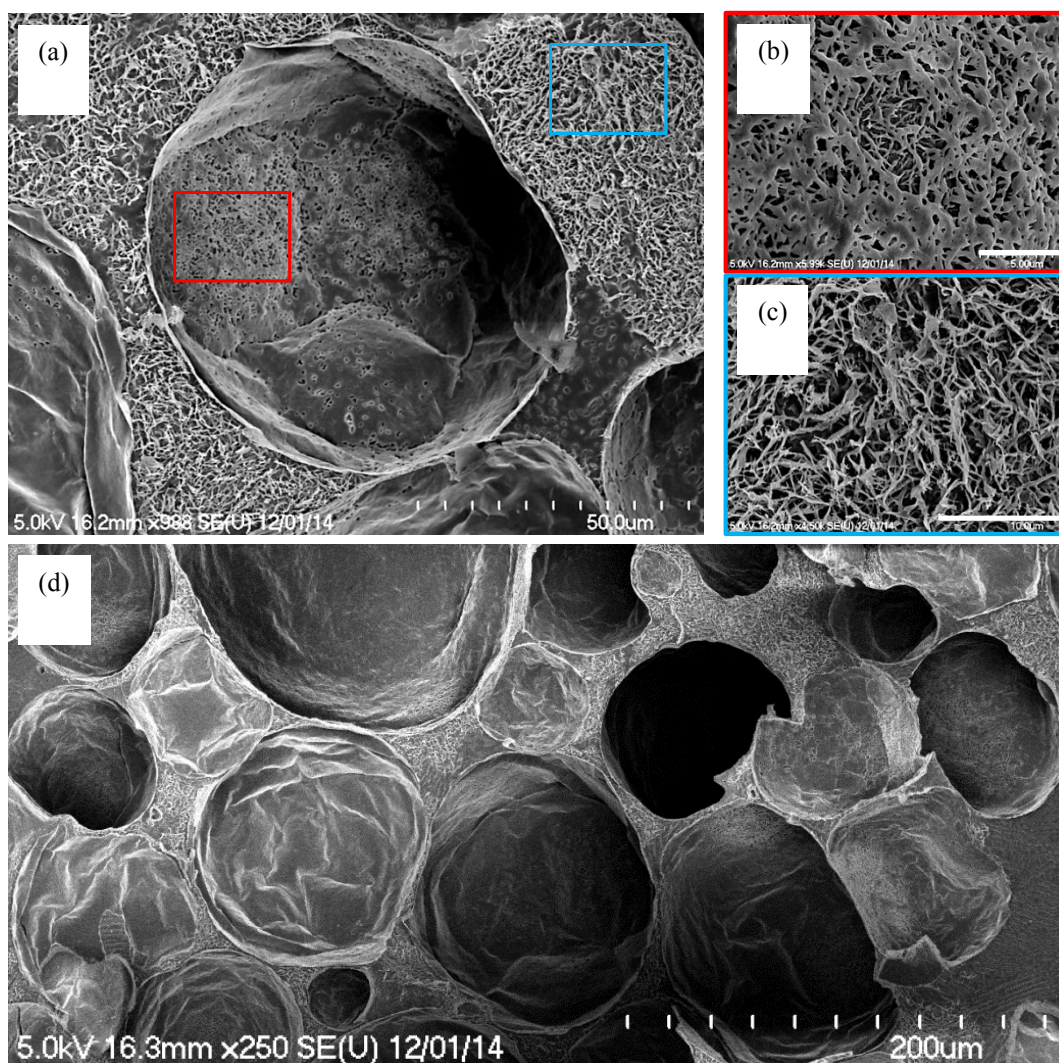
Figure 6.3 *(a) Cryo-SEM image of the hydrogel networks stabilizing the foam. (b) Interfacial networks around the air bubbles (marked red in (a)) showing the organization of the strands with greater clarity than ever previously seen. Scale bar is 5 μm. (c) The fibrous structures of the dipeptide aggregations in the continuous phase (marked blue in (a)). The scale bar is 10 μm. (d) Surface buckling of the interfacial films around the air bubbles.*
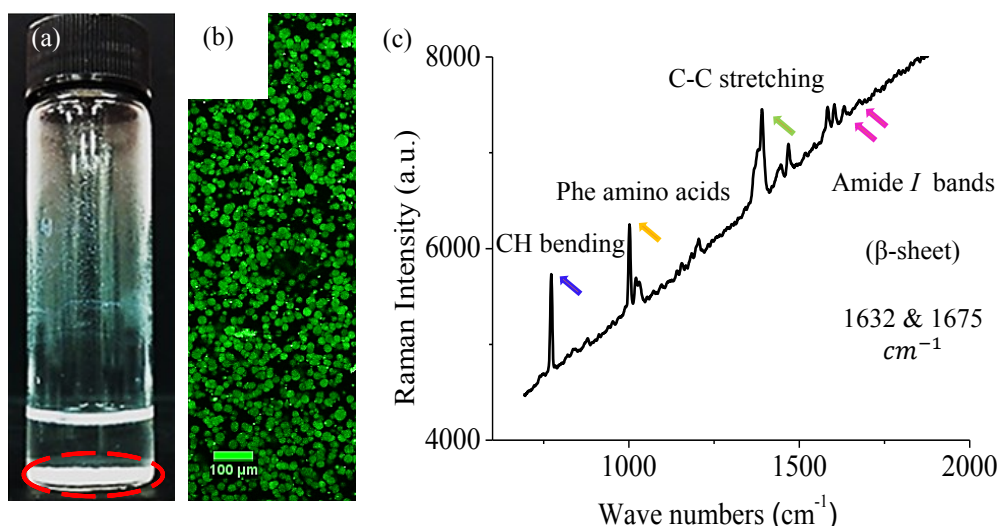
Figure 6.4 (a) BrNapAV cannot stabilize a wet foam. (b) Spherical structures in (a) at the bottom of the vial. (c) Raman spectra of the self-assembled NapFF molecules in the foam following drying on a metal substrate.

Here, the hydrophobicity of the dipeptides could be important, leading to preferential adsorption at the air-water interface which protects the air bubbles; alternatively the molecules could be flocculated in the continuous phase or in the underlying liquid (as shown in Figure 6.2d). In contrast, under the same conditions, BrNapAV (a more hydrophilic dipeptide) cannot form any network to stabilize the bubbles. The hydrophobicity of the molecules further controls their self-assembled structures. Previous studies show that BrNapAV forms spherical aggregates in solution at high pH, which cannot self-assemble into a fibre-like network [10]. Similar spherical aggregates have been observed in the foam experiments (Figure 6.4a, b). For NapFF, worm-like structures were formed before the gelation process and can be critical for the foam stabilization. In this case, the secondary structure of the foam must be investigated.

It is common for powder x-ray diffraction (PXRD) to be used to study this kind of dipeptide hydrogel. However, recent data has shown that PXRD can be inappropriate for these systems. It is very common for the gels to change conformation on drying and hence the PXRD represents a different packing to that within the gel phase [12]. In addition, the data available by IR is quite difficult to collect in the gel phase. In this case, we have focussed on Raman spectra to study the foam. Raman spectroscopy has

the ability to provide a variety of signatures of the secondary structure of self-assembled peptides. Figure 6.4c shows the Raman spectra of the wet foam. The weak peak at 1675 cm^{-1} could be indicative of β–sheet formation; a related peak has been observed in FTIR spectra of the interfacial films at the air-water interface [10]. The bands at 1003 cm^{-1}, 1030 cm^{-1}, 1205 cm^{-1}, 1583 cm^{-1} and 1602 cm^{-1} are all associated with the phenylalanine groups [13]. The bands at 772 cm^{-1}, 1390 cm^{-1}, 1446 cm^{-1}, 1468 cm^{-1} and 1632 cm^{-1} are close to those of molecular naphthalene [14]. These strong sets of peaks from the aromatic groups might suggest that they are relatively free to vibrate within the hydrogel. Indeed, the 1003 cm^{-1} phenylalanine peak has been used extensively as a signature that phenyl groups are exposed and free to vibrate [15]. These data indicates that the self-assembly might be driven primarily by hydrogen bonding between the dipeptide molecules with little role for π-π stacking in these interfacial systems.

6.3.2 The Effect of Concentrations on Foam Stability

The concentration of dipeptide molecules plays an important role in the foam stability. In the experiments, it is found that although there are excess NapFF molecules which remain in the liquid phase, a high concentration of NapFF in the foaming solution is necessary. By decreasing the concentration of NapFF, drainage occurs in the wet foam system. Figure 6.5a and b are foams with NapFF concentration of 5mg/mL and 2mg/mL, respectively. For 5mg/mL NapFF system, drainage occurs on the second day after preparation. Water leaks out of the foam macroscopically, causing the appearance of some large, irregularly shaped air bladders (Figure 6.5a). As a result, the volume of foam decreases whereas the volume of liquid phase increases. After two weeks, the foam separates from the vial wall and floats on the surface of the rest liquid. For 2mg/mL system, there is a large liquid phase just after the foaming process and the foam collapses in only one week (Figure 6.5b). Figure 6.5c shows the confocal images of the air bubbles from 5mg/mL system. During the drainage process, most bubbles are no longer spheres and tend to be pushed into one another and hence distorted. Additionally, the aggregations in the continuous phase begin to become visible. This phenomenon becomes more obvious 50 days after the foam formation, with more aggregates of dipeptides seen between the bubbles. It should be noted that
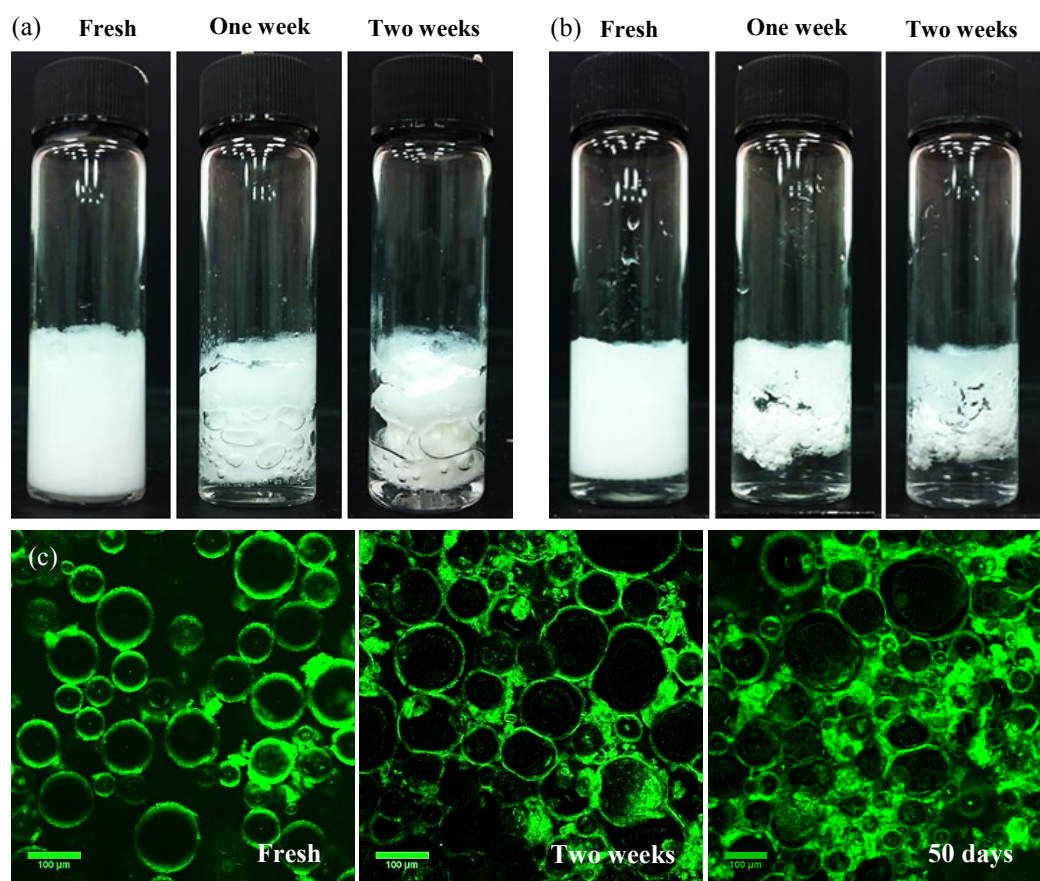
Figure 6.5 *The effect of dipeptide concentration on the foam stability. Foams are stabilized by NapFF gel with 5mg/mL (a) and 2mg/mL (b) dipeptide, respectively. Both samples have the same amount of CaCl$_2$·2H$_2$O (0.08g). Drainage can be observed after one week of foam formation. From left to right: freshly prepared foam; one week after preparation; two weeks after preparation. (c) Confocal images of the air bubbles in foam with 5mg/mL NapFF. During the drainage process, the bubbles distort and adopt non-spherical shapes, and the hydrogel in the continuous phase becomes more visible. From left to right: freshly prepared foam; two weeks after preparation; 50 days after preparation.*

although there is a wide bubble size-distribution, the average diameter of the air bubbles remains unchanged during the drainage process, which means no coalescence or coarsening takes place.

It is not surprising that reducing the concentration of metal cations also affects the foam stability. The foam height recorded as a function of time with different amount of CaCl$_2$·2H$_2$O is given in figure 6.6a. Note here that the foam height is defined as the distance between the top surface of the foam and the surface of the liquid phase. It
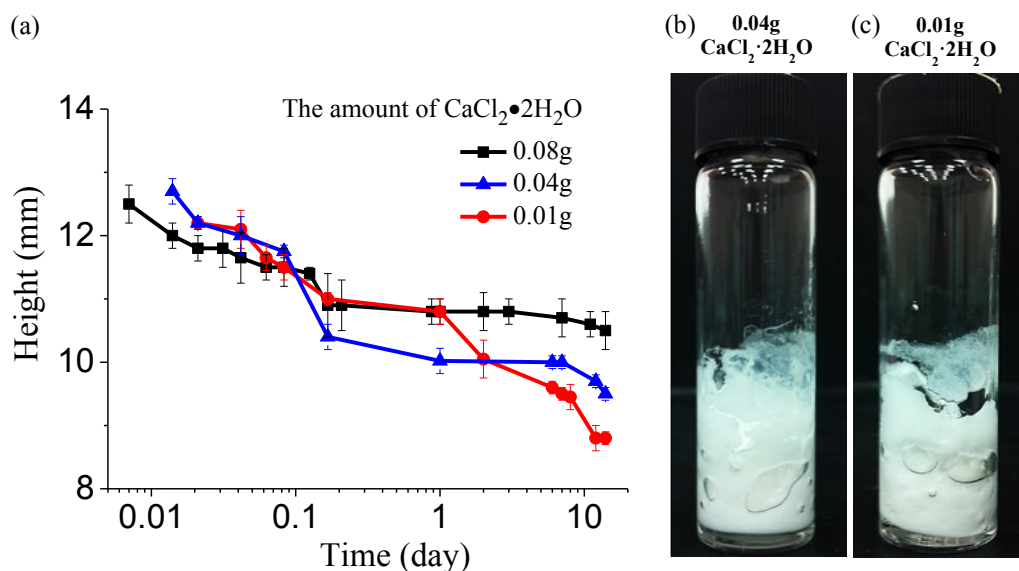
Figure 6.6 The effect of metal ions concentration on the foam stability. (a) Time dependence of the height of foams with different amount of CaCl₂·2H₂O. (b, c) Foam stabilized by 8mg/ml NapFF with 0.04g and 0.01g CaCl₂·2H₂O, respectively. Both photographs were taken one week after the preparation of the foam.

decreases noticeably within the first few hours and then remains approximately the same for more than two weeks. The long-term foam height depends on the amount of metal ions. Drainage has been observed in samples with lower metal ion concentration (figure 6.6b and c). Again, no obvious coalescence and coarsening occur during the drainage process. Here, it should be mentioned that only Ca^{2+} is studied in the concentration related experiments; another two metal ions (Mg^{2+}, K^+) will be studied in next section.

Hydrogels (no bubbles) with different amount of NapFF and CaCl₂·2H₂O were investigated to establish the origin of the decrease in foam volume (Figure 6.7a-c). Phase separation of the hydrogel and the surplus aqueous phase occurred within 10 min for all compositions. When the concentration of NapFF or Ca^{2+} was reduced, the volume of the hydrogel decreased as well. However, during the following two weeks of observation, no obvious further shrinkage or syneresis occurred in any of the gel samples. This indicates that the hydrogel itself cannot be the reason for the drainage. After six months each of the hydrogels had noticeably decreased in volume: those in
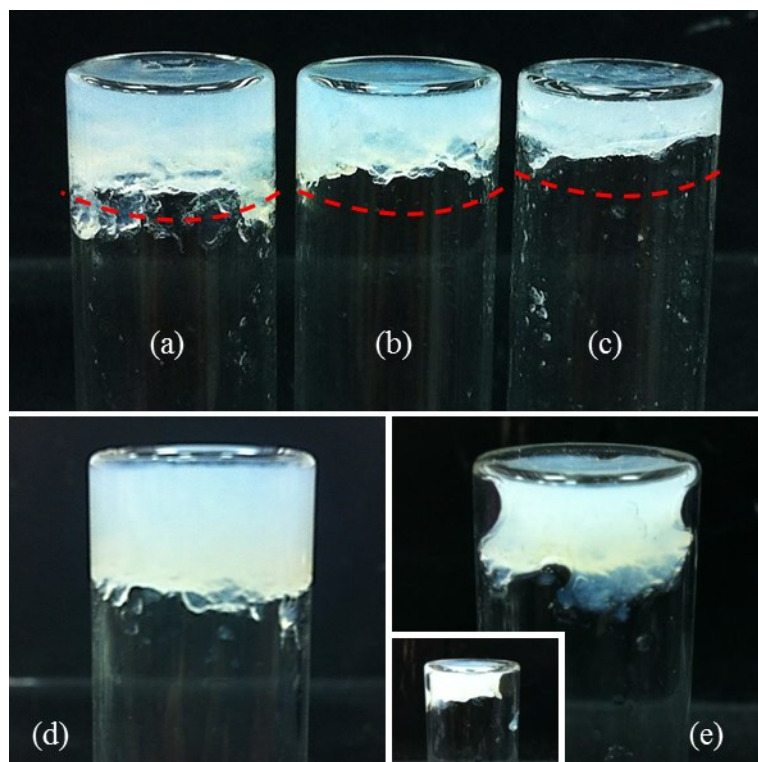
Figure 6.7 *Hydrogel (no bubbles) with different concentrations of NapFF and CaCl$_2$·2H$_2$O/MgSO$_4$. (a–c) The red dashed line indicates the total sample volume prior to inversion; the remainder of the sample volume is liquid and has descended out of the images. There is an obvious decrease in hydrogel volume with decreasing the concentration of NapFF or Ca^{2+}. (a) 2ml NapFF solution (8mg/ml) with 0.08g CaCl$_2$·2H$_2$O, the gel height is 9.1mm. (b) 2ml NapFF solution (8mg/ml) with 0.01g CaCl$_2$·2H$_2$O, the gel height is 7.5mm. (c) 2ml NapFF solution (2mg/ml) with 0.08g CaCl$_2$·2H$_2$O, the gel height is 3mm. All the samples are two weeks after preparation. No shrinkage or syneresis occurred in any of the gel samples. Some further shrinkage is observed over a timescale of months. d) NapFF (8 mg/mL) gelation induced by 0.065g MgSO4 two weeks after preparation; e) six months after preparation; inset showing the extent of shrinkage.*

Figure 6.7a, c by about 10%; the hydrogel in Figure 6.7b had undergone a more pronounced loss of volume (about 40%) and had begun to pull away from the sides of the vial. Figure 6.7d, e shows that a hydrogel induced using MgSO$_4$ also undergoes significant shrinkage over a six month period.

The bulk phase separation behaviour presented in Figure 6.7 can now be compared to the aging of the foam. The hydrogel in Figure 6.7a has the same composition (8 mg mL^{-1} NapFF; 0.08g CaCl$_2$·2H$_2$O) as the foam height data in Figure 6.6a (the black

146

curve). Evidently, the initial loss of height of the foam could be an attenuated version of the phase separation of the bulk hydrogel. However, the steady but unspectacular loss in height of the foam over subsequent days has no counterpart in the bulk hydrogel behaviour. Instead this is presumably due to slow rearrangements of bubbles leading to compaction as frequently occurs during foam aging [16]. The hydrogel in Figure 6.7b has the same composition (8 mg mL^{-1} NapFF; 0.01g CaCl$_2$·2H$_2$O) as the foam in Figure 6.6c and the height data in Figure 6.6a (the red curve). For this composition there is no equivalent in the foam of the immediate loss of ~30% of the hydrogel volume. Instead there is a steady loss of foam volume over many days. What slows the phase separation in this case (Figure 6.7b) and attenuates the volume change for Figure 6.7a? Adsorption of the dipeptide strands onto the bubble surfaces will reduce the effective concentration of dipeptide in the spaces between the bubbles. By comparing Figure 6.7a and c, we suggest this would only serve to make phase separation more pronounced. By contrast, the fixed volume of the hydrogel-rich phase, enforced by the arrangement of bubbles, may prevent (arrest) complete phase separation. The consequence is a foam sample with a composition which would be unstable for a bulk hydrogel. Some phase separation may occur over time associated with the compaction of the bubbles, with hydrogel forming between the bubbles. This compaction picture is backed up by the imaging data in Figure 6.5c which shows additional structure appearing in the continuous phase as the foam ages.

6.3.3 The Role of Hydrogel Storage Modulus on Foam Stability

NapFF dipeptides tend to form fibres under conditions in which no gel exists. The addition of Ca^{2+} leads to cross-links being formed between these fibres, which further gives rise to the gel. So far, it is demonstrated that the dipeptide hydrogel induced by Ca^{2+} could stabilize a wet foam system for weeks. The decrease of dipeptides or Ca^{2+} would reduce the hydrogel formation in the continuous phase which leads to the drainage process. However, besides the concentration of the dipeptides, the foam stability can also be related to other hydrogel components. Previous studies report that metal ions have a dramatic effect on the molecular self-assembly of the dipeptides in
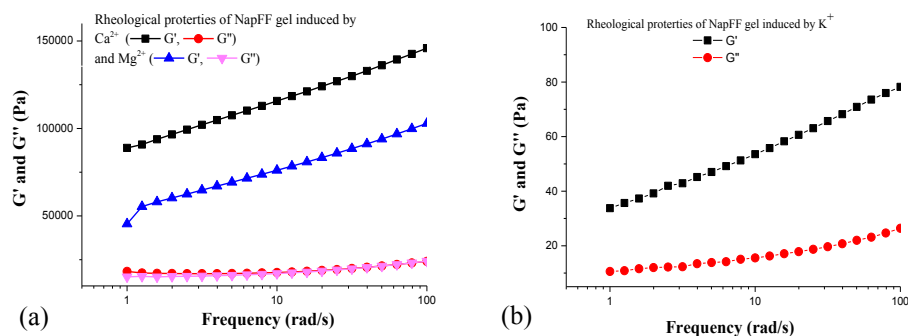
Figure 6.8. *Showing the response of the gel (without bubbles) to oscillating shear. Here the oscillation amplitude is 0.5% strain and the frequency is varied from 1-100 rad/s. Hydrogels of NapFF (8 mg/mL, 4 mL) induced by different salts were prepared and left 24 hours at room temperature before the measurement. (a) Storage, G', and loss, G", moduli for gels induced using Ca^{2+} and Mg^{2+} ions (b) Storage and loss module for gels induced using K^+ ions.*

aqueous media [7]. Divalent cations lead to gels with much higher storage moduli *G'* than monovalent cations. In particular, Ca^{2+} leads to a NapFF gel with the highest *G'*, followed by Mg^{2+}, Na^+ and K^+ [7]. Since gel plays an important role in the formation and stability of foams, it is essential to demonstrate how different gels can affect the foam behaviours.

To this end, another two salts, ―$MgSO_4$ and KCl, have been used to induce the gelation. Figure 6.8 is the storage, G', and loss, G'', moduli for their original hydrogels (no bubbles). We assume that the gel retains its native characteristics between the bubbles. If G' is smaller than the Laplace pressure (P_L), gas from the smaller bubbles (with a larger P_L) can escape and diffuse through the continuous phase to the lower pressure, larger bubbles. When G' is greater than P_L, bubbles cannot change size and hence, the gas transfer can be slowed down and eventually stopped. For a bubble of 120 μm diameter, P_L is about 10^3 Pa, while G' of a NapFF gel induced by Ca^{2+} is about 10^5 Pa [17]. As a result, the foam can be stabilized for weeks without obvious coarsening and coalescence. G' of a $MgSO_4$-induced gel is also higher than P_L, indicating that the foam can also be quite stable. However, for a gel induced by K^+, its G' ($<10^2$ Pa) is smaller than Laplace pressure ($\sim 10^3$ Pa) [7], which makes the gas transfer between bubbles possible.

Figure 6.9a shows the foam stabilized by KCl-induced gel. Over a period of one week, the diameters of air bubbles dramatically increased and some of them can even be seen suspended at the bottom of the continuous phase (marked red). The latter supports the idea that a three-dimensional network of dipeptide gel has been formed in the continuous phase. By recording a 48 hours film of the bubbles with a bright-field microscopy, the change of the diameters of air bubbles can be observed clearly (Figure 6.9b). Only large bubbles (diameter >200µm) are expanding. The other smaller ones, however, vanish by the end of the film. This is a coarsening process which involves the transport of gas from the smaller bubbles to the larger bubbles due to the difference in Laplace pressure, and increases the average bubble diameters with time.
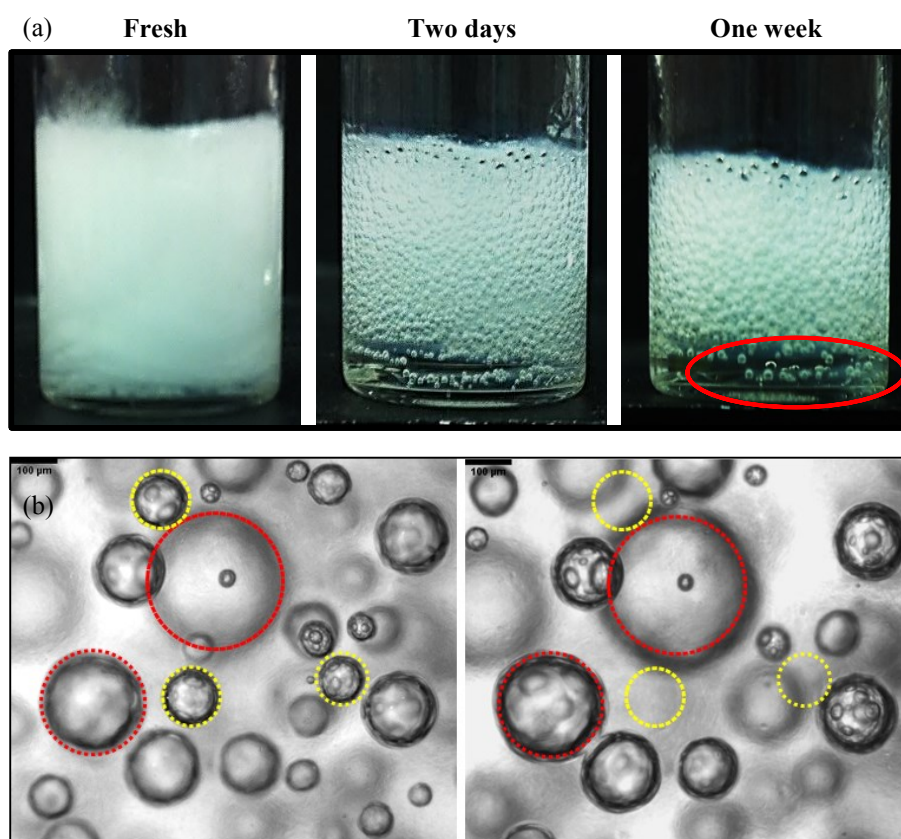
Figure 6.9 (a) The foam stabilized by KCl-induced gel. From left to right: freshly prepared foam; two days after preparation; one week after preparation. Bubbles suspending in the continuous phase are marked by the red circle. (b) Bright-field images of the air bubbles in foam (a) for 48 hours. Larger bubbles expand (marked red) whereas smaller ones shrink to vanish (marked yellow). The scale bar is 100µm.
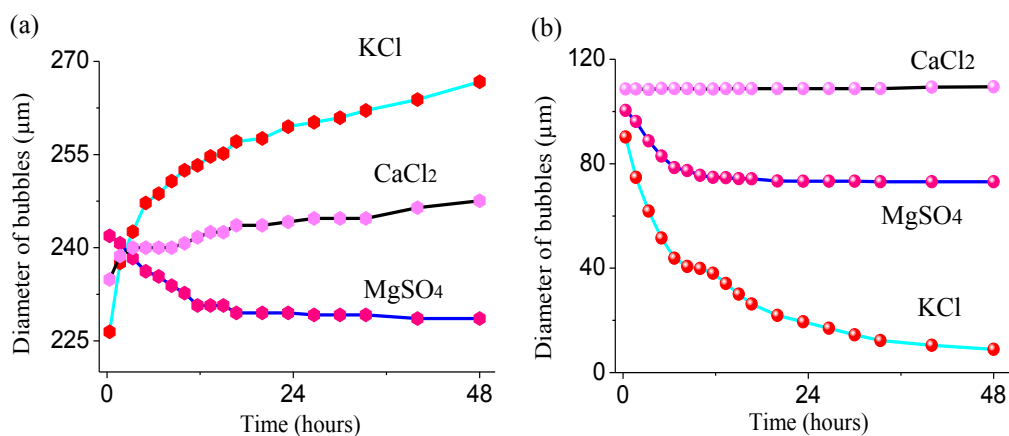
Figure 6.10 *Time dependence of the diameter of bubbles stabilized by different gel. (a) Bubbles with large diameter (~230µm). (b) Bubbles with smaller diameter (~100µm).*

Figure 6.10 shows the coarsening process of foams stabilized by all these three gels. Two average diameters (~100µm and ~230µm) have been chosen as representative small and large bubbles. The foam stabilized by KCl-induced gel exhibits a characteristic coarsening profile, with larger bubbles expanding and smaller ones shrinking; the latter vanish when all of their gas has been transferred to their large neighbours. In contrast, for the foam stabilized by $CaCl_2$-induced gel, no obvious coarsening occurs on either smaller or larger bubbles. This is consistent with the previous results. In $MgSO_4$-induced system, however, bubbles with both diameters are shrinking. Compared with K^+-induced system, this shrinkage is much slower and the bubbles would not vanish soon. Only some much larger bubbles (diameter >400µm) slightly increase their sizes. A foam prepared by $MgCl_2$ shows a similar coarsening behaviour as the $MgSO_4$-induced system, as shown in Figure 6.11. It should be noted that different representative diameters of the air bubbles can be chosen for analysis, which may make the gel effect more (or even less) evident in Figure 6.10 and 6.11e.

Structural difference can also be noticed by cryo-SEM. Even at a low dipeptide concentration (2mg/mL), there is still a clear interfacial network around the air bubbles for Ca^{2+}-induced system (Figure 6.12a). The fibres thickness, here, is about 40nm, which is smaller than Figure 6.3 since the decrease of NapFF molecules. For the foam stabilized by K^+-induced gel, no air bubbles can be seen since they are not stable in the frozen environment. However, some fibre-like structures can still be observed. These fibres are much thinner (~10nm in diameter) and very long (~10µm), and do not

cross-link with each other to form a network (Figure 6.12b). This can further cause the low storage modulus G' of K$^+$-induced hydrogel. Furthermore, some crystal structures are observed around the fibres in K$^+$-induced system (Figure 6.12c).
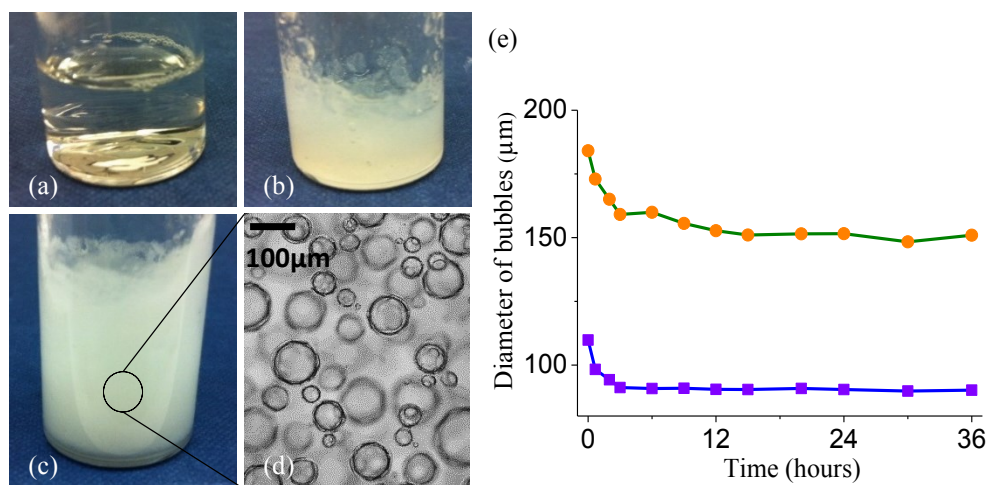
Figure 6.11 *(a) The dispersion of NapFF prior to the addition of salt. (b) The hydrogel formed due to the addition of MgCl$_2$. (c) A macroscopic image of the resulting foam. (d) A bright field image of the bubbles in the foam. (e) The bubbles exhibit a slight reduction in size with time in a similar way to the MgSO$_4$-induced system. Here diameter 115μm (orange) and 180μm (blue) have been chosen as representative small and large bubbles.*
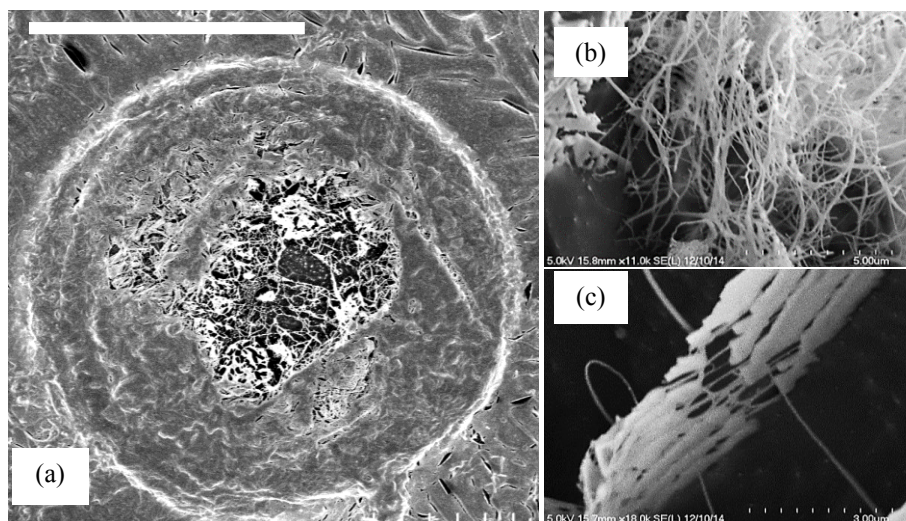
Figure 6.12 *(a) Cryo-SEM of an air bubble stabilized by Ca^{2+}-induced gel (2mg/mL NapFF with 0.08g CaCl$_2$·2H$_2$O). The scale bar is 50μm. (b) Cryo-SEM of the fibre-like structures in K+-induced system. (c) Some crystal structures are around the single fibre.*

6.4 Conclusions

It has been demonstrated that a bulk NapFF hydrogel, induced by metal cations, can be used to stabilize wet foams for more than two weeks. The mechanism involves the interfacial gel films and the continuous bulk gels, stabilizing the air bubbles from coarsening and drainage. Cryo-SEM demonstrates these fibre-like networks and the Raman spectra reveal their β-sheet order.

The foam stability is affected by the concentration of dipeptide and of metal cations. Because of the hydrophobicity of the dipeptides, the fibres preferentially form interfacial films to protect the air bubbles. Drainage occurs when less bulk gel is formed in the continuous phase. Three different metal ions have been used to study the role of gel properties. The foam stabilized by KCl-induced gel shows an obvious coarsening process, whereas the bubbles in $CaCl_2$-induced system are very stable. A much slower coarsening has been observed in $MgSO_4$-induced system. This can be explained by the different compression modulus of the interfacial layers around the bubbles, as well as the bulk gel in the continuous phase. A gel with higher compression modulus can slow down the transport of gas between the bubbles.

This is a simple and scalable method to create a wet foam with long-term stability, which also has the advantages of low cost, easy preparation and good biocompatibility. It has potential applications in food manufacturing, drug delivery and personal care industries.

Acknowledgment

References:

[1] Bai, S.; Pappas, C.; Debnath, S.; Frederix,P.W.J.M.; Leckie, J.; Fleming, S.; Ulijn, R.V. Stable Emulsions Formed by Self-Assembly of Interfacial Networks of Dipeptide Derivatives. *ACS Nano*, **2014**, *8*, 7005–7013.

[2] Gonzenbach,U. T.; Studart, A. R.; Tervoort, E.; Gauckler, L. J. Ultrastable Particle-Stabilized Foams. *Angew. Chem., Int. Ed*. **2006**, *45*, 3526−3530.

[3] Shi, J. F.; Gao, Y.; Zhang, Y.; Pan, Y.; Xu, B. Calcium Ions to Cross-Link Supramolecular Nanofibers to Tune the Elasticity of Hydrogels over Orders of Magnitude. *Langmuir* **2011**, *27*, 14425−14431.

[4] Yang, Z.; Liang, G.; Ma, M.; Gao, Y.; Xu, B. Conjugates of naphthalene and dipeptides produce molecular hydrogelators with high efficiency of hydrogelation and superhelical nanofibers. *J. Mater. Chem.*, **2007**, *17*, 850−854.

[5] Grant, G. T.; Morris, E. R.; Rees, D. A.; Smith, P. J. C.; Thom, D. Biological interactions between polysaccharides and divalent cations: the egg-box model, *FEBS Lett.*, **1973**, *32*, 195−198.

[6] Raeburn, J.; McDonald, T. O.; Adams, D. J. Dipeptide hydrogelation triggered via ultraviolet light. *Chem. Commun.*, **2012**, *48*, 9355–9357.

[7] Chen, L.; Pont, G.; Morris, K.; Lotze, G.; Squires, A.; Serpell, L. C.; Adams, D. J. Salt-induced hydrogelation of functionalised-dipeptides at high pH. *Chem. Commun.* **2011**, *47*, 12071−12073.

[8] Jung, J. M.; Gunes, D. Z.; Mezzenga, R. Interfacial Activity and Interfacial Shear Rheology of Native *β*-Lactoglobulin Monomers and Their Heat-Induced Fibers. *Langmuir* **2010**, *26*, 15366−15375.

[9] Baniasadi, M; Minary-Jolandan, M. Alginate-Collagen Fibril Composite Hydrogel. *Materials*, **2015**, *8*, 799−814.

[10] Li, T.; Kalloudis, M.; Cardoso, A. Z.; Adams, D. J.; Clegg, P. S. Drop-Casting Hydrogels at a Liquid Interface: The Case of Hydrophobic Dipeptides. *Langmuir* **2014**, *30*, 13854–13860.

[11] Binks, B. P.; Kirkland, M.; Rodrigues, J. A. Origin of stabilisation of aqueous foams in nanoparticle–surfactant mixtures. *Soft Matter* **2008**, *4*, 2373−2382.

[12] Houton, K. A.; Morris, K. L.; Chen, L.; Schmidtmann, M.; Jones, J. T. A.; Serpell, L. C.; Lloyd, G. O.; Adams, D. J. On Crystal versus Fiber Formation in Dipeptide Hydrogelator Systems. *Langmuir* **2012**, *28*, 9797−9806.

[13] L. G. Tensmeyer, E. W. Kauffman in *Spectroscopic Methods for Determining Protein Structure in Solution*, Ed. H. A. Havel, VCH, New York, **1996**, Ch. 5.

[14] Shinohara, H.; Yamakita, Y.; Ohno, K. Raman spectra of polycyclic aromatic hydrocarbons. Comparison of calculated Raman intensity distributions with observed spectra for naphthalene, anthracene, pyrene, and perylene. *J. Mol. Struct.* **1998**, *442*, 221−234.

[15] Xie, C.; Li, Y.-Q.; Tang, W.; Newton, R. J. Study of dynamical process of heat denaturation in optically trapped single microorganisms by near-infrared Raman spectroscopy. *J. Appl. Phys*. **2003**, *94*, 6138−6142.

[16] Durian, D. J.; Weitz, D. A.; Pine, D. J. Multiple Light-Scattering Probes of Foam Structure and Dynamics. *Science,* **1991**, *252*, 686−688.

[17] Chen, L.; McDonald, T. O.; Adams, D. J. Salt-induced hydrogels from functionalised-dipeptides. *RSC Adv.* **2013**, *3*, 8714−8720.

Chapter 7

Conclusions & Outlook

As introduced in Chapter 1, this thesis focuses on Langmuir films of colloids formed by self-assembly. More specifically, it is a fundamental research, investigating on the interfacial properties of rod-like colloidal materials. Monolayers of micro-scale spherocylinders were created in a Langmuir trough. Their phase transitions and interfacial behaviours under compression were studied. The dynamics of flipping process in a compressed monolayer were also discussed. For self-assembled dipeptides, which essentially form micro-scale rod-like structures, a 2D hydrogel film has been easily created at the water interface. This is an elastic film with β-sheet formation. On this basis, a wet foam system with long-term stability has been created.

Monolayers of Spherocylinders at Liquid Interfaces

Three different kinds of rod-like colloidal particles, *i.e.*, ellipsoid, cylinders and spherocylinders, were compared in chapter 2. These particles exhibit different behaviours at liquid interfaces. Specifically, cylinders create a higher capillary at their ends, leading to end-to-end configurations when several cylinders close to each other. For ellipsoids, however, the higher capillary occurs along the sides, which makes side-to-side configurations more preferable for neighbouring ellipsoids. Different from both ellipsoids and cylinders, spherocylinders would not induce any capillary interactions at liquid interfaces because of the decreasing of edge sharpness. However, in experiments, the ends of the synthesized spherocylinders are never perfectly round. Their surface defects can also cause capillary interactions. So far, the interfacial properties of micro-scale spherocylinders have not been investigated in detail.

To fulfil this need, in chapter3, we synthesize akaganéite-silica core-shell rods with different aspect ratios. They are fluorescent rods and can be observed under optical microscope. After washing them with IPA, the rods become quite hydrophobic and

can stay at the air-water interface. In a Langmuir trough, monolayers containing these rods were formed under compression. Surface pressure measurements were carried out to study these monolayers. A strong dependence of Π-*A* isotherms on the aspect ratio of the rods was observed, indicating that the phase transitions of the monolayers are related to the rods' aspect ratios. Longer rods (aspect ratio ~9 and 15) exhibit a clear gas-liquid phase transition in the measured Π-*A* isotherm, while short rods (aspect ratio ~3) as somewhat like hard spheres and somewhat like rods, with no obvious liquid phase observed.

Microscopic observations were combined with the Langmuir trough to observe the rearrangements of the rods in a compressed monolayer. Generally speaking, in response to the compressional stress, a monolayer can transform into a multilayer, buckle at the interface, or collapse into some random three-dimensional structure. In our observations, during compression, rods with aspect ratio ~9 can flip their long axes perpendicular to the interface to release some compressional stress and create more space for the monolayer. It is calculated that the energy required for supporting this flipping process is proportional to the rod's aspect ratio. More energy would be needed to flip a rod with very large aspect ratio. This is assistant with our observations. For rods with larger aspect ratio (~15), instead of flipping, they form bilayer aggregates under compression. Moreover, microscopic observations also expose that flippers typically appear in some disordered and dense regions. More ordered structures, like raft-like domains, are more stable and less likely to flip or form bilayers.

Understanding the interfacial properties of spherocylinders is important for the self-assembly of anisotropic colloidal particles at liquid interfaces. Currently, these rods are applied to stabilize ethanediol-nitromethane bijels. The mechanical properties of these bijels will then be tested by centrifugal compression and compared to those of spherical particle-stabilised bijels. It is expected that the rod-stabilised bijels will be stronger due to the rod particles forming stronger networks at interfaces. Of course flippers at interfaces to reduce the stress on the network could also affect the mechanical properties of the bijel.

Magnetic Rods in an External Field

In chapter 4, magnetic rods were converted from the akaganéite rods. XRD analysis proved that the magnetic properties of these rods are from Fe_3O_4. To measure their magnetic moment, we applied a new technique called differential dynamic microscopy (DDM), which can access the dynamics along any direction in real space. The measured magnetic moment is 1.6×10^{-15} A·m^{-2}.

It is known that, at liquid interfaces, magnetic particles subjected to a uniform constant magnetic field experience a torque, forcing their magnetic moment to be aligned with the applied field. Because of this, previous theoretical works believed that when a strong vertical field is applied, magnetic rods can flip at the liquid interface. To prove this, we spread the rods at an air-water interface and then applied a vertical field. It was observed that the tilt angle of the rods increases with the field strength. During action observation, some of the rods changed into a sphere after turning the field on, corresponding to a flipping process. To our best knowledge, this is the first time that the field-induced flipping process has been observed experimentally.

Monolayers containing these magnetic rods were formed in a Langmuir trough. A horizontal field was created to align the rods in the monolayers. The measured Π-A isotherms exhibit a steeper liquid-solid phase transition, which might be caused by the alignment of the rods. Using these rods as stabilizers, a magnetic emulsion system has been created. The droplets can be controlled to travel with a permanent magnet. It is believed that this controllable emulsion has potential in applications of novel materials and drug-delivery mechanisms.

During the DDM measurements, it was found that the rods can be oriented by the earth field. This caused some errors in the magnetic moment calculation. Future work needs to cancel the earth field, and apply a stronger external field if it is required. For the vertical field experiments, a high-speed, high-resolution CCD camera can be helpful. Creating a stable air-water interface is also important. More different field strength can be used in the calculation. For the magnetic monolayers, microscopic observations are necessary to characterize the rearrangements of the rods in an external field. Furthermore, future work can investigate the influence of a magnetic field on rods with

different size and magnetic moment, and the role played by surface tension of the subphase. This will be very helpful for the directional self-assembly of magnetic particles.

Two-Dimensional Hydrogel Films

In recent years, low molecular weight hydrogelators (LWMGs) have attracted significant attention since the simplicity and relatively low cost of the molecules, and their potential applications in various biological processes. One class of LMWGs are the dipeptides. Many dipeptide molecules can form hydrogels in bulk solution as the solvent conditions are changed. A pH change from high to low can induce gelation process since the carboxylic acid becomes protonated and hence the molecule becomes increasingly hydrophobic. This behaviour is fascinating because it is the organized supramolecular strands which are woven together to create the hydrogel. In the light of the bulk behaviour, chapter 5 in this thesis focuses on the objective that what would happen if a dipeptide in a high pH solvent was drop-cast on a liquid subphase with low pH.

By measuring the fluorescent single from the subphase, it has been proved that hydrophobic dipeptides can be trapped at an air-water interface, self-assembling an interfacial film. AFM images of the film illustrates some woven strands which exhibits beta-sheet order. Here both the dipeptide concentration and the subphase pH are critical for the gelation process. Firstly, the dipeptide concentration needs to be high enough for some fibre-like strands to have assembled in the spreading solvent. Secondly, the subphase pH must be well below the pKa of the molecule.

This hydrogel film is also an elastic sheet which exhibits a periodic wrinkle under compression, and can be used to stabilize large air bubbles for days. These results suggest that the hydrogel film offers an excellent approach to control the stability of interfaces in foams and emulsions more generally.

Therefore, in chapter 6, we investigated this stability. A wet foam system has been created using the dipeptide hydrogel as stabilizers. The mechanism involves the

interfacial gel films and the continuous bulk gels, stabilizing the air bubbles from coarsening and drainage. Instead of changing pH of the solvent, we applied metal cations to induce the gelation process. The obtained wet foam has a long-term stability.

The foam stability can be affected by the concentration of dipeptide and metal cations. Drainage occurs if less bulk gel is formed in the continuous phase. Besides the concentrations, the metal ions used in the experiments are also important. It has been reported that the compression modulus of a hydrogel induced by different metal ions varies considerably, and a gel with higher compression modulus can slow down the transport of gas between the bubbles. Because of this, in our experiments, the foam stabilized by KCl-induced gel shows an obvious coarsening process, whereas the bubbles in $CaCl_2$-induced system are very stable. A much slower coarsening has been observed in $MgSO_4$-induced system.

The presented foam system has the advantages of long-term stability, low cost, and easy preparation. It can be expected to be applied in food manufacturing, drug delivery and personal care industries.